High-performance SnTe-based Thermoelectric Materials *via* Synergistically Band and Nanostructure Engineering

Raza Moshwan

Master of Engineering Science

A thesis submitted for the degree of Doctor of Philosophy at

The University of Queensland in 2020

School of Mechanical and Mining Engineering

Abstract

Thermoelectric materials and generators, enabling to convert thermal energy into electrical energy or vice versa, offer great potentials in solving the energy problem from an environmental-sustainable perspective. As one of emerging thermoelectric materials, tin telluride (SnTe) shows uniuqe characterisitcs, such as low-toxicity and eco-friendly behaviour. The recent trend shows that band engineering and nanostructuring can enable to achieve enhanced thermoelectric performance of SnTe in the temperature range from 300 to 800 K, which provides an alternative for toxic PbTe with the same operational temperature. This thesis firstly highlights the key strategies to enhance the thermoelectric performance of SnTe materials through band engineering, carrier concentration optimization, synergistic engineering and structure design. On the basis of the fundamental analysis, the underpinnings for the property improvement are elucidated and can boost the relevant research with a view to work on further performance enhancement of SnTe materials.

While most of the reported work on SnTe uses conventional melting method, this thesis governs with the solvothermal synthesis method which has unique advantages over melting method. In solvothermal method, the reactant ions and/or molecules react in solution which can lead to different final structures of products even if the same reactants are used with the melting method. In addition to this, solvothermal method can yield well-controlled nanomaterials with low energy consumption. In theoretical perspective, it is important to see the electronic band structure of doped and undoped SnTe, hence, density functional theory calculations are preformed to see the effect of suitable dopants including In, In/Sr, In/Ag on the band structure and density of states (DOS) of SnTe. The success of the solvothermal method in this thesis with synergistic band engineering and structure engineering is summarized as follows

- To improve the thermoelectric performance of pristine SnTe, single In dopant was introduced to modify the crystal structure and band structure of SnTe. In dopant creates InTe nanoprecipiate in the $Sn_{1-x}In_xTe$ matrix and the structure of this nanoprecipitates has been clearly identified by extensive transmission electron microscopy analysis. It is found that the structure of InTe (a = 6.14 Å) is face-centred cubic which is the similar crystal structure with pristine SnTe (a = 6.32 Å). These nanoprecipitates together with the point defects and grain boundaries significantly reduce lattice thermal conductivity to ~0.45 W m^{-1} K^{-1}. Density functional theory calculation shows that the distortion of DOS (resonance energy level) near the Fermi

level leads to enhanced seebeck coefficient (S) from ~23 μV K^{-1} to ~88 μV K^{-1}. Finally, a high power factor of ~21.8 μW cm^{-1} K^{-2} and a corresponding figure of merit, a figure of merit (ZT) of ~ 0.78 have been obtained in $Sn_{0.99}In_{0.01}Te$ at 773 K.

- The co-dopants of In and Cd with extra Te were used to further improve the thermoelectric performance of pristine SnTe. In and Cd rich nanoprecipitates can be found in the SnTe matrix and can significantly ameliorate the thermal transport properties. Pisarenko plot shows higher S in the In/Cd co-doped SnTe compared with the pristine SnTe, revealing that the significant valence band convergence and the resonant energy effect co-exist in the $Sn(CdIn)_xTe_{1+2x}$. Consequently, a high ZT of ~1.12 is obtained at 773 K in the p-type $SnIn_{0.03}Cd_{0.03}Te_{1.06}$.

- A systematic theoretical and extensive experimental analyses have been successfully perceived in the In/Sr co-doped SnTe. The synergistic band and structure engineering significantly improve the electrical and thermal transport properties of $Sn_{1-3x}In_xSr_{2x}Te$. The contribution of different phonon scattering centers such as grain boundaries, point defects and nanoprecipitates on the reduction of the lattice thermal conductivity has been well understood by using phonon modelling calculations. Besides, strain field associated with the In/Sr rich nanoprecipates is also analyzed by geometrical phase analysis (GPA). As a result, a record high power factor of ~33.88 μWcm^{-1}K^{-2} and a peak ZT of ~1.31 has been achieved at 823 K for the $Sn_{0.925}In_{0.025}Sr_{0.05}Te$ pellet.

- A solvothermal synthesis method was developed to increase the solubility of In/Ag co-dopant in SnTe. It is has been found that In/Ag co-doping with appropriate dopant ratio (In:Ag = 1:2) can significantly improve the valence band convergence and resonant energy effect by using extensive density functional theory calculations. High-density strain field, dislocations, point defects and grain boundaries are observed in the matrix, which significantly scatter heat carrying phonons and yield low lattice thermal conductivity in a whole temperature range. Consequently, a high peak ZT of ~1.38 at 823 K has been achieved in $Sn_{0.85}In_{0.05}Ag_{0.10}Te$, outperforming most of SnTe-based materials.

In summary, this thesis successfully demonstrates the effectiveness of the facile and reliable solvothermal method for synthesising high-performance SnTe based thermoelectric materials by using synergistic band engineering and structure engineering. The simulation investigations on electronic transport and the phonon modeling fundamentally illustrate the

effect of the proposed concepts, which will direct the future development of other thermoelectric system.

Declaration by author

This thesis is composed of my original works, and contains no material previously published or written by another person except where due reference has been made in the text. I have clearly stated the contribution by others to jointly authored works that I have included in my thesis.

I have clearly stated the contribution of others to my thesis as a whole, including statistical assistance, survey design, data analysis, significant technical procedures, professional editorial advice, and any other original research work used or reported in my thesis. The content of my thesis is the result of work I have carried out since the commencement of my research higher degree candidature and does not include a substantial part of work that has been submitted to qualify for the award of any other degree or diploma in any university or other tertiary institution. I have clearly stated which parts of my thesis, if any, have been submitted to qualify for another award.

I acknowledge that an electronic copy of my thesis must be lodged with the University Library and, subject to the policy and procedures of The University of Queensland, the thesis be made available for research and study in accordance with the Copyright Act 1968 unless a period of embargo has been approved by the Dean of the Graduate School.

I acknowledge that copyright of all material contained in my thesis resides with the copyright holder(s) of that material. Where appropriate I have obtained copyright permission from the copyright holder to reproduce material in this thesis.

Publications included in this thesis

<u>**Moshwan, R.**</u>; Yang, L.; Zou, J.; Chen, Z.-G. Eco-Friendly SnTe Thermoelectric Materials: Progress and Future Challenges. Adv. Funct. Mater. 2017, 27, 1703278. - incorporated as **Chapter 2**.

Contributor	Statement of contribution
Raza Moshwan (Candidate)	Carried out reference summary (90 %) Wrote and edited paper (60 %)
Lei Yang	Wrote and edited paper (10 %)
Jin Zou	Wrote and edited paper (10 %) Supervised the project (40 %)
Zhi-Gang Chen	Wrote and edited paper (20 %) Supervised the project (60 %) Carried out reference summary (10 %)

<u>**Moshwan, R**</u>.; Shi, X.-L.; Liu, W.-D.; Wang, Y.; Xu, S.; Zou, J.; Chen, Z.-G. Enhancing Thermoelectric Properties of InTe Nanoprecipitate-Embedded $Sn_{1-x}In_xTe$ Microcrystals through Anharmonicity and Strain Engineering. ACS Appl. Energy Mater. 2019, 2, 2965-2971. - incorporated as **Chapter 4**.

Contributor	Statement of contribution
Raza Moshwan (Candidate)	Carried out sample synthesis (85 %) Designed experiments (60 %) Wrote and edited paper (60 %) Carried out characterization (90 %) Carried out data analysis (60 %)
Xiaolei Shi	Carried out data analysis (15 %)

Weidi Liu	Carried out sample synthesis (10 %)
Yuan Wang	Carried out characterization (5 %)
Shengduo Xu	Carried out characterization (5 %)
Jin Zou	Wrote and edited paper (30 %)
	Supervised the project (40 %)
	Carried out data analysis (20 %)
Zhi-Gang Chen	Designed experiments (40 %)
	Wrote and edited paper (10 %)
	Supervised the project (60 %)
	Carried out data analysis (5 %)

Moshwan, R.; Shi, X.-L.; Liu, W.-D.; Yang, L.; Wang, Y.; Hong, M.; Auchterlonie, G.; Zou, J.; Chen, Z.-G. High Thermoelectric Performance in Sintered Octahedron-Shaped $Sn(CdIn)_xTe_{1+2x}$ Microcrystals. ACS Appl. Mater. Interf. 2018, 10, 38944-38952. - incorporated as **Chapter 5**.

Contributor	Statement of contribution
Raza Moshwan (Candidate)	Carried out sample synthesis (70 %)
	Designed experiments (70 %)
	Wrote and edited paper (60 %)
	Carried out characterization (80 %)
	Carried out data analysis (50 %)
Xiaolei Shi	Carried out sample synthesis (15 %)
	Carried out characterization (5 %)
	Carried out data analysis (5 %)
Weidi Liu	Carried out data analysis (5 %)

	Carried out characterization (5 %)
Lei Yang	Carried out data analysis (5 %)
Yuan Wang	Carried out data analysis (5 %)
Min Hong	Carried out data analysis (5 %)
Graeme Auchterlonie	Carried out characterization (10 %)
Jin Zou	Wrote and edited paper (30 %)
	Supervised the project (40 %)
	Carried out data analysis (20 %)
Zhi-Gang Chen	Designed experiments (30 %)
	Wrote and edited paper (10 %)
	Supervised the project (60 %)
	Carried out data analysis (5 %)

Moshwan, R.; Liu, W.-D.; Shi, X.-L.; Wang, Y.-P.; Zou, J.; Chen, Z.-G. Realizing high thermoelectric properties of SnTe *via* synergistic band engineering and structure engineering. *Nano Energy* **2019,** *65,* 104056.- incorporated as **Chapter 6**.

Contributor	Statement of contribution
Raza Moshwan (Candidate)	Carried out sample synthesis (85 %)
	Designed experiments (70 %)
	Wrote and edited paper (60 %)
	Carried out characterization (70 %)
	Carried out data analysis (70 %)
Weidi Liu	Carried out characterization (10 %)
	Carried out sample synthesis (15 %)

Xiaolei Shi	Carried out characterization (20 %)
Yunpeng Wang	Carried out theoretical calculations (100 %)
	Carried out data analysis (10 %)
Jin Zou	Wrote and edited paper (20 %)
	Supervised the project (40 %)
	Carried out data analysis (30 %)
Zhi-Gang Chen	Designed experiments (30 %)
	Wrote and edited paper (20 %)
	Supervised the project (60 %)

Moshwan, R.; Liu, W.-D.; Shi, X.-L.; Qiang, S.; Gao, H.; Wang, Y.-P.; Zou, J.; Chen, Z.-G. Outstanding thermoelectric properties of solvothermal-synthesized $Sn_{1-3x}In_xAg_{2x}Te$ micro-crystals through defect engineering and band tuning. *J Mater. Chem. A* **2020** (DOI: 10.1039/c9ta11614a)**,** incorporated as **Chapter 7**.

Contributor	Statement of contribution
Raza Moshwan (Candidate)	Carried out sample synthesis (100 %)
	Designed experiments (70 %)
	Wrote and edited paper (60 %)
	Carried out characterization (50 %)
	Carried out data analysis (60 %)
Weidi Liu	Carried out characterization (20 %)
Xiaolei Shi	Carried out data analysis (5 %)
Sun Qiang	Carried out characterization (10 %)
Han Gao	Carried out characterization (10 %)

Yupeng Wang	Carried out theoretical calculations (100 %)
	Carried out data analysis (10 %)
Jin Zou	Wrote and edited paper (30 %)
	Supervised the project (40 %)
	Carried out data analysis (20 %)
Zhi-Gang Chen	Designed experiments (30 %)
	Wrote and edited paper (10 %)
	Supervised the project (60 %)
	Carried out data analysis (5 %)

Submitted manuscripts included in this thesis

No manuscripts submitted for publication

Other publications during candidature

1. Shi, X.; Wu, A.; Liu, W.; **Moshwan, R.**; Wang, Y.; Chen, Z.-G.; Zou, J., Polycrystalline SnSe with Extraordinary Thermoelectric Property via Nanoporous Design. *ACS Nano* **2018,** *12* (11), 11417-11425.

2. Liu, W.-D.; Shi, X.-L.; **Moshwan, R.**; Yang, L.; Chen, Z.-G.; Zou, J., Solvothermal Synthesis of High-purity porous $Cu_{1.7}Se$ Approaching Low Lattice Thermal Conductivity. *Chem. Eng. J.* **2019**, 121996.

3. Shi, X.; Zheng, K.; Hong, M.; Liu, W.; **Moshwan, R.**; Wang, Y.; Qu, X.; Chen, Z.-G.; Zou, J., Boosting the thermoelectric performance of p-type heavily Cu-doped polycrystalline SnSe via inducing intensive crystal imperfections and defect phonon scattering. *Chem. Sci.* **2018,** *9* (37), 7376-7389.

4. Shi, X.; Chen, Z.-G.; Liu, W.; Yang, L.; Hong, M.; **Moshwan, R.**; Huang, L.; Zou, J., Achieving high figure of Merit in p-type polycrystalline Sn0.98Se via self-doping and anisotropy-strengthening. *Energy Storage Mater.* **2018,** *10*, 130-138.

5. Liu, W.; Shi, X.; Hong, M.; Yang, L.; **Moshwan, R.**; Chen, Z.-G.; Zou, J., Ag doping induced abnormal lattice thermal conductivity in Cu2Se. *J. Mater. Chem. C* **2018,** *6* (48), 13225-13231.

6. Liu, W.-D.; Shi, X.-L.; Gao, H.; **Moshwan, R.**; Xu, S.-D.; Wang, Y.; Yang, L.; Chen, Z.-G.; Zou, J., Kinetic condition driven phase and vacancy enhancing thermoelectric performance of low-cost and eco-friendly Cu$_{2-x}$S. *J. Mater. Chem. C* **2019**.

7. Liu, W.-D.; Shi, X.-L.; **Moshwan, R**.; Sun, Q.; Yang, L.; Chen, Z.-G.; Zou, J., Effectively restricting MnSi precipitates for simultaneously enhancing the Seebeck coefficient and electrical conductivity in higher manganese silicide. *J. Mater. Chem. C* **2019,** *7* (24), 7212-7218.

8. Liu, W.; Shi, X.; **Moshwan, R.**; Hong, M.; Yang, L.; Chen, Z.-G.; Zou, J., Enhancing thermoelectric performance of (Cu$_{1-x}$Ag$_x$)$_2$Se via CuAgSe secondary phase and porous design. *Sustainable Mater.Technol.* **2018,** *17*, e00076.

Conference proceedings

1. **Moshwan, R.**; Liu, W.-D.; Shi, X.-L.; Zou, J.; Chen, Z.-G. Enhanced thermoelectric properties of SnTe-based materials. EAIT Postgraduate Conference 2017, (EPC 2017), 6th June 2017, The University of Queensland, Australia.

Contributions by others to the thesis

No contributions by others.

Statement of parts of the thesis submitted to qualify for the award of another degree

No works submitted towards another degree have been included in this thesis.

Research Involving Human or Animal Subjects

No animal or human subjects were involved in this research.

Acknowledgements

First of all, I pay my deep sense of gratitude and heartfelt thanks to my supervisors, Professor Zhi-Gang Chen and Professor Jin Zou for their valuable guidance, intensive suggestions and support throughout this research. I consider it as a great opportunity for me to learn patience, passion, and seriousness from their profound knowledge, critical thinking and fortified determination. They teach me how to be a smart, dedicated researcher with strong enthusiasm and also designing experiments and writing scientific papers.

Meanwhile, I would like to acknowledge my colleagues, Dr Xiaolei Shi, Dr Min Hong, Mr Weidi Liu, Mr Han Gao, Mr Van Nguyen, Mr Qiang Sun, Mr Shengduo Xu, Miss Yuzhe Yang, Miss Lijun Wang, Miss Wanyu Lv, Mr Youichirou Kawami, Mr Meng Li, Mr Qizhen Li, Mr Angyin Wu, Mr Junjie Li, Mr Ting Liu and Mr Zijie Lin in our research group at The University of Queensland. Thank you very much for sharing your knowledge and skills, providing great help and support in both of my research and life in Brisbane.

Last but not least, I would like to thank to my family: my dad, my mum, my wife Dr. Armina Khatun, my daughter Nusaibah Afsheen, my siblings and all my friends around the world. Their endless love and encouragement are always the great power in my life.

Keywords

Thermoelectric materials, tin telluride, solvothermal synthesis, characterization, nanostructuring, band engineering.

Australian and New Zealand Standard Research Classifications (ANZSRC)

ANZSRC code: 091205, Functional Materials, 50%

ANZSRC code: 100706, Nanofabrication, Growth and Self Assembly, 30%

ANZSRC code: 100712, Nanoscale Characterisation, 20%

Fields of Research (FoR) Classification

FoR code: 0912, Materials Engineering, 50%

FoR code: 1007, Nanotechnology, 50%

Table of Contents

to the κ; $\kappa - \kappa_e$ as a function of 1000/T for pure SnTe and $Sn_{0.91}Mn_{0.09}Te$; the dashed lines are representing the linear fitting to the $\kappa - \kappa_e$ from 300 to 900 K; deviation of thermal conductivity indicates a significant $\kappa_{bipolar}$.[42]

Figure 2.9 a) Schematic representation of the frequency dependent phonon scattering rates for various mechanisms.[124] b) Schematic illustration showing the multiple scattering centres that can be introduced into a given materials to reduce κ_l.

Figure 2.10 Schematic representation of various types of point defects: a) single doping; b) cross-substitution; c) lattice vacancy formation. d) Comparison of κ_l as a function of temperature for SnTe with different point defects.[21, 37, 38]

Figure 2.11 a) Concept of endotaxial nanostructuring in SnTe system. b) Typical HRTEM image of nanoprecipitates in $Sn_{0.96}Sb_{0.04}Te$ showing coherent interfaces, highlighted by the white circle. The corresponding inset FFT pattern proved the cubic rocksalt structure. Reproduced with permission.[34] Copyright 2016, Royal Society of Chemistry.c) κ_l and d) ZT of SnTe,[44] $Sn_{0.97}Bi_{0.03}Te$-3%SrTe[52] and Sn-Sb-Te.[34]

Figure 2.12 a) Schematic diagram of the integration of three different types of defects; atomic scale point defects, nanoscale precipitates, and mesoscale grains in one single material for all-scale hierarchical architectures of phonon scattering. Reproduced with permission.[10] Copyright 2012, Nature Publishing Group. Effect of all-scale hierarchical architecture on the thermoelectric performance of SnTe system: b) κ_l and c) ZT of SnTe[44] and SnTe-Cd-CdS.[39]

Figure 2.13 a) Phonon density of states of SnTe.[168] b) Comparison of room temperature κ_l of different doped SnTe system. Red dotted line shows the theoretical minimum κ_l.[34, 35, 37, 39, 42, 44, 53]

Figure 2.14 Electronic band structure and DOS of a) $Sn_{16}Te_{16}$ b) $Sn_{15}AgTe_{16}$ c) $Sn_{14}InTe_{16}$ d) $Sn_{14}AgInTe_{16}$ supercells as a function of wave vector in the supercell Brillouin zone. The energies are shifted with respect to the Fermi energy, which is set to zero. The band gap appears at the Γ point and heavy-hole band at Z + δ in the √2×√2×2 tetragonal supercells. The VBM and CBM occurring at the L point in the rock-salt cell of SnTe fold onto the Γ point, and the heavy-hole valence band appearing along Σ folds onto Z + δ in the case of the present 32-atom √2×√2×2 tetragonal supercell. e) Synergistic effect of In and Ag on DOS near the top of the valence band. f) Energy separations, ΔE, between the upper valence band at the Γ point and the lower valence band at the Z + δ point for pristine SnTe, In- and Ag-doped

SnTe, and In and Ag co-doped SnTe. Reproduced with permission[51]. Copyright 2016, American Chemical Society.

Figure 2.15 a) Predicted ZT values of SnTe with the valence band degeneracy at optimal n and lattice thermal conductivity to amorphous limit[90]. b) Temperature dependent ZT of SnTe based thermoelectric materials.[21, 35, 39, 44, 52, 73, 75]

Figure 3.1 Flow chart of the research work

Figure 4.1 XRD patterns of solvothermally synthesized $Sn_{1-x}In_xTe$ products. (a) Powder XRD patterns and (b) Enlarged (222) peaks of $Sn_{1-x}In_xTe$ (x = 0 %, 0.5 %, 1 %, 1.5 %, and 2 %) samples.

Figure 4.2 Characterisation of as-synthesised $Sn_{1-x}In_xTe$ samples: Typical SEM image of (a) x =1 % (b) x =1.5 % and (c) x =2 % samples. (d) SEM image of one of the In doped single crystal SnTe and (e-g) EDS maps of In, Sn, Te, respectively.

Figure 4.3 Thermoelectric properties of sintered $Sn_{1-x}In_xTe$ pellets. (a) σ, (b) S, (c) $S^2\sigma$, (d) κ, (e) κ_l, (f) ZT. Error limit 5 %.

Figure 4.4 (a) Comparative study of present result with the reported results; Pisarenko plot[41] and the reported doped samples such undoped SnTe,[51] Hg-doped SnTe,[50] Mg-doped SnTe,[52] Ca-doped SnTe,[25] Cu-doped SnTe,[51] Sb-doped SnTe,[53] Bi-doped SnTe,[54] In-doped SnTe,[41] Cd-doped SnTe,[40] Ag-doped,[26] Mn-doped SnTe,[29] and I-doped SnTe.[30] (b) Calculated density of states (DOS) of In doped and undoped SnTe samples.

Figure 4.5 Characterizations of sintered products. (a) Low magnification bright-field TEM image of sintered $Sn_{0.99}In_{0.01}Te$ sample, showing several precipitates embedded in the SnTe matrix. (b) TEM image of a typical precipitate, and inset is its EDS-line scan analysis. (c) SAED pattern showing [001] zone-axis of the matrix containing a precipitate. (d) TEM image showing interfaces between the precipitate and its SnTe matrix; (e) and (f) Enlarged HRTEM image of marked area A and B of **d**, showing coherent interface and dislocation, respectively.

Figure 4.6 Characterizations of sintered pellet. (a) HRTEM image of matrix containing nanoprecipitate with the size of ~5-10 nm (b) Enlarged view of nanoprecipitate shows edge dislocation; (c) and (d) calculated strain map associated with the nanoprecipitates.

Figure 4.7 Investigation of vibrational effect of In dopant in SnTe system. (a) Raman spectra of $Sn_{1-x}In_xTe$ (x = 0 %, 0.5 %, 1 %, 1.5 % and 2 %) (b) Schematic representation of off-centering due to In doping.

Figure 4.S1 Thermal diffusivity, D as a function of temperature for different In doped SnTe samples. Error limit 5 %.

Figure 4.S2 Calculated Lorenz number, L as function of temperature for $Sn_xIn_{1-x}Te$. Error limit 5 %.

Figure 4.S3 Calculated κ_s for $Sn_{0.99}In_{0.01}Te$ pellet with various phonon scatterings at 300 K.

Figure 5.1 Schematic illustration of the fabrication process of In/Cd co-doped $Sn(CdIn)_xTe_{1+2x}$ samples by solvothermal route and the possible phonon scattering mechanism.

Figure 5.2 Characterisation of as-synthesised and sintered $SnIn_{0.03}Cd_{0.03}Te_{1.06}$ samples: (a) Typical SEM image; inset regular octahedral-shape with eight large {111} planes. (b) SEM image of the sintered $SnIn_{0.03}Cd_{0.03}Te_{1.06}$ pellet, (c-f) EDS maps of Sn, Te, In and Cd, respectively.

Figure 5.3 Temperature-dependent thermoelectric properties of sintered $SnIn_xCd_xTe_{1+2x}$ samples. (a) σ, (b) S, (c) $S^2\sigma$, (d) κ.

Figure 5.4 Characterizations of sintered pellets. (a) XRD patterns of the sintered pellets showing extra peaks as highlighted dashed line along with the main peaks at 3 % and 4 % In/Cd co-doped samples. (b) Typical bright field TEM image of $SnIn_{0.03}Cd_{0.03}Te_{1.06}$ sintered sample shows multiple grain boundaries. (c) High-density nanoprecipitates and (c1) Moiré pattern. (d) STEM-EDS spectrum of In rich and Cd rich nanoprecipitates and the matrix.

Figure 5.5 Characterizations of sintered pellets. (a) HRTEM image showing multiple nanoprecipitates; (a1) SAED pattern along [001] zone axis, (b) Enlarged view of a nanoprecipitate as marked by red ellipse in (a), showing strain field developed around the nanoprecipitate; (b1) FFT pattern of matrix (b2) FFT pattern of the nanoprecipitate. (c) HRTEM image of a typical nanoprecipitate showing that lattice distortion occurs at the interface between nanoprecipitates and matrix, (d) Enlarged view of box area in (c).

Figure 5.6 Comparison of performance. (a) Room-temperature S *vs. n* plot of the current study and the previously reported results. Calculated S *vs. n*,[39] undoped SnTe,[68] Ag-doped SnTe,[41] Ag/In co-doped SnTe,[41] Cd-doped SnTe,[49] Cd/In doped SnTe,[49] Ca-doped SnTe,[35] Ca/In co-doped SnTe,[44] Mn-doped SnTe,[46] and Mn/In co-doped SnTe.[46] (b) Effect of doping concentration on n and μ at room temperature.

Figure 6.4 Temperature-dependent thermal transport properties of sintered $Sn_{1-3x}In_xSr_{2x}Te$ ($x = 0$ %, 0.5 %, 1 %, 1.5 %, 2 %, 2.5 % and 3 %) samples (a) κ, (b) κ_l. (error limit is 5 %) (c) Calculated spectral lattice thermal conductivity (κ_s) using Debye-Callaway model at 300 K. (d) Schematic illustration of various phonon scattering mechanisms in In/Sr co-doped SnTe system, PD (point defect), NP (nanoprecipitates), GB (grain boundaries).

Figure 6.5 (a) Typical bright field TEM image of $Sn_{0.925}In_{0.025}Sr_{0.05}Te$ sintered sample shows multiple crystal imperfection (inset is the low magnification TEM image). (b) Selected area electron diffraction (SAED) pattern along [001] zone axis (c) High resolution transmission electron microscopy (HRTEM) image showing numerous nanoprecipitates in SnTe matrix (d) Enlarged view of a nanoprecipitate shows strain and inset is the calculated strain map associated with the nanoprecipitate.

Figure 6.6 (a) Temperature dependent (a) n (error limit is 15 %) (c) μ, and (c) ZT values of $Sn_{1-3x}In_xSr_{2x}Te$ ($x = 0$ %, 0.5 %, 1 %, 1.5 %, 2 %, 2.5 % and 3 %) samples (error limit is 5 %) (b) A comparative thermoelectric performance of the current work and the previously reported results [34, 40, 42-43, 68].

Figure 6.S1 Thermal diffusivity D as a function of temperature for different $Sn_{1-3x}In_xSr_{2x}Te$ samples.

Figure 6.S2 Calculated Lorenz number L as function of temperature of $Sn_{1-3x}In_xSr_{2x}Te$.

Figure 6.S3 Temperature dependent electronic thermal conductivities of $Sn_{1-3x}In_xSr_{2x}Te$.

Figure 6.S4 Average ZT values of the current work and the previously reported work; SnTe system (300 K – 823 K).[1-6]

Figure 7.1 (a) Typical SEM micrograph of $Sn_{1-3x}In_xAg_{2x}Te$ ($x \leq 3\%$) powders; (b) enlarged image of highlighted area of (a) shows the regular {111} planes of the as-synthesized crystal. (c) SEM micrograph of $Sn_{1-3x}In_xAg_{2x}Te$ ($x \geq 5\%$) powders; (d) enlarged image of highlighted area of (c) shows severe deformation of regular crystal shapes; (e) a typical SEM image of the sintered $Sn_{0.85}In_{0.05}Ag_{0.10}Te$ pellet; (f) corresponding EDS spectra of spot A and B of (e), showing significant peaks of Sn, Te, In and Ag.

Figure 7.2 (a) XRD patterns of the sintered $Sn_{1-3x}In_xAg_{2x}Te$ ($x = 0\%$, 1.0%, 3.0%, 5.0% and 6%) pellets. (b) Calculated lattice parameter with respect to In/Ag co-doping concentration

Figure 7.3 Electrical transport properties of sintered $Sn_{1-3x}In_xAg_{2x}Te$ ($x = 0\%$, 1.0%, 3%, 5%, and 6%) samples: (a) σ, (b) n and μ, (c) m^* (d) E_{def} (e) S, and (f) $S^2\sigma$. (error bar 5%).

List of Tables

List of Abbreviations

CBM: conduction-band minimum

DOS: density of state

DFT: density functional theory

EDS: energy dispersive X-ray spectroscopy

EG: ethylene glycol

EPMA: electron probe micro analysis

ESI: electronic supplementary information

FFT: fast Fourier transform

FIB: focused ion beam

GGA: generalized gradient approximation

HAADF: high angle annular dark field

HP: hot-pressing

HRTEM: high-resolution transmission electron microscopy

JCPDS: the joint committee on powder diffraction standards

PBE: the Perdew-Burke-Ernzerhof functional

SAED: selected area electron diffraction

SEM: scanning electron microscopy

SPB: single parabolic band

SPS: spark plasma sintering

STEM: scanning transmission electron microscopy

TEM: transmission electron microscopy

VASP: Vienna *Ab initio* Simulation Package

VBM: valence-band minimum

XRD: X-ray diffraction

Chapter 1. Introduction

In this chapter, a background of current global energy dilemma and a brief summary of state-of-art thermoelectric materials including SnTe are presented, followed by the objectives and scopes of this thesis. In the end of this chapter, the thesis outline is described.

1.1 Background

The advancement in human civilization strongly related with the energy. Utilizing fossil fuel (oil, coal, and natural gas) combustion as energy sources by heat engines is about 90 % of the world's total power production.[1-2] The maximum conversion efficiencies of most electricity-generation devices is about 40 % or lower and vast majority is lost as waste heat to the environment.[1, 3] The scarcity of natural resources has limitation to meet the ever-growing energy demand.[2, 4] Therefore, seeking for new technologies for energy harvesting are urgent to address the global energy crisis.[1-3, 5] Thermoelectric materials, which has potential to covert heat directly into electricity, can be a robust candidate for making full use of this large scale waste heat.[6-12]

As a solid-state energy conversion technique thermoelectric energy converters possess zero pollution and long-time operational reliability. These thermoelectric devices can be used as refrigerator too, such as cooling computers, infrared detectors, electronics and other equipment. Thermoelectric materials can also be incorporated in photovoltaic cells to harvest solar energy to a great extent, thereby provide promising solution for solar panel.[5, 13-14] Radioisotope thermoelectric generator has recently been used in Mars *Curiosity* rover space probes to generate electricity whose heat source was a radioactive element.[2] The fuel efficiency of a car in automotive industry can be increased by its waste heat harvesting. In this regard, the replacement of alternators in cars by thermoelectric generators can trigger the 3.25 % reduction in fuel consumption that saves billions of dollars annually.[1, 15]

It is now clear that there is large potential market for thermoelectric materials far beyond the few applications discussed here. However, the low efficiency of existing thermoelectric materials hinders to use on a large scale. Some materials are toxic and environmental unfriendly. Hence, selecting the right materials system and synthesis method is of crucial important to fabricate high efficient thermoelectric devices. Complex alloys, metal chalcogenides and materials with complicated crystal structures such as clathrates[16] and skutterudites[17] are well known good thermoelectric materials so far. Improvement of the existing materials as well as seeking for new materials systems with high efficiency is a big challenge. Hence, it is worth to understand the behaviour of electronic and thermal transport properties by extensive experimental and theoretical works which may offer a new approach to achieve high performance thermoelectric materials and can play a crucial role for power generation and refrigeration in near future.

1.2 Objective and Scopes

In the industrial and automotive sectors, most of the waste heat produced is in the temperature range of 500-900 K. Therefore, it is necessary to develop high performance mid-temperature range (400-800 K) thermoelectric materials in order to recover this waste heat. For this purpose, lead telluride (PbTe) and its alloys are considered as a primary focus material. However, the toxicity is associated with this material causes severe threat to the environment and need to be alternated for domestic usage. Hence, as an analogue of PbTe, SnTe possesses similar electronic band structure and rock-salt crystal structure with PbTe, which made it possible to similar temperature range application. Moreover, SnTe is non-toxicity, abundancy and environment friendly, which makes it as a great alternative of PbTe. Intrinsic SnTe has inherent Sn vacancies, a high hole concentration (n) with an n of $\sim 10^{20}$ to 10^{21} cm^{-3} and leading to a poor S with ZT of 0.5 at 900 K. The main goal of this thesis is to enhance the thermoelectric properties of SnTe through nanostructuring, compositional tuning and band engineering. We also understand the decrease in lattice thermal conductivity by phonon modelling studies.

1.3 Thesis Outline

To develop high performance SnTe based thermoelectric materials we adopted high energy efficient, facile and controllable solvothermal synthesis method. The phase composition and structural properties are extensively investigated by advanced electron microscopy and other methods. The electrical and thermal transport properties of the synthesized sintered samples have been carefully executed. Additionally, we provide some band engineering calculation and phonon modelling studies in some cases.

Based on these results, this thesis is organized as follows

Chapter 1 is the introduction part; highlight the necessity of developing thermoelectric materials, the potential aspects of practical applications, and the goal of this research project.

Chapter 2 is the literature review. We demonstrated the fundamental of thermoelectricity, how does it work, the parameters that govern thermoelectric performance. We summarized the recent progress of SnTe based thermoelectric materials and its future challenges. This chapter is based on the paper published in Advanced Functional Materials journal, which is already cited 92 times.

Chapter 3 is the methodology and approach. Here, we presented the experimental details in this thesis, including equipment used for electrical and thermal transport property measurements, electronic microscopy such as SEM, TEM, Raman spectroscopy for characterization of synthesized and sintered samples.

Chapter 4 presents the improved thermoelectric performance in SnTe due to In resonant doping. This chapter is based on the paper published in ACS Applied Energy Materials journal.

Chapter 5 illustrates the enhanced performance of In/Cd co-doped SnTe system by rationally designing the nanostructures. This chapter is based on the paper published in ACS Applied Materials & Interfaces journal.

Chapter 6 shows the realizing high thermoelectric properties of SnTe via synergistic band engineering and structure engineering. This chapter is based on the paper published in Nano Energy.

Chapter 7 incorporate with the enhanced thermoelectric transport properties of In/Ag co-doped SnTe system *via* defect engineering and band tuning. This chapter is based on the paper published in Journal of Materials Chemistry A.

Chapter 8 draws the conclusions of this thesis and point out the potential future directions.

References

(1) Yao, C.-J.; Zhang, H.-L.; Zhang, Q. *Polymers* **2019**, *11*, 107.

(2) Beretta, D.; Neophytou, N.; Hodges, J. M.; Kanatzidis, M. G.; Narducci, D.; Martin-Gonzalez, M.; Beekman, M.; Balke, B.; Cerretti, G.; Tremel, W.; Zevalkink, A.; Hofmann, A. I.; Müller, C.; Dörling, B.; Campoy-Quiles, M.; Caironi, M. *Mater. Sci. Eng. R* **2018**.

(3) Patil, D. S.; Arakerimath, R. R.; Walke, P. V. *Renew. Sust. Energ. Rev* **2018**, *95*, 1-22.

(4) Moshwan, R.; Yang, L.; Zou, J.; Chen, Z.-G. *Adv. Funct. Mater.* **2017**, *27*, 1703278.

(5) Shen, Z.-G.; Tian, L.-L.; Liu, X. *Energ. Convers. Manage* **2019**, *195*, 1138-1173.

(6) Ando Junior, O. H.; Maran, A. L. O.; Henao, N. C. *Renew. Sust. Energ. Rev* **2018**, *91*, 376-393.

(7) Moshwan, R.; Shi, X.-L.; Liu, W.-D.; Wang, Y.; Xu, S.; Zou, J.; Chen, Z.-G. *ACS Appl. Energy Mater.* **2019**, *2*, 2965-2971.

(8) Hong, M.; Wang, Y.; Feng, T.; Sun, Q.; Xu, S.; Matsumura, S.; Pantelides, S. T.; Zou, J.; Chen, Z.-G. *J. Am. Chem. Soc.* **2019**, *141*, 1742-1748.

(9) Moshwan, R.; Shi, X.-L.; Liu, W.-D.; Yang, L.; Wang, Y.; Hong, M.; Auchterlonie, G.; Zou, J.; Chen, Z.-G. *ACS Appl. Mater. Interf.* **2018**, *10*, 38944-38952.

(10) Hong, M.; Chen, Z. G.; Yang, L.; Liao, Z. M.; Zou, Y. C.; Chen, Y. H.; Matsumura, S.; Zou, J. *Adv. Energy Mater.* **2018**, *8*, 1702333.

(11) Tan, G.; Zhao, L.-D.; Kanatzidis, M. G. *Chem. Rev.* **2016**, *116*, 12123-12149.

(12) Sadia, Y.; Ohaion-Raz, T.; Ben-Yehuda, O.; Korngold, M.; Gelbstein, Y. *J. Solid State Chem.* **2016**, *241*, 79-85.

(13) Allouhi, A. *Sol. Energ. Mat. Sol. C.* **2019**, *200*, 109954.

(14) Irshad, K.; Habib, K.; Saidur, R.; Kareem, M. W.; Saha, B. B. *Journal of Cleaner Production* **2019**, *209*, 1376-1395.

(15) Fairbanks, J. W. In *Automotive thermoelectric generators and air conditioner/heaters*, Program and Abstracts of the Advanced Research Workshop on Recent Trends and Prospects for Renewable Energy: From Low-Dimensional Functional Materials to Innovation Management, Uzbekistan, Turin Polytechnic University in Tashkent: Uzbekistan, 2012; p 23.

(16) Iversen, B. B.; Palmqvist, A. E. C.; Cox, D. E.; Nolas, G. S.; Stucky, G. D.; Blake, N. P.; Metiu, H. *J. Solid State Chem.* **2000**, *149*, 455-458.

(17) Rull-Bravo, M.; Moure, A.; Fernández, J. F.; Martín-González, M. *RSC Adv.* **2015**, *5*, 41653-41667.

Chapter 2. Literature Review

In this chapter, we aim to provide a thorough summary of current research on structural characteristics, theoretical calculations, syntheses, characterizations, and thermoelectric performance of doped and undoped SnTe based thermoelectric materials. On this basis, we also discuss the challenges and strategies toward future enhancements of the thermoelectric performance of SnTe-based materials.

-Published as **Moshwan *et al.***, Eco-Friendly SnTe Thermoelectric Materials: Progress and Future Challenges. *Adv. Funct. Mater.* **2017,** *27*, 1703278.

2.1 Introduction

Thermoelectric materials, converting between heat and electricity without any emissions or vibrational parts, offer a sustainable solution to overcome the upcoming energy crisis.[1] The thermoelectric conversion efficiency is governed by the dimensionless figure of merit, ZT,[1]

$$ZT = \frac{S^2 \sigma T}{k} = \frac{S^2 \sigma T}{k_l + k_e + k_{bipolar}}$$ (2-1)

where S is the Seebeck coefficient, σ is the electrical conductivity, T is the absolute temperature, and κ is the thermal conductivity including the electrical (κ_e), lattice (κ_l) and bipolar ($\kappa_{bipolar}$) components.

To achieve high ZT value, a large power factor ($S^2\sigma$) and/or low κ should be secured, in which a large $S^2\sigma$ implies the high heat-electricity conversion efficiency of charge carriers while a low κ indicates the ability of remaining the suitable temperature gradient.[2] In general, S, σ and κ_e are coupled by the carrier concentration n,[3] and can be expressed as,[4]

$$S = \frac{8\pi^2}{3} \frac{k_B^2}{eh^2} m^* T \left(\frac{\pi}{3n}\right)^{2/3},$$ (2-2)

$$\sigma = ne\mu, \text{ and}$$ (2-3)

$$\kappa_e = L\sigma T,$$ (2-4)

where k_B, e, h, m^*, μ, L are the Boltzmann constant, the carrier charge, the Planck's constant, the effective mass of the charge carrier, the carrier mobility, and the Lorenz number, respectively. As can be seen, S, σ and κ_e are interacted and conflict, which raises the difficulty to obtain high ZT. To solve these conflicts, extensive research has been carried out through band engineering to optimize S and σ,[5-7] and structuring to reduce the κ_l.[8-12] **Figure 2.1a** summarises recent significant achievements, from which the current ZT values of the thermoelectric materials are lies between 1 and 2,[7, 13-23] resulting in that the current thermoelectric energy conversion efficiency is comparable to the other energy conversion technologies, such as photovoltaic cells,[22] and solar thermal plants.[22] Considerable research has been continuing to further drive ZT higher than 2 with the predicted efficiency over 20%,[24, 25] which can attract highly exciting prospect in the energy generation and conservation fields.

In term of the industrial and automotive applications, waste-heats are generally produced in the temperature range of 500 - 900 K.[26-28] To recover such waste heats, developing of high

performance mid-temperature (400 - 900 K) thermoelectric materials is highly desired. For this purpose, lead telluride (PbTe) and its alloys have been considered as a primary material system.[7, 10, 14, 17, 29] However, the toxicity associated with Pb causes severe threat to the environment and need to be alternated for domestic usage.[30] Hence, as its analogue, tin telluride (SnTe)[21, 30-44] with the rock-salt crystal structure has been inspired with great interests.[32] Especially, SnTe is non-toxic, earth-abundant, and environment friendly,[45] which makes it a great alternative of PbTe in the real industry applications.[30] Compare to PbTe, intrinsic SnTe has inherent Sn vacancies and a high hole concentration of $\sim 10^{20}$ to $\sim 10^{21}$ cm^{-3},[46] leading to a low S.[47, 48] However, with the effective approaches, including band engineering[31-33, 36, 49-51] and nanostructuring,[34, 52] significant ZT improvements of SnTe have been achieved. **Figure 2.1b** and **Table 2.1** summarize the recent achievements and it can be seen that the ZT value of pristine SnTe can be enhanced as high as 1.6 through Cu$_2$Te alloying,[53] which is competitive with most of the other thermoelectric material systems.[19, 54, 55] Such a significant progress has made SnTe as a robust candidate to replace PbTe-based thermoelectric materials. Hence, SnTe and its alloys have become a key material system for further research due to their potentials in green energy applications.

In this review, firstly we highlighted the key strategies to enhance the thermoelectric performance of SnTe and then we proposed the future development of SnTe associated structures through synergetic optimization, which will guide and inspire researchers to explore advanced SnTe based thermoelectric materials.
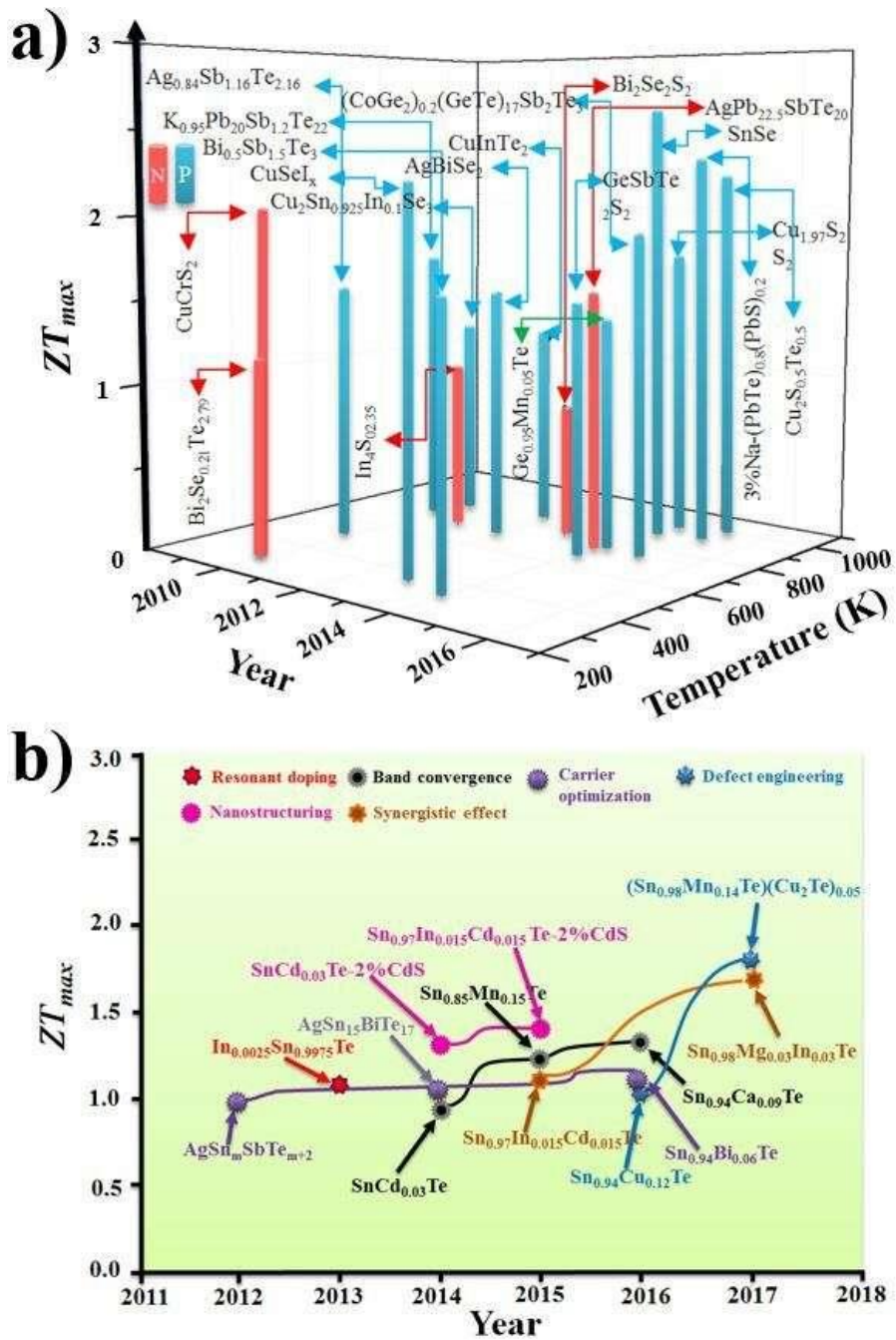
Figure 2.1 (a) State of-the-art of bulk thermoelectric materials over the last few years. Green and red cylinders represent the *p*-type and *n*-type materials, respectively. $Ag_{0.84}Sb_{1.16}Te_{2.16}$,[56] $K_{0.95}Pb_{20}Sb_{1.2}Te_{22}$,[57] $Bi_{0.5}Sb_{1.5}Te_3$,[58] $Cu_2Sn_{0.925}In_{0.1}Se_3$,[59] $Cu_2Se_{1-x}I_x$,[24] $(CoGe_2)_{0.2}(GeTe)_{19}Sb_2Te_3$,[60] $CuCrS_2$,[61] $Bi_2Se_{0.21}Te_{2.79}$,[62] $In_4Se_{2.35}$,[63] $(Ba,La,Yb)_xCo_4Sb_{12}$,[64] $AgBiSe_2$,[65] $FeNb_{1-x}Ti_xSb$,[66] $FeNb_{1-x}Hf_xSb$,[67] $Bi_2Se_1S_2$,[68] $AgPb_{22.5}SbTe_{20}$,[69] $SnSe$,[25] $3\%Na$-$(PbTe)_{0.8}(PbS)_{0.2}$,[70] $Cu_2S_{0.5}Te_{0.5}$,[71] $GeSbTe$,[72] (b) Recent progress in SnTe-based thermoelectric materials; $(Sn_{0.98}Mn_{0.14}Te)(Cu_2Te)_{0.05}$,[73] $Sn_{0.98}Mg_{0.03}In_{0.03}Te$,[74] $Sn_{0.97}In_{0.015}Cd_{0.015}Te$,[21] $In_{0.0025}Sn_{0.9975}Te$,[44] $SnCd_{0.03}Te$-$2\%CdS$,[39] $Sn_{0.97}In_{0.015}Cd_{0.015}Te$-$2\%$

CdS,[21] SnCd$_{0.03}$Te,[39] Sn$_{0.85}$Mn$_{0.15}$Te,[75] Sn$_{0.94}$Ca$_{0.09}$Te,[31] AgSn$_m$SbTe$_{m+2}$,[76] AgSn$_{15}$BiTe$_{17}$,[37] and Sn$_{0.94}$Bi$_{0.06}$Te.[77]

Table 2.1 Recently reported thermoelectric properties of SnTe based materials

Material system	Carrier type	$S^2\sigma$ (µWcm^{-1}K^{-2})	κ (Wm^{-1}K^{-1})	κ_l (Wm^{-1}K^{-1})	ZT	Synthesis method	Temperature (K)	Ref.
Sn$_{0.94}$Ca$_{0.09}$Te	P	26	2	~0.78	1.35	Melting	873	31
In$_{0.015}$Sn$_{0.985}$Te$_{0.85}$Se$_{0.15}$	P	~19.2	-	-	~0.8	Melting	860	30
Sn$_{0.95}$Ag$_{0.05}$Te$_{0.95}$I$_{0.05}$	P	~25	~2	~1.2	~1.05	Melting	860	32
Sn$_{0.94}$Mg$_{0.09}$Te	P	~30.3	~2.2	~0.78	~1.2	Melting	860	33
SnAg$_{0.025}$In$_{0.025}$Te$_{1.05}$	P	~31.4	~2.73	~1.18	≈1	Melting	856	51
Sn$_{0.85}$Sb$_{0.15}$Te	P	~22	~1.9	-	~1	Melting	800	34
SnMn$_{0.07}$Te	P	~26	~2	~1.38	~1.25	Melting	920	49
SnCd$_{0.12}$Te	P	~25	~2	~1.25	~1.03	Melting	820	78
Sn$_{0.85}$Mn$_{0.15}$Te$_{0.98}$I$_{0.02}$	P	-	~1.6	~1	~1.3	Melting	900	75
Nano sized SnTe	P	~13.5		0.6	0.49	Hydrothermal	803	79
In$_{0.005}$Sn$_{0.995}$Te (annealed)	P	-	~2	~0.61	0.92	^{a}SHS-^{b}PAS	920	80
Sn$_{0.94}$Cu$_{0.12}$Te	P	-	~1.8	~0.5	~1.05	Melting	850	53
Sn$_{0.98}$Bi$_{0.02}$Te-3%HgTe	P	~28	~2	~0.68	~1.35	Melting	910	35
Sn$_{0.88}$Mn$_{0.12}$Te	P	~21.4	~1.48	~0.96	1.3	Melting	900	36
Sn$_{0.97}$In$_{0.015}$Cd$_{0.015}$Te-2% CdS	P	~23	~1.62	~0.6	~1.4	Melting	923	21
AgSn$_{15}$BiTe$_{17}$	P	~23.1	~1.9	~0.7	~1.1	Melting	775	37

(SnTe$_{0.994}$I$_{0.006}$)$_{2.88}$ (In$_2$Te$_{2.982}$I$_{0.018}$)$_{0.04}$	P	~24.3	~2.5	~0.6	~1.1	Melting	923	[38]
SnCd$_{0.03}$Te	P	~19	~1.8	~1	~0.96	Melting	823	[39]
SnCd$_{0.03}$Te-2% CdS	P	~18	~1.25	~0.65	~1.3	Melting	873	[39]
SnCd$_{0.03}$Te-2% ZnS	P	~16	~1.3	~0.75	~1.1	Melting	873	[39]
Sn$_{0.926}$In$_{0.037}$Cd$_{0.037}$Te	P	-	-	-	~1.8	Calculation	920	[40]
Sn$_{0.93}$Mn$_{0.04}$Te	P	~18.7	-	-	~1.32	Calculation	800	[41]
Sn$_{0.93}$Cd$_{0.04}$Te	P	~34.5	-	-	~1.65	Calculation	750	[41]
Sn$_{0.83}$Mn$_{0.17}$Te	P	~24	~1.5	~0.65	1.3	Melting	900	[42]
Ag$_{0.11}$Gd$_{0.06}$Sn$_{0.94}$Te	P	~18	~1.7	~0.6	~1.1	Melting	873	[43]
In$_{0.0025}$Sn$_{0.9975}$Te	P	~21	~1.9	~0.9	~1.1	Ball Milling	873	[44]
Sn$_{0.97}$Bi$_{0.03}$Te-3%SrTe	P	~20	~1.75	~0.9	1.2	Melting	823	[52]
In$_{0.01}$Sn$_{0.99}$Te$_{0.985}$I$_{0.015}$	P	-		-	~0.63	Melting + Hot pressing	773	[81]
SnTe$_{0.985}$I$_{0.015}$	P	-	~2	~1.2	0.6	Melting	700	[50]
Sn$_{0.94}$Bi$_{0.06}$Te	P	~20	~1.9	~0.89	1.1	Melting	873	[77]
AgSn$_4$SbTe$_6$	P	~22	~1.3	-	≈1	Melting	710	[76]
Sn$_{0.86}$ Mn$_{0.14}$Te (Cu$_2$Te)$_{0.05}$	P	-	~1	0.5	1.6	Melting	925	[73]
Sn$_{0.98}$Mg$_{0.03}$In$_{0.03}$Te	P	~42	~2.3	-	1.5	Melting	840	[74]
Sn$_{0.91}$Mg$_{0.12}$Te(Cu$_2$Te)$_{0.05}$	P		~1	~0.5	~1.4	Melting	900	[82]

[a]SHS= self-propagating-high-temperature-synthesis; [b]PAS= plasma activated sintering

2.2 Crystal Structure of SnTe

Figure 2.2 shows three phases of SnTe, namely α-SnTe with a rhombohedral structure and lattice parameters of a = 6.325 Å, and $α$ = 89.895° and a space group of R3m, β-SnTe with

a rocksalt structure and the lattice parameter of a = 6.3268 Å and α = 90° a space group of Fm-3m, and γ-SnTe with a orthorhombic structure and lattice parameters of a = 11.95 Å, b = 4.37 Å, c = 4.48 Å and a space group of Pnma.[83] α-SnTe is a low temperature (< 100 K) phase, while β-SnTe exists above 100 K and stable at room temperature and atmospheric pressure. When a distortion happens along the [111] direction of β-SnTe, β-SnTe can change to the rhombohedral α-SnTe phase. Under the pressure of over 18 kbar, β-SnTe can transform into orthorhombic γ-SnTe.[83] Since α-SnTe only exists at very low temperature (< 100 K) and γ-SnTe is found at very high pressure of 18 kbar, β-SnTe is a well-investigated system, generally stated as SnTe.
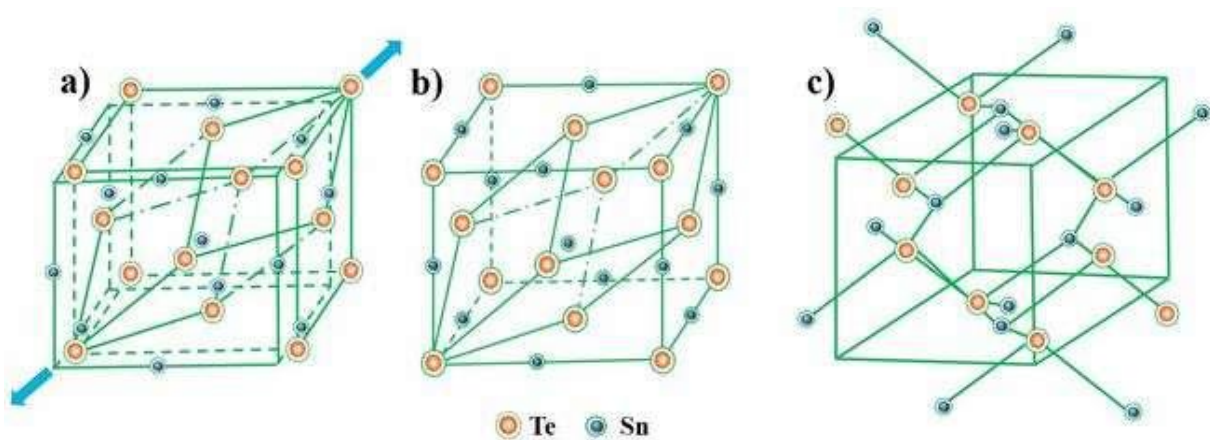
Figure 2.2 The crystal structure of different phases of SnTe (a) α-SnTe (b) β-SnTe (c) γ-SnTe.

2.3 Band Structure of SnTe

Figure 2.3a is an illustration of Brillouin zone of pristine face-centered-cubic (FCC) SnTe, and shows that the main conduction and valence band edges occur at or near the centres of the hexagonal faces (L points of the Brillouin zone, the valence band top with L_6^-, the conduction band edge with L_6^+ symmetry).[84] In 1966, Dimmock *et al.*[85] first observed the band gap (E_g) between two principal bands of SnTe by photoluminescence experiment and found that the value of E_g is 0.18 eV while in 1968 Rogers[86] quantitatively determined the energy separation ($\Delta E_{VB_{L-\Sigma}}$) between two valence bands considering that the light hole valence band is always highly non-parabolic and the heavy hole valence band is parabolic and found that at 300 K $\Delta E_{VB_{L-\Sigma}}$ is about 300 meV.

Figure 2.3b shows the typical band structures of pristine SnTe via first principles calculation including without and with spin orbit coupling (SOC). It can be observed that some degenerate bands at high symmetry points split up by SOC interaction. The SOC direct E_g of SnTe is 110 meV at L point which is little smaller than the experimental values (180 meV). The energy separation between light hole valence band (at L point) and the heavy hole valence band (at Σ) is 240 meV which is slightly smaller than the experimental value.[41] However, the non-SOC E_g is much underestimated (only 40 meV) while the $\Delta E_{VBL-\Sigma}$ is relatively overestimated (360 meV). The larger $\triangle E_{VBL-\Sigma}$ results in a low S due to the lack of participation of heavy hole from the VB_{Σ} during electron hole transportation system.[31] However, the small E_g can lead to bipolar conduction at the elevated temperature.[31, 41, 49] Consequently, poor thermoelectric performance is always observed in pristine SnTe.[31, 32, 36, 41, 49, 50]
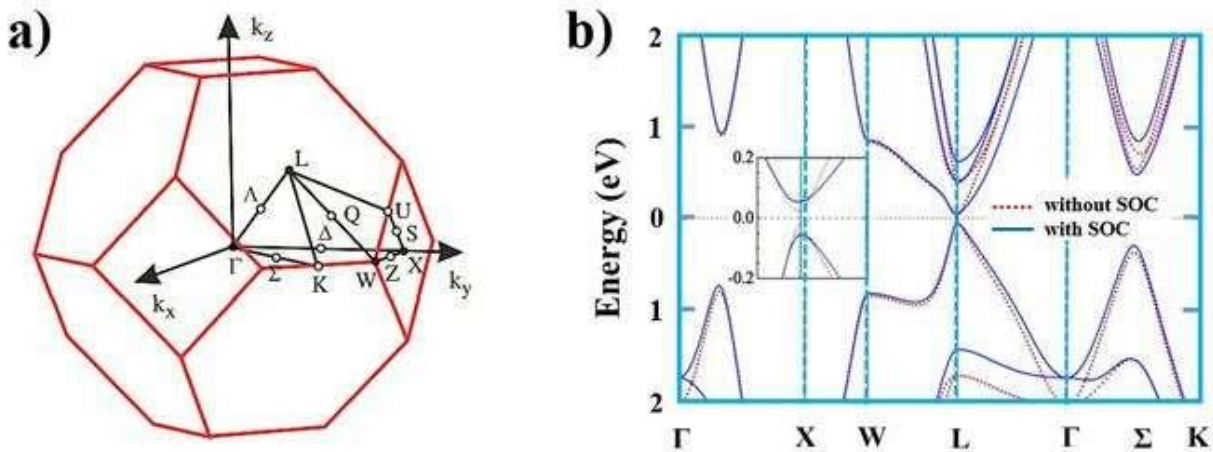
Figure 2.3 a) The bulk Brillouin zone (red lines) of SnTe. Reproduced with permission.[87] Copyright 2010, American Physical Society b) Calculated energy band structure for SnTe without and with spin orbit coupling (SOC). The Fermi level is at 0 eV. Reproduced with permission.[41] Copyright 2016, Royal Society of Chemistry.

2.4 Power Factor Optimization

Theoretically, the thermoelectric power generation efficiency is related to ZT[88] while the output power density (ω_{max}) strongly depends on $S^2\sigma$ by the following relationship[88]

$$\omega_{max} = \frac{1}{4}\frac{(T_H-T_C)^2}{L} S^2\sigma,$$
(2-5)

where T_H, T_C and L are the hot-side temperature, cold-side temperature, and thermoelectric leg length, respectively. From Equation (5), the two working boundary conditions are the temperature difference ($T_H - T_C$) and the temperature gradient ($\frac{T_H - T_C}{L}$). For a given boundary condition, ω_{max} is only governed by $S^2\sigma$. Thus, materials with high $S^2\sigma$ are demanded in order to obtain high output power density.

2.4.1 Carrier Concentration Engineering

SnTe almost invariably forms as *p*-type material due to the shape of the liquidus line in the SnTe binary phase diagram, which results in Sn deficiency.[46] The ratio of the apparent hole concentration to the Sn vacancy in SnTe system varies between 3.4 and 3.2 at 300 K.[46] One of the fundamental challenge to obtain maximum efficiency of a thermoelectric material is to determine the optimal carrier concentration.[89] Pristine SnTe possesses a high *n* of $\sim 10^{20}$ to 10^{21} cm^{-3},[47] resulting in high σ of $\sim$ 7000 *S* cm^{-1} but an extremely low *S* of 20 µV K^{-1} at room temperature.[52] To obtain an enhanced thermoelectric performance, optimising *n* is needed according to Equations (2) and (3). To illustrate the relationship of *n* with $S^2\sigma$ and *ZT* of SnTe, numerical simulations have been investigated under different temperatures.[90] **Figure 2.4a** and b show $S^2\sigma$ and *ZT* as a function of *n* under different temperatures,[90] in which each curve has a peak *n* value (marked as *n*^{opt}). The *n*^{opt} for *ZT* is lower than that for $S^2\sigma$ under a given *T*, which is attributed to the increase in κ_e at large *n*.[90] It has been observed that the temperature-dependent *n*^{opt} for $S^2\sigma$ is $\sim 8 \times 10^{20}$ cm^{-3} with the maximum $S^2\sigma$ of $\sim$ 18 µW cm^{-1} K^{-2} at 800 K.

To suppress the high hole concentration in SnTe Bi or I was mostly applied as donor atoms.[32, 50, 52, 91] Dopant I can effectively tune *n* through modifying the light hole valence band of SnTe.[50] Banik *et al.*[32] explored I-doped SnTe by substituting Te with I and observed that *n* significantly reduced from 3.31×10^{20} cm^{-3} to 3.01×10^{19} cm^{-3} in SnTe$_{0.95}$I$_{0.05}$. This reduced *n* leads to significant $S^2\sigma$ enhancement (up to $\sim$14.8 µW cm^{-1} K^{-2} at 650 K).[32] However, due to the presence of electron-hole bipolar effect above 600 K, dopant I can not provide the expected effectiveness of *ZT* enhancement.[50] Zhou *et al.*[50] introduced Gd and Te as acceptors (**Figure 2.4c**) and I as donors (**Figure 2.4d**) in the SnTe system and obtained a peak *ZT* value of 0.6 in SnTe$_{0.985}$I$_{0.015}$ with an *n* of 4×10^{19} cm^{-3}, which is 200% higher than the peak *ZT* value of 0.2 for pristine SnTe. In the same study, extra Te and Gd can increase both *n* and *S*.[50] A peak *ZT* value of 0.4 was obtained in Gd$_{0.01}$Sn$_{0.99}$Te and SnTe$_{1.015}$ at the *n* of 4-6 $\times 10^{19}$ cm^{-3} at 773 K, which is 74% higher than that of the pristine SnTe.[50] It has been

found that Sn self-compensation can also significantly reduce high n of the pristine SnTe.[39] For instance 3 mol % self-compensated Sn can reduce n from 4.7×10^{20} cm^{-3} to 2.2×10^{20} cm^{-3}, resulting in a 50% ZT enhancement. Further Cd alloying in the Sn$_{1+x}$Te system can decrease n to an optimal level of ~5×10^{19} cm^{-3}.[39]
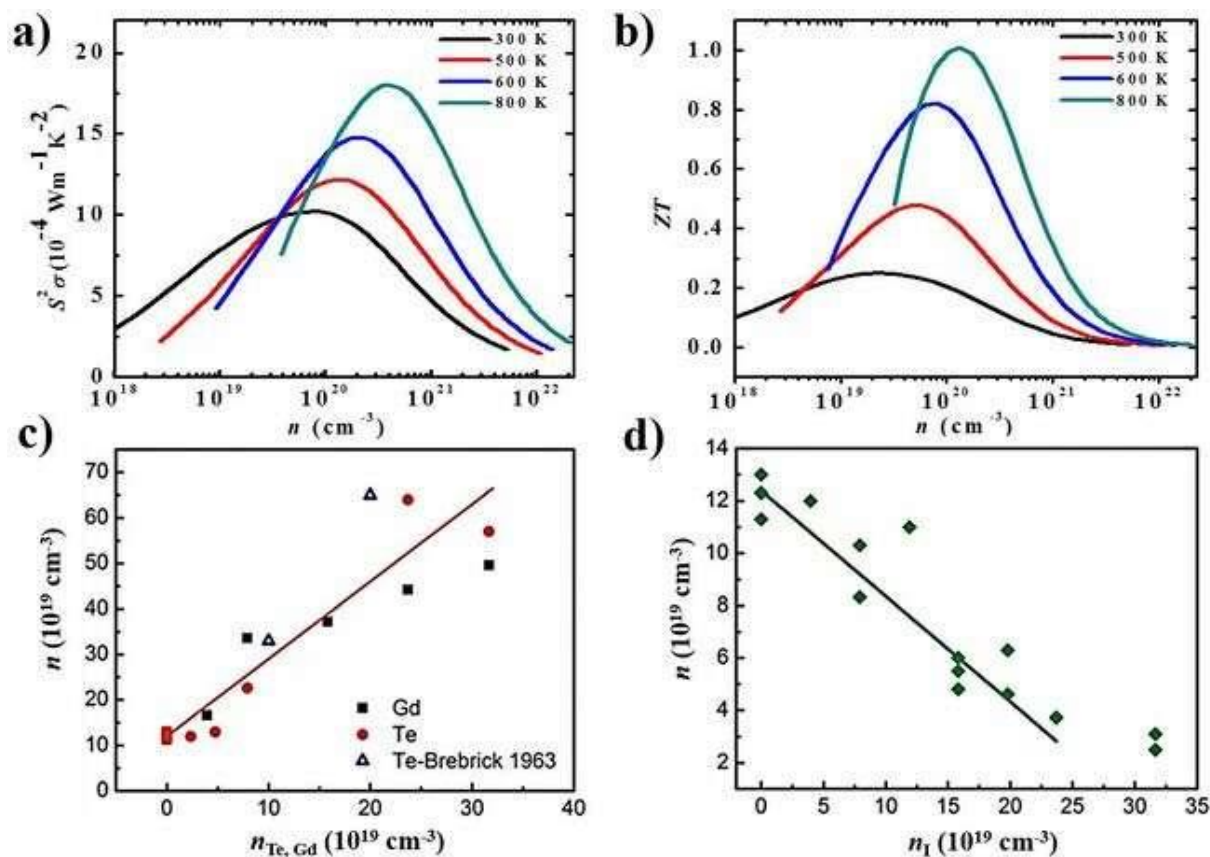
Figure 2.4 Calculated temperature dependent a) $S^2\sigma$ and b) ZT at under different n. Hall carrier concentration as a function of n c) Gd and Te as acceptors and d) I as a donor. Reproduced with permission.[50] Copyright 2014, Royal Society of Chemistry.

2.4.2 Band Engineering

The S value of a thermoelectric material can be enhanced by increasing the equivalent degenerated valleys of the band structures.[92-95] Band engineering enables the increasing of degenerated valleys by converging different bands in the Brillouin zone through doping or alloying.[96] In pristine SnTe, $\Delta E_{VB_{L-\Sigma}}$ is sufficiently large to make VB_Σ irreverent to charge transport. Thus, it is imperative to engineer the band structure of SnTe to increase the degenerated valleys by converging two valence bands as well as to facilitate the heavy hole to contribute to the S enhancement. There are two major strategies adopted to engineer the band structure of SnTe, namely valence band convergence and resonance level engineering.

2.4.2.1 Increasing Carrier Effective Mass (m^*)

According to Equation (2) shown above, S of a thermoelectric material is proportional to m^*. In fact, m^* depends on the number of degenerated valleys (N_V) of the band structure and the band effective mass (m_b^*) by the following relationship[96]

$$m^* = (N_V)^{2/3} m_b^* \qquad (2\text{-}6)$$

Thus, by maximizing both N_V and m_b^*, m^* can be enhanced, and in turn a high S can be secured. Orabi et al.[31] investigated the effect of Ca doping on m_b^* in SnTe, and found that Ca can significantly enhance m_b^* of the valence bands near the Fermi level by increasing overall iconicity for the split off band at Γ and Σ (**Figure 2.5a**).[31] With increasing the Ca concentration in SnTe, m^* increases from 0.133 m_e in $Sn_{1.03}Te$ to 0.35 m_e in $Sn_{0.94}Ca_{0.09}Te$ (**Figure 2.5b**).[31] This leads to significant enhancement in S from ~10 µV K^{-1} in $Sn_{1.03}Te$ at room temperature to ~200 µV K^{-1} in $Sn_{0.94}Ca_{0.09}Te$ at 856 K.[31]

Banik et al.[33] extensively studied the influence of Mg doping on m^* of $Sn_{1.03-x}Mg_xTe$ system considering a single parabolic band model and found that the m^* increases from ~0.16 m_e to ~0.69 m_e with increasing Mg concentration from 0 to 9 mole % which is attributed to the electronic band structure modification and increasing charge transport contribution of the heavy hole valence band. The high effective mass upon Mg doping causes significant enhancement in S from ~10 µV K^{-1} in $Sn_{1.03}Te$ at room temperature to ~200 µV K^{-1} in $Sn_{0.95}Mg_{0.08}Te$ at 856 K.

It is worthy to mention that the μ of a thermoelectric material is inversely proportional to m_b^* by the following relationship, $\mu \propto (m_I^*)^{-1}(m_b^*)^{-1}$, where m_I^* is the transport mass, hence increase in m_b^* that produces large S will result in low μ. A low μ will leads to a low σ. Therefore, a compromisation is required between this two parameters. However, in case of SnTe the carrier concentration is still high at high doping level, for instance 3.3×10^{20} cm^{-3} in $Sn_{0.96}Mg_{0.07}Te$ which is the 1-2 order higher than that of PbTe.[33, 97] Hence the simultaneously enhanced S due to the high m^* completely compensate the low µ to obtain high $S^2\sigma$. Similar phenomenon observed in other materials systems, including $ZrNiSn$,[98] $CoSb_3$[99] and $FeNbSb$[100] which makes these promising heavy effective mass thermoelectric for power generation.[101]
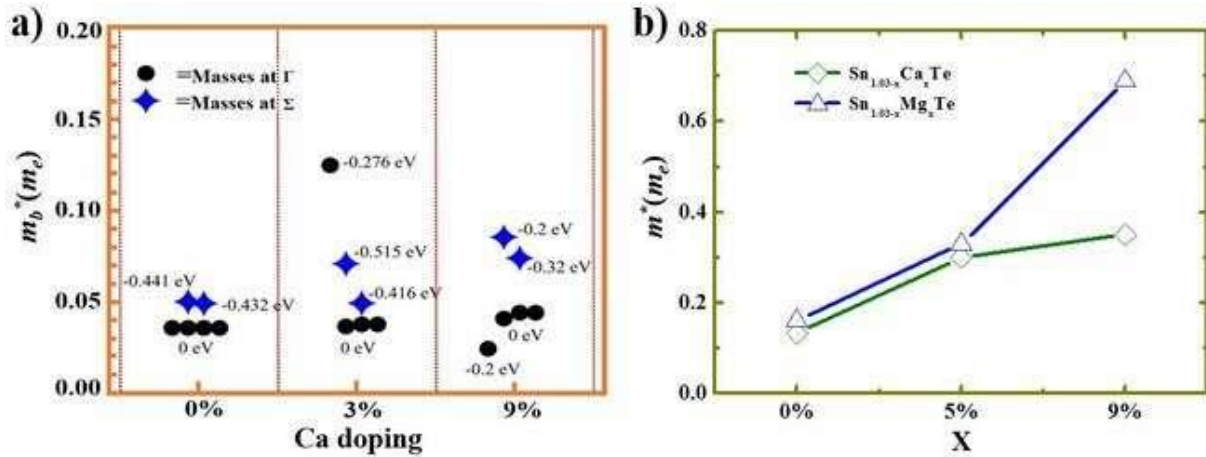
Figure 2.5 a) Effect of Ca doping on m_b^* at Γ and Σ point in the cubic Brillouin zone.[31] b) Effect of Mg and Ca doping on m^* of SnTe system.[31, 33]

2.4.2.2 Valence Band Convergence

Band convergence is an effective tool to achieve a significant variance in $S^2\sigma$ of a thermoelectric material.[102-105] Following the previous discussion, Mg and Ca not only increase the m^* of SnTe but also significantly reduce the $\Delta E_{VB_{L-\Sigma}}$ from 0.375 eV to 0.18 eV and from ~0.42 eV to ~0.2 eV, respectively. This consequences a high $S^2\sigma$ from 11 μW cm^{-1} K^{-2} at room temperature to 26 μW cm^{-1} K^{-2} at 873 K in Sn$_{1.03-x}$Ca$_x$Te [31] and from ~3.5 μW cm^{-1} K^{-2} at room temperature to ~30.3 μW cm^{-1} K^{-2} at 856 K in Sn$_{1.03-x}$Mg$_x$Te.[33] Tan *et al.*[41] investigated the changes in the electronic band structures of Mg/Mn/Cd/Hg doped SnTe using first-principles calculations, and found that these dopants can significantly modify the band structure and reduce $\Delta E_{VB_{L-\Sigma}}$. **Table 2.2** summarizes $\Delta E_{VB_{L-\Sigma}}$ after doping of Mg/Mn/Cd/Hg in SnTe, in which Hg is found to be the most effective element to reduce $\Delta E_{VB_{L-\Sigma}}$ comparing to other elements.

Table 2.2 The $\Delta E_{VB_{L-\Sigma}}$ for doped SnTe[41]

Structure	$\Delta E_{VB_{L-\Sigma}}$ (eV)
SnTe	0.24
Sn$_{0.96}$Te	0.22
Sn$_{0.93}$Mg$_{0.04}$Te	0.13
Sn$_{0.93}$Mn$_{0.04}$Te	0.13
Sn$_{0.93}$Cd$_{0.04}$Te	0.067
Sn$_{0.93}$Hg$_{0.04}$Te	0.028

Figure 2.6a is a schematic band structure of dopant-modified SnTe and shows that the doping can significantly reduce $\Delta E_{VB_{L-\Sigma}}$ by converging two valence bands that allow the heavy hole to participate in the electron hole transport and thus increase S.[31, 33, 49] **Figure 2.6b-d** show the temperature-dependent S, $S^2\sigma$, and ZT of Mn-doped SnTe,[49] Ca-doped SnTe,[31] Mg-doped SnTe,[33] and pristine SnTe.[44] As can be seen, Mn doping results in the largest S of ~270 μV K^{-1} compare to other elements while Mg doping has the highest $S^2\sigma$ of ~30.3 μW cm^{-1} K^{-2}. Ca-doped SnTe has the highest ZT of ~1.35 owing to the significant valence band convergence and reduction in κ_l. In general, all the doped SnTe showed enhanced S, $S^2\sigma$, and ZT values compare to pristine SnTe owing to the decreasing of $\Delta E_{VB_{L-\Sigma}}$.[31, 33, 49]
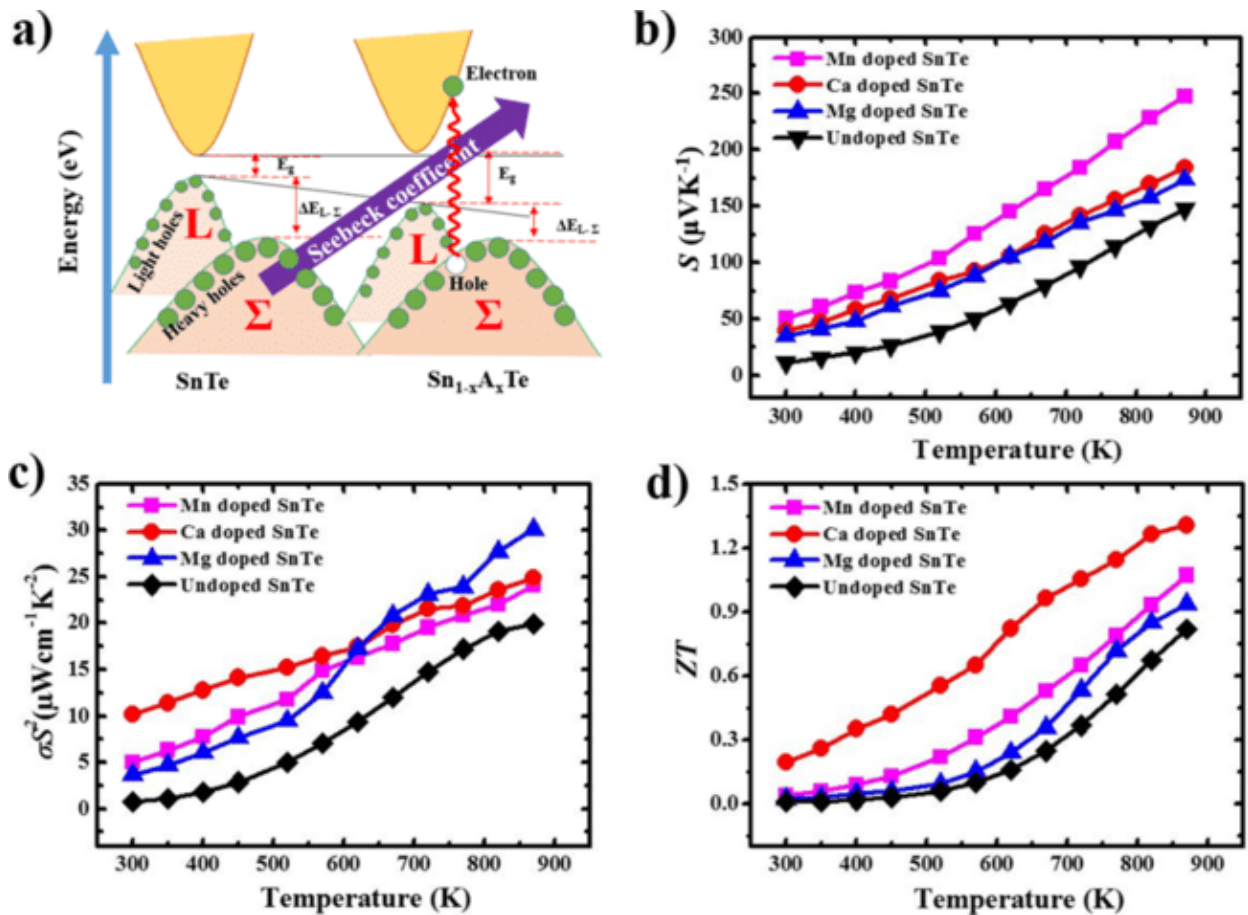
Figure 2.6 a) schematic of band convergence of two valence bands. b) S; c) $S^2\sigma$; and d) ZT of Mn-doped SnTe,[49] Ca-doped SnTe,[31] Mg-doped SnTe,[33] and pristine SnTe.[44]

2.4.2.3 Resonance Energy Level Engineering

According to Mahan-Sofo theory,[106] the S of a thermoelectric material can be increased by the local increasing in density of states (DOS) over a narrow energy range at Fermi level.[106]

The effect of local increase in DOS on S can be expressed as follows which is known as Mott expression,[107]

$$S = \frac{\pi^2}{3}\frac{\kappa_B}{q}\kappa_B T\{\frac{d[\ln(\sigma(E))]}{dE}\}_{E=E_F} \tag{2-7}$$

The energy-dependent electrical conductivity $\sigma(E)$ can be written as

$$\sigma(E) = n(E)q\mu(E) \tag{2-8}$$

$$\text{and } n(E) = g(E)f(E) \tag{2-9}$$

where, $f(E)$ is the Fermi function, $n(E)$ is the carrier density, $g(E)$ is the DOS, q is the carrier charge, E_F is the Fermi energy, κ_B is the Boltzmann constant and $\mu(E)$ is the carrier mobility. If we combine Equations (7), (8) and (9) then,

$$S = \frac{\pi^2}{3}\frac{\kappa_B}{q}\kappa_B T\{\frac{1}{n}\frac{dn(E)}{dE} + \frac{1}{\mu}\frac{d\mu(E)}{dE}\}_{E=E_F} \tag{2-10}$$

Hence, if we can increase the energy dependent $n(E)$, for instance by a local increase in DOS then S will be increased, provided that E_F of the materials aligns properly in the range of the excess density of states in the band. This can be accomplished in SnTe by resonant doping which is ascribed as the distortion of the DOS near the fermi energy level. It has been proved that resonant doping is an effective way to enhance the S without affecting the n.[92]

For a given thermoelectric material, the hybridizations of electrons between dilute impurity and the host valence or conduction band can generate the resonant energy level,[108] which can locally increase DOS over a narrow energy range at the Fermi level, leading to a S enchantment.[109] The concept of resonant doping was first introduced by Korringa and Gerritsen[108] in 1950, and has been widely implemented in different thermoelectric systems, such as Tl-doped PbTe,[17] Sn-doped Bi_2Te_3[110] and Al-doped PbSe,[111] suggesting that the resonant doping is an effective way to enhance S without affecting n.[92] In the case of SnTe, In has been found to produce a resonant state in the valence band and can significantly increase S by increasing DOS near the Fermi level as schematically illustrated in **Figure 2.7a**. [40, 44, 112] **Figure 2.7b** shows the calculated DOS of In-doped and pristine SnTe. Compare to pristine SnTe, high DOS is observed near the Fermi level in In-doped SnTe.[21] Due to the In resonant doping effect, the enhanced $S^2\sigma$ and in turn ZT of SnTe are shown in **Figure 2.7c** and **d**, respectively. A high $S^2\sigma$ of ~20.3 μW cm^{-1} K^{-2} and ZT of ~1.1 at 873 K is obtained in $In_{0.0025}Sn_{0.9975}Te$.[44]
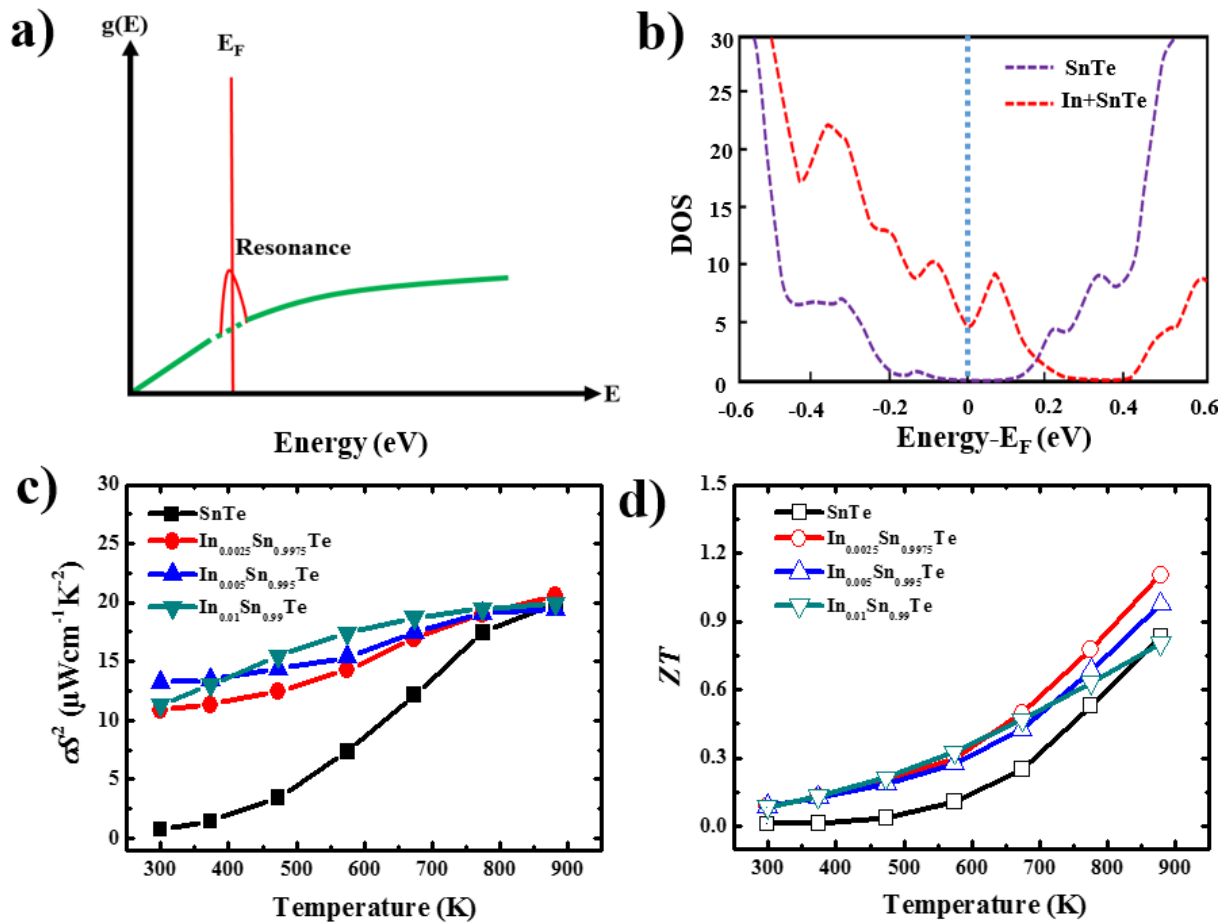
Figure 2.7 a) Schematic illustration of the distortion of density of states DOS, *g(E)*. The green line corresponds to pristine SnTe, and the red peak corresponds to In-doped SnTe (with resonant energy levels from In; E_F = Fermi energy level. b) Changing of DOS in SnTe due to the resonance states.[21] c) $S^2\sigma$ and d) *ZT* of the In-doped SnTe[44] and pristine SnTe[44] showing the effect of resonant doping on thermoelectric performance.

2.5 Band Gap Enlargement

When a thermoelectric material with a narrow E_g is set at an elevated temperature, the bipolar effect cannot be ignored.[113] **Figure 2.8a** is a schematic illustration of the bipolar effect in the thermoelectric materials, in which if a temperature gradient is imposed on a thermoelectric material with the hot-end and cold-end, more excitation of electrons/holes near the hot-end than the cold-end, and more annihilation of electrons/holes near the cold-end than the hot-end will take place.[113] This implies that more heat will be absorbed near the hot-end due to the electron/hole excitation and more heat will be released near the cold-end due to the electron/hole recombination, which enlarges *κ*.[113] Also, the bipolar effects degrade *S*,

because the thermally excited minority carriers have opposited S and offset those of majority ones.[92, 113]

With increasing the temperature, the thermally excited minority carriers across E_g significantly reduce S.[92] The S degradation along with the bipolar effect eventually leads to the ZT reduction. Therefore, to secure a high ZT at a high temperature requires a high E_g.[114] This leads to a strategy to increase E_g to prevent the degradation of the thermoelectric performance from the thermally activated minority carriers at high temperatures.[115-119]

Due to its small E_g of $\sim$ 0.18 eV, pristine SnTe has significant bipolar conduction at the elevated temperature.[48, 120] Thus it is imperative to engineer the band structure of SnTe in order to suppress the bipolar transport behaviour. Wu et $al.$[42] studied Mn-doped SnTe and found that Mn can significantly enlarge E_g, and thus hinder minority carriers (electrons) that affect S adversely. **Figure 2.8b** shows the effect of alloyed Mn on $\kappa_{bipolar}$ of SnTe. Obviously, pristine SnTe showed strong deviation from the linear dependency at the elevated temperature, which is ascribed to the high bipolar diffusion.[42] However, 9% Mn alloyed SnTe has no significant deviance from the linear dependence at high temperature.[42] This is attributed to the enlarged E_g that can diminish the bipolar contribution of 9% Mn alloyed SnTe. Tan et $al.$[35] reported that a significant increase in E_g can be achieved from 0.12 eV for SnTe to 0.39 eV for Hg-doped SnTe that greatly reduced the bipolar diffusion. The bipolar diffusion contribution to κ decreases rapidly with increasing the Hg concentration from a pronounced ~50% for the sample with x=0 to a negligible ~3% for the sample with x=4 in $Sn_{0.98}Bi_{0.02}Te$-x%HgTe.[35] Such band gap enlargement technique also extensively studied in other materials systems like n-type $Bi_2Te_{3-x}Se$.[79] and Na-doped $Mg_xPb_{1-x}Te$.[117]
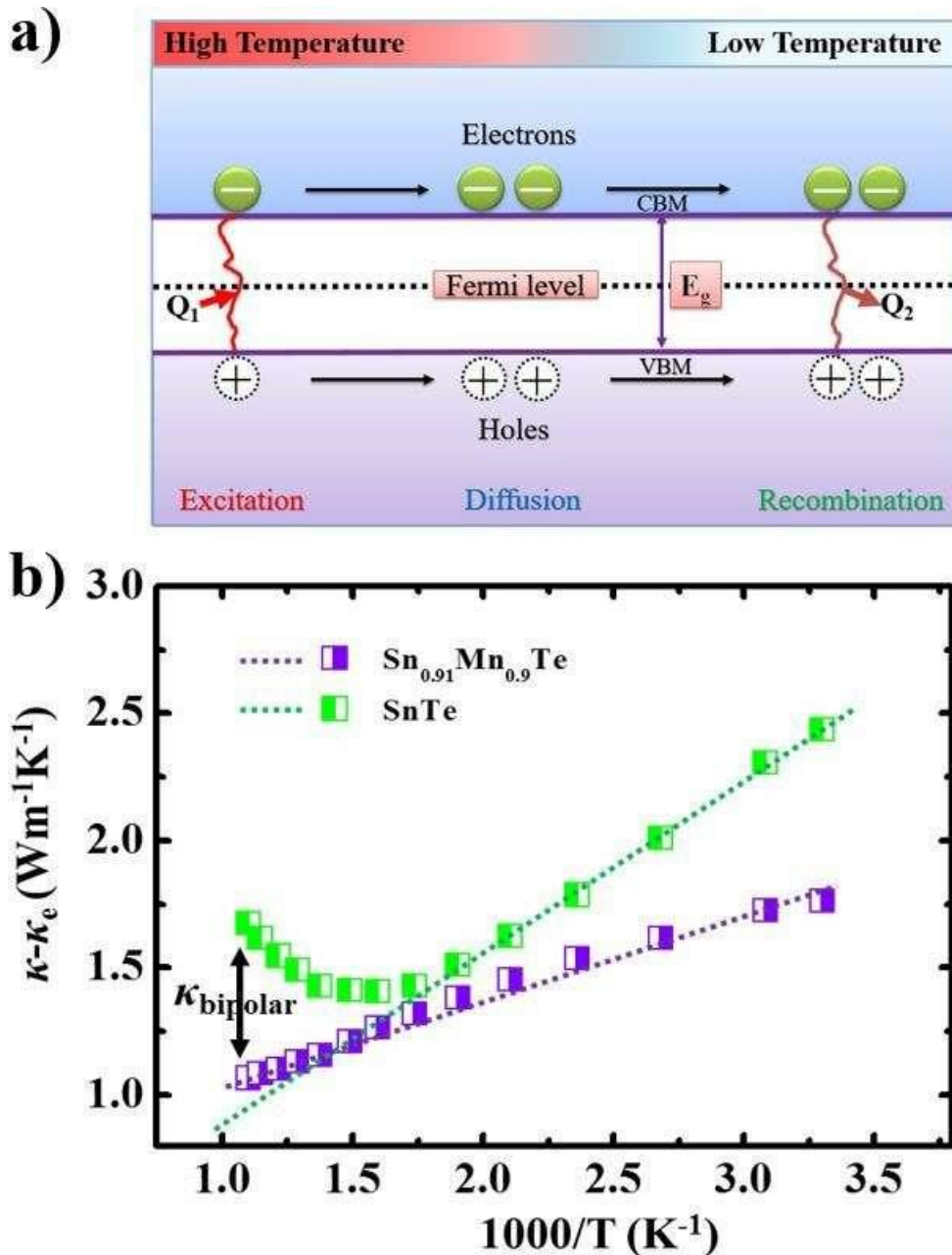
Figure 2.8 a) A schematic illustration of bipolar effect in a thermoelectric material system; Q_1 = Energy absorbed at hot end, Q_2 = Energy released at cold end.[110] b) Bipolar contribution to the κ; $\kappa - \kappa_e$ as a function of $1000/T$ for pure SnTe and $Sn_{0.91}Mn_{0.09}Te$; the dashed lines are representing the linear fitting to the $\kappa - \kappa_e$ from 300 to 900 K; deviation of thermal conductivity indicates a significant $\kappa_{bipolar}$.[42]

2.6 Reducing the Lattice Thermal Conductivity

It is well-known that phonon waves can be scattered, contributing to the additional thermal resistance that causes the κ_l reduction by introducing various types of crystal defects, such

as point defects,[53] dislocations,[121] interfaces,[14] and precipitates.[122, 123] **Figure 2.9a** is a schematic diagram of the frequency dependent phonon scattering rates for various phonon scattering mechanisms. As can be seen, nano-inclusion and point defect scatterings are the two major ways to increase the scattering rates for high and medium frequency phonons.[124] In addition, single rattle can also significantly enhance the phonon scattering rate. Increasing in phonon scattering rate decreases κ_l.[124] **Figure 2.9b** schematically illustrates the multiple scattering centres that can be introduced into a given materials in order to reduce κ_l.

According to Equations (3) and (4), κ_e and σ both directly proportional to n, so that we cannot simply change n to alter both κ_e and σ. Hence the key strategy to reduce overall κ is to reduce κ_l as low as possible. In this regard, in 1950s and 1990s, Ioffe *et al.*[125] and Slack[126] proposed two major strategies, namely alloying and introducing phonon rattlers, respectively, with the concept that introducing an atomic disorder either substitutionally or interstitially inside the crystal lattice.[18, 64, 127] Defect engineering and the formation of grain boundaries are two conventional approaches to reduce κ_l,[2, 122, 128-131] while modern technology launched nanostructuring[132] that can further reduce κ_l owing to the harnessing phonon interface scattering without severely disturbing electronic properties.[96] Significant enhancements in ZT have been achieved through nanostructuring in different materials systems including PbTe-based nanostructured materials,[14, 55, 57, 133-147] Bi_2Te_3-based nanocomposites,[54, 122, 148-156] and SiGe-based nanocomposites.[157, 158] Here, a few crucial tactics to reduce κ_l in SnTe system are summarised.
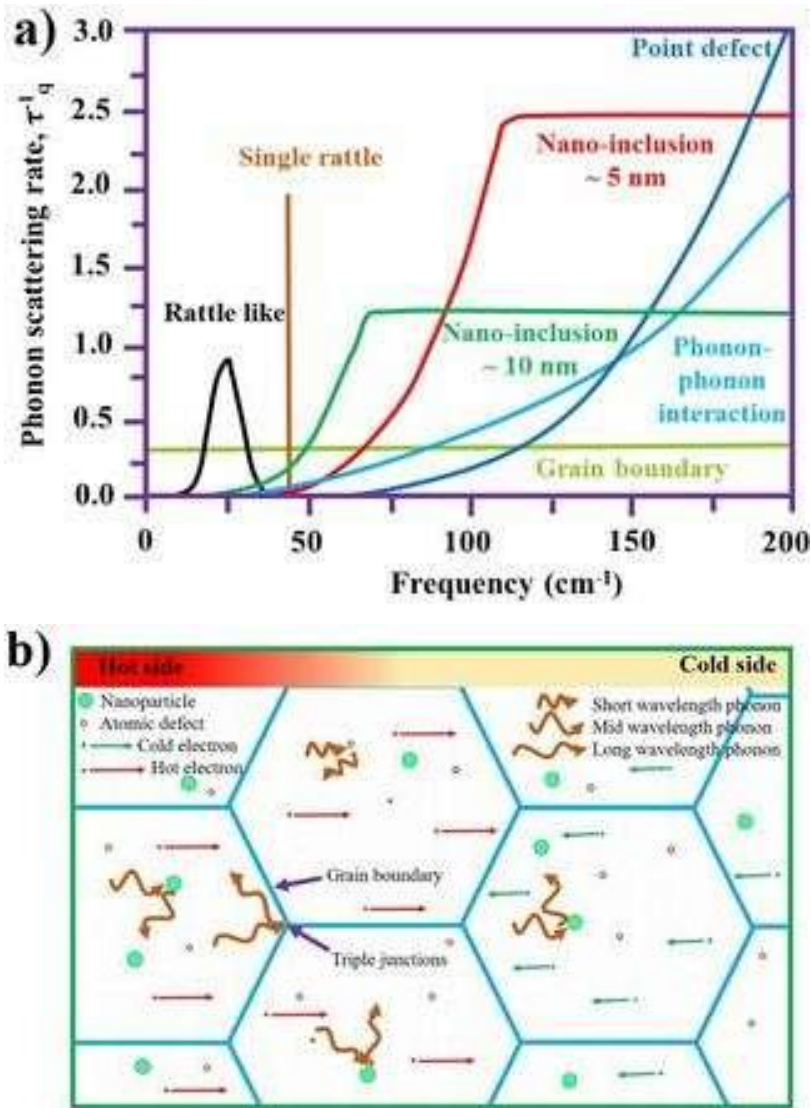
Figure 2.9 a) Schematic representation of the frequency dependent phonon scattering rates for various mechanisms.[124] b) Schematic illustration showing the multiple scattering centres that can be introduced into a given materials to reduce κ_l.

2.6.1 Point Defect Scattering

Point defects occur only at or around a single lattice point,[159] which can be achieved by introducing lattice imperfection in the host lattice through doping or alloying.[96] The fluctuation of strain fields and mass contrast in a host lattice of a material system can significantly enhance phonon scattering to reduce κ_l.[96] **Figure 2.10a-c** schematically illustrates different types of doping approaches to generate point defects, namely single element doping, cross-substitution, and formation of lattice vacancies, respectively. In the case of the single element doping, the dopant can be either isovalent with the host element to generate lattice disorder or aliovalent to control n while the cross-substitution comprises of replacing one or more of

the host element by pairs from other groups of elements owing to keeping overall valence electron constant.[96] As suggested in **Figure 2.10a-c** of SnTe, single element, such as I, can induce point defect in the lattice,[21] while the cross-substitution can be produced by Ag and Bi doping.[37] The formation of lattice vacancies can be created by introducing compounds, such as In_2Te_3.[38] **Figure 2.10d** shows the comparison of κ_l with different point defects in SnTe system. The room temperature κ_l of undoped SnTe is significantly reduced from ~2.5 W m^{-1} K^{-1} to ~ 0.7 W m^{-1} K^{-1} at 750 K due to the cross-substitution by Ag and Bi while vacancy formation due to the In_2Te_3 reduced from ~3.5 W m^{-1} K^{-1} to ~0.6 W m^{-1} K^{-1} at 923 K.[37, 38] Thus, cross-substitution and vacancy formation are two excellent ways to impede the phonon propagation that yields very low κ_l in SnTe.[38] Similar effects are observed in InSb-In_2Te_3[8] and GeTe-In_2Te_3,[9] where κ_l is greatly reduced due to the significant vacancy phonon scattering induced by In_2Te_3 vacancies. Acharya et al.[45] investigated point defect scattering in self-compensated $Sn_{1.03}Te$ with Mn doping and found that an anharmonicity of the phonon dispersion and soft transverse optical phonon modes can be generated in the SnTe matrix upon Mn doping, which decreases κ_l from ~4.37 W m^{-1} K^{-1} in $Sn_{1.03}Te$ to ~2.6 W m^{-1} K^{-1} in $Sn_{0.93}Mn_{0.1}Te$ at 300 K. Point defects produced by Mn doping causes the scatterings of high energy phonons and a soft transverse optical phonon mode that affect the group velocity and the mean free path in the lattice.[45] Recently Pei et al. extensively carried out research on interstitial point defect scattering in SnTe through Cu_2Te alloying and found that interstitial Cu atoms in SnTe lattice can significantly scatter phonons, which yields an extremely low κ_l of 0.5 W m^{-1} K^{-1}, leading to a peak ZT of >1 in $Sn_{0.94}Cu_{0.12}Te$ at 850 K.[53]
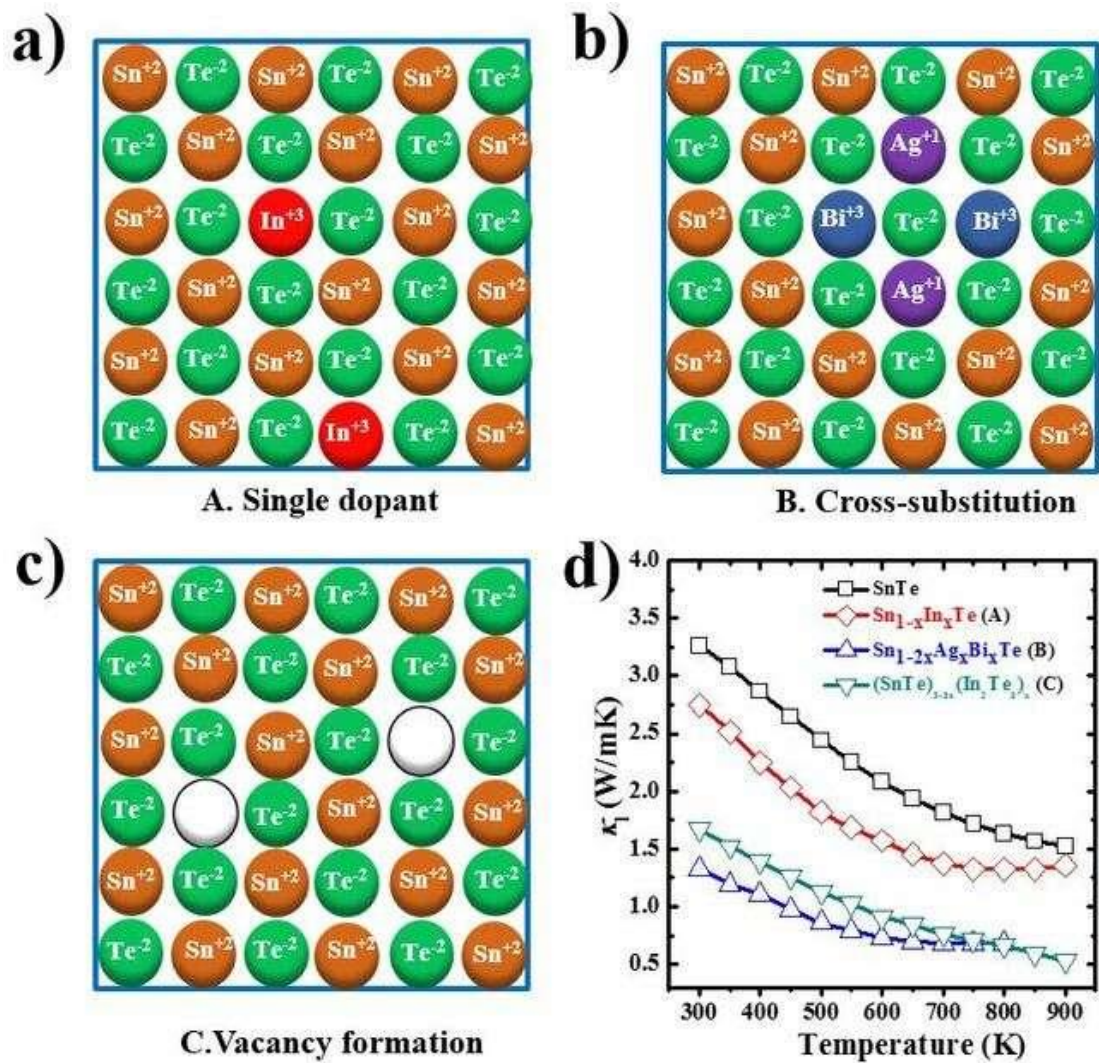
Figure 2.10 Schematic representation of various types of point defects: a) single doping; b) cross-substitution; c) lattice vacancy formation. d) Comparison of κ_l as a function of temperature for SnTe with different point defects.[21, 37, 38]

2.6.2 Nanoprecipitates

As a kind of nanoscale defects in the crystal lattice, nanoprecipitates can significantly scatter phonons with various wavelengths that resulted in low κ_l. In the case of SnTe, high Mn-doping level of 12% can form Mn-rich nanoprecipitates, which are embedded in the SnTe matrix. Mn-rich nanoprecipitates largely suppressed the phonon propagation in the $Sn_{1-x}Mn_xTe$ system and scatter a wide spectrum of phonons, which consequently makes a significant κ_l reduction of ~ 0.9 W m^{-1} K^{-1} at 800 K and a high ZT of 1.3 at 900 K in $Sn_{0.88}Mn_{0.12}Te$.[36] By introducing a proper amount of $AgSbTe_2$ in SnTe, Han *et al.*[76] observed quaternary system of $AgSn_mSbTe_{m+2}$ (m=2,4,5,7,10,14,18) with remarkable low κ_l of ~ 0.41 W m^{-1} K^{-1} at 300 K in

AgSn$_2$SbTe$_4$. They[36] reported that the obtained κ_l reduction could be attributed to the extensive and diverse inhomogeneity of Ag-Sb rich nanoscale phases in AgSn$_m$SbTe$_{m+2}$ matrix. Consequently, a high $ZT \approx 1$ is obtained at 710 K for m = 4, indicating that the AgSn$_m$SbTe$_{m+2}$ system holds a great potential as an alternative p-type, lead free thermoelectric material.

The coherently embedment and completely aligned of a guest component with the host matrix is known as endotaxial nanostructuring.[14] Such endotaxial nanostructuring uses the acoustic mismatch between the superlattice components to reduce κ_l rather than alloy scattering of charge carriers.[14] **Figure 2.11a** schematically illustrates the endotaxial nanostructuring in SnTe, in which small valence band offsets between second phase (guest component) and the SnTe allows facile carrier transmission throughout the system and significantly scatters heat carrying phonons at SnTe matrix/second phase interface. **Figure 2.11b** is a typical high-resolution transmission electron microscopy image of endotaxial nanostructuring in the Sn$_{0.96}$Sb$_{0.04}$Te system and shows the coherent interface as highlighted by the white dashed circle.[34] The corresponding fast Fourier transform image (inset) can be indexed to the cubic rock-salt structure. Spontaneous formation of endotaxial Sb rich nanoprecipitates along with the super-structured intergrowth nanodomains (Sn$_m$Sb$_{2n}$Te$_{3n+m}$) remarkably reduced κ_l from ~2.88 W m^{-1} K^{-1} to ~0.67 W m^{-1} K^{-1} at room temperature in the Sn$_{1-x}$Sb$_x$Te system, leading to an enhanced ZT of ~1 in Sn$_{0.85}$Sb$_{0.15}$Te at 800 K (**Figure 2.11c** and **d**).[34] By employing SrTe as a second phase alloying in Sn$_{0.97}$Bi$_{0.03}$Te, endotaxial nanostructures are formed in the Sn$_{0.97}$Bi$_{0.03}$Te-x%SrTe matrix.[52] A lattice distortion between two nanoprecipitates and the strain exerted around the precipitates can extensively scatter phonon from different directions.[52] When the SrTe content is increased from 0 to 5.0% κ_l of Sn$_{0.97}$Bi$_{0.03}$Te decreased from ~2.0 Wm^{-1}K^{-1} to ~1.2 W m^{-1} K^{-1} at room temperature and from ~1.1 to ~0.70 W m^{-1} K^{-1} at 823 K (**Figure 2.11c**), respectively. A maximum ZT of 1.2 is obtained at 823 K in Sn$_{0.97}$Bi$_{0.03}$Te-3%SrTe (**Figure 2.11d**). Such strategies are also extensively investigated in other thermoelectric materials systems, including PbTe-MTe (M=Ge, Mg, Ca, Sr, Ba),[10, 13, 14, 109, 160] PbTe-PbS,[70] and PbSe-MSe (M=Ca, Sr, Ba).[161]
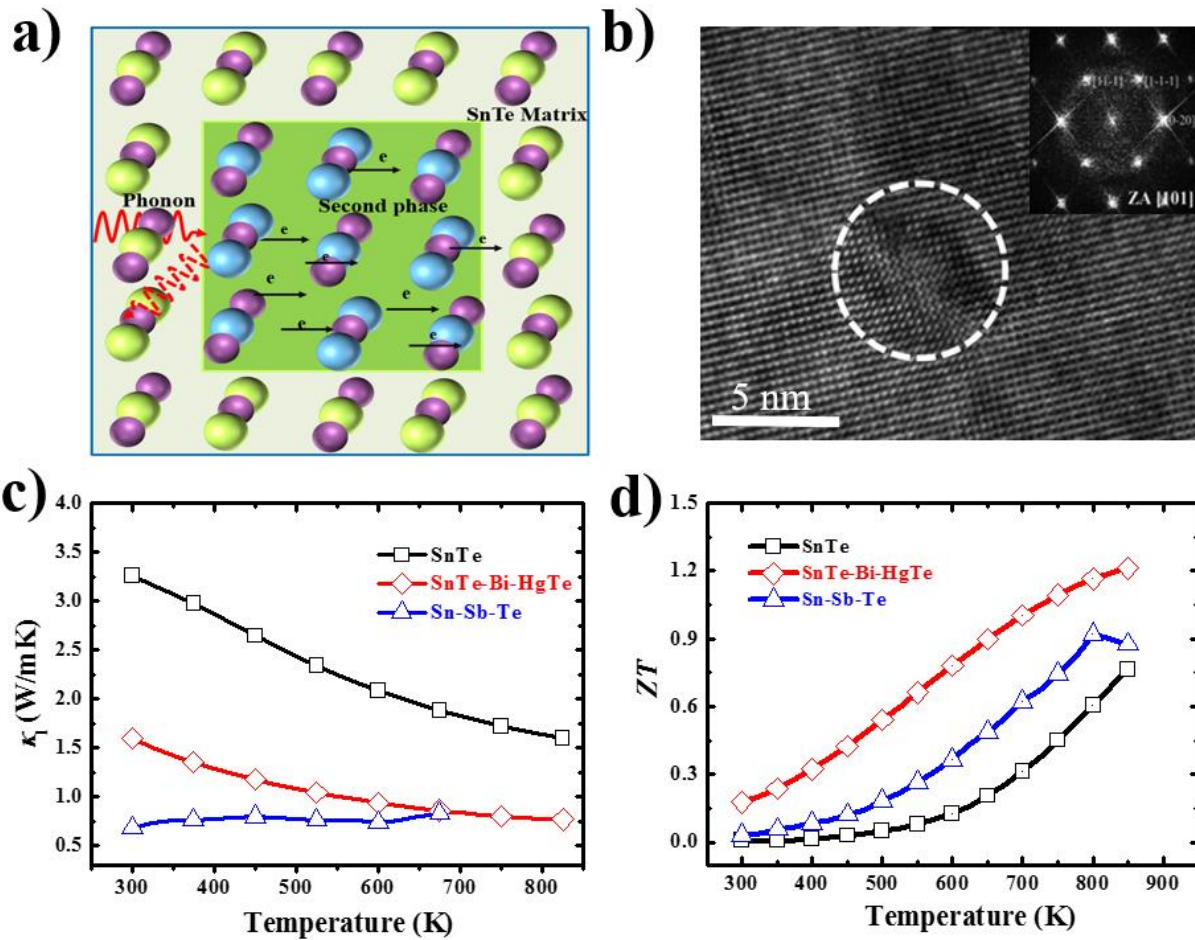
Figure 2.11 a) Concept of endotaxial nanostructuring in SnTe system. b) Typical HRTEM image of nanoprecipitates in $Sn_{0.96}Sb_{0.04}Te$ showing coherent interfaces, highlighted by the white circle. The corresponding inset FFT pattern proved the cubic rocksalt structure. Reproduced with permission.[34] Copyright 2016, Royal Society of Chemistry.c) κ_l and d) *ZT* of SnTe,[44] $Sn_{0.97}Bi_{0.03}Te$-3%SrTe[52] and Sn-Sb-Te.[34]

2.6.3 All-scale Hierarchical Architectures

The combination of point defects, nanostructuring, and mesoscale structuring into a thermoelectric material is known as all-scale hierarchical architecture.[10, 96] **Figure 2.12a** schematically illustrates all scale hierarchical architecturing, which includes the scatterings from atomic scale, nanoscale and mesoscale. In fact, phonon scattering rate is strongly associated with the phonon mean free path (MFP).[96] MFP of < 1 nm can be scattered by the atomic-scale point defects while MFP of 1-10 nm and 10-1000 nm can be scattered by nanoprecipitates and mesoscale grains, respectively.[96] All scale hierarchical architecturing can facilitate the strongest phonon scattering in many systems.[13, 109, 162, 163] Tan *et al.*[39] extensively studied all-scale hierarchical architecture in SnTe where Sn was substituted by

Cd to form atomic-scale point defects, CdS was used for nanostructuring to create nanoprecipitates and mesoscale grains produced by spark plasma sintering. Mesostructuring causes a significant κ_l reduction to a value of ~ 2.1 W m^{-1} K^{-1} at room temperature which is 22 % lower than the pristine SnTe. Additional phonon scatterings from the atomic point defects and nanoscale precipitates can lead to further reduction in κ_l by ~22 % and ~20 %, respectively (**Figure 2.12b**). Consequently a significant high *ZT* of ~ 1.3 is achieved at 873 K (**Figure 2.12c**). A high doping fraction of Mn can significantly modify the microstructure into an all-scale hierarchical architectures including nanoscale MnTe precipitates/ laminates, stocking faults, layered structure and atomic scale point defects, which resulted in a very low κ_l of 0.6 W m^{-1} K^{-1} and high *ZT* of 1.3 at 900 K.[42] All-scale hierarchical architectures were also successfully implemented in the other materials systems, including GeTe,[160] AgCrSe$_2$,[164] In$_2$O$_3$,[165] Bi$_2$Te$_3$,[166] and AgSbSe$_2$.[167]
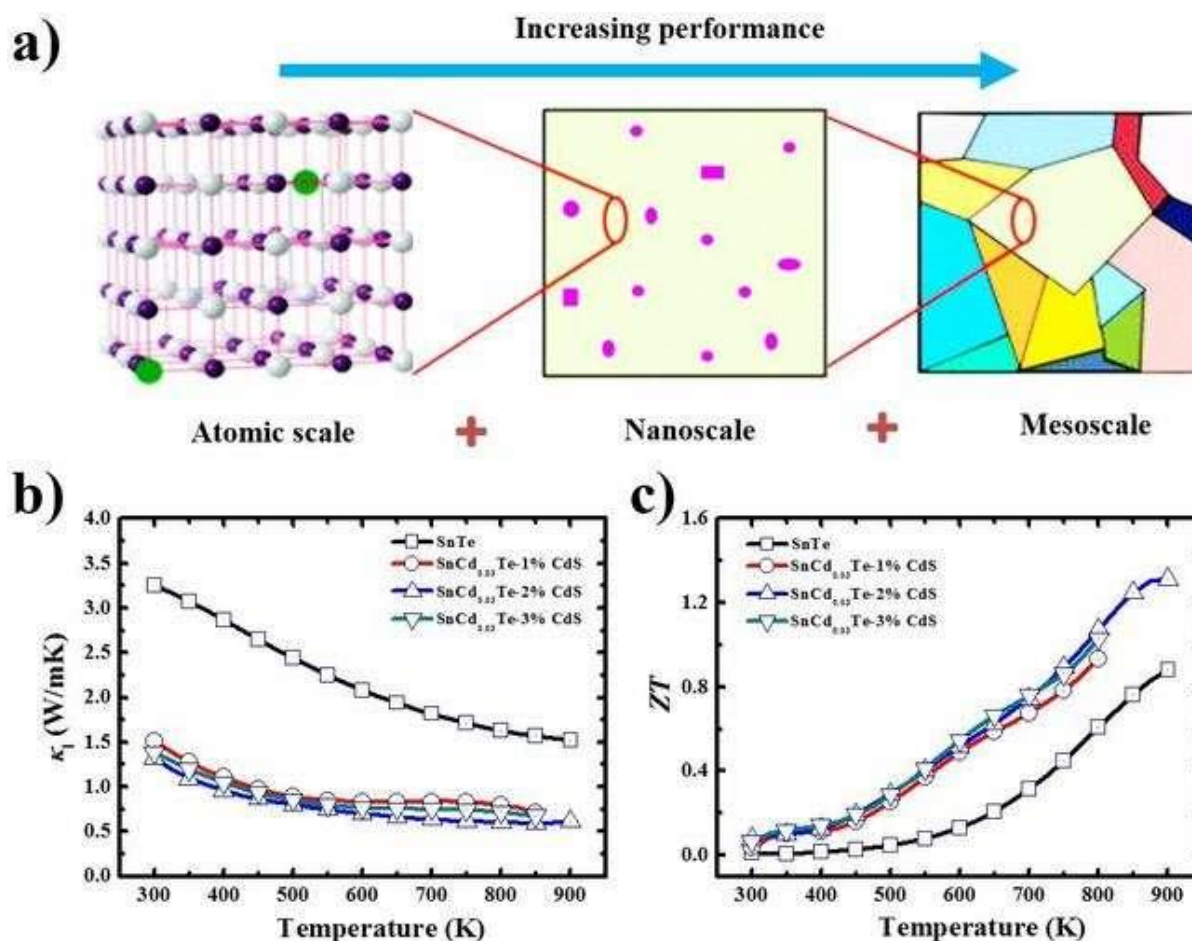
Figure 2.12 a) Schematic diagram of the integration of three different types of defects; atomic scale point defects, nanoscale precipitates, and mesoscale grains in one single material for

all-scale hierarchical architectures of phonon scattering. Reproduced with permission.[10] Copyright 2012, Nature Publishing Group. Effect of all-scale hierarchical architecture on the thermoelectric performance of SnTe system: b) κ_l and c) ZT of SnTe[44] and SnTe-Cd-CdS.[39]

Understanding phonon dynamics is very important in improving the thermoelectric efficiency of a material system.[168] **Figure 2.13a** shows the temperature dependent phonon DOS of SnTe. The temperature dependence of the phonon DOS provides insights into the thermal effects on the vibrational energies in the lattice. A comparative study on room temperature κ_l due to the different doping elements in SnTe is shown in **Figure 2.13b**.[34, 35, 37, 39, 42, 44, 53] As can be seen, pristine SnTe shows a high κ_l of ~2.88 W m^{-1} K^{-1} which is significantly reduced after doping and eventually reaches close to the theoretical minimum value (~0.4 W m^{-1} K^{-1}) in Sn$_{1-x}$Sb$_x$Te (~0.67 W m^{-1} K^{-1}) system.[34, 53]
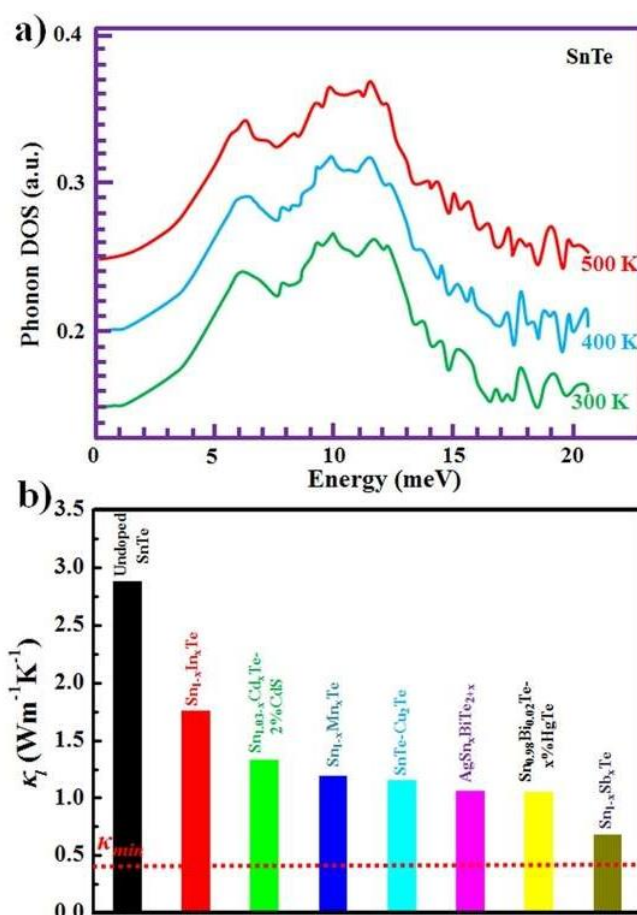
Figure 2.13 a) Phonon density of states of SnTe.[168] b) Comparison of room temperature κ_l of different doped SnTe system. Red dotted line shows the theoretical minimum κ_l.[34, 35, 37, 39, 42, 44, 53]

2.7 Synergistic Effect

A typical example of synergistic effect is the combination of resonance energy level (by In doping) and valence band convergence (by Ag doping) in SnTe.[34] **Figure 2.14a-e** is the calculated electronic band structures and DOS of pristine and doped SnTe by In and Ag via the density functional theory. The pristine SnTe shows the large $\Delta E_{VB_{L-\Sigma}}$ (**Figure 2.14a**). The incorporation of Ag in SnTe leads to an increase in the valence band degeneracy (**Figure 2.14b**) while In doping creates resonance level which provide DOS peaks within the valence band near the Fermi energy level (**Figure 2.14c**). The electronic structure of Ag and In co-doped SnTe reveals both the formation of resonance state and the convergence of the valence bands (**Figure 2.14d**). Such valence band convergence and resonance effect resulted in asymmetry in slope of the DOS at or near Fermi energy (**Figure 2.14e**). A significant decrease in $\Delta E_{VB_{L-\Sigma}}$ of pristine SnTe is achieved with Ag doping, from ~0.382 eV in pristine SnTe to ~0.178 eV in the 6.25 mol % Ag-doped SnTe. The $\Delta E_{VB_{L-\Sigma}}$ further reduces to ~0.105 eV (**Figure 2.14f**), showing the synergistic effects of Ag and In. Therefore, coexistence of resonance level and valence band convergence in $SnAg_xIn_xTe_{1+2x}$ gives a synergistic enhancement in S over a broad temperature range of 300-860 K compared to that of In-doped SnTe and Ag-doped SnTe. Moreover, co-doping with In and Ag significantly tunes the electronic transport properties of SnTe, leading to a $S^2\sigma \approx 31.4$ μW cm^{-1} K^{-2} and a high $ZT \approx 1$ at 856 K.

Meanwhile, the synergistic effect to In/Cd co-doped in SnTe is investigated by Tan *et al.*[21] In and Cd played distinct but complementary role to enhance S over a broad range of high temperatures. In dopants not only create resonance level but also reduce $\Delta E_{VB_{L-\Sigma}}$. As a result, In/Cd co-doped SnTe exhibits a high S of 199 μV K^{-1} at 923 K that lead to a high ZT of ~1.4 at ~923 K. Furthermore, Banik *et al.*[30] carried out research on synergistic effect of In/Se co-doped SnTe system and found that Se doping can significantly converge the two valence bands while In creates resonance states. The room temperature σ of pristine SnTe was reduced from 6110 S cm^{-1} to 1670 S cm^{-1} due to 1.5 mol % In doping in $In_ySn_{1-y}Te_{0.85}Se_{0.15}$.[30] Consequently a high S of ~175 μV K^{-1} at 855 K and high ZT of ~0.8 at 860 K obtained in $In_{0.015}Sn_{0.985}Te_{0.85}Se_{0.15}$.[30] A most recent study by Bhat *et al.*[74] showed that In/Mg co-doping in SnTe can synergistically leads to a high $S^2\sigma$ of 42 μW cm^{-1} K^{-2} and a high ZT of 1.5 at 840 K.
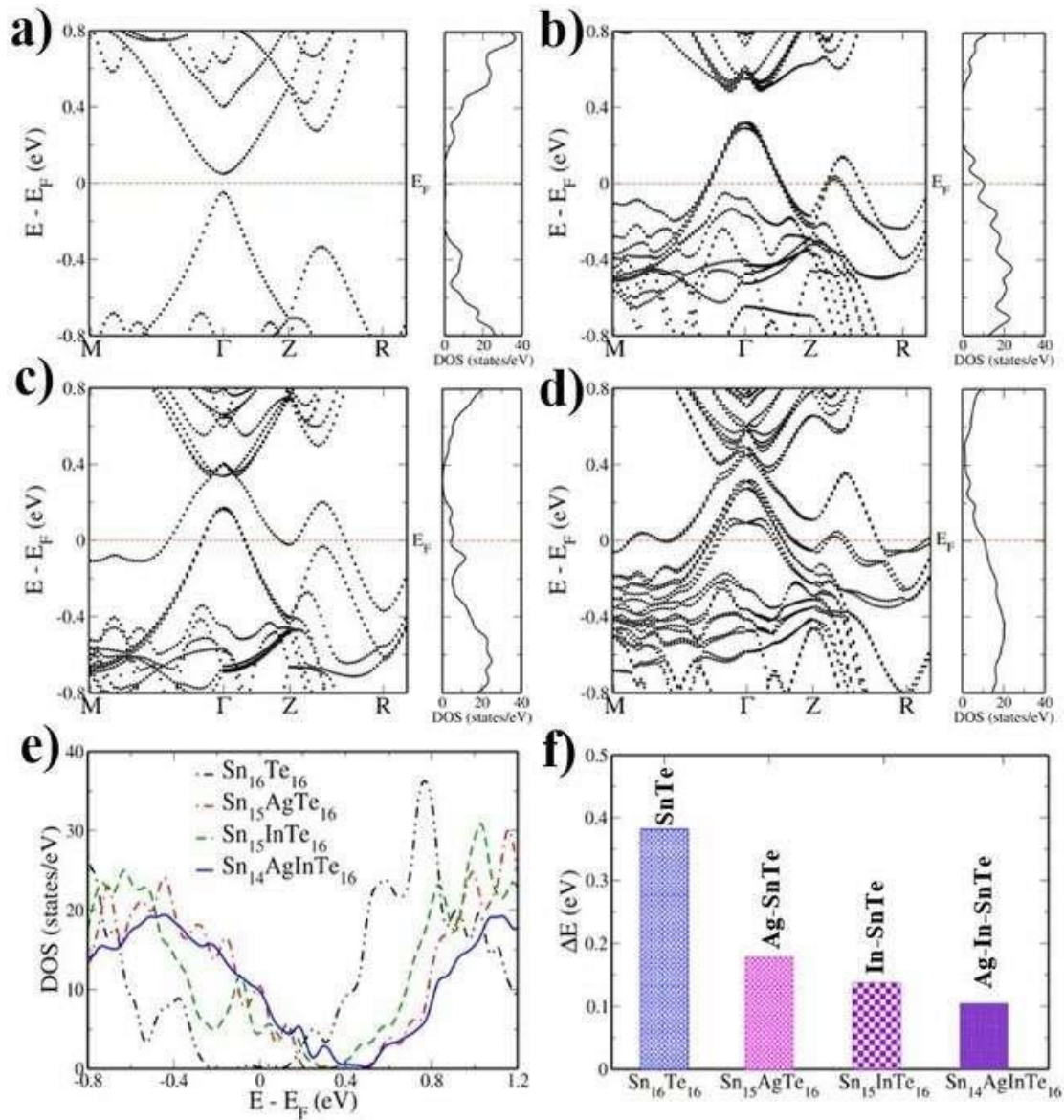
Figure 2.14 Electronic band structure and DOS of a) $Sn_{16}Te_{16}$ b) $Sn_{15}AgTe_{16}$ c) $Sn_{14}InTe_{16}$ d) $Sn_{14}AgInTe_{16}$ supercells as a function of wave vector in the supercell Brillouin zone. The energies are shifted with respect to the Fermi energy, which is set to zero. The band gap appears at the Γ point and heavy-hole band at $Z + \delta$ in the $\sqrt{2} \times \sqrt{2} \times 2$ tetragonal supercells. The VBM and CBM occurring at the L point in the rock-salt cell of SnTe fold onto the Γ point, and the heavy-hole valence band appearing along Σ folds onto $Z + \delta$ in the case of the present 32-atom $\sqrt{2} \times \sqrt{2} \times 2$ tetragonal supercell. e) Synergistic effect of In and Ag on DOS near the top of the valence band. f) Energy separations, ΔE, between the upper valence band at the Γ point and the lower valence band at the $Z + \delta$ point for pristine SnTe, In- and Ag-doped

SnTe, and In and Ag co-doped SnTe. Reproduced with permission[51]. Copyright 2016, American Chemical Society.

2.8 Conclusion

Remarkable progresses have been achieved in SnTe so far with a peak ZT >1. However, more efforts are still needed to further improve its performance with a goal to obtain ZT >2 in order to boost the practical applications of SnTe. The limit of the ZT enhancement in rock-salt structured chalcogenides has been calculated by Hong et $al.$[90] and showed that ZT of SnTe can reach up to 2.2 if κ_l can be reduced to its amorphous limit in conjunct with the simultaneous band convergence (**Figure 2.15a**). A most recent study led by Li et $al.$[73] suggested that by applying valence band convergence and interstitial defects, the ZT value of SnTe can be enhanced as high as 1.6 at 900 K (**Figure 2.15b**). By reducing the number of phonon modes that propagate through the material system is the effective way to reduce κ_l below the amorphous limit.[10] However, the fundamentals are not yet fully understood. Hence, theoreticians and experimentalists should continue to investigate the underlying scattering mechanisms and to develop new approaches that will simultaneously further increase $S^2\sigma$ and reduce κ to ultimately enhance ZT over 2 to boost the thermoelectrics.

One of the fundamental challenge to obtain high performance thermoelectric material is the inter-dependence between electron and phonon transport properties.[169] By introducing magnetization or spin to the matrix this inter-dependence can be mitigated.[170] Besides, The coupled transport properties can be further critically decoupled through chemical intuition.[171] By understanding the relationship of band gap, carrier effective mass and band degeneracy with the bond, bond energy, bond length and electronegativity while the lattice thermal conductivity with the crystal structure and bond strength one can inspire to design advanced high performance SnTe based thermoelectric materials.[171]

Generally, optimal n of a thermoelectric material does not remain the same at all temperature and it varies with the power law of $(T)^{3/2}$.[115] It is therefore essential to maintain the n at its optimal level under different temperatures in order to obtain the maximum output. Similar with PbTe, by identifying temperature dependent solubility of specific elements in SnTe one can achieve optimized n under different specific temperature.[172-175] This optimized n along with the band engineering and nanostructuring will guide to achieve high thermoelectric performance of SnTe under different temperature.

Especially, the accurate multi-scale phonon modelling of nanocomposites are still challenging since our understanding of phonon-interface scattering is still limited in spite of encouraging progress has been made on the calculation of mode-dependent phonon interface transmission.[176] Although first principle calculations give us fundamental idea about the phonon transport physics, however more simulation work is highly needed to understand the defects and their effect on phonon transport in the bulk as well as nanostructured materials. Additionally, mechanical properties also need to be investigated to clarify the stability of the developed materials.

It is still great interest to develop *n*-type SnTe thermoelectric material even pure SnTe is invariably a *p*-type semiconductor due to Sn deficiency. Singh[47] calculated the thermopower of the *n*-type SnTe considering electron carrier, and found that the *S* for *n*-type SnTe is significantly superior than that of *n*-type PbTe. This implies if the lattice thermal conductivities of both SnTe and PbTe is same then optimized *n*-type SnTe could have superior thermoelectric performance to *n*-type PbTe. However, it is already mentioned that the shape of the liquidus line in the SnTe binary phase diagram results in a high concentration of native defects, particularly Sn vacancies, which hinders to obtain *n*-type SnTe.[46] Moreover, if the modern new strategies such as controlled co-doping (possibly including the Te site, e.g., alloying with both Bi and Se) may result in *n*-type materials, then it will be helpful to determine the thermoelectric performance of heavily doped *n*-type SnTe and design full SnTe-based thermoelectric device.

All in all, we believe this comprehensive review will kindle broader interest in SnTe-based thermoelectric materials within the new generation that lead it as one of the promising solutions for energy crisis.
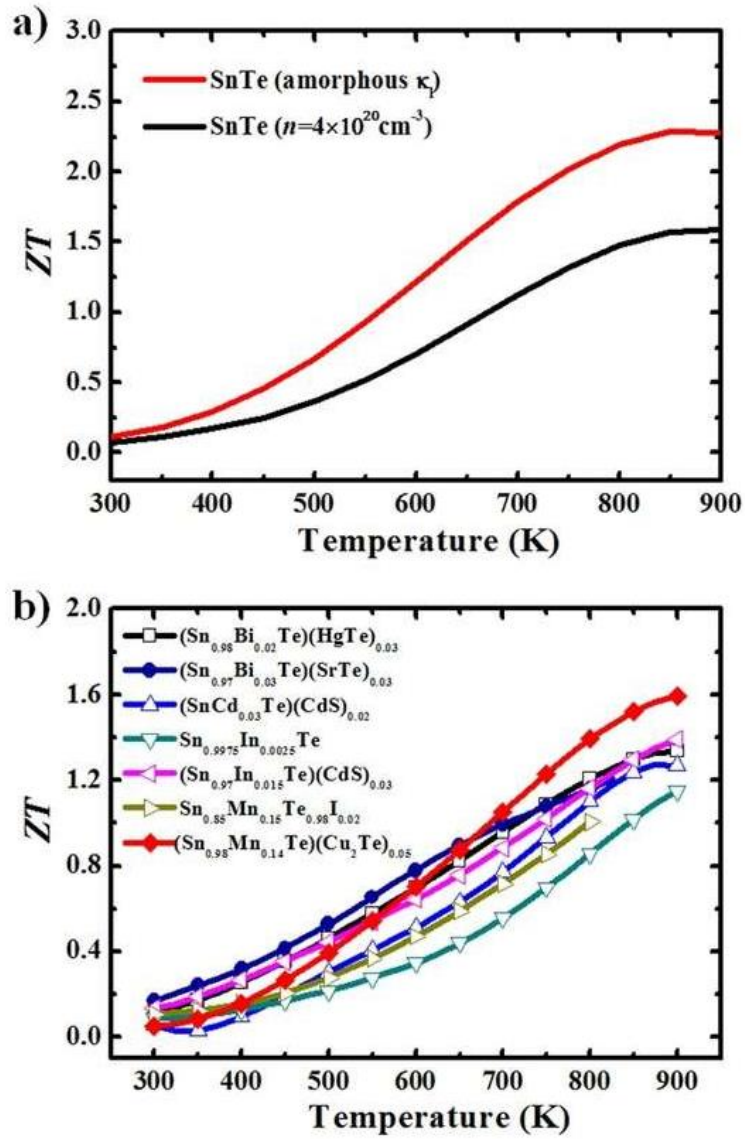
Figure 2.15 a) Predicted *ZT* values of SnTe with the valence band degeneracy at optimal *n* and lattice thermal conductivity to amorphous limit[90]. b) Temperature dependent *ZT* of SnTe based thermoelectric materials.[21, 35, 39, 44, 52, 73, 75]

References

(1) Wood, C. *Rep. Prog. Phys.* **1988**, *51*, 459.

(2) Snyder, G. J.; Toberer, E. S. *Nat. Mater.* **2008**, *7*, 105-114.

(3) Chen, Z. G.; Han, G.; Yang, L.; Cheng, L.; Zou, J. *Prog. Nat. Sci.* **2012**, *22*, 535-549.

(4) Cutler, M.; Leavy, J. F.; Fitzpatrick, R. L. *Phys. Rev.* **1964**, *133*, A1143-A1152.

(5) Zhao, L.-D.; He, J.; Hao, S.; Wu, C.-I.; Hogan, T. P.; Wolverton, C.; Dravid, V. P.; Kanatzidis, M. G. *J. Am. Chem. Soc.* **2012**, *134*, 16327-16336.

(6) Liu, W.; Tan, X.; Yin, K.; Liu, H.; Tang, X.; Shi, J.; Zhang, Q.; Uher, C. *Phys. Rev. Lett.* **2012**, *108*, 166601.

(7) Pei, Y.; Shi, X.; LaLonde, A.; Wang, H.; Chen, L.; Snyder, G. J. *Nature* **2011**, *473*, 66-69.

(8) Pei, Y.; Morelli, D. T. *Appl. Phys. Lett.* **2009**, *94*, 122112.

(9) Sun, H.; Lu, X.; Chi, H.; Morelli, D. T.; Uher, C. *Phys. Chem. Chem. Phys.* **2014**, *16*, 15570-15575.

(10) Biswas, K.; He, J.; Blum, I. D.; Wu, C.-I.; Hogan, T. P.; Seidman, D. N.; Dravid, V. P.; Kanatzidis, M. G. *Nature* **2012**, *489*, 414-418.

(11) Hong, M.; Chen, Z.-G.; Yang, L.; Zou, J. *Nanoscale* **2016**, *8*, 8681-8686.

(12) Hong, M.; Chen, Z. G.; Yang, L.; Zou, J. *Nano Energy* **2016**, *20*, 144-155.

(13) Biswas, K.; He, J.; Wang, G.; Lo, S.-H.; Uher, C.; Dravid, V. P.; Kanatzidis, M. G. *Energy Environ. Sci.* **2011**, *4*, 4675-4684.

(14) Biswas, K.; He, J.; Zhang, Q.; Wang, G.; Uher, C.; Dravid, V. P.; Kanatzidis, M. G. *Nat. Chem.* **2011**, *3*, 160-166.

(15) Dow, H. S.; Oh, M. W.; Kim, B. S.; Park, S. D.; Min, B. K.; Lee, H. W.; Wee, D. M. *J. Appl. Phys.* **2010**, *108*, 113709.

(16) Du, B.; Li, H.; Xu, J.; Tang, X.; Uher, C. *J. Solid State Chem.* **2011**, *184*, 109-114.

(17) Heremans, J. P.; Jovovic, V.; Toberer, E. S.; Saramat, A.; Kurosaki, K.; Charoenphakdee, A.; Yamanaka, S.; Snyder, G. J. *Science* **2008**, *321*, 554-557.

(18) Jana, M. K.; Pal, K.; Waghmare, U. V.; Biswas, K. *Angew. Chem., Int. Ed.* **2016**, *55*, 7792-7796.

(19) Pei, Y.; Wang, H.; Gibbs, Z. M.; LaLonde, A. D.; Snyder, G. J. *NPG Asia Mater.* **2012**, *4*, e28.

(20) Wang, N.; West, D.; Liu, J.; Li, J.; Yan, Q.; Gu, B.-L.; Zhang, S. B.; Duan, W. *Phys. Rev. B* **2014**, *89*, 045142.

(21) Tan, G.; Shi, F.; Hao, S.; Chi, H.; Zhao, L.-D.; Uher, C.; Wolverton, C.; Dravid, V. P.; Kanatzidis, M. G. *J. Am. Chem. Soc.* **2015**, *137*, 5100-5112.

(22) Zebarjadi, M.; Esfarjani, K.; Dresselhaus, M. S.; Ren, Z. F.; Chen, G. *Energy Environ. Sci.* **2012**, *5*, 5147-5162.

(23) Zhang, Q.; Cao, F.; Liu, W.; Lukas, K.; Yu, B.; Chen, S.; Opeil, C.; Broido, D.; Chen, G.; Ren, Z. *J. Am. Chem. Soc.* **2012**, *134*, 10031-10038.

(24) Liu, H.; Yuan, X.; Lu, P.; Shi, X.; Xu, F.; He, Y.; Tang, Y.; Bai, S.; Zhang, W.; Chen, L.; Lin, Y.; Shi, L.; Lin, H.; Gao, X.; Zhang, X.; Chi, H.; Uher, C. *Adv. Mater.* **2013**, *25*, 6607-6612.

(25) Zhao, L.-D.; Lo, S.-H.; Zhang, Y.; Sun, H.; Tan, G.; Uher, C.; Wolverton, C.; Dravid, V. P.; Kanatzidis, M. G. *Nature* **2014**, *508*, 373-377.

(26) Barr, T. D.; Dahlen, F. A. *J. Geophys. Res. Solid Earth* **1989**, *94*, 3923-3947.

(27) Hsu, C.-T.; Huang, G.-Y.; Chu, H.-S.; Yu, B.; Yao, D.-J. *Appl. Energy* **2011**, *88*, 1291-1297.

(28) Wu, C. *Appl. Therm. Eng.* **1996**, *16*, 63-69.

(29) Yang, L.; Chen, Z.-G.; Hong, M.; Wang, L.; Kong, D.; Huang, L.; Han, G.; Zou, Y.; Dargusch, M.; Zou, J. *Nano Energy* **2017**, *31*, 105-112.

(30) Banik, A.; Biswas, K. *J. Mater. Chem. A* **2014**, *2*, 9620-9625.

(31) Al Rahal Al Orabi, R.; Mecholsky, N. A.; Hwang, J.; Kim, W.; Rhyee, J. S.; Wee, D.; Fornari, M. *Chem. Mater.* **2016**, *28*, 376-384.

(32) Banik, A.; Biswas, K. *J. Solid State Chem.* **2016**, *242, Part 2*, 43-49.

(33) Banik, A.; Shenoy, U. S.; Anand, S.; Waghmare, U. V.; Biswas, K. *Chem. Mater.* **2015**, *27*, 581-587.

(34) Banik, A.; Vishal, B.; Perumal, S.; Datta, R.; Biswas, K. *Energy Environ. Sci.* **2016**, *9*, 2011-2019.

(35) Tan, G.; Shi, F.; Doak, J. W.; Sun, H.; Zhao, L.-D.; Wang, P.; Uher, C.; Wolverton, C.; Dravid, V. P.; Kanatzidis, M. G. *Energy Environ. Sci.* **2015**, *8*, 267-277.

(36) Tan, G.; Shi, F.; Hao, S.; Chi, H.; Bailey, T. P.; Zhao, L.-D.; Uher, C.; Wolverton, C.; Dravid, V. P.; Kanatzidis, M. G. *J. Am. Chem. Soc.* **2015**, *137*, 11507-11516.

(37) Tan, G.; Shi, F.; Sun, H.; Zhao, L.-D.; Uher, C.; Dravid, V. P.; Kanatzidis, M. G. *J. Mater. Chem. A* **2014**, *2*, 20849-20854.

(38) Tan, G.; Zeier, W. G.; Shi, F.; Wang, P.; Snyder, G. J.; Dravid, V. P.; Kanatzidis, M. G. *Chem. Mater.* **2015**, *27*, 7801-7811.

(39) Tan, G.; Zhao, L. D.; Shi, F.; Doak, J. W.; Lo, S. H.; Sun, H.; Wolverton, C.; Dravid, V. P.; Uher, C.; Kanatzidis, M. G. *J. Am. Chem. Soc.* **2014**, *136*, 7006-7017.

(40) Tan, X. J.; Liu, G. Q.; Xu, J. T.; Shao, H. Z.; Jiang, J.; Jiang, H. C. *Phys. Chem. Chem. Phys.* **2016**, *18*, 20635-20639.

(41) Tan, X. J.; Shao, H. Z.; He, J.; Liu, G. Q.; Xu, J. T.; Jiang, J.; Jiang, H. C. *Phys. Chem. Chem. Phys.* **2016**, *18*, 7141-7147.

(42) Wu, H.; Chang, C.; Feng, D.; Xiao, Y.; Zhang, X.; Pei, Y.; Zheng, L.; Wu, D.; Gong, S.; Chen, Y.; He, J.; Kanatzidis, M. G.; Zhao, L.-D. *Energy Environ. Sci.* **2015**, *8*, 3298-3312.

(43) Zhang, L.; Wang, J.; Cheng, Z.; Sun, Q.; Li, Z.; Dou, S. *J. Mater. Chem. A* **2016**, *4*, 7936-7942.

(44) Zhang, Q.; Liao, B.; Lan, Y.; Lukas, K.; Liu, W.; Esfarjani, K.; Opeil, C.; Broido, D.; Chen, G.; Ren, Z. *Proc. Natl. Acad. Sci. USA* **2013**, *110*, 13261-13266.

(45) Acharya, S.; Pandey, J.; Soni, A. *Appl. Phys. Lett.* **2016**, *109*, 133904.

(46) Brebrick, R. F. *J. Phys. Chem. Solids* **1963**, *24*, 27-36.

(47) Singh, D. J. *Funct. Mater. Lett.* **2010**, *03*, 223-226.

(48) Brebrick, R. F.; Strauss, A. J. *Phys. Rev.* **1963**, *131*, 104-110.

(49) He, J.; Tan, X.; Xu, J.; Liu, G.-Q.; Shao, H.; Fu, Y.; Wang, X.; Liu, Z.; Xu, J.; Jiang, H.; Jiang, J. *J. Mater. Chem. A* **2015**, *3*, 19974-19979.

(50) Zhou, M.; Gibbs, Z. M.; Wang, H.; Han, Y.; Xin, C.; Li, L.; Snyder, G. J. *Phys. Chem. Chem. Phys.* **2014**, *16*, 20741-20748.

(51) Banik, A.; Shenoy, U. S.; Saha, S.; Waghmare, U. V.; Biswas, K. *J. Am. Chem. Soc.* **2016**, *138*, 13068-13075.

(52) Zhao, L.-D.; Zhang, X.; Wu, H.; Tan, G.; Pei, Y.; Xiao, Y.; Chang, C.; Wu, D.; Chi, H.; Zheng, L.; Gong, S.; Uher, C.; He, J.; Kanatzidis, M. G. *J. Am. Chem. Soc.* **2016**, *138*, 2366-2373.

(53) Pei, Y.; Zheng, L.; Li, W.; Lin, S.; Chen, Z.; Wang, Y.; Xu, X.; Yu, H.; Chen, Y.; Ge, B. *Adv. Electron. Mater.* **2016**, *2*.

(54) Ma, Y.; Hao, Q.; Poudel, B.; Lan, Y.; Yu, B.; Wang, D.; Chen, G.; Ren, Z. *Nano Lett.* **2008**, *8*, 2580-2584.

(55) Androulakis, J.; Hsu, K. F.; Pcionek, R.; Kong, H.; Uher, C.; D'Angelo, J. J.; Downey, A.; Hogan, T.; Kanatzidis, M. G. *Adv. Mater.* **2006**, *18*, 1170-1173.

(56) Zhang, S. N.; Zhu, T. J.; Yang, S. H.; Yu, C.; Zhao, X. B. *J. Alloys Compd.* **2010**, *499*, 215-220.

(57) Poudeu, P. F. P.; Guéguen, A.; Wu, C.-I.; Hogan, T.; Kanatzidis, M. G. *Chem. Mater.* **2010**, *22*, 1046-1053.

(58) Jiang, Q.; Yan, H.; Khaliq, J.; Ning, H.; Grasso, S.; Simpson, K.; Reece, M. J. *J. Mater. Chem. A* **2014**, *2*, 5785-5790.

(59) Shi, X.; Xi, L.; Fan, J.; Zhang, W.; Chen, L. *Chem. Mater.* **2010**, *22*, 6029-6031.

(60) Fahrnbauer, F.; Souchay, D.; Wagner, G.; Oeckler, O. *J. Am. Chem. Soc.* **2015**, *137*, 12633-12638.

(61) Tewari, G. C.; Tripathi, T. S.; Rastogi, A. K. *J. Electron. Mater.* **2010**, *39*, 1133-1139.

(62) Zhou, Y.; Li, X.; Bai, S.; Chen, L. *J. Cryst. Growth* **2010**, *312*, 775-780.

(63) Zhu, G. H.; Lan, Y. C.; Wang, H.; Joshi, G.; Hao, Q.; Chen, G.; Ren, Z. F. *Phys. Rev. B* **2011**, *83*, 115201.

(64) Shi, X.; Yang, J.; Salvador, J. R.; Chi, M.; Cho, J. Y.; Wang, H.; Bai, S.; Yang, J.; Zhang, W.; Chen, L. *J. Am. Chem. Soc.* **2011**, *133*, 7837-7846.

(65) Xiao, C.; Qin, X.; Zhang, J.; An, R.; Xu, J.; Li, K.; Cao, B.; Yang, J.; Ye, B.; Xie, Y. *J. Am. Chem. Soc.* **2012**, *134*, 18460-18466.

(66) Fu, C.; Zhu, T.; Liu, Y.; Xie, H.; Zhao, X. *Energy Environ. Sci.* **2015**, *8*, 216-220.

(67) Fu, C.; Bai, S.; Liu, Y.; Tang, Y.; Chen, L.; Zhao, X.; Zhu, T. *Nat. Commun.* **2015**, *6*, 8144.

(68) Liu, W.; Lukas, K. C.; McEnaney, K.; Lee, S.; Zhang, Q.; Opeil, C. P.; Chen, G.; Ren, Z. *Energy Environ. Sci.* **2013**, *6*, 552-560.

(69) Li, Z.-Y.; Li, J.-F. *Adv. Energy Mater.* **2014**, *4*, 1300937-n/a.

(70) Wu, D.; Zhao, L.-D.; Tong, X.; Li, W.; Wu, L.; Tan, Q.; Pei, Y.; Huang, L.; Li, J.-F.; Zhu, Y.; Kanatzidis, M. G.; He, J. *Energy Environ. Sci.* **2015**, *8*, 2056-2068.

(71) Wang, X.; Qiu, P.; Zhang, T.; Ren, D.; Wu, L.; Shi, X.; Yang, J.; Chen, L. *J. Mater. Chem. A* **2015**, *3*, 13662-13670.

(72) Sankar, R.; Wong, D. P.; Chi, C.-S.; Chien, W.-L.; Hwang, J.-S.; Chou, F.-C.; Chen, L.-C.; Chen, K.-H. *Cryst. Eng. Commun.* **2015**, *17*, 3440-3445.

(73) Li, W.; Zheng, L.; Ge, B.; Lin, S.; Zhang, X.; Chen, Z.; Chang, Y.; Pei, Y. *Adv. Mater.* **2017**, *29*, 1605887-n/a.

(74) Bhat, D. K.; Shenoy U, S. *J. Phys. Chem. C* **2017**, *121*, 7123-7130.

(75) Li, W.; Chen, Z.; Lin, S.; Chang, Y.; Ge, B.; Chen, Y.; Pei, Y. *J. Materiomics* **2015**, *1*, 307-315.

(76) Han, M.-K.; Androulakis, J.; Kim, S.-J.; Kanatzidis, M. G. *Adv. Energy Mater.* **2012**, *2*, 157-161.

(77) Zhou, Z.; Yang, J.; Jiang, Q.; Luo, Y.; Zhang, D.; Ren, Y.; He, X.; Xin, J. *J. Mater. Chem. A* **2016**.

(78) He, J.; Xu, J.; Liu, G. Q.; Shao, H.; Tan, X.; Liu, Z.; Xu, J.; Jiang, H.; Jiang, J. *RSC Adv.* **2016**, *6*, 32189-32192.

(79) Li, Z.; Chen, Y.; Li, J.-F.; Chen, H.; Wang, L.; Zheng, S.; Lu, G. *Nano Energy* **2016**, *28*, 78-86.

(80) Liang, T.; Su, X.; Tan, X.; Zheng, G.; She, X.; Yan, Y.; Tang, X.; Uher, C. *J. Mater. Chem. C* **2015**, *3*, 8550-8558.

(81) Zhou, M.; Gibbs, Z. M.; Wang, H.; Han, Y.; Li, L.; Jeffrey Snyder, G. *Appl. Phys. Lett.* **2016**, *109*, 042102.

(82) Zheng, L.; Li, W.; Lin, S.; Li, J.; Chen, Z.; Pei, Y. *ACS Energy Lett.* **2017**, *2*, 563-568.

(83) Madelung O.; Rössler, U.; Schulz, M. *Non-Tetrahedrally Bonded Elements and Binary Compounds I, Springer, Berlin* **1998**.

(84) Madelung, O. IVx-VIy compounds. In *Semiconductors: Data Handbook*, Springer, Berlin, Heidelberg, **2004**.

(85) Dimmock, J. O.; Melngailis, I.; Strauss, A. J. *Phys. Rev. Lett.* **1966**, *16*, 1193-1196.

(86) Rogers, L. M. *J. Phys. D: Appl. Phys.* **1968**, *1*, 845-852.

(87) Littlewood, P. B.; Mihaila, B.; Schulze, R. K.; Safarik, D. J.; Gubernatis, J. E.; Bostwick, A.; Rotenberg, E.; Opeil, C. P.; Durakiewicz, T.; Smith, J. L.; Lashley, J. C. *Phys. Rev. Lett.* **2010**, *105*, 086404.

(88) Liu, W.; Kim, H. S.; Jie, Q.; Ren, Z. *Scr. Mater.* **2016**, *111*, 3-9.

(89) Borrego, J. M. *IEEE Trans. Electron Dev ev.* **1963***, 10, 364.*

(90) Hong, M.; Chen, Z.-G.; Pei, Y.; Yang, L.; Zou, J. *Phys. Rev. B* **2016**, *94*, 161201.

(91) Vedeneev, V. P.; Krivoruchko, S. P.; Sabo, E. P. *Semiconductors* **1998**, *32*, 241-244.

(92) Pei, Y.; Wang, H.; Snyder, G. J. *Adv. Mater.* **2012**, *24*, 6125-6135.

(93) Chasmar, R. P.; Stratton, R. *J. Electronic Control* **1959**, *7*, 52-72.

(94) Rowe, D. M., *CRC Handbook of Thermoelectrics*. CRC Press, Boca Raton, USA **1995**.

(95) Goldsmid, H. J., *Thermoelectric Refrigeration*. Plenum Press: New York, **1964**.

(96) Tan, G.; Zhao, L.-D.; Kanatzidis, M. G. *Chem. Rev.* **2016**.

(97) Pei, Y.; LaLonde, A.; Iwanaga, S.; Snyder, G. J. *Energy Environ. Sci.* **2011**, *4*, 2085-2089.

(98) Xie, H.; Wang, H.; Fu, C.; Liu, Y.; Snyder, G. J.; Zhao, X.; Zhu, T. *Sci. Rep.* **2014**, *4*, 6888.

(99) Kawaharada, Y.; Kurosaki, K.; Uno, M.; Yamanaka, S. *J. Alloys Compd.* **2001**, *315*, 193-197.

(100) Wenfeng, L.; Gui, Y.; Jianwei, Z. *J. Phys. D: Appl. Phys.* **2016**, *49*, 195601.

(101) Zhu, T.; Liu, Y.; Fu, C.; Heremans, J. P.; Snyder, J. G.; Zhao, X. *Adv. Mater.* **2017**, 1605884-n/a.

(102) Singh, D. J.; Mazin, I. I. *Phys. Rev. B* **1997**, *56*, R1650-R1653.

(103) Mecholsky, N. A.; Resca, L.; Pegg, I. L.; Fornari, M. *Phys. Rev. B* **2014**, *89*, 155131.

(104) Parker, D.; Chen, X.; Singh, D. J. *Phys. Rev. Lett.* **2013**, *110*, 146601.

(105) Shirai, K.; Yamanaka, K. *J. Appl. Phys.* **2013**, *113*, 053705.

(106) Mahan, G. D.; Sofo, J. O. *Proc. Natl. Acad. Sci. USA* **1996**, *93*, 7436-7439.

(107) Cutler, M.; Mott, N. F. *Phys. Rev.* **1969**, *181*, 1336-1340.

(108) Korringa, J.; Gerritsen, A. N. *Physica* **1953**, *19*, 457-507.

(109) Zhao, L. D.; Wu, H. J.; Hao, S. Q.; Wu, C. I.; Zhou, X. Y.; Biswas, K.; He, J. Q.; Hogan, T. P.; Uher, C.; Wolverton, C.; Dravid, V. P.; Kanatzidis, M. G. *Energy Environ. Sci.* **2013**, *6*, 3346-3355.

(110) Kulbachinskii, V. A.; Brandt, N. B.; Cheremnykh, P. A.; Azou, S. A.; Horak, J.; Lostak, P. *Phys. Status Solidi B* **1988**, *150*, 237-343.

(111) Zhang, Q.; Wang, H.; Liu, W.; Wang, H.; Yu, B.; Zhang, Q.; Tian, Z.; Ni, G.; Lee, S.; Esfarjani, K.; Chen, G.; Ren, Z. *Energy Environ. Sci.* **2012**, *5*, 5246-5251.

(112) Bushmarina, G. G., B.; Drabkin, I.; Lev, E. Y.; Yuneev, V. Sov. *Sov. Phys.—Semicond.* **1984**, *18*, 1374–1377.

(113) Gong, J. J.; Hong, A. J.; Shuai, J.; Li, L.; Yan, Z. B.; Ren, Z. F.; Liu, J. M. *Phys. Chem. Chem. Phys.* **2016**, *18*, 16566-16574.

(114) Mahan, G. D., Good Thermoelectrics. In *Solid State Physics*, Henry, E.; Frans, S., Eds. Academic Press: **1998**.

(115) Ioffe, A. F., *Semiconductor thermoelements, and Thermoelectric cooling*. Infosearch: London, **1957**.

(116) Goldsmid, H. J., *Introduction to Thermoelectricity*. Springer: Heidelberg, **2009**.

(117) Pei, Y.; LaLonde, A. D.; Heinz, N. A.; Shi, X.; Iwanaga, S.; Wang, H.; Chen, L.; Snyder, G. J. *Adv. Mater.* **2011**, *23*, 5674-5678.

(118) Pei, Y.; Heinz, N. A.; Snyder, G. J. *J. Mater. Chem.* **2011**, *21*, 18256-18260.

(119) Goldsmid, H. J., *Applications of thermoelectricity*. Methuen: New York **1960**.

(120) Rogers, L. M. *J. Phys. D: Appl. Phys.* **1968**, *1*, 845.

(121) Chen, Z.; Ge, B.; Li, W.; Lin, S.; Shen, J.; Chang, Y.; Hanus, R.; Snyder, G. J.; Pei, Y. *Nat. Commun.* **2017**, *8*, 13828.

(122) Poudel, B.; Hao, Q.; Ma, Y.; Lan, Y.; Minnich, A.; Yu, B.; Yan, X.; Wang, D.; Muto, A.; Vashaee, D.; Chen, X.; Liu, J.; Dresselhaus, M. S.; Chen, G.; Ren, Z. *Science* **2008**, *320*, 634.

(123) Bux, S. K.; Blair, R. G.; Gogna, P. K.; Lee, H.; Chen, G.; Dresselhaus, M. S.; Kaner, R. B.; Fleurial, J.-P. *Adv. Funct. Mater.* **2009**, *19*, 2445-2452.

(124) Yang, J.; Xi, L.; Qiu, W.; Wu, L.; Shi, X.; Chen, L.; Yang, J.; Zhang, W.; Uher, C.; Singh, D. J. *Npj Comput. Mater.* **2016**, *2*, 15015.

(125) Ioffe, A. F., Airapetiants, S. V., Ioffe, A. V., Kolomoetz, N. V. and Stilbans, L. S. *Dokl. Akad. Nauk SSSR* **1956**, *106*, 981-

981.

(126) Slack, G. A., *CRC handbook of thermoelectrics.* CRC Press: **1995**.

(127) Euchner, H.; Pailhès, S.; Nguyen, L. T. K.; Assmus, W.; Ritter, F.; Haghighirad, A.; Grin, Y.; Paschen, S.; de Boissieu, M. *Phys. Rev. B* **2012**, *86*, 224303.

(128) Zhao, L.-D.; Dravid, V. P.; Kanatzidis, M. G. *Energy Environ. Sci.* **2014**, *7*, 251-268.

(129) Sootsman, J. R.; Chung, D. Y.; Kanatzidis, M. G. *Angew. Chem., Int. Ed.* **2009**, *48*, 8616-8639.

(130) Zhang, X.; Zhao, L.-D. *J. Materiomics* **2015**, *1*, 92-105.

(131) Kim, S. I.; Lee, K. H.; Mun, H. A.; Kim, H. S.; Hwang, S. W.; Roh, J. W.; Yang, D. J.; Shin, W. H.; Li, X. S.; Lee, Y. H.; Snyder, G. J.; Kim, S. W. *Science* **2015**, *348*, 109.

(132) Vineis, C. J.; Shakouri, A.; Majumdar, A.; Kanatzidis, M. G. *Adv. Mater.* **2010**, *22*, 3970-3980.

(133) Hsu, K. F.; Loo, S.; Guo, F.; Chen, W.; Dyck, J. S.; Uher, C.; Hogan, T.; Polychroniadis, E. K.; Kanatzidis, M. G. *Science* **2004**, *303*, 818.

(134) Poudeu, P. F. P.; D'Angelo, J.; Downey, A. D.; Short, J. L.; Hogan, T. P.; Kanatzidis, M. G. *Angew. Chem., Int. Ed.* **2006**, *45*, 3835-3839.

(135) Kanatzidis, M. G. *Chem. Mater.* **2009**, *22*, 648–659.

(136) Cook, B. A.; Kramer, M. J.; Harringa, J. L.; Han, M.-K.; Chung, D.-Y.; Kanatzidis, M. G. *Adv. Funct. Mater.* **2009**, *19*, 1254-1259.

(137) Girard, S. N.; He, J.; Li, C.; Moses, S.; Wang, G.; Uher, C.; Dravid, V. P.; Kanatzidis, M. G. *Nano Lett.* **2010**, *10*, 2825-2831.

(138) Sootsman, J. R.; Kong, H.; Uher, C.; D'Angelo, J. J.; Wu, C.-I.; Hogan, T. P.; Caillat, T.; Kanatzidis, M. G. *Angew. Chem., Int. Ed.* **2008**, *47*, 8618-8622.

(139) He, J.; Girard, S. N.; Kanatzidis, M. G.; Dravid, V. P. *Adv. Funct. Mater.* **2010**, *20*, 764-772.

(140) Poudeu, P. F. P.; D'Angelo, J.; Kong, H.; Downey, A.; Short, J. L.; Pcionek, R.; Hogan, T. P.; Uher, C.; Kanatzidis, M. G. *J. Am. Chem. Soc.* **2006**, *128*, 14347-14355.

(141) Quarez, E.; Hsu, K.-F.; Pcionek, R.; Frangis, N.; Polychroniadis, E. K.; Kanatzidis, M. G. *J. Am. Chem. Soc.* **2005**, *127*, 9177-9190.

(142) He, J.; Sootsman, J. R.; Girard, S. N.; Zheng, J.-C.; Wen, J.; Zhu, Y.; Kanatzidis, M. G.; Dravid, V. P. *J. Am. Chem. Soc.* **2010**, *132*, 8669-8675.

(143) Sootsman, J. R.; Pcionek, R. J.; Kong, H.; Uher, C.; Kanatzidis, M. G. *Chem. Mater.* **2006**, *18*, 4993-4995.

(144) Han, M.-K.; Hoang, K.; Kong, H.; Pcionek, R.; Uher, C.; Paraskevopoulos, K. M.; Mahanti, S. D.; Kanatzidis, M. G. *Chem. Mater.* **2008**, *20*, 3512-3520.

(145) Guéguen, A.; Poudeu, P. F. P.; Li, C.-P.; Moses, S.; Uher, C.; He, J.; Dravid, V.; Paraskevopoulos, K. M.; Kanatzidis, M. G. *Chem. Mater.* **2009**, *21*, 1683-1694.

(146) Lioutas, C. B.; Frangis, N.; Todorov, I.; Chung, D. Y.; Kanatzidis, M. G. *Chem. Mater.* **2010**, *22*, 5630-5635.

(147) Zhou, M.; Li, J.-F.; Kita, T. *J. Am. Chem. Soc.* **2008**, *130*, 4527-4532.

(148) Cao, Y. Q.; Zhao, X. B.; Zhu, T. J.; Zhang, X. B.; Tu, J. P. *Appl. Phys. Lett.* **2008**, *92*, 143106.

(149) Fan, S.; Zhao, J.; Guo, J.; Yan, Q.; Ma, J.; Hng, H. H. *Appl. Phys. Lett.* **2010**, *96*, 182104.

(150) Fan, X. A.; Yang, J. Y.; Xie, Z.; Li, K.; Zhu, W.; Duan, X. K.; Xiao, C. J.; Zhang, Q. Q. *J. Phys. D: Appl. Phys.* **2007**, *40*, 5975.

(151) Lan, Y.; Poudel, B.; Ma, Y.; Wang, D.; Dresselhaus, M. S.; Chen, G.; Ren, Z. *Nano Lett.* **2009**, *9*, 1419-1422.

(152) Xie, W.; He, J.; Kang, H. J.; Tang, X.; Zhu, S.; Laver, M.; Wang, S.; Copley, J. R. D.; Brown, C. M.; Zhang, Q.; Tritt, T. M. *Nano Lett.* **2010**, *10*, 3283-3289.

(153) Xie, W.; Tang, X.; Yan, Y.; Zhang, Q.; Tritt, T. M. *J. Appl. Phys.* **2009**, *105*, 113713.

(154) Xie, W.; Tang, X.; Yan, Y.; Zhang, Q.; Tritt, T. M. *Appl. Phys. Lett.* **2009**, *94*, 102111.

(155) Yan, X.; Poudel, B.; Ma, Y.; Liu, W. S.; Joshi, G.; Wang, H.; Lan, Y.; Wang, D.; Chen, G.; Ren, Z. F. *Nano Lett.* **2010**, *10*, 3373-3378.

(156) Zhao, X. B.; Yang, S. H.; Cao, Y. Q.; Mi, J. L.; Zhang, Q.; Zhu, T. J. *J. Electron. Mater.* **2009**, *38*, 1017-1024.

(157) Joshi, G.; Lee, H.; Lan, Y.; Wang, X.; Zhu, G.; Wang, D.; Gould, R. W.; Cuff, D. C.; Tang, M. Y.; Dresselhaus, M. S.; Chen, G.; Ren, Z. *Nano Lett.* **2008**, *8*, 4670-4674.

(158) Wang, X. W.; Lee, H.; Lan, Y. C.; Zhu, G. H.; Joshi, G.; Wang, D. Z.; Yang, J.; Muto, A. J.; Tang, M. Y.; Klatsky, J.; Song, S.; Dresselhaus, M. S.; Chen, G.; Ren, Z. F. *Appl. Phys. Lett.* **2008**, *93*, 193121.

(159) Park, J. G.; Lee, Y. H. *Curr. Appl. Phys.* **2016**, *16*, 1202-1215.

(160) Wu, D.; Zhao, L.-D.; Hao, S.; Jiang, Q.; Zheng, F.; Doak, J. W.; Wu, H.; Chi, H.; Gelbstein, Y.; Uher, C.; Wolverton, C.; Kanatzidis, M.; He, J. *J. Am. Chem. Soc.* **2014**, *136*, 11412-11419.

(161) Lee, Y.; Lo, S.-H.; Androulakis, J.; Wu, C.-I.; Zhao, L.-D.; Chung, D.-Y.; Hogan, T. P.; Dravid, V. P.; Kanatzidis, M. G. *J. Am. Chem. Soc.* **2013**, *135*, 5152-5160.

(162) Tan, G.; Wang, S.; Li, H.; Yan, Y.; Tang, X. *J. Solid State Chem.* **2012**, *187*, 316-322.

(163) Zheng, Y.; Zhang, Q.; Su, X.; Xie, H.; Shu, S.; Chen, T.; Tan, G.; Yan, Y.; Tang, X.; Uher, C.; Snyder, G. J. *Adv. Energy Mater.* **2015**, *5*, 1401391.

(164) Bhattacharya, S.; Bohra, A.; Basu, R.; Bhatt, R.; Ahmad, S.; Meshram, K. N.; Debnath, A. K.; Singh, A.; Sarkar, S. K.; Navneethan, M.; Hayakawa, Y.; Aswal, D. K.; Gupta, S. K. *J. Mater. Chem. A* **2014**, *2*, 17122-17129.

(165) Lan, J.-L.; Liu, Y.; Lin, Y.-H.; Nan, C.-W.; Cai, Q.; Yang, X. *Sci. Rep.* **2015**, *5*, 7783.

(166) Zhang, Q.; Ai, X.; Wang, L.; Chang, Y.; Luo, W.; Jiang, W.; Chen, L. *Adv. Funct. Mater.* **2015**, *25*, 966-976.

(167) Guin, S. N.; Negi, D. S.; Datta, R.; Biswas, K. *J. Mater. Chem. A* **2014**, *2*, 4324-4331.

(168) Li, C. W.; Ma, J.; Cao, H. B.; May, A. F.; Abernathy, D. L.; Ehlers, G.; Hoffmann, C.; Wang, X.; Hong, T.; Huq, A.; Gourdon, O.; Delaire, O. *Phys. Rev. B* **2014**, *90*, 214303.

(169) Minnich, A. J.; Dresselhaus, M. S.; Ren, Z. F.; Chen, G. *Energy Environ. Sci.* **2009**, *2*, 466-479.

(170) Boona, S. R.; Watzman, S. J.; Heremans, J. P. *APL Mater.* **2016**, *4*, 104502.

(171) Zeier, W. G.; Zevalkink, A.; Gibbs, Z. M.; Hautier, G.; Kanatzidis, M. G.; Snyder, G. J. *Angew. Chem. Int., Ed.* **2016**, *55*, 6826-6841.

(172) Pei, Y.; May, A. F.; Snyder, G. J. *Adv. Energy Mater.* **2011**, *1*, 291-296.

(173) Yamini, S. A.; Ikeda, T.; Lalonde, A.; Pei, Y.; Dou, S. X.; Snyder, G. J. *J. Mater. Chem. A* **2013**, *1*, 8725-8730.

(174) Bergum, K.; Ikeda, T.; Jeffrey Snyder, G. *J. Solid State Chem.* **2011**, *184*, 2543-2552.

(175) Brebrick, R. F.; Gubner, E. *J. Chem. Phys.* **1962**, *36*, 1283-1289.

(176) Tian, Z.; Lee, S.; Chen, G. *J. Heat Mass Transfer* **2013**, *135*, 061605.

Chapter 3. Methodologies

In this thesis, SnTe micro size crystals are synthesized by solvothermal method. After the centrifuging and drying process, SnTe powders are characterized by XRD, SEM and TEM to analyse morphologies, chemical compositions and crystal structures. SnTe powder particles are then sintered by SPS technique, and the thermoelectric properties of sintered SnTe pellets are measured by laser-flash method, ZEM-3 and Hall equipment. In addition to this, the SnTe pellets are also characterized by XRD, SEM, and TEM to analyse their chemical compositions, morphologies, and crystal structures after sintering.

3.1 Synthesis Methods and Work Flow Chart

Tin telluride based thermoelectric materials are synthesized by solvothermal route. There are numerous advantages of solvothermal synthesis method compare to other conventional synthesis methods such as melting, solid state reaction methods. Solvothermal synthesis methods is relatively cheap, low temperature process and highly energy efficient. Controllable size of crystalline products can be easily fabricated by solvothermal method. A complete flow chart of the current thesis is shown in **Figure 3.1**.
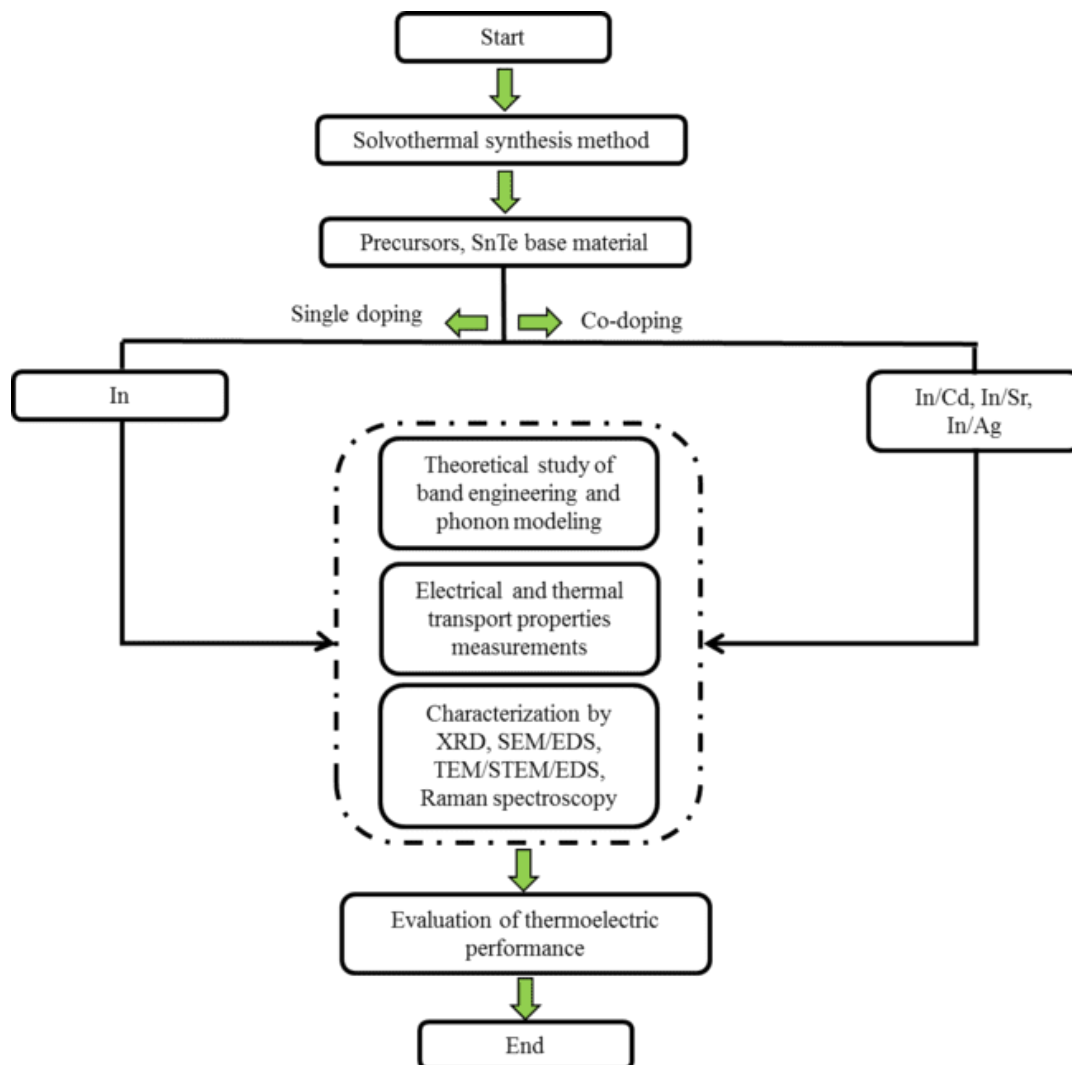
Figure 3.1 Flow chart of the research work

3.2 Materials and Reagents

Table 3.1 represents a summary of the chemicals and reagents used for the synthesis of SnTe based thermoelectric materials. The chemicals were used as received condition without further treatment.

Table 3.1 List of chemicals and reagents used

Name of the chemicals	Molecular Weight (g/mol)	Company	Purity/grade
Sodium tellurite	221.5777	Sigma-Aldrich	99.99 %
Tin (II) chloride dihydrate	225.63	Sigma-Aldrich	99.99 %
cadmium chloride	183.32	Sigma-Aldrich	99.99 %
Indium (III) chloride tetrahydrate	293.23	Sigma-Aldrich	97 %
Strontium chloride hexahydrate	266.62	Sigma-Aldrich	99 %
Ethylene glycol	62.07	Sigma-Aldrich	99.8 %
Sodium Hydroxide	39.997	Sigma-Aldrich	99.99 %
Silver Nitrate	169.87	Sigma-Aldrich	> 99 %

3.3 Spark Plasma Sintering (SPS)

We used SPS to sinter the synthesized powder materials in order to measure the thermoelectric properties of SnTe-based materials. SPS-211Lx, Fuji Electronic Co., Ltd. was used in this project.

3.4 Characterization Methods

3.4.1 X-ray Diffraction (XRD)

X-ray diffraction is a well-established technique to analyze the composition, atomic or molecular structure of materials. In the present work XRD carried out on both synthesized powder and sintered samples. CuKα radiation (wavelength λ=1.54056 Å) with a step size of 2 degrees per minute with a voltage of 40 KV is used and 2 theta ranging from 10 to 80°. XRD experiments were performed in Bruker D8 Advance MKII XRD machine.

3.4.2 Scanning Electron Microscopy (SEM)

Field emission scanning electron microscope analysis were carried out on JEOL 6610 electron microscope at 25-30 kV beam voltage with a spot size of 55-60. The samples to be investigated were mounted onto a carbon tape placed on a stainless steel stub. In SEM, a focused electron beam scanned the surface of the sample to form the image. The electron beam is usually generated from an electron gun and then accelerated by anode. The electron gun voltage ranges from 1 to 50 kV and the beam diameter is of several nanometers.

3.4.3 Transmission Electron Microscopy (TEM)

High resolution transmission electron microscopy analysis carried out in Philips Tecnai F20 FEG-S/TEM machine. The accelerating voltage is 200 kV. TEM lamella was placed in a Cu-grid and mounted on the FEI double tilt holder. The holder was inserted in the machine for TEM imaging. Energy dispersive X-ray point analysis/mapping was also carried out to investigate the elemental composition of the sample. We have also used aberration corrected TEM machine (Hitachi HF 5000) to see the nanostructure of our samples.

3.4.4 Raman Spectroscopy

Raman spectroscopy can give the information about molecular vibrations in the samples. In this thesis raman spectra were collected using a Raman Spectrometer (Reinshaw) with a 514 nm laser. The synthesized sintered samples were isolated onto a glass plate for the measurements.

3.5 Thermoelectric Property Measurements

3.5.1 Electrical Transport Properties

The electrical resistivity was measured by ZEM-3 (ULVAC). Seebeck coefficient of the samples was measured using chromel-niobium thermal couples. Seebeck coefficient of samples were determined by ZEM-3 (ULVAC). We also used NETZSCH (SBA458) to measure S and σ.

Hall carrier concentration and carrier mobility symultaneously measured by Van der Pauw technique. This technique can measure the carrier concentration and the mobility of a two dimensional sample. The electrode are placed on its perimeter.

3.5.2 Thermal Transport Properties

Thermal conductivity of the sintered sample is calculated via $\kappa = DC_p d$ relationship, where D is thermal diffusivity and C_p is the specific heat capacity, respectively. LFA 457 (NETZSCH) laser flash method was used to measure D. Specific heat capacity, C_p was measured by DSC 404 F3 (NETZSCH).

3.6 Theoretical Calculations

In order to see the electronic states near the Fermi level of our undoped SnTe and In doped SnTe we performed density functional theory (DFT) calculations using Perdew-Burke-Ernzerhof generalized gradient approximation using Quantum Espresso package. First-principles band structure and density of states (DOS) calculations are performed using the VASP code adopting the Perdew-Burke-Ernzerhof generalized gradient approximation for the exchange –correlation potential is used to see the band structure of In/Sr and In/Ag co-doped SnTe system.

Chapter 4. Enhancing Thermoelectric Properties of SnTe *via* Resonant Doping

Enhancing Thermoelectric Properties of InTe Nanoprecipitate-Embedded Sn$_{1-x}$In$_x$Te Microcrystals through Anharmonicity and Strain Engineering

Raza Moshwan,[†] Xiao-Lei Shi,[†] Wei-Di Liu,[†] Yuan Wang,[†,§] Shengduo Xu,[†] Jin Zou,[*,†,‡] and Zhi-Gang Chen[*,†,§]

[†]Materials Engineering and [‡]Centre for Microscopy and Microanalysis, The University of Queensland, St. Lucia, QLD 4072, Australia
[§]Centre for Future Materials, The University of Southern Queensland, Springfield Central, QLD 4300, Australia

4.1 Publication

4.1.1 Abstract

As one of Pb-free thermoelectric materials, tin telluride (SnTe) has received extensive attention. Here, we report InTe nanoprecipitates embedded $Sn_{1-x}In_xTe$ microcrystals with an improved thermoelectric performance prepared *via* a facile solvothermal method. In dopants can strikingly enhance the room-temperature thermopower from ~ 23 µV K^{-1} to ~ 88 µV K^{-1}, which is attributed to the distortion of density of states near the Fermi level in the valence band of $Sn_{1-x}In_xTe$. Our detailed structural characterizations indicate that point defects, anharmonic-bonding, dislocations and strain around nanoprecipitates can effectively strengthen phonon scattering, and in turn significantly reduce lattice thermal conductivity. Raman spectroscopy analysis shows that optical phonon modes shifts toward higher wavenumber, indicating the change of the bonding force and the chemical environment in the system, which facilitates additional resistance to propagate heat carrying phonons. Finally, a high power factor of ~ 21.8 µW cm^{-1} K^{-2} and a corresponding figure of merit, *ZT* of ~ 0.78 are obtained in $Sn_{0.99}In_{0.01}Te$ at 773 K. This study explores the fundamental In-doping mechanisms in a SnTe matrix, and demonstrates anharmonicity and strain engineering as effective approaches to boosting thermoelectric performance, which provides a new avenue in achieving high-performance thermoelectric properties of materials.

4.1.2 Introduction

Thermoelectricity has attracted considerable interest in past few years and shows great potential in the electronic industry to cool microprocessors and sensors for increasing their speed and capacity.[1-3] Apart from its electronic applications, as a solid-state energy conversion technology, thermoelectricity can directly convert thermal gradient into electrical energy, intensifying itself in the space and automotive industry.[4-5] The energy conversion efficiency of a thermoelectric material is determined by the so-called dimensionless figure of merit (*ZT*), defined as $ZT = \frac{S^2\sigma}{\kappa}T = \frac{S^2\sigma}{\kappa_e + \kappa_l}T$, where *S, σ, T* are the Seebeck coefficient, electrical conductivity, and absolute temperature, respectively. In addition, κ is the total thermal conductivity, contributed by the electrical (κ_e) and lattice (κ_l) thermal conductivites, respectively. An inevitable compromise between *S* and *σ* is always needed to obtain superior thermoelectric performance of a particular material system. Hence, substantial studies on theoretical and experimental perspective have been executed to improve the electrical

transport properties through band engineering,[6-7] carrier scattering[8] and carrier concentration optimization.[4, 9-10] The decrease of κ can be obtained via nanostructuring,[11-14] defect engineering,[15-17], porous design[18-19], phonon-phonon interactions,[20] and all-scale hierarchical architecturing.[21-22]

As an environment-friendly alternative of toxic PbTe, SnTe has been shown promising thermoelectric performance in recent years.[23-24] SnTe possesses similar crystal and band structures with PbTe. However, due to the large energy offset (~0.3-0.4 eV) between two valence bands (light hole and heavy hole) and small energy gap (~ 0.18 eV) between two principal bands (valence band and conduction band),[37] SnTe suffers from a low S and a high κ_e from its inherent excessive hole carrier concentration (n) (~10^{20} to 10^{21} cm^{-3}).[23, 25] In order to overcome this challenge, various strategies have been carried out, including optimising n,[26-27] modifying valence band structures,[28-30] and nanostructuring.[31-33] It has been proposed that In produces resonance energy level in the valence band of SnTe that gives distortion of density of states.[34-37] Even though some work have investigated the effect of In on the electronic properties of SnTe, but there are still some unclear points that need to be addressed, particularly for the role of In in improving the thermal transport properties. Most of the previous works are lacking insufficient characterization of the samples.[34, 38-41]

In our present study, we, for the first time, revealed the strain engineering by embedding cubic InTe nanophases in cubic structured SnTe matrix *via* a facile solvothermal method, which is of crucial important to strengthen phonon scattering in order to achieve a low κ_l in a thermoelectric material system.[42-44] The unique feature of solvothermal synthesis is its liquid nucleation mechanism which is different from the diffusing mechanism of solid-state reaction method.[45] On top of that the reactant ions and/or molecules under the solution environment can yield simultaneous growth of nanophase in the main matrix which is good for thermoelectric materials in some cases. Introducing nanoscale strain clusters from these nanophases in the host material can significantly shorten the phonon relaxation time and scatter heat carrying phonons, ultimately contribute to low κ_l and give rise to overall high ZT values.[35, 46] The detailed structural and morphological characterization revealed that intensive strain clusters are dispersed in Sn$_{1-x}$In$_x$Te matrix that leads to substantial decrease of κ_l = ~ 0.45 W m^{-1} K^{-1} at 773 K. Meanwhile, S is greatly enhanced from ~ 23 µV K^{-1} of undoped SnTe to ~ 88 µV K^{-1} of In-doped SnTe at room temperature, which is ascribed to the increase in density of states near the Fermi level. Consequently, a high peak ZT of ~0.78 in nominal

$Sn_{0.99}In_{0.01}Te$ is achieved at 773 K, which is ~143 % improvement over undoped SnTe counterparts.

4.1.3 Experimental Section

For the synthesis of $Sn_{1-x}In_xTe$ (x = 0 %, 0.5 %, 1 %, 1.5 %, and 2 %) microcrystals, the starting materials were Na_2TeO_3 (99.99 %), $SnCl_2·2H_2O$ (99.99 %), $InCl_3·4H_2O$ (97 %), ethylene glycol (EG, 99.8 %) and NaOH (99.99 %) purchased from Sigma-Aldrich. For a typical synthesis of 1.5 g $Sn_{0.99}In_{0.01}Te$, the starting precursors were 35 ml EG, 5 ml NaOH (10 M L^{-1}), 1.3606 g $SnCl_2·2H_2O$, 1.3495 g Na_2TeO_3, and 0.0178 g $InCl_3·4H_2O$, loaded into a Teflon jar with a size of 120 ml. After magnetic stirring for several minutes, the Teflon jar with a clear solution was put into a stainless-steel autoclave, sealed and placed in an oven and heated at 230 °C for 24 h. After that, the synthesized products were collected at room temperature and centrifuged, washed with deionized water and absolute ethanol for several times. After dried at 60 °C for 12 h in an oven, the as-synthesised powders were compacted by spark plasma sintering (SPS) at 50 MPa pressure and 683 K. Archimedes' method[47] was used to measure the densities of the sintered product (~96 % of the theoretical values). κ was calculated by using $\kappa = DC_pd$, where D and C_p are the thermal diffusivity and specific heat capacity, respectively. D was measured by a laser flash method with a LFA 457 (NETZSCH) (**Figure 4.S1** in the supporting information) and C_p was calculated according to previous study.[30] σ and S were determined by ZEM-3 (ULVAC), and confirmed by NETZSCH (SBA458).

The sintered products were characterized by X-ray diffraction (XRD) (Cu Kα, λ = 1.5418 Å), scanning electron microscopy (SEM), transmission electron microscopy (TEM) and energy dispersive spectroscopy (EDS). The TEM specimens were prepared by using an ultramicrotome and FEI-Scios FIB. A Renishaw Raman microscope and spectrometer with a 514.5 nm Ar laser were used to characterize the vibrational peaks of sintered $Sn_{1-x}In_xTe$ pellets.

In order to see the electronic states near the Fermi level of our undoped SnTe and In doped SnTe we performed density functional theory (DFT) calculations using Perdew-Burke-Ernzerhof generalized gradient approximation using Quantum Espresso package. To compare the impact of the In doping on SnTe, we simulate two samples of $Sn_{32}Te_{32}$ and $In_1Sn_{31}Te_{32}$. A plane wave cut-off energy of 81.825 Ry and an energy conversion threshold of 327.302 Ry per atom were applied.

4.1.4 Results and Discussion

Figure 4.1a displays the XRD patterns of the sintered $Sn_{1-x}In_xTe$ (x = 0 %, 0.5 %, 1 %, 1.5 %, and 2%, here x is nominal), where the main diffraction peaks can be exclusively indexed to the face-centred-cubic (FCC) structured SnTe (standard identification card, PDF #65−0239) with a $Fm\bar{3}m$ space group and the lattice parameter of a = 6.32 Å. **Figure 4.1b** shows the enlarged view of the 222* diffraction peak for different In-containing samples. Obviously, the 222* peak is shifted towards higher angle at In = 0.5 % and remains nearly same at In ≥ 1.0 %, indicating that $Sn_{1-x}In_xTe$ has a lattice contraction after In doping and that In has successful doped into the SnTe matrix. The smaller ionic size of In^{3+} (80 pm) as compared with the Sn^{2+} (118 pm) leads to the lattice contraction.
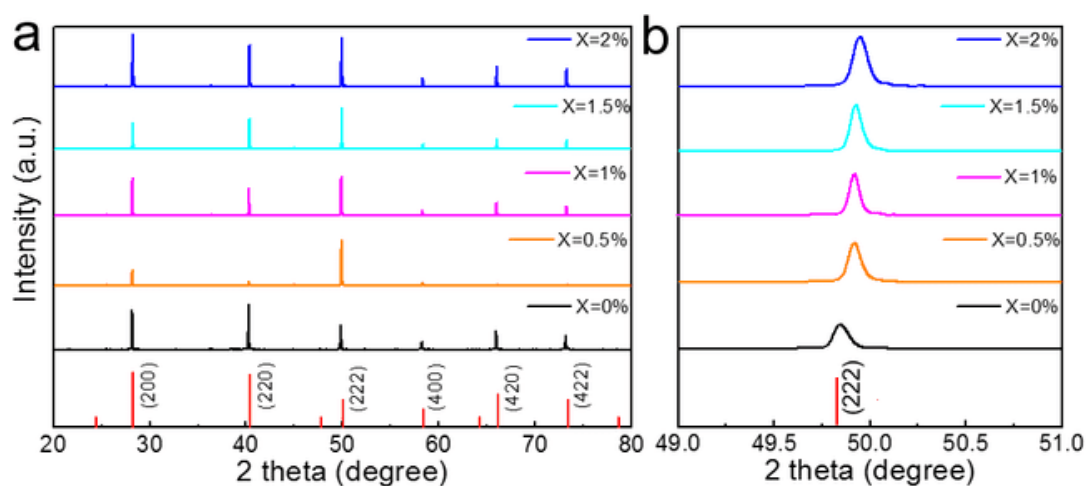
Figure 4.1 XRD patterns of solvothermally synthesized $Sn_{1-x}In_xTe$ products. (a) Powder XRD patterns and (b) Enlarged (222) peaks of $Sn_{1-x}In_xTe$ (x = 0 %, 0.5 %, 1 %, 1.5 %, and 2 %) samples.

To study the morphology of our synthesized products, we carried out SEM analysis and results are shown in **Figure 4.2**. As can be seen, the products with In ≤1 % are regular octahedral-shaped crystals consisting of eight {111} planes (**Figure 4.2a** and the inset). With increasing the In doping level to 1.5 % and 2 %, the {111} planes are severely deformed into different facets (**Figure 4.2b** and **2c** and insets) which has a detrimental effect on the thermal property of the samples (shown later). **Figure 4.2d** is a cross-section SEM image of a $Sn_{0.99}In_{0.01}Te$ single crystal, cut by ultramicrotome and its corresponding composition analysis of In, Sn, and Te elements is shown in **Figure 4.2e-g**.
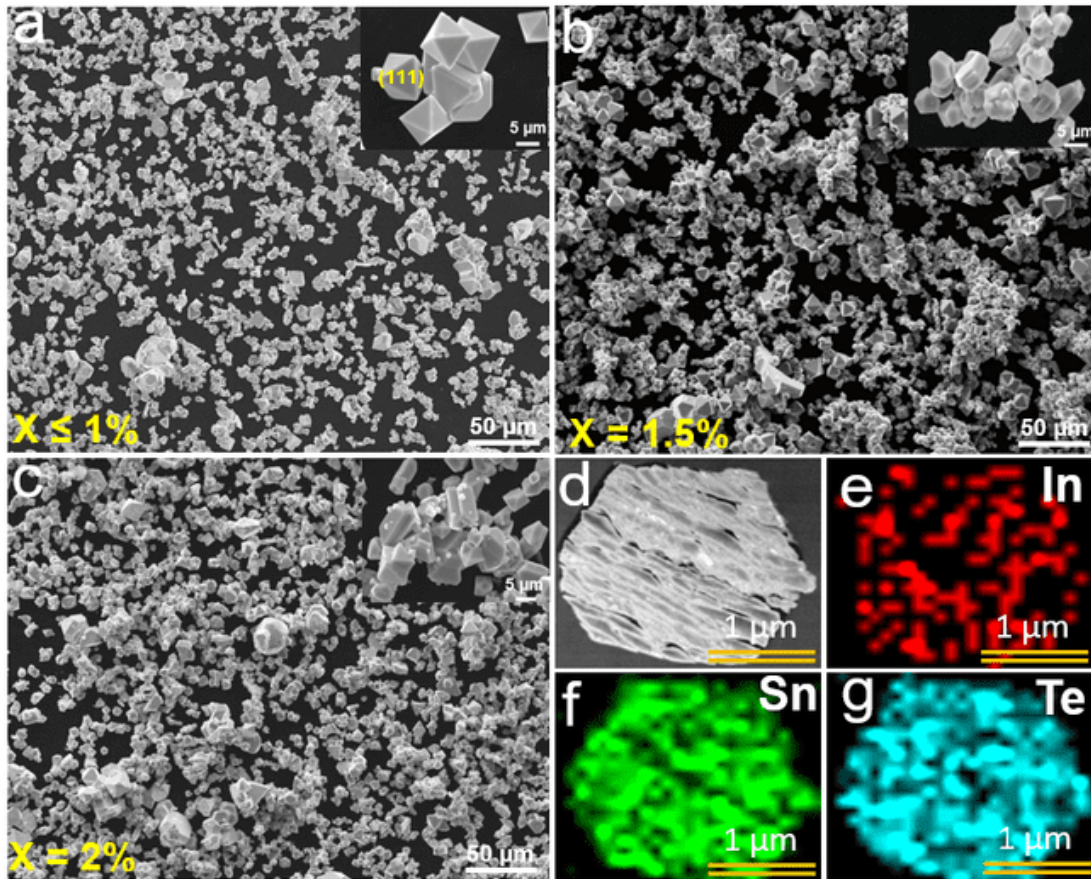
Figure 4.2 Characterisation of as-synthesised $Sn_{1-x}In_xTe$ samples: Typical SEM image of (a) $x = 1$ % (b) $x = 1.5$ % and (c) $x = 2$ % samples. (d) SEM image of one of the In doped single crystal SnTe and (e-g) EDS maps of In, Sn, Te, respectively.

Figure 4.3 shows the temperature-dependent thermoelectric properties of sintered $Sn_{1-x}In_xTe$ ($x = 0$ %, 0.5 %, 1 %, 1.5 %, and 2 %) pellets. The high σ of pristine SnTe is greatly reduced with increasing the temperature, showing a typical behaviour of high degenerated semiconductors.[48] The σ values significantly reduces upon In doping especially at room temperature from 7240 S cm^{-1} to 2025 S cm^{-1} (**Figure 4.3a**). **Figure 4.3b** represents S of the sintered pellets at different temperatures. The positive S value demonstrate a p-type conduction, indicating holes are the majority carriers.[23] The In-doped pellets have superior S at room temperature compared with the undoped SnTe, which is enhanced from ~23 µV K^{-1} to ~88 µV K^{-1}. As the temperature rises more excitation of carriers between conduction and valence band occurs that gradually increases S. The maximum S value of ~141 µV K^{-1} is obtained at 773 K for $Sn_{0.98}In_{0.02}Te$. **Figure 4.3c** shows $S^2\sigma$ of $Sn_{1-x}In_xTe$ pellets from 300 K to 773 K. Compared with undoped SnTe, $S^2\sigma$ values are enhanced significantly after In doping due to the increased S, especially from room- to mid-temperature. For instance, the

room-temperature $S^2\sigma$ for undoped SnTe is ~4 μW cm^{-1} K^{-2} and is increased to ~17.1 μW cm^{-1} K^{-2} for Sn$_{0.99}$In$_{0.01}$Te and at 773 K $S^2\sigma$ for undoped SnTe is ~14.3 μW cm^{-1} K^{-2} and increases to ~21.8 μW cm^{-1} K^{-2} for Sn$_{0.99}$In$_{0.01}$Te. Temperature-dependent κ of all pellets from 300 to 773 K is plotted in **Figure 4.3d**. It is found that the ambient κ of undoped SnTe is greatly decreased from ~8.5 W m^{-1} K^{-1} to ~3.22 W m^{-1} K^{-1} for Sn$_{0.99}$In$_{0.01}$. κ_l is calculated by deducting κ_e from κ and **Figure 4.3e** shows the results. κ_e was determined by using $\kappa_e = L\sigma T$,[49] where L

is the Lorenz number. The L value is estimated from the following relationship,[49] $L = 1.5 + \exp\left(-\dfrac{|S|}{116}\right)$ where L is in 10^{-8} WΩ K^{-2} and S is in μV K^{-1}. The obtained L lies in the range from 2.32 × 10^{-8} to 1.79 × 10^{-8} W Ω K^{-2} (**Figure 4.S2** in the supporting information). The room-temperature κ_l of In-doped samples decreases from ~3.4 W m^{-1} K^{-1} for $x = 0$ % to ~1.92 W m^{-1} K^{-1} for $x = 1$ %. The κ_l value at 773 K substantially reduces from ~1.21 W m^{-1} K^{-1} for $x = 0$ % to ~0.45 W m^{-1} K^{-1} for $x = 1$ %. Such a low value of $\kappa_l = $ ~0.45 W m^{-1} K^{-1} for our

pellets is lower than that of the previously reported Hg-doped SnTe (0.6 W m^{-1} K^{-1} at 780 K).[50]
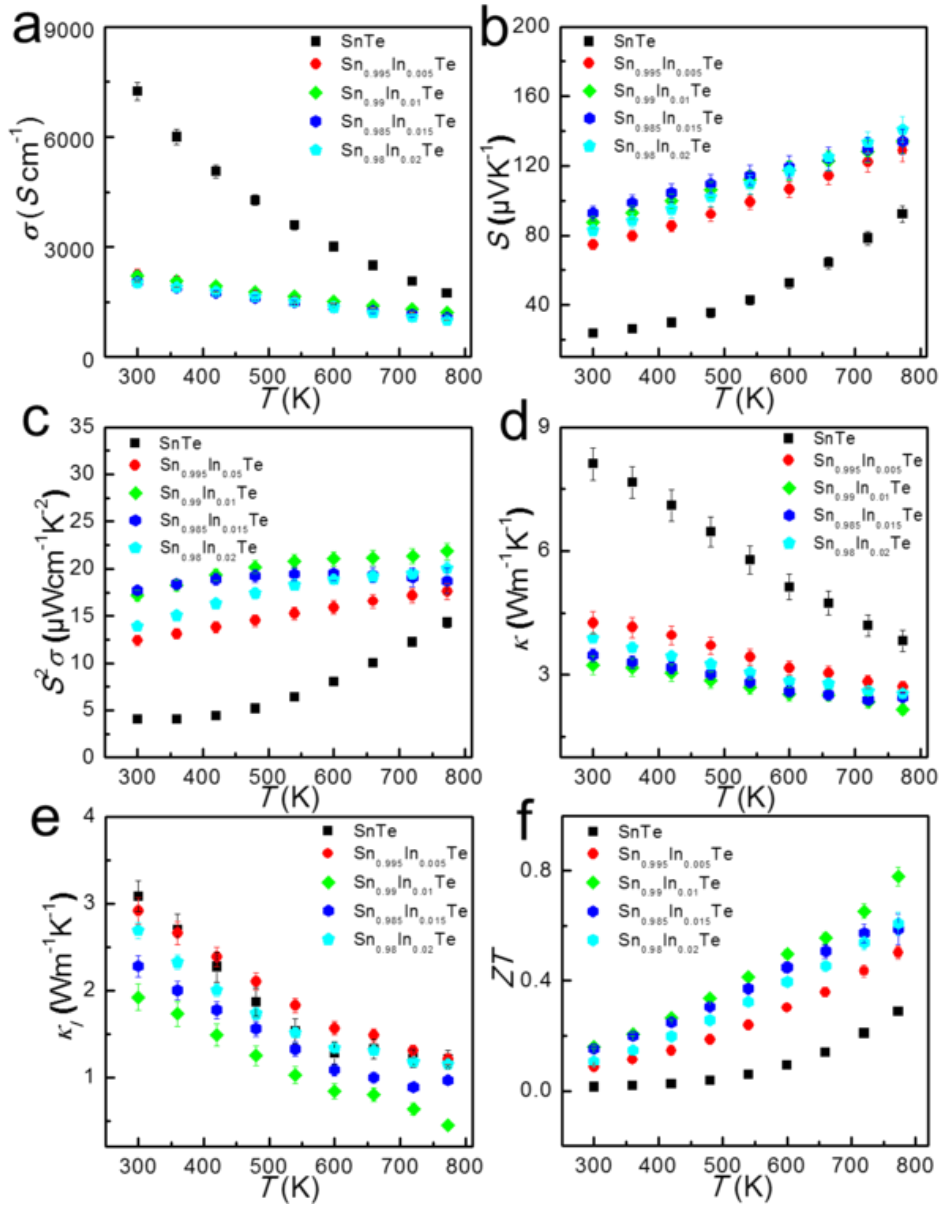
Figure 4.3 Thermoelectric properties of sintered $Sn_{1-x}In_xTe$ pellets. (a) σ, (b) S, (c) $S^2\sigma$, (d) κ, (e) κ_l, (f) ZT. Error limit 5 %.

To understand the effect of In dopant on the valence band of SnTe, we compare S of the current In-doped SnTe samples with the Pisarenko plot[41] and the reported doped samples, such as undoped SnTe,[51] Hg-doped SnTe,[50] Mg-doped SnTe, [52] Ca-doped SnTe,[25] Cu-doped SnTe,[51] Sb-doped SnTe,[53] Bi-doped SnTe,[54] In-doped SnTe,[41] Cd-doped SnTe,[40] Ag-doped,[26] Mn-doped SnTe,[29] and I-doped SnTe.[30] Obviously, the S values of all the In doped samples lies far above the Pisarenko line, indicating that In-doped SnTe has a modified band structure. To illustrate the underlying mechanism of the remarkable enhanced S, we conducted DFT calculation and the results are shown in **Figure 4.4b**. As can be seen, In

dopants can increases density of states (DOS) around the Fermi level. Such an enhanced DOS can lead to S increase,[41, 55] according to the equation of $S = \frac{\pi^2}{3}\frac{\kappa_B}{q}\kappa_B T[\frac{g(E)}{n(E)} + \frac{1}{\mu E}\frac{d\mu(E)}{dE}]$, where q is the electron charge and $g(E)$ is the DOS.[56]
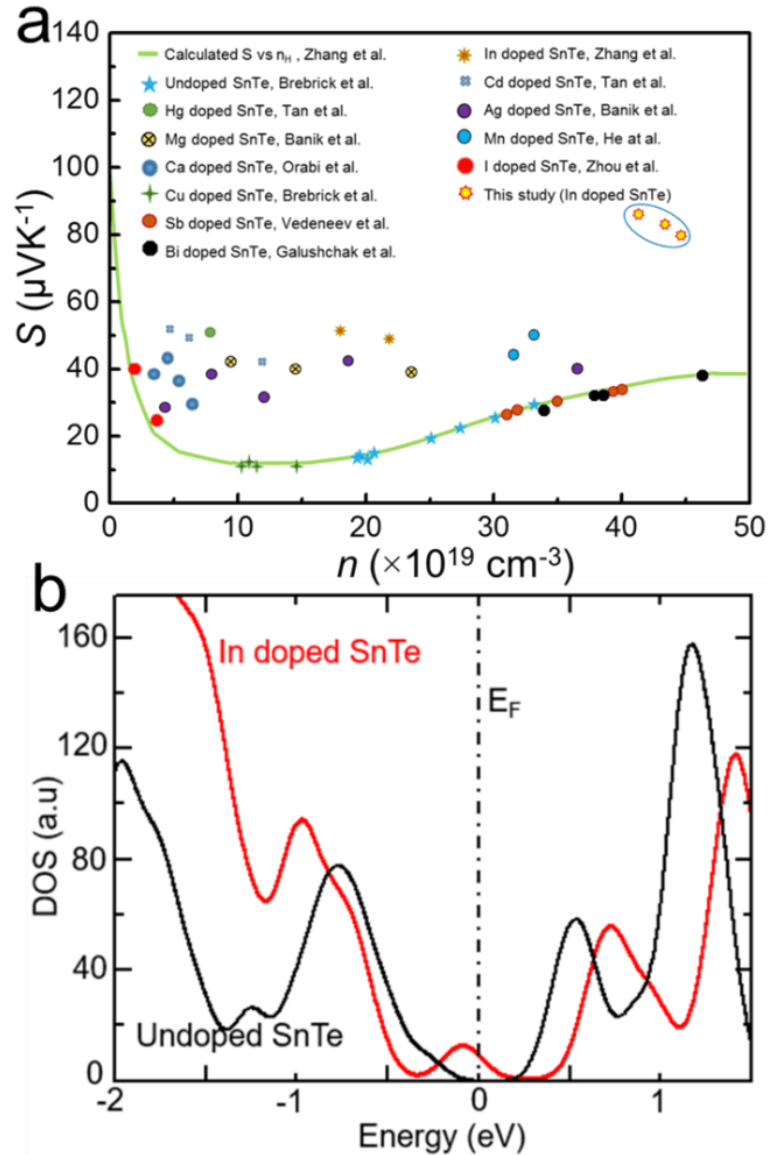
Figure 4.4 (a) Comparative study of present result with the reported results; Pisarenko plot[41] and the reported doped samples such undoped SnTe,[51] Hg-doped SnTe,[50] Mg-doped SnTe,[52] Ca-doped SnTe,[25] Cu-doped SnTe,[51] Sb-doped SnTe,[53] Bi-doped SnTe,[54] In-doped SnTe,[41] Cd-doped SnTe,[40] Ag-doped,[26] Mn-doped SnTe,[29] and I-doped SnTe.[30] (b) Calculated density of states (DOS) of In doped and undoped SnTe samples.

To understand the low κ_l found in our pellets, we perform detailed TEM characterisation and the results are shown in **Figure 4.5**. **Figure 4.5a** is a bright-field TEM image of $Sn_{0.99}In_{0.01}Te$, in which many precipitates with an average size of ~150-200 nm can be found embedded in

the SnTe matrix. **Figure 4.5b** shows an enlarged TEM image of a typical precipitate, and corresponding EDS line scan analysis was performed and shows in the inset. As can be seen, the In counts in the precipitate is much higher compare to the SnTe matrix, while the Sn counts decrease; indicating that the precipitate is the In-Te compound. **Figure 4.5c** is selected area electron diffraction (SAED) pattern taken from an area containing the precipitate, in which the diffraction spots are splitted. For example, the 220 diffraction spots can be indexed as the interplaner spacing of (220) planes of SnTe (2.23 Å) and InTe (2.17 Å), respectively. Therefore, the SAED pattern is [001] zone-axis of FCC structured SnTe and FCC InTe. **Figure 4.5d** is a high-resolution TEM image taken from the interface between a precipitate and its surrounding SnTe matrix. The magnified two regions of the interface as marked by A and B of **Figure 4.5d** are shown in **Figure 4.5e** and **Figure 4.5f**. As shown in **Figure 4.5e**, coherent interface is formed between InTe precipitate and SnTe matrix in area A, while a dislocation can be observed in area B. The slight lattice mismatch between two FCC structured InTe (a = 6.14 Å) and SnTe (a = 6.32 Å) can lead to a lattice distortion. These dislocations can cause severe strain field that can act as effective media to scatter heat carrying phonons in the matrix.[57]
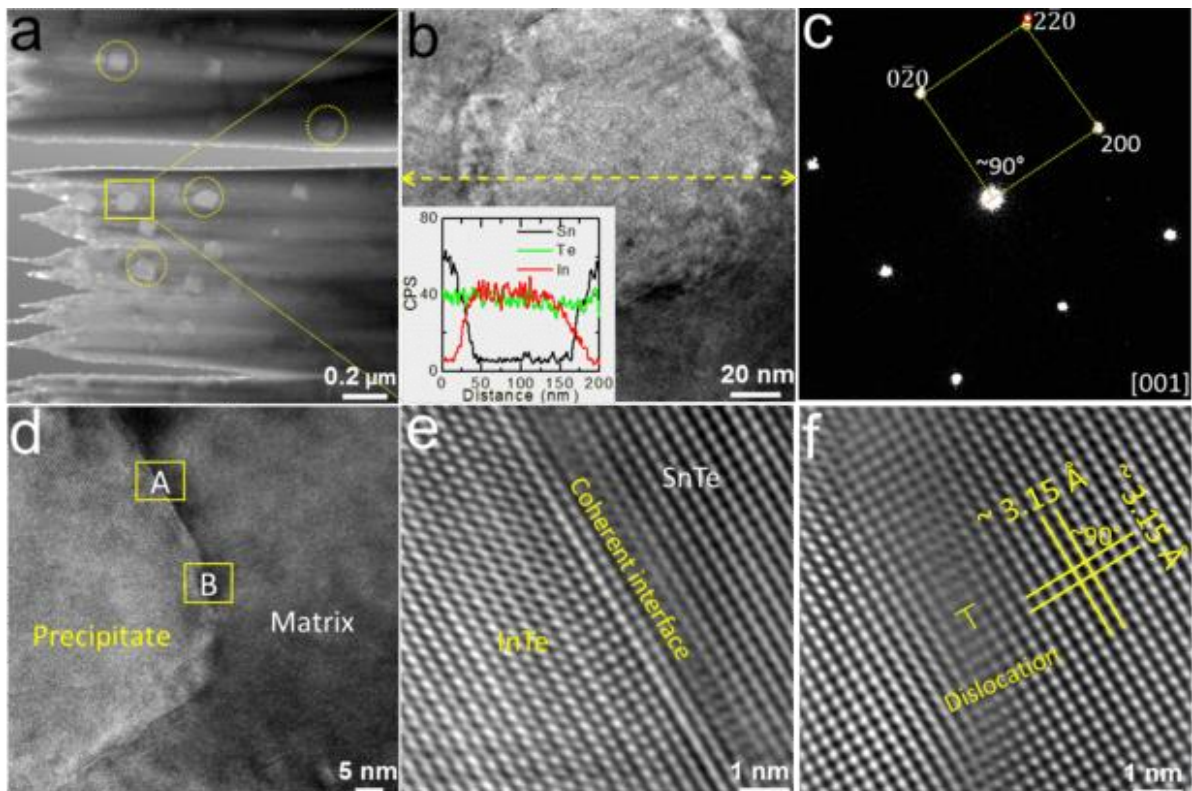
Figure 4.5 Characterizations of sintered products. (a) Low magnification bright-field TEM image of sintered $Sn_{0.99}In_{0.01}Te$ sample, showing several precipitates embedded in the SnTe matrix. (b) TEM image of a typical precipitate, and inset is its EDS-line scan analysis. (c) SAED pattern showing [001] zone-axis of the matrix containing a precipitate. (d) TEM image showing interfaces between the precipitate and its SnTe matrix; (e) and (f) Enlarged HRTEM image of marked area A and B of **d**, showing coherent interface and dislocation, respectively.

Apart from submicro-sized precipitates, smaller precipitates in the size of 5-10 nm are also frequently observed. **Figure 4.6a** is a TEM image showing some dark contrast (caused by strain). **Figure 4.6b** is a HRTEM image of the enlarged area of a typical nanoprecipitate, in which a dislocation core can be identified. The strain field associated with this dislocation retrieved by geometrical phase analysis (GPA) software. The colour contrast of strain maps (**Figure 4.6c-d**) show the spatially varying strain that impede to normal transportation of phonon in the matrix. Such lattice dislocations are effective factors in reducing the lattice thermal conductivity of melt-centrifuged $(Bi, Sb)_2Te_3$ System.[58] The effect of strain on phonon scattering has been theoretically discussed.[46, 59] From the detailed TEM characterization outlined above, significant reduction in lattice thermal conductivities must be ascribed to the high density of strained nanoprecipitates in the matrix, along with the point defects and dislocations consequences severe scattering of heat carrying phonons in all direction and ultimately yield low κ_l.
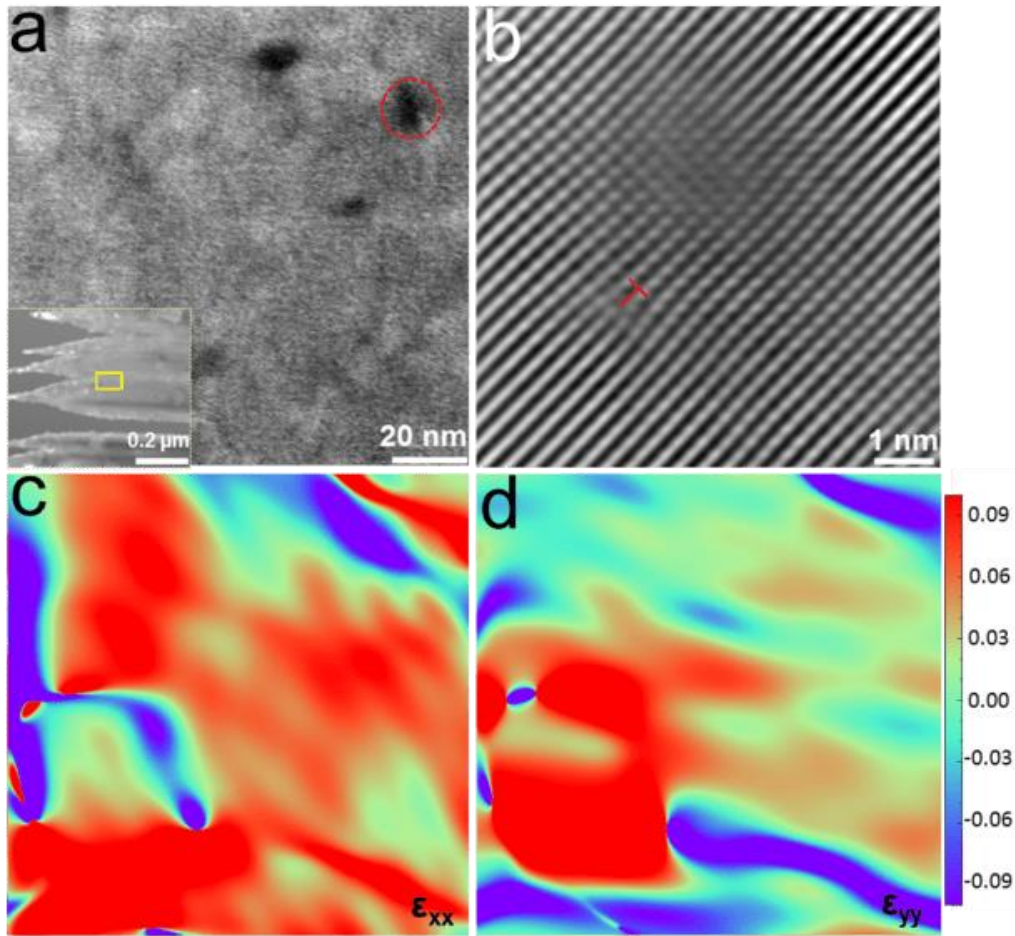
Figure 4.6 Characterizations of sintered pellet. (a) HRTEM image of matrix containing nanoprecipitate with the size of ~5-10 nm (b) Enlarged view of nanoprecipitate shows edge dislocation; (c) and (d) calculated strain map associated with the nanoprecipitates.

Lattice anharmonicity is the deviation of a balance system from being a harmonic vibration mode which is another key parameter to intensify the phonon-phonon scattering, which can be developed by changing net polarizablitiy in a material system.[60-61] The polarizability is strongly linked with the vibrational mode of a material system.[62] To identify the vibrational modes of our $Sn_{1-x}In_xTe$ (x = 0 %, 0.5 %, 1 %, 1.5 %, and 2 %) pellets, we further conducted Raman spectroscopy analysis. **Figure 4.7a** shows typical Raman spectra, in which two vibrational modes centered at 119 and 139 cm^{-1} for pristine SnTe, which are ascribed as A_1 symmetry (optical phonon) and E_{TO} (transverse optic phonon) modes.[63] With increasing the In doping level, these two peaks shift to high wavenumber, indicating the Sn substitution or annihilation of Sn vacancies by In dopant. SnTe have predominantly two peaks at 119 and 139 cm^{-1}. The shifting in these modes indicate the possible alteration of overall chemical environment around Te and can generate additional impurity driven soft phonon mode. The

interaction between In and SnTe can yield soft transverse optical phonon modes around the Brillouin zone center.[64] The propagation of global phonon group velocity is affected by these soft phonon modes which along with the point defects can contribute to poor κ and improve the thermoelectric transport properties.[62] **Figure 4.7b** shows the schematic illustration of coordination geometry of Te atom in SnTe and $Sn_{1-x}In_xTe$ where one single Sn^{2+} ion is substituted by In^{3+}. The off-site In atoms can create force differences between host atoms and impurity atoms. Such impurities inducting force differences have been well observed in the other system such as Mn-doped SnTe[62] and Pb/Bi doped $AgSbSe_2$.[65] Therefore, local soft phonon mode can be generated and affect the global phonon propagation at elevated temperature.
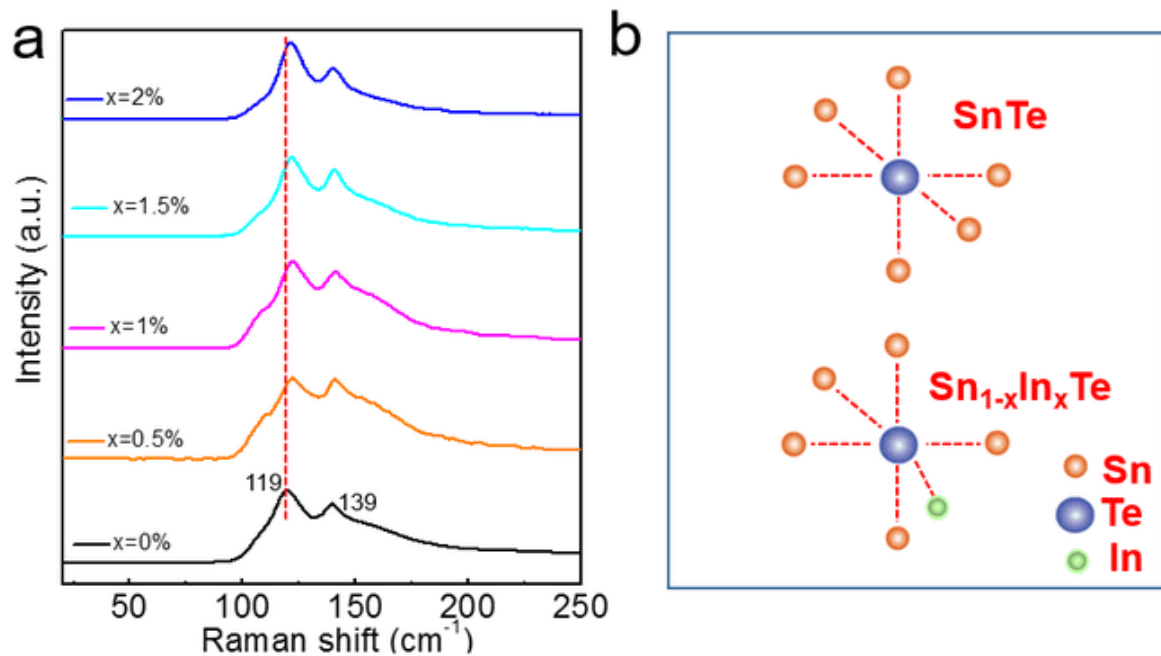
Figure 4.7 Investigation of vibrational effect of In dopant in SnTe system. (a) Raman spectra of $Sn_{1-x}In_xTe$ (*x* = 0 %, 0.5 %, 1 %, 1.5 % and 2 %) (b) Schematic representation of off-centering due to In doping.

To quantitatively understand the obtained lowest κ_l, we estimate the phonon transport by using Callaway model.[66-67] We consider various phonon scattering mechanisms, including Umklapp processes (U), grain boundaries (GB), point defects (PD), and nanoprecipitates (NP). The details of phonon transport calculations are shown in Section 1 of the Supporting Information. Since the integral of the spectral lattice thermal conductivity (κ_s) with respect to the phonon frequency equals to κ_l, thus, we can get an impression which kind of phonons contributes to κ_l by evaluating κ_s.[68] **Figure 4.S3** plots the phonon frequency (ω) dependent

κ_s, at 300 K determined by models considering different scattering mechanisms, including U, U+GB, U+GB+PD, U+GB+PD+NP, respectively. Areas (I), (II), and (III) correspond to the reduction in κ_l caused by GB, PD, and NP, respectively. As can be seen, introducing point defects and nanoparticle can significantly reduce κ_l. Likewise, it is believed that anharmonicity which is originally generated from PD and NP have significant influence on reducing κ_l in $Sn_{0.99}In_{0.01}Te$ system.

4.1.5 Conclusion

In conclusion, we studied the nano-strain engineering in SnTe through In doping prepared by a facile solvothermal method. From our detailed structure analysis, we found that the structure of the In rich precipitates are FCC structured InTe. These InTe precipitates, together with nanoprecipitates, can induce severe strain in SnTe matrix and in turn significantly scatter the heat carrying phonons together with the point defects, dislocations and anharmonicity, yielded a ultra-low lattice thermal conductivity of ~ 0.45 W m^{-1} K^{-1} at 773 K. Apart from this, the increased DOS in the valence band near the Fermi level of SnTe by In atom contributes to large enhancement of S and ultimately yielded high $S^2\sigma$ of ~21.8 µW cm^{-1} K^{-2} at 773 K. Consequently, a striking enhancement in ZT of ~ 0.78 is obtained in the In doped SnTe at 773 K, which is ~ 143 % improvement over undoped SnTe. This study demonstrates the great potential to produce high-performance thermoelectric materials *via* nano-strain engineering.

References

(1) Snyder, G. J.; Lim, J. R.; Huang, C.-K.; Fleurial, J.-P. *Nat. Mater.* **2003**, *2*, 528-531.

(2) Chowdhury, I.; Prasher, R.; Lofgreen, K.; Chrysler, G.; Narasimhan, S.; Mahajan, R.; Koester, D.; Alley, R.; Venkatasubramanian, R. *Nat. Nano.* **2009**, *4*, 235-238.

(3) Hudak, N. S.; Amatucci, G. G. *J. Appl. Phys.* **2008**, *103*, 101301.

(4) Krez, J.; Schmitt, J.; Jeffrey Snyder, G.; Felser, C.; Hermes, W.; Schwind, M. *J. Mater. Chem. A* **2014**, *2*, 13513-13518.

(5) Yang, L.; Chen, Z. G.; Dargusch, M. S.; Zou, J. *Adv. Energy Mater.* **2018**, *8*, 1701797.

(6) Hong, M.; Chen, Z. G.; Yang, L.; Liao, Z. M.; Zou, Y. C.; Chen, Y. H.; Matsumura, S.; Zou, J. *Adv. Energy Mater.* **2018**, *8*, 1702333.

(7) Zhao, L.-D.; He, J.; Hao, S.; Wu, C.-I.; Hogan, T. P.; Wolverton, C.; Dravid, V. P.; Kanatzidis, M. G. *J. Am. Chem. Soc.* **2012**, *134*, 16327-16336.

(8) Hong, M.; Chasapis, T. C.; Chen, Z.-G.; Yang, L.; Kanatzidis, M. G.; Snyder, G. J.; Zou, J. *ACS Nano* **2016**, *10*, 4719-4727.

(9) Guin, S. N.; Negi, D. S.; Datta, R.; Biswas, K. *J. Mater. Chem. A* **2014**, *2*, 4324-4331.

(10) Yang, J.; Xi, L.; Qiu, W.; Wu, L.; Shi, X.; Chen, L.; Yang, J.; Zhang, W.; Uher, C.; Singh, D. J. *Npj Comput. Mater.* **2016**, *2*, 15015.

(11) Chen, Z.-G.; Han, G.; Yang, L.; Cheng, L.; Zou, J. *Prog. Nat. Sci.* **2012**, *22*, 535-549.

(12) Hong, M.; Chen, Z.-G.; Yang, L.; Zou, J. *Nanoscale* **2016**, *8*, 8681-8686.

(13) Biswas, K.; He, J.; Wang, G.; Lo, S.-H.; Uher, C.; Dravid, V. P.; Kanatzidis, M. G. *Energy Environ. Sci.* **2011**, *4*, 4675-4684.

(14) Zhou, M.; Li, J.-F.; Kita, T. *J. Am. Chem. Soc.* **2008**, *130*, 4527-4532.

(15) Shi, X.; Chen, Z.-G.; Liu, W.; Yang, L.; Hong, M.; Moshwan, R.; Huang, L.; Zou, J. *Energy Storage Mater.* **2018**, *10*, 130-138.

(16) Shi, X.; Zheng, K.; Hong, M.; Liu, W.; Moshwan, R.; Wang, Y.; Qu, X.; Chen, Z.-G.; Zou, J. *Chem. Sci.* **2018**, *9*, 7376-7389.

(17) Lee, M. H.; Byeon, D.-G.; Rhyee, J.-S.; Ryu, B. *J. Mater. Chem. A* **2017**, *5*, 2235-2242.

(18) Liu, W.; Shi, X.; Moshwan, R.; Hong, M.; Yang, L.; Chen, Z.-G.; Zou, J. *Sustainable Mater.Technol.* **2018**, *17*, e00076.

(19) Shi, X.; Wu, A.; Liu, W.; Moshwan, R.; Wang, Y.; Chen, Z.-G.; Zou, J. *ACS Nano* **2018**, *12*, 11417-11425.

(20) Hong, M.; Wang, Y.; Feng, T.; Sun, Q.; Xu, S.; Matsumura, S.; Pantelides, S. T.; Zou, J.; Chen, Z.-G. *J. Am. Chem. Soc.* **2019**, *141*, 1742-1748.

(21) Biswas, K.; He, J.; Blum, I. D.; Wu, C.-I.; Hogan, T. P.; Seidman, D. N.; Dravid, V. P.; Kanatzidis, M. G., *Nature* **2012**, *489*, 414-418.

(22) Zhao, L. D.; Wu, H. J.; Hao, S. Q.; Wu, C. I.; Zhou, X. Y.; Biswas, K.; He, J. Q.; Hogan, T. P.; Uher, C.; Wolverton, C.; Dravid, V. P.; Kanatzidis, M. G. *Energy Environ. Sci.* **2013**, *6*, 3346-3355.

(23) Moshwan, R.; Yang, L.; Zou, J.; Chen, Z.-G. *Adv. Funct. Mater.* **2017**, *27*, 1703278.

(24) Moshwan, R.; Shi, X.-L.; Liu, W.-D.; Yang, L.; Wang, Y.; Hong, M.; Auchterlonie, G.; Zou, J.; Chen, Z.-G. *ACS Appl. Mater. Interf.* **2018**, *10*, 38944-38952.

(25) Al Rahal Al Orabi, R.; Mecholsky, N. A.; Hwang, J.; Kim, W.; Rhyee, J. S.; Wee, D.; Fornari, M. *Chem. Mater.* **2016**, *28*, 376-384.

(26) Banik, A.; Biswas, K. *J. Solid State Chem.* **2016**, *242, Part 2*, 43-49.

(27) Banik, A.; Vishal, B.; Perumal, S.; Datta, R.; Biswas, K. *Energy Environ. Sci.* **2016**, *9*, 2011-2019.

(28) Han, M.-K.; Androulakis, J.; Kim, S.-J.; Kanatzidis, M. G. *Adv. Energy Mater.* **2012**, *2*, 157-161.

(29) He, J.; Tan, X.; Xu, J.; Liu, G.-Q.; Shao, H.; Fu, Y.; Wang, X.; Liu, Z.; Xu, J.; Jiang, H.; Jiang, J. *J. Mater. Chem. A* **2015**, *3*, 19974-19979.

(30) Zhou, M.; Gibbs, Z. M.; Wang, H.; Han, Y.; Xin, C.; Li, L.; Snyder, G. J. *Phys. Chem. Chem. Phys.* **2014**, *16*, 20741-20748.

(31) Zhao, L.-D.; Zhang, X.; Wu, H.; Tan, G.; Pei, Y.; Xiao, Y.; Chang, C.; Wu, D.; Chi, H.; Zheng, L.; Gong, S.; Uher, C.; He, J.; Kanatzidis, M. G. *J. Am. Chem. Soc.* **2016**, *138*, 2366-2373.

(32) Tan, G.; Zhao, L. D.; Shi, F.; Doak, J. W.; Lo, S. H.; Sun, H.; Wolverton, C.; Dravid, V. P.; Uher, C.; Kanatzidis, M. G. *J. Am. Chem. Soc.* **2014**, *136*, 7006-7017.

(33) Shi, F.; Lo, S. H.; Tan, G.; Zhao, L. D.; Kanatzidis, M. G.; Dravid, V. *Microsc. Microanal.* **2014**, *20*, 438-439.

(34) Bhat, D. K.; Shenoy U, S. *J. Phys. Chem. C* **2017**, *121*, 7123-7130.

(35) Nan, P.; Liu, R.; Chang, Y.; Wu, H.; Wang, Y.; Yu, R.; Shen, J.; Guo, W.; Ge, B. *Nanotechnology* **2018**, *29*, 26LT01.

(36) Wang, H.; Wang, T.; Hwang, J.; Su, W.; Kim, H.; Zhai, J.; Wang, X.; Wang, C.; Kim, W. *Inorg. Chem. Front.* **2018**, *5*, 793-801.

(37) Wang, L.; Tan, X.; Liu, G.; Xu, J.; Shao, H.; Yu, B.; Jiang, H.; Yue, S.; Jiang, J. *ACS Energy Lett.* **2017**, *2*, 1203-1207.

(38) Banik, A.; Shenoy, U. S.; Saha, S.; Waghmare, U. V.; Biswas, K. *J. Am. Chem. Soc.* **2016**, *138*, 13068-13075.

(39) Bhat, D. K.; Shenoy, U. S. *Mater. Today Phys.* **2018**, *4*, 12-18.

(40) Tan, G.; Shi, F.; Hao, S.; Chi, H.; Zhao, L.-D.; Uher, C.; Wolverton, C.; Dravid, V. P.; Kanatzidis, M. G. *J. Am. Chem. Soc.* **2015**, *137*, 5100-5112.

(41) Zhang, Q.; Liao, B.; Lan, Y.; Lukas, K.; Liu, W.; Esfarjani, K.; Opeil, C.; Broido, D.; Chen, G.; Ren, Z. *Proc. Natl. Acad. Sci.* **2013**, *110*, 13261-13266.

(42) Hu, L.; Zhang, Y.; Wu, H.; Li, J.; Li, Y.; Mckenna, M.; He, J.; Liu, F.; Pennycook, S. J.; Zeng, X. *Adv. Energy Mater.* **2018**, *8*, 1802116.

(43) Guo, D.; Hu, C.; Xi, Y.; Zhang, K. *J. Phys. Chem. C* **2013**, *117*, 21597-21602.

(44) Yu, C.; Zhang, G.; Zhang, Y.-W.; Peng, L.-M. *Nano Energy* **2015**, *17*, 104-110.

(45) Feng, S. H.; Li, G. H., Chapter 4 - Hydrothermal and Solvothermal Syntheses. In *Modern Inorganic Synthetic Chemistry (Second Edition)*, Xu, R.; Xu, Y., Eds. Elsevier: Amsterdam, 2017; pp 73-104.

(46) Carruthers, P. *Rev. Mod. Phys.* **1961**, *33*, 92-138.

(47) Mason, B., The Determination of the Density of Solids. *Geologiska Föreningen i Stockholm Förhandlingar* **1944**, *66*, 27-51.

(48) Poudeu, P. F. P.; D'Angelo, J.; Downey, A. D.; Short, J. L.; Hogan, T. P.; Kanatzidis, M. G. *Angew. Chem. Int. Ed* **2006**, *45*, 3835-3839.

(49) Kim, H.-S.; Gibbs, Z. M.; Tang, Y.; Wang, H.; Snyder, G. J. *APL Mater.* **2015**, *3*, 041506.

(50) Tan, G.; Shi, F.; Doak, J. W.; Sun, H.; Zhao, L.-D.; Wang, P.; Uher, C.; Wolverton, C.; Dravid, V. P.; Kanatzidis, M. G. *Energy Environ. Sci.* **2015**, *8*, 267-277.

(51) Brebrick, R. F.; Strauss, A. J. *Phys. Rev.* **1963**, *131*, 104-110.

(52) Banik, A.; Shenoy, U. S.; Anand, S.; Waghmare, U. V.; Biswas, K. *Chem. Mater.* **2015**, *27*, 581-587.

(53) Vedeneev, V. P.; Krivoruchko, S. P.; Sabo, E. P. *Semiconductors* **1998**, *32*, 241-244.

(54) Galushchak, M.; Freik, D.; Ivanyshyn, I.; Lisak, A.; Pyts, M. *J. Thermoelectr.* **2000**, *1*, 42-50.

(55) Zhou, M.; Gibbs, Z. M.; Wang, H.; Han, Y.; Li, L.; Jeffrey Snyder, G. *Appl. Phys. Lett.* **2016**, *109*, 042102.

(56) Heremans, J. P.; Wiendlocha, B.; Chamoire, A. M. *Energy Environ. Sci.* **2012**, *5*, 5510-5530.

(57) Kim, S. I.; Lee, K. H.; Mun, H. A.; Kim, H. S.; Hwang, S. W.; Roh, J. W.; Yang, D. J.; Shin, W. H.; Li, X. S.; Lee, Y. H.; Snyder, G. J.; Kim, S. W. *Science* **2015**, *348*, 109-114.

(58) Pan, Y.; Aydemir, U.; Grovogui, J. A.; Witting, I. T.; Hanus, R.; Xu, Y.; Wu, J.; Wu, C.-F.; Sun, F.-H.; Zhuang, H.-L.; Dong, J.-F.; Li, J.-F.; Dravid, V. P.; Snyder, G. J. *Adv. Mater.* **2018**, *30*, 1802016.

(59) Zou, J.; Kotchetkov, D.; Balandin, A. A.; Florescu, D. I.; Pollak, F. H. *J. Appl. Phys.* **2002**, *92*, 2534-2539.

(60) Li, C. W.; Ma, J.; Cao, H. B.; May, A. F.; Abernathy, D. L.; Ehlers, G.; Hoffmann, C.; Wang, X.; Hong, T.; Huq, A.; Gourdon, O.; Delaire, O. *Phys. Rev. B* **2014**, *90*, 214303.

(61) Ribeiro, G. A. S.; Paulatto, L.; Bianco, R.; Errea, I.; Mauri, F.; Calandra, M. *Phys. Rev. B* **2018**, *97*, 014306.

(62) Acharya, S.; Pandey, J.; Soni, A. *Appl. Phys. Lett.* **2016**, *109*, 133904.

(63) Pine, A. S.; Dresselhaus, G. *Phys. Rev. B* **1971**, *4*, 356-371.

(64) Ju, S.; Shiga, T.; Feng, L.; Shiomi, J. *Phys. Rev. B* **2018**, *97*, 184305.

(65) Guin, S. N.; Chatterjee, A.; Negi, D. S.; Datta, R.; Biswas, K. *Energy Environ. Sci.* **2013**, *6*, 2603-2608.

(66) Callaway, J. *Phys. Rev.* **1959**, *113*, 1046-1051.

(67) Callaway, J.; von Baeyer, H. C. *Phys. Rev.* **1960**, *120*, 1149-1154.

(68) Zhu, T. J.; Fu, C. G.; Xie, H. H.; Liu, Y. T.; Feng, B.; Xie, J.; Zhao, X. B. *EPL (Europhys. Lett.)* **2013**, *104*, 46003.

4.1.6 Supporting Information
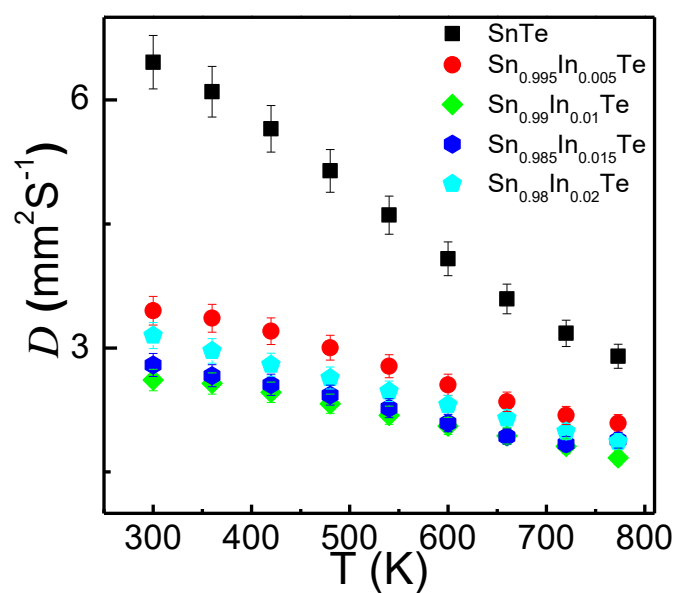
Figure 4.S1 Thermal diffusivity, *D* as a function of temperature for different In doped SnTe samples. Error limit 5 %.
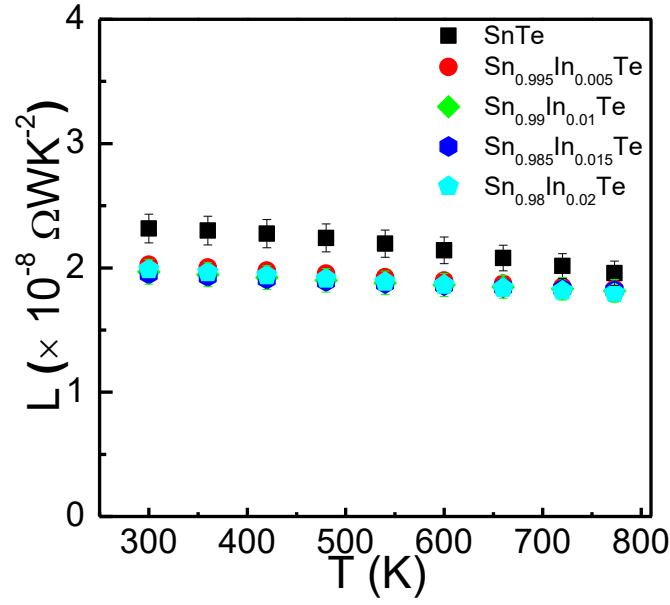
Figure 4.S2 Calculated Lorenz number, *L* as function of temperature for $Sn_xIn_{1-x}Te$. Error limit 5 %.

Section 1. Phonon modeling studies

According to the Debye-Callaway model,[1-3] κ_l can be calculated by

$$\kappa_l = \frac{k_B}{2\pi^2 \upsilon} \left(\frac{k_B T}{\hbar} \right)^3 \int_0^{\frac{\theta_D}{T}} \tau_{tot} \frac{z^4 \exp(z)}{\left[\exp(z) - 1 \right]^2} dz$$

(4-S1)

The integrand item in conjunction with the coefficient of the above equation is the spectral lattice thermal conductivity (κ_s),[4] namely

$$\kappa_s = \frac{k_B}{2\pi^2 \upsilon} \left(\frac{k_B T}{\hbar} \right)^3 \tau_{tot} \frac{z^4 \exp(z)}{\left[\exp(z) - 1 \right]^2}$$

(4-S2)

In the above equations, $z = \frac{\hbar \omega}{k_B T}$ (with ω denoting the phonon frequency) is the reduced phonon frequency, $\hbar$ is the reduced Plank constant, θ_D is the Debye temperature,

$\upsilon = \left[\frac{1}{3} \left(\frac{1}{\upsilon_L^3} + \frac{2}{\upsilon_T^3} \right) \right]^{-1/3}$ (with υ_L and υ_T respectively denoting the longitudinal and transverse sound velocities) is the sound velocity, and τ_{tot} is the total relaxation time. The phonon scattering pathways generally include phonon-phonon Umklapp (U), grain boundaries (GB),

94

point defects (PD).[4-5] The relevant phonon relaxation times are given by Umklapp phonon scattering

$$\tau_U^{-1} = \frac{\hbar \gamma^2 \omega^2 T}{\bar{M} \upsilon^2 \theta_D} \exp\left(-\frac{\theta_D}{3T}\right),$$ (4-S3)

Grain boundary phonon scattering

$$\tau_B^{-1} = \frac{\upsilon}{d},$$ (4-S4)

Point defect phonon scattering

$$\tau_{PD}^{-1} = \frac{\bar{V} \omega^4}{4\pi\upsilon^3}\Gamma, \text{ and}$$ (4-S5)

Nano precipitates (NP) phonon scattering [6-7]

$$\tau_{np}^{-1} = \upsilon \left[(2\pi R)^{-1} + \left(\pi R^2 \frac{4}{9}\left(\frac{\Delta D}{D}\right)^2 \left(\frac{\omega R}{\upsilon}\right)^4 \right)^{-1} \right]^{-1} N_p$$ (4-S6)

In the above equations, γ is the Grüneisen parameter, ρ is the sample density, $\bar{V}$ is the average atomic volume, $\bar{M}$ is the average atomic mass, Γ is the point defect scattering parameter, d is the grain size, a is the lattice parameter, R is the average radius for the precipitates D is the matrix density, ΔD is the density difference between the precipitate and matrix, N_p is the number density of precipitates, respectively.

Table 4.S1. Parameters for phonon modelling studies

Parameters	Values
Longitudinal sound velocity υ_L (ms^{-1})	3171
Transverse sound velocity υ_T (ms^{-1})	1220
Sound velocity υ (ms^{-1})	1967
Atomic mass Sn (kg)	1.97×10^{-25}
Atomic mass Te (kg)	2.12×10^{-25}
Atomic mass In (kg)	1.91×10^{-25}
Grain size d (µm)	10
Grüneisen parameter γ	1.5

Matrix density D (g cm^{-3})	6.44
Density difference between matrix and precipitates ΔD (g cm^{-3})	0.15
Number density of precipitates N_p (m^{-3})	4.6×10^{18}
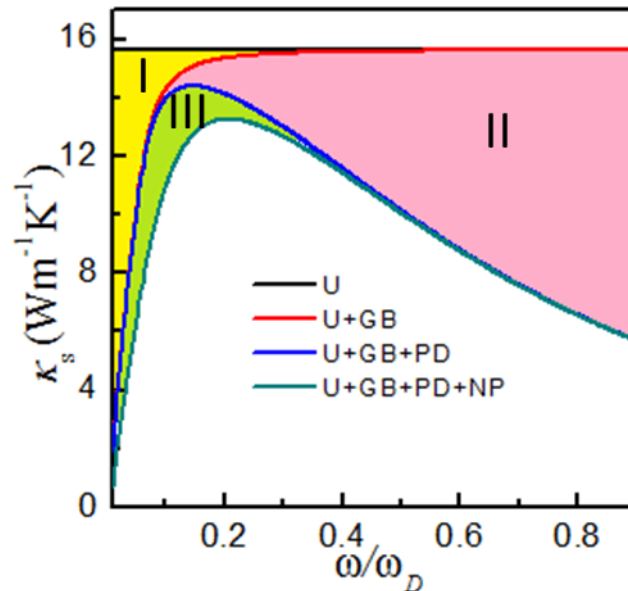
Figure 4.S3 Calculated κ_s for Sn$_{0.99}$In$_{0.01}$Te pellet with various phonon scatterings at 300 K.

References

(1) Callaway, J.; von Baeyer, H. C. *Phys. Rev.* **1960**, *120*, 1149-1154.

(2) Bessas, D.; Sergueev, I.; Wille, H. C.; Perßon, J.; Ebling, D.; Hermann, R. P. *Phys. Rev. B* **2012**, *86*, 224301.

(3) Hong, M.; Chasapis, T. C.; Chen, Z.-G.; Yang, L.; Kanatzidis, M. G.; Snyder, G. J.; Zou, J. *ACS Nano* **2016**, *10*, 4719-4727.

(4) Zhu, T. J.; Fu, C. G.; Xie, H. H.; Liu, Y. T.; Feng, B.; Xie, J.; Zhao, X. B. *EPL* **2013**, *104*, 46003.

(5) Xie, H.; Wang, H.; Pei, Y.; Fu, C.; Liu, X.; Snyder, G. J.; Zhao, X.; Zhu, T. *Adv. Funct. Mater.* **2013**, *23*, 5123-5130.

(6) Mingo, N.; Hauser, D.; Kobayashi, N. P.; Plissonnier, M.; Shakouri, A. *Nano Lett.* **2009**, *9*, 711-715.

(7) Chen, Z.; Jian, Z.; Li, W.; Chang, Y.; Ge, B.; Hanus, R.; Yang, J.; Chen, Y.; Huang, M.; Snyder, G. J.; Pei, Y. *Adv. Mater.* **2017**, *29*, 1606768.

Chapter 5. High Thermoelectric performance in In/Cd co-doped SnTe system

-Published as **Moshwan *et al.*,** High Thermoelectric Performance in Sintered Octahedron-Shaped Sn(CdIn)$_x$Te$_{1+2x}$ Microcrystals. *ACS Appl. Mater. Interf.* **2018,** *10*, 38944-38952.

High Thermoelectric Performance in Sintered Octahedron-Shaped Sn(CdIn)$_x$Te$_{1+2x}$ Microcrystals

Raza Moshwan,[†] Xiao-Lei Shi,[†] Wei-Di Liu,[†] Lei Yang,[†] Yuan Wang,[‡,†] Min Hong,[‡,†] Graeme Auchterlonie,[§] Jin Zou,[*,†,§] and Zhi-Gang Chen[*,‡,†]

[†]Materials Engineering and [§]Centre for Microscopy and Microanalysis, The University of Queensland, St Lucia, Queensland 4072, Australia

[‡]Centre for Future Materials, The University of Southern Queensland, Springfield, Queensland 4300, Australia

5.1 Publication

5.1.1 Abstract

In this study, we fabricate In/Cd co-doped octahedron-shape $Sn(CdIn)_xTe_{1+2x}$ microcrystals with a promising thermoelectric performance by using a facile solvothermal method. The high hole carrier concentration of pristine SnTe is significantly reduced through effectively In/Cd co-doping, which increase the Seebeck coefficient in a wide temperature range. Moreover, co-doped In/Cd not only modify the band structure by creating resonance energy level at the valence band and converging light hole and heavy hole valence bands of SnTe, but also provides In/Cd rich nanoprecipitates in the matrix, leading to a high power factor of ~26.76 $\mu Wcm^{-1}K^{-2}$ at 773 K in the sintered $SnIn_{0.03}Cd_{0.03}Te_{1.06}$. Compared with the bulk counterparts, a much lower lattice thermal conductivity is achieved over a wide temperature range due to strong phonon scatterings by point defects, nanoprecipitates, lattice distortion, and grain boundaries in sintered $SnIn_xCd_xTe_{1+2x}$ ($x = 3$ %, and 4 %) samples. Consequently, a high ZT of ~ 1.12 is obtained at 773 K in the p-type $SnIn_{0.03}Cd_{0.03}Te_{1.06}$, suggesting that nanoprecipitate-included Cd/In co-doped octahedron-shape $Sn(CdIn)_xTe_{1+2x}$ microcrystals are a convincing candidate for medium temperature thermoelectric applications.

5.1.2 Introduction

The effective usage of large-scale and untapped waste-heat from the consumption of the limited fossil fuel is of immense economic and environmental advantage to the ever-growing world population.[1-2] Thermoelectric materials, converting heat into electricity, offer a potential to utilize such a huge waste-heat for power generation. The efficiency of a thermoelectric material is determined by the dimensionless figure of merit, ZT, defined as:

$$ZT = \frac{S^2\sigma}{\kappa}T = \frac{S^2\sigma}{\kappa_e + \kappa_l}T$$

(5-1)

where S is the Seebeck coefficient, σ is the electrical conductivity, T is the absolute temperature, and κ is the thermal conductivity comprises of electrical (κ_e) and lattice (κ_l) thermal conductivities, respectively. Extensive theoretical and experimental studies have been carried out to enhance the ZT by increasing power factor ($S^2\sigma$), including band engineering,[3-6] and carrier concentration optimization,[7-10] or/and by reducing κ *via* nanostructuring,[11-13] defect engineering,[14-17] anisotropy-strengthening,[18] and all-scale

hierarchical architecturing.[19-21] Hence, the simultaneous enhancement in $S^2\sigma$ and reduction in κ_l are of crucial important to achieve high ZT.

Lead chalcogenides and their alloys are widely used thermoelectric materials for mid-temperature (400-800 K) thermoelectric applications.[22-24] Recent studies have reported extraordinary p-type lead chalcogenides with $ZT \geqslant 2$ by employing resonant level,[25] band convergence[3, 26] and structure engineering with nano-, micro-, and their hierarchical structures.[20, 27-28] However, the environmental hazardousness associated with Pb has restricted their wide applications, particularly for domestic purposes. Owing to the similar electronic band structure and rock-salt crystal structure with PbTe, SnTe is a potential alternative for the application in the field of solid-state waste heat recovery if its ZT can be brought close to that of toxic PbTe. In fact, the key limitations of SnTe are its intrinsic high carrier concentration (n) of ~10^{20} to 10^{21} cm^{-3} and a relatively large energy separation (ΔE) between light hole valence band (at L point) and the heavy hole valence band (at Σ) of 0.3 eV, which leads to low S and high κ_e.[1] The thermoelectric performance of SnTe significantly improved by optimising n[7, 29-30] and modifying valence band structures.[31-33] A small number of dopants including I,[29] Bi,[7] or Sb[30] were used to optimise n, while the substitution of Sn by Cd,[34] Ca,[35] Mn,[36] Mg,[37] and Hg[38] can significantly enhance S through reducing ΔE of SnTe. Particularly, it has been reported that In dopants can create resonance states near the Fermi level at the top of the valence band of SnTe, and increase the local density of states (DOS), leading to high S.[39] The synergistic effect of resonance energy level and the convergence of valence bands on the thermoelectric performance of SnTe have been extensively investigated by the previous researchers,[40-45] for instance, Banik et al.[41] worked on In/Ag co-doped SnTe system where they reported an extraordinary $S^2\sigma$ of ~ 31.4 μW cm^{-1} K^{-2} and ZT of ~1. Bhat et al. successfully introduced Mg/In,[40] Ca/In[44] in SnTe where both $S^2\sigma$ and ZT greatly enhanced upon co-doping. Wang et al.[46] and Tan et al.[45] studied Mn/In and Hg/In co-doping in SnTe, respectively where they reported significant enhancement in $S^2\sigma$ and ZT. κ of SnTe can be reduced through second phase nanoprecipitate engineering. For instance, SrTe,[47] CdS[48] or ZnS[48] nanoprecipitates have been introduced in SnTe to reduce κ_l by solid state reaction. It should be pointed out that an offset of $S^2\sigma$ may occur when the nanoprecipitate engineering was introduced in the SnTe matrix.[49] Therefore, it is essential to reduce κ without severely deteriorating electronic transport properties. The conventional synthesis approaches (such as ball-milling,[39] and melting[31-33, 48, 50-51] for obtaining high-performance SnTe materials) are highly energy-intensive. In comparison with these

conventional approaches, the solvothermal method can yield well-controlled nanomaterials with high crystallinity and low process temperature as well as low energy consumption.[52]

Herein, we developed nanoprecipitate-included Cd/In co-doped octahedron-shape $Sn(CdIn)_xTe_{1+2x}$ microcrystals by a facile solvothermal method, as schematically shown in **Figure 5.1.** After detailed structural characterization, we found that high-density In/Cd-rich nanoprecipitates have been dispersed in $Sn(CdIn)_xTe_{1+2x}$ matrix along with the point defects, lattice distortion, and grain boundaries, leading to a low κ_l of ~0.75 W m^{-1} K^{-1} and a high $S^2\sigma$ of ~26.76 µW cm^{-1} K^{-2} at 773 K. As a result, a high ZT of ~1.12 is achieved in $SnIn_{0.03}Cd_{0.03}Te_{1.06}$ at 773 K. Our scalable synthesis approach thus opens up new pathways for producing high-performance SnTe thermoelectric materials, which can be extended to other material systems as well.
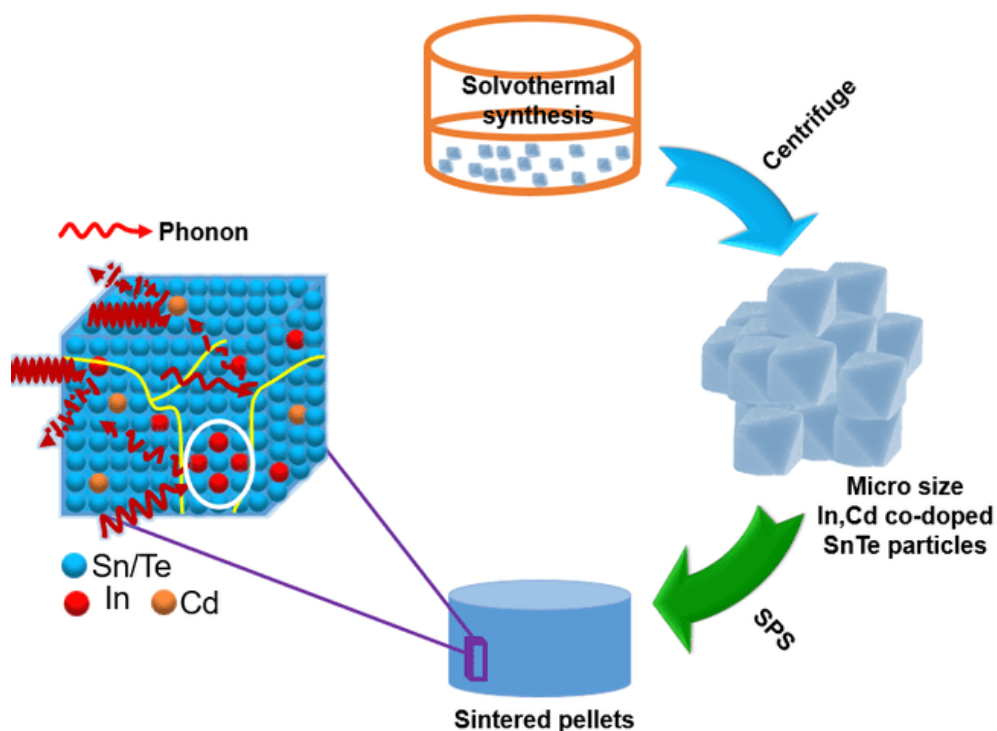
Figure 5.1 Schematic illustration of the fabrication process of In/Cd co-doped $Sn(CdIn)_xTe_{1+2x}$ samples by solvothermal route and the possible phonon scattering mechanism.

5.1.3 Experimental Section

Sodium tellurite (Na_2TeO_3, 99.99 %), Tin (II) chloride dihydrate ($SnCl_2 \cdot 2H_2O$, 99.99 %), cadmium chloride ($CdCl_2$, 99.99 %), Indium (III) chloride tetrahydrate ($InCl_3 \cdot 4H_2O$, 97 %), ethylene glycol (99.8 %) and NaOH (99.99 %) were used as precursors without further purification.

A series of $SnIn_xCd_xTe_{1+2x}$ (x = 0 %, 1 %, 2 %, 3 %, and 4 %) samples were synthesized via a facile solvothermal route. For a typical synthesis of $SnIn_{0.03}Cd_{0.03}Te_{1.06}$ (1.5 g), precursors including 35 ml EG, 5 ml NaOH (10 M), 1.2975 g $SnCl_2 \cdot 2H_2O$, 1.3511 g Na_2TeO_3, 0.0506 g $InCl_3 \cdot 4H_2O$, and 0.0316 g $CdCl_2$, were added into a 120 ml Teflon jar under magnetic stirring. The Teflon jar was then put into a stainless-steel autoclave and sealed which was then heated up to 230 °C for 24 h in an oven. After that, the products were cooled down to room temperature. Deionized water and absolute ethanol are used during centrifuging of the product. The final product is then dried at 60 °C for 12 h.

To evaluate the thermoelectric properties of the as-synthesized $SnIn_xCd_xTe_{1+2x}$ samples, the powders were compressed into pellets by spark plasma sintering (SPS) under a pressure of 50 MPa and heated at 683 K for 5 min in a vacuum. The densities of the sintered pellets were determined by Archimedes' method[53] and they are all ~97 % of the theoretical values. κ was obtained from $\kappa = DC_pd$ relationship, where D is thermal diffusivity and C_p is the specific heat capacity, respectively. LFA 457 (NETZSCH) (**Figure 5.S1**) was used to measure D. C_p was calculated from $C_p = C_{p,300} + C_{p1} \times ((T/300)^\alpha -1)/((T/300)^\alpha + C_{p1}/C_{p,300})$[33] where $C_{p,300}$ is the specific heat capacity at 300 K. For SnTe, $C_{p,300}$ is 0.1973 J g^{-1} K^{-1}, C_{p1} is 0.115 J g^{-1} K^{-1}, and α is 0.63.[33] σ and S were simultaneously measured by ZEM-3 (ULVAC). The Hall carrier consternation (n) and Hall carrier mobility (μ) were measured by using the van der Pauw technique under a reversible magnetic field of 1.5 T.

The phase purity of the sintered products was characterized by X-ray diffraction (XRD) equipped with graphite monochromatized, Cu Kα (λ = 1.5418 Å). Scanning electron microscopy (SEM, JEOL 6610, operated at 30 kV) and transmission electron microscopy (TEM, Philips Tecnai F20, operated at 200 kV) with scanning transmission electron microscopy detector (STEM) and energy dispersive X-ray spectroscopy (EDS) were used to see the morphological, structural, and chemical properties of our as-synthesized and sintered samples. Focused ion beam (FEI-SCIOS FIB) was deployed to obtain the specimens for TEM investigation. The compositions of the sintered pellets are obtained by electron probe micro analysis (EPMA) using JEOL JXA-8200 (operated at 20 kV).

5.1.4 Results and Discussion

From our extensive SEM characterisations, all as-synthesised $SnIn_xCd_xTe_{1+2x}$ samples have similar morphologies. Here, we use $SnIn_{0.03}Cd_{0.03}Te_{1.06}$ as a representative sample and its typical SEM images are shown in **Figure 5.2a**. As can be seen, regular octahedral-shape

crystals with eight {111} planes (refer to the inset of **Figure 5.2a**). are observed. Due to the nonstoichiometric behaviour of SnTe, it has inherent Sn vacancies and results in lower surface energy of {111} planes which is more stable than the {100} planes.[54-55] Therefore, SnTe particles have an inclination to grow into octahedral-shape with eight {111} planes. **Figure 5.2b** and **Figure 5.2(c-f)** are typical SEM images taken from the sintered $SnIn_{0.03}Cd_{0.03}Te_{1.06}$ pellet and corresponding EDS maps of Sn, Te, In and Cd elements, respectively. As can be seen, In and Cd are distributed in the matrix, suggesting that In and Cd are doped into SnTe.
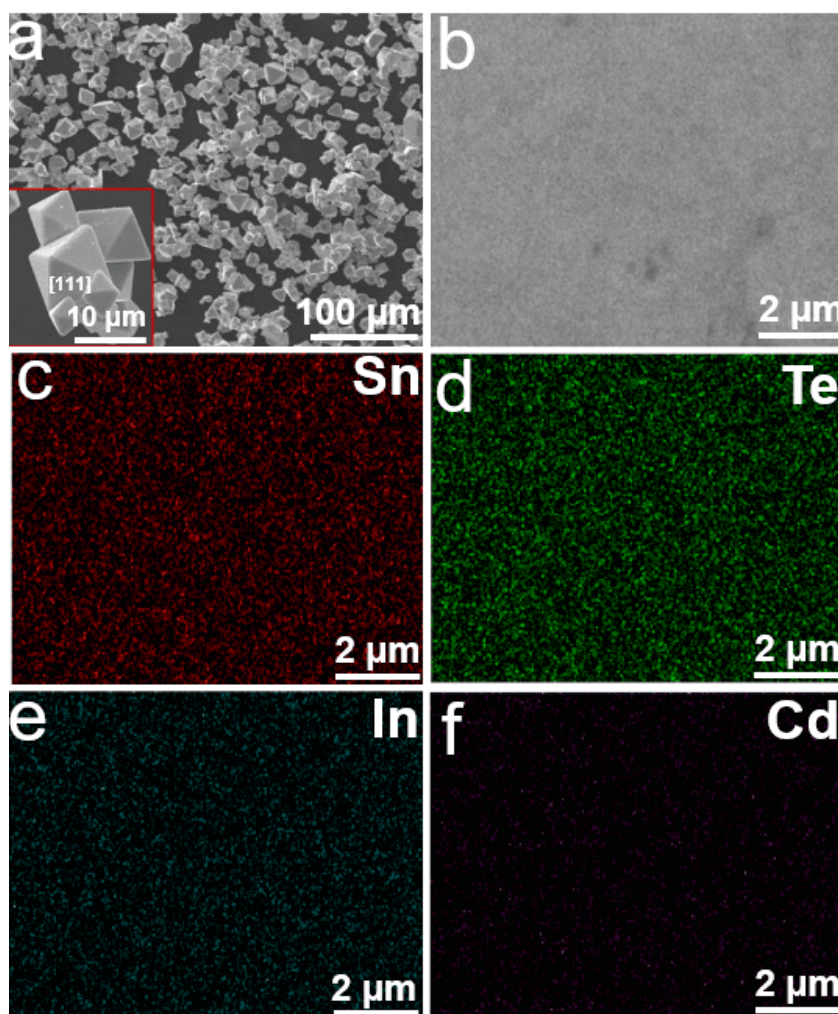
Figure 5.2 Characterisation of as-synthesised and sintered $SnIn_{0.03}Cd_{0.03}Te_{1.06}$ samples: (a) Typical SEM image; inset regular octahedral-shape with eight large {111} planes. (b) SEM image of the sintered $SnIn_{0.03}Cd_{0.03}Te_{1.06}$ pellet, (c-f) EDS maps of Sn, Te, In and Cd, respectively.

The thermoelectric properties of the sintered $SnIn_xCd_xTe_{1+2x}$ pellets were measured in the temperature ranges of 300 to 773 K. The temperature dependent σ of sintered pellets is

presented in **Figure 5.3a**. As can be seen, for all pellets, σ reduces with increasing the temperature from 300 to 773 K. In addition, with increasing the In/Cd co-doping concentration, σ decreases, possibly due to the reduction of Sn vacancies caused from the donor In and Cd atoms and variation of stoichiometry, in turn leading to the reduction of n.[1] We carried out EPMA analysis to see the actual composition in our sintered bulk In/Cd co-doped SnTe smaples which have good agreement with the nominal composition (**Figure 5.S2**). It is interesting to see In and Cd always interact with Sn site and the percentage of Sn always reduces with the increase of In/Cd concentration. Thus, it is believed that In/Cd both played significant role to suppress high Sn vacancies. **Figure 5.3b** shows the temperature-dependent S of as-sintered pellets. The positive sign of S indicates that hole is a major charge carrier and p-type nature. Comparing with the undoped SnTe, all doped pellets show much higher S. For instance, room-temperature S of the $SnIn_{0.03}Cd_{0.03}Te_{1.06}$ pellet is ~79 μV K^{-1}, which is improved by 243 % than that of the undoped SnTe (~23 μV K^{-1}). Such an improved S should be attributed to the local increasing DOS derived from In doping[39] and the reduction of ΔE by Cd.[49, 56] Earlier studies showed that Cd can significantly alter the band structure and converge the two valence bands to enhance S by facilitating the heavy hole valence band to participate in the electron-hole transport system.[34, 48-49] Cd also enlarge the band gap and minimize the minority carriers at high temperature, consequently prevent bipolar conduction.[48-49] The obtained maximum S is ~167 μV K^{-1} in $SnIn_{0.03}Cd_{0.03}Te_{1.06}$ at 773 K, which is enhanced by 79 % than that of the undoped SnTe under the same temperature. **Figure 5.3c** repersents the temperature-dependent $S^2\sigma$ of as-sintered pellets. A peak $S^2\sigma$ of ~26.76 μW cm^{-1} K^{-2} is observed at 773 K in the $SnIn_{0.03}Cd_{0.03}Te_{1.06}$ pellet, which is the 82 % improvement over the undoped SnTe. The steep increase of $S^2\sigma$ after 650 K should be attributed to the gradually increased S due to the band convergence induced by Cd.[48-49] The efficacy of resonant level in enhancing the S relies critically on the amount of overlap between impurity states and the band structure of the host material. Too much overlap or too little overlap both have detrimental effect on boosting S by changing in density of states.[26] The anomalous behaviour of S in $SnIn_{0.04}Cd_{0.04}Te_{1.08}$ could be attributed to the defect chemistry of the system which is also reported in Tl-doped $PbTe_{1-x}S_x$ system.[26, 41, 57] **Figure 5.3d** represents the temperature-dependent κ of as-sintered pellets. Obviously, a significant reduction of κ has been achieved *via* In/Cd co-doping. The κ of the undoped SnTe at room temperature extraordinarily decreased from ~8.5 W m^{-1} K^{-1} to ~1.68 W m^{-1} K^{-1} in $SnIn_{0.04}Cd_{0.04}Te_{1.08}$ which is due to the significant reduction in κ_e and κ_l.
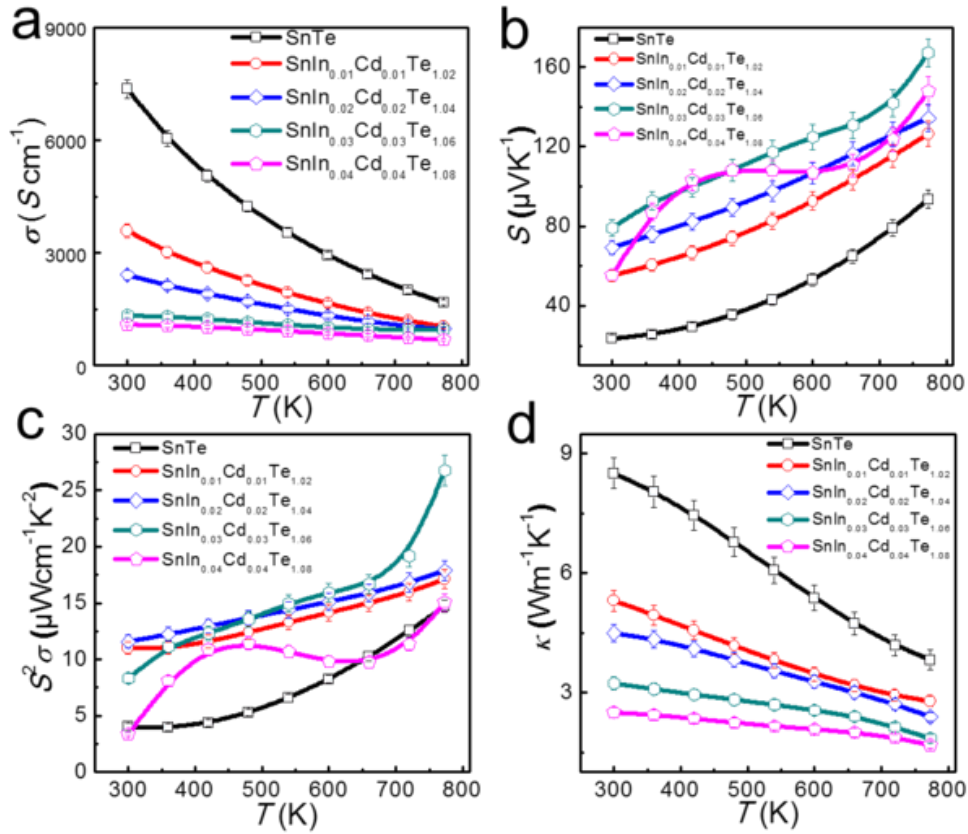
103

Figure 5.3 Temperature-dependent thermoelectric properties of sintered $SnIn_xCd_xTe_{1+2x}$ samples. (a) σ, (b) S, (c) $S^2\sigma$, (d) κ.

To illustrate the underlying mechanism for the reduced κ in the $SnIn_xCd_xTe_{1+2x}$ pellets, κ_e and κ_l were determined by $\kappa_e = L\sigma T$ and $\kappa_l = \kappa - \kappa_e$ according to the Wiedemann-Franz law $\kappa_e = L\sigma T$,[38] where L is the Lorenz number; and the results are shown in **Figure 5.S3**. The L value was estimated using the equation[58] of:

$$L = 1.5 + \exp\left(-\frac{|S|}{116}\right)$$

(5-2)

where L can be determined in the order of 10^{-8} W Ω K^{-2}. Specifically, the calculated L ranges from 2.32×10^{-8} to 1.77×10^{-8} W Ω K^{-2}. The temperature-dependent κ_e is plotted in **Figure 5.S4**, in which with increasing the In/Cd concentration, κ_e systematically decreases from ~5.1 W m^{-1} K^{-1} at 300 K to ~0.94 W m^{-1} K^{-1} at 773 K. In fact, the reduction in σ with increasing In/Cd concentration contributes to the reduction in κ_e. **Figure 5.S5a** shows the temperature dependent κ_l which was obtained by subtracting κ_e from κ. The room-temperature κ_l values significantly reduce from ~ 3.4 W m^{-1} K^{-1} of the undoped SnTe to ~0.74 W m^{-1} K^{-1} of

$SnIn_{0.04}Cd_{0.04}Te_{1.08}$ at 773 K (**Figure 5.S5a**), approaching to the theoretical limit (~0.5 W m^{-1} K^{-1}) of κ_l for pure SnTe.[30] **Figure 5.S5b** shows the comparison of κ_l both at room temperature and high temperature (773 K). As can be seen, both room-temperature and high-temperature κ_l systematically decrease in all the doped samples.

To understand the significant reduction of κ_l isn $SnIn_xCd_xTe_{1+2x}$ pellets, we performed phase analysis of our sintered pellets by XRD and detailed structural characterisations using TEM. **Figure 5.4a** displays the XRD results of the sintered $SnIn_xCd_xTe_{1+2x}$ pellets and all the main peaks can be exclusively indexed as face-centred-cubic (FCC) structured SnTe (PDF #65−0239, the pink line in **Figure 5.4a**) with a $Fm\bar{3}m$ space group. We did not observe any secondary phases at x = 1 % and 2 %, which is attributed to the In and Cd fully dissolved in SnTe with extra Te. Along with the main peaks, two additional peaks are obvious for 3 % and 4 % In/Cd co-doped samples (highlighted by dotted lines) and they are likely to be indexed as In_2Te_5 (PDF#30-0637) and CdTe (PDF#19-0192). **Figure 5.S6** shows the enlarged spectra for (200) Bragg peaks show the right shifting trend of the diffraction peaks with increasing the doping concentration (up to x = 2 %) which indicates a lattice shrinkage of the In/Cd co-doped SnTe samples. The substitution of Sn^{2+} (118 pm) atoms with smaller ionic radius of In^{3+} (80 pm) and Cd^{2+} (95 pm) influenced the shifting of diffraction peak.[59] The variation of diffraction angle suggest that In and Cd are successfully doped into SnTe lattice. **Figure 5.4b** is a typical bright-field TEM image taken from the $SnIn_{0.03}Cd_{0.03}Te_{1.06}$ pellet, and shows that the multiple grain boundaries as indicated by red arrows form in the matrix, suggesting that the SPS process can deform the original octahedral micro-size particles to form high-density grain boundaries. These grain boundaries help to scatter the heat carrying phonons significantly and reduce κ_l. **Figure 5.4c** shows that a high density of nanoprecipitates with the size ranging from ~10 to 15 nm exist in the $SnIn_{0.03}Cd_{0.03}Te_{1.06}$ matrix. Additionally, Moiré pattern with a width of 10 ~ 15 nm can be observed at the grain boundaries as shown in inset of **Figure 5.4c**, indicating the possibility of the obscured dislocation at the grain boundaries.[60] To further verify the composition of the nanoprecipitates, we investigated by STEM EDS and the result is shown in **Figure 5.4d**. Sn vacancies cause high electrical conductivity (σ) that leads to high electronic thermal conductivity (κ_e). Such high σ and κ_e can be suppressed after In/Cd co-doping via intensifying point defects, nanoprecipitates, and grain boundaries. According to the previous studies,[61-63] phonons are composed of a broad range of mean free path (MFP). Point defects are highly responsible to scatter high-frequency phonons (MFP <1 nm). The remaining medium frequency phonon

(MFP of 1-10 nm) and low frequency phonon (MFP of 10-1000 nm) are significantly scattered by nanoprecipitates and grain boundaries, respectively.[61-63] We believe Cd/In nanoprecipitates playing an important role to suppress thermal conductivity that comes from phonon modes with MFP of 1-10 nm.
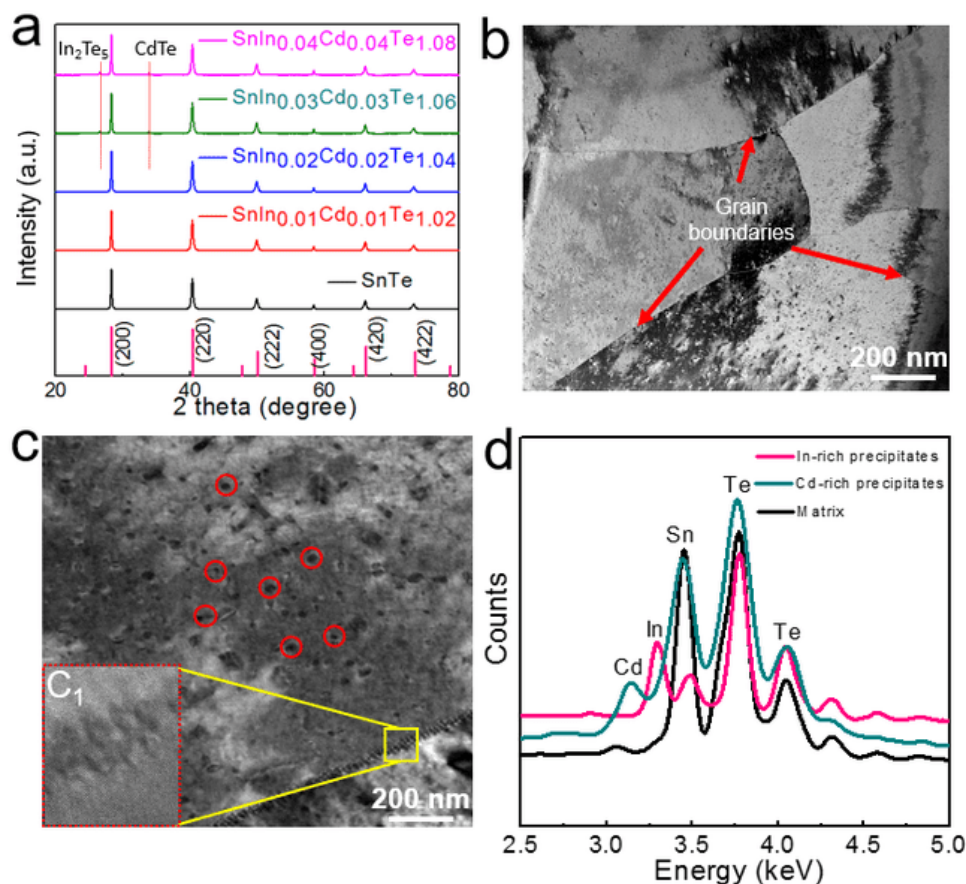

Figure 5.4 Characterizations of sintered pellets. (a) XRD patterns of the sintered pellets showing extra peaks as highlighted dashed line along with the main peaks at 3 % and 4 % In/Cd co-doped samples. (b) Typical bright field TEM image of $SnIn_{0.03}Cd_{0.03}Te_{1.06}$ sintered sample shows multiple grain boundaries. (c) High-density nanoprecipitates and (c1) Moiré pattern. (d) STEM-EDS spectrum of In rich and Cd rich nanoprecipitates and the matrix.

To understand the behaviour of nanoprecipitates and matrix, we further analyse their atomic structures and the results are shown in **Figure 5.5(a-d)**. **Figure 5.5a** shows a typical HRTEM image of the sintered $SnIn_{0.03}Cd_{0.03}Te_{1.06}$ pellet containing several nanoprecipitates. The bottom left inset is the corresponding selected area electron diffraction (SAED) pattern taken along the [001] zone-axis. **Figure 5.5b** is a magnified view of one nanoprecipitate in **Figure 5.5a** and displays the antiphase domain where the contrast of top left part reverses or shifts one atomic layer along the [100] direction with respect to the bottom-right part of the

nanoparticle as marked by the red arrows.[64] Moreover, fast Fourier transform (FFT) pattern of nanoprecipitate (**Figure 5.5b$_2$**) shows additional spots as highlighted by red circle compare to FFT pattern of matrix (**Figure 5.5b$_1$**), which supports the possible existence of antiphase domain.[64] These antiphase domains are responsible to generate high strain field in the surrounding matrix and play a vital role to scatter heat carrying phonons and remarkably reduce κ_l.[64] Geometrical phase analysis (GPA) was used to show the strain distribution around the nanoprecipitate and the result is shown in **Figure 5.S7**. The sharp contrast indicate the high strain concentration around the precipitates area. Such a strain effect is well observed in $AgPb_{18}SbTe_{20}$ by Wu et al. [64]. It should be pointed out that the atomic mass difference between guest atoms and host matrix provides sufficient atomic strain to scatter heat-carrying phonons.[63] Moreover, the atomic size difference between the solute (In and Cd) and solvent atoms (Sn and Te) contributes to changing in phonon velocity,[65] which can reinforce the anharmonic phonon scattering of the strain field.[66] Similar investigations have been observed in case of Cu-Al alloy,[66] and $(AgSbTe_2)_{1-x}(GeTe)_x$.[65] **Figure 5.5c** is another HRTEM image taken from a nanoprecipitate and its enlarged view is shown in **Figure 5.5d**, which clearly shows the lattice distortion occurs at the interface between the nanoprecipitate and the matrix. This lattice distortion could be attributed to the lattice misfit between the precipitate and the matrix. Such a lattice distortion can increase the scattering of propagating phonons and lower κ_l of the system. The high-density nanoprecipitates, coupled with the strain effect on the coherent interfaces, play the significant roles on scattering the majority of transported phonons.[67]
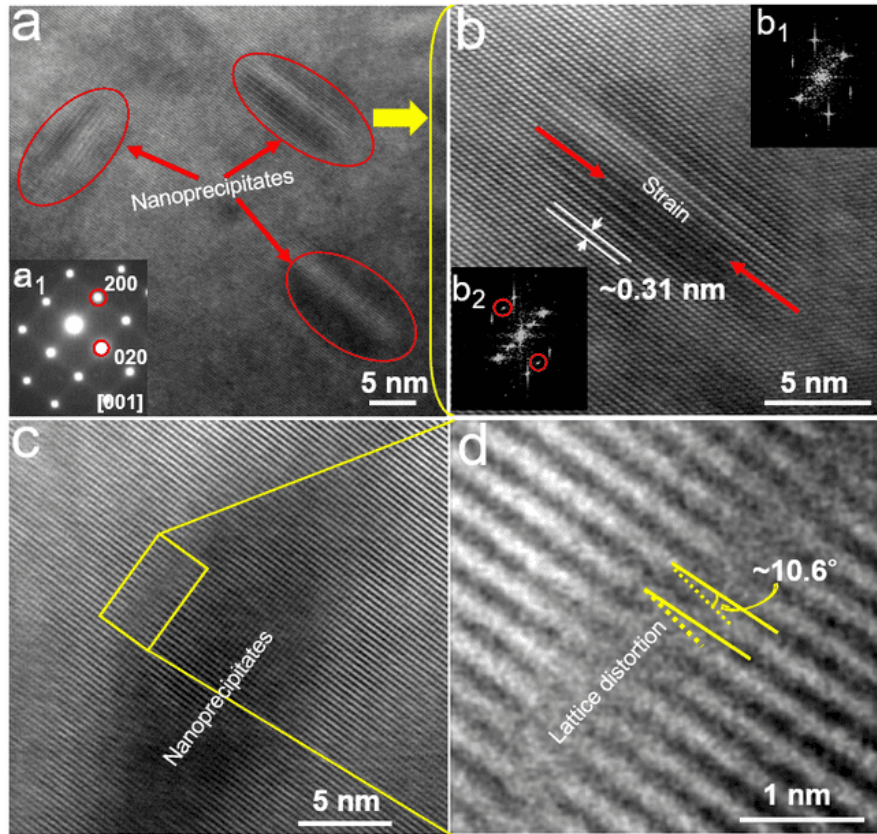
Figure 5.5 Characterizations of sintered pellets. (a) HRTEM image showing multiple nanoprecipitates; (a$_1$) SAED pattern along [001] zone axis, (b) Enlarged view of a nanoprecipitate as marked by red ellipse in (a), showing strain field developed around the nanoprecipitate; (b$_1$) FFT pattern of matrix (b$_2$) FFT pattern of the nanoprecipitate. (c) HRTEM image of a typical nanoprecipitate showing that lattice distortion occurs at the interface between nanoprecipitates and matrix, (d) Enlarged view of box area in (c).

In order to obtain more insight on the variation and origin of high *S* due to In and Cd co-doping, it is worthy to compare the room-temperature *S vs. n* of as-sintered SnIn$_x$Cd$_x$Te$_{1+2x}$ pellets with the well-known Pisarenko plot,[39] and the results are plotted in **Figure 5.6a**. Theoretical Pisarenko plot has been calculated by considering the contribution of both the light hole and heavy hole valence bands in SnTe.[39] Obviously, the *S* values of our SnIn$_x$Cd$_x$Te$_{1+2x}$ (for *x* = 1 % - 4 %) pellets reside far above the theoretical Pisarenko line and comparable to those of the other reported systems including undoped SnTe,[68] Ag-doped SnTe,[41] Ag/In co-doped SnTe,[41] Cd-doped SnTe,[49] Cd/In doped SnTe,[49] Ca-doped SnTe,[35] Ca/In co-doped SnTe,[44] Mn-doped SnTe,[46] and Mn/In co-doped SnTe.[46] These results indicate the effectiveness of tuneable band structures in our In/Cd co-doped SnTe system, suggesting that In/ Cd co-doping can reduce Δ*E* of SnTe and thereby facilitate the heavy

holes to engage in the electron-hole transport system and ultimately increase S, which was also reported by Tan et al..[49] In order to realise the underpinnings of decreased σ, we further measured the room-temperature n and μ and plotted in **Figure 5.6b**. As can be seen, a decreasing trend of n and μ is observed with increasing x. Room-temperature n reduces from ~6.45×10^{20} cm^{-3} of the undoped SnTe to ~3.03×10^{20} cm^{-3} of $SnIn_{0.04}Cd_{0.04}Te_{1.08}$ pellet while for μ from ~71.2 cm^2 v^{-1} s^{-1} to ~21.6 cm^2 v^{-1} s^{-1}, respectively. This trend is consistent with the Bi-doped SnTe reported by Zhou et al.[7] It can also be noted that n does not fluctuate much with respect to temperature (**Figure 5.S8**). Undoped SnTe composed of high density of Sn vacancies. The small amount co-dopants of In and Cd may firstly occupy the intrinsic Sn vacancies, which leads to the reduced hole carrier concentration. At some point when the doping level increased the co-dopants start to act as a donor which moderately decrease the hole carrier concentration.[10, 39] Previous studies reported that the reduction in carrier mobility is closely connected with the induced scattering centers, such as point defects while barrier scattering at grain boundaries/interfaces are often responsible to deteriorate the mobility.[19, 66] The reduction in μ also in this work could be attributed to the carrier scattering by acoustic phonons, grain boundaries and the interface between nanoprecipitates and matrix.[7]
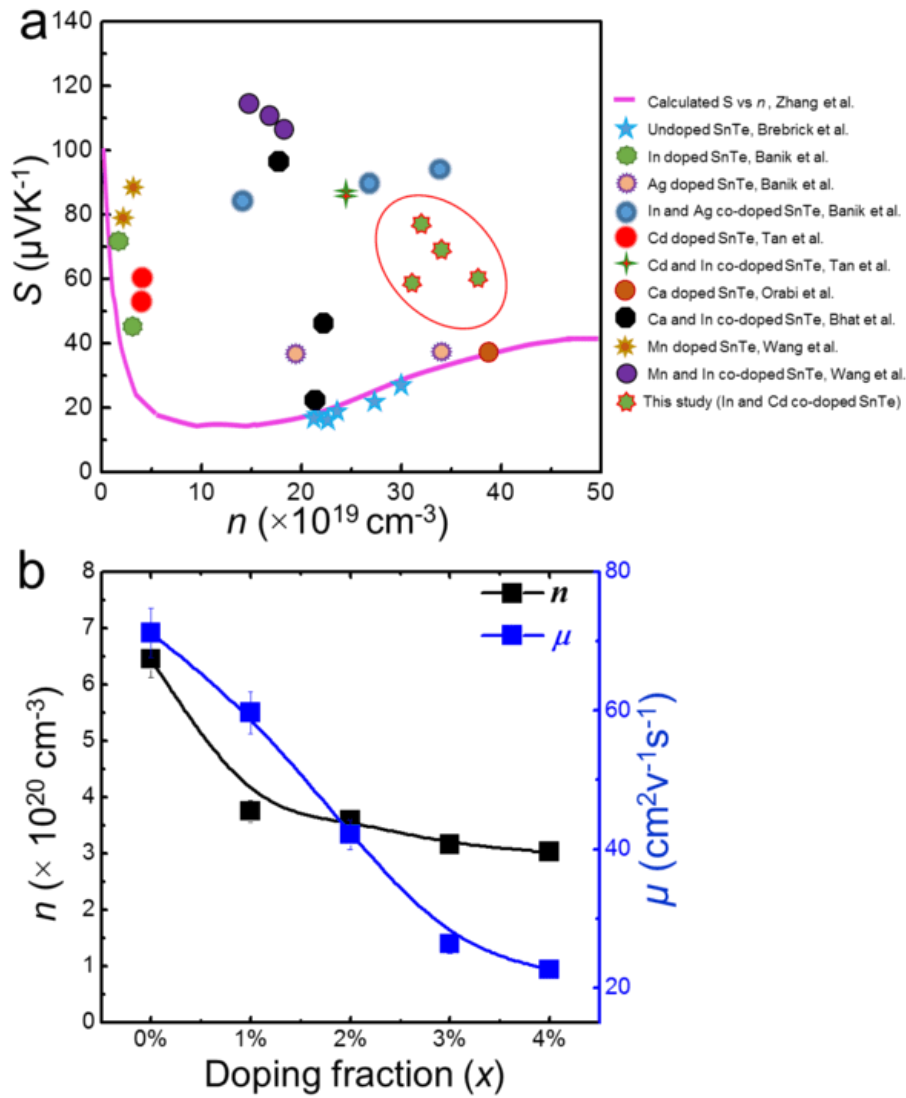
Figure 5.6 Comparison of performance. (a) Room-temperature S *vs. n* plot of the current study and the previously reported results. Calculated S *vs. n*,[39] undoped SnTe,[68] Ag-doped SnTe,[41] Ag/In co-doped SnTe,[41] Cd-doped SnTe,[49] Cd/In doped SnTe,[49] Ca-doped SnTe,[35] Ca/In co-doped SnTe,[44] Mn-doped SnTe,[46] and Mn/In co-doped SnTe.[46] (b) Effect of doping concentration on n and μ at room temperature.

Figure 5.7a shows the calculated ZT of as-sintered $SnIn_xCd_xTe_{1+2x}$ pellets. As can be seen, a high ZT of ~1.12 at 773 K is observed in $SnIn_{0.03}Cd_{0.03}Te_{1.06}$ pellet, attributed to the low κ of ~1.84 W m^{-1} K^{-1} and the high $S^2\sigma$ of ~26.76 μW cm^{-1} K^{-2}. **Figure 5.7b** shows the comparison of peak ZT between our current study and the previously reported results for the different SnTe systems, which suggests that our bottom-up solvothermal synthesis method shows a superior thermoelectric performance over the other synthesis approaches, such as ball milling,[39] and melting.[48-49, 69] The precise control over the growth size of the particles, shape

distribution and nanostructuring opens the window for the significant thermoelectric performance enhancement in SnTe system.[70]
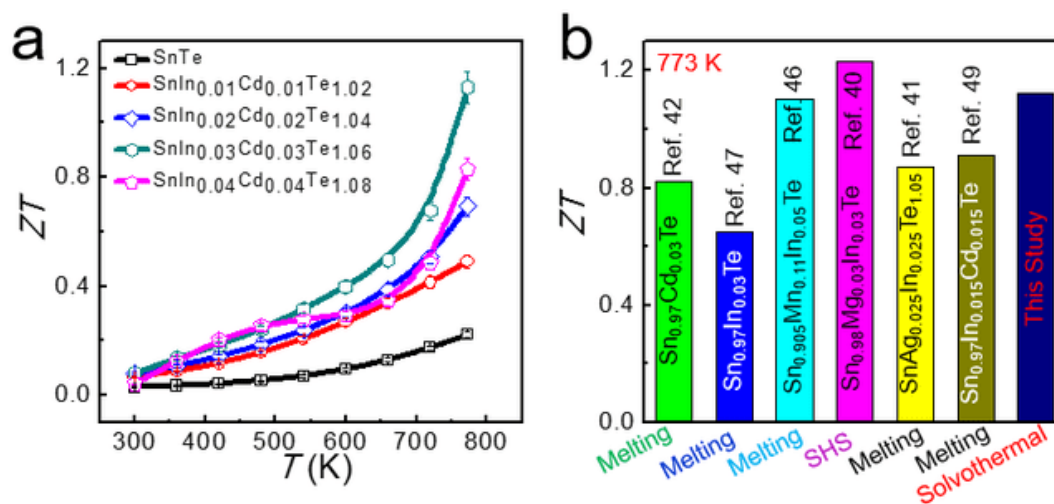

Figure 5.7 Comparison of *ZT*. (a) Temperature dependent *ZT* values of $SnIn_xCd_xTe_{1+2x}$ (error bar is 5 %) (b) A comparative thermoelectric performance of the current work and the previously reported results.[40-42, 46-47, 49]

5.1.5 Conclusion

In conclusion, we for the first time, developed a facile solvothermal method to synthesis nanoprecipitate-included octahedron-shape $Sn(CdIn)_xTe_{1+2x}$ microcrystals with a high peak *ZT* of ~1.12 at 773 K. The alteration of electronic band structure of undoped SnTe by In/Cd co-doping significantly enhanced $S^2\sigma$ from ~4.02 $\mu W\ cm^{-1}\ K^{-2}$ to ~26.76 $\mu W\ cm^{-1}\ K^{-2}$ at 773 K. Benefitted from the strong phonon scatterings due to the co-existence of point defects, nanoprecipitates, lattice distortion, and grain boundaries, κ_l is significantly reduced over a wide temperature range. Moreover, the nanostructuring *via* the facile solvothermal method provides a promising path to preserve good σ while distinctively scatter phonons to degrade κ_l. This study offers an alternative insight to fabricate high-performance SnTe-based thermoelectric materials through synergistic band engineering and nanostructuring *via* the facile solvothermal method.

Acknowledgement

References

(1) Moshwan, R.; Yang, L.; Zou, J.; Chen, Z.-G. *Adv. Funct. Mater.* **2017,** *27*, 1703278.

(2) Chen, Z.-G.; Han, G.; Yang, L.; Cheng, L.; Zou, J. *Prog. Nat. Sci.* **2012,** *22*, 535-549.

(3) Pei, Y.; Shi, X.; LaLonde, A.; Wang, H.; Chen, L.; Snyder, G. J. *Nature* **2011,** *473*, 66-69.

(4) Hong, M.; Chen, Z. G.; Yang, L.; Zou, Y. C.; Dargusch, M. S.; Wang, H.; Zou, J. *Adv. Mater.* **2018,** *30*, 1705942.

(5) Yang, L.; Chen, Z. G.; Dargusch, M. S.; Zou, J. *Adv. Energy Mater.* **2018,** *8*, 1701797.

(6) Shenoy, S.; Bhat, D. K. *J. Phys. Chem. C* **2017,** *121*, 20696-20703.

(7) Zhou, Z.; Yang, J.; Jiang, Q.; Luo, Y.; Zhang, D.; Ren, Y.; He, X.; Xin, J. *J. Mater. Chem. A* **2016,** *4*, 13171-13175.

(8) Krez, J.; Schmitt, J.; Jeffrey Snyder, G.; Felser, C.; Hermes, W.; Schwind, M. *J. Mater. Chem. A* **2014,** *2*, 13513-13518.

(9) Li, J.; Chen, Z.; Zhang, X.; Yu, H.; Wu, Z.; Xie, H.; Chen, Y.; Pei, Y. *Adv. Sci.* **2017,** *4*, 1700341.

(10) Pei, Y.; May, A. F.; Snyder, G. J. *Adv. Energy Mater.* **2011,** *1*, 291-296.

(11) Kanatzidis, M. G. *Chem. Mater.* **2010,** *22*, 648-659.

(12) Biswas, K.; He, J.; Zhang, Q.; Wang, G.; Uher, C.; Dravid, V. P.; Kanatzidis, M. G. *Nat. Chem.* **2011,** *3*, 160-166.

(13) Poudeu, P. F. P.; D'Angelo, J.; Kong, H.; Downey, A.; Short, J. L.; Pcionek, R.; Hogan, T. P.; Uher, C.; Kanatzidis, M. G. *J. Am. Chem. Soc.* **2006,** *128*, 14347-14355.

(14) Lan, J.-L.; Liu, Y.; Lin, Y.-H.; Nan, C.-W.; Cai, Q.; Yang, X. *Sci. Rep.* **2015,** *5*, 7783.

(15) Pei, Y.; Zheng, L.; Li, W.; Lin, S.; Chen, Z.; Wang, Y.; Xu, X.; Yu, H.; Chen, Y.; Ge, B. *Adv. Electron. Mater.* **2016,** *2*, 1600019.

(16) Hu, L.; Zhu, T.; Liu, X.; Zhao, X. *Adv. Funct. Mater.* **2014,** *24*, 5211-5218.

(17) Hong, M.; Chen, Z. G.; Yang, L.; Liao, Z. M.; Zou, Y. C.; Chen, Y. H.; Matsumura, S.; Zou, J. *Adv. Energy Mater.* **2018,** *8*, 1702333.

(18) Shi, X.; Chen, Z.-G.; Liu, W.; Yang, L.; Hong, M.; Moshwan, R.; Huang, L.; Zou, J. *Energy Storage Mater.* **2018,** *10*, 130-138.

(19) Zhao, L. D.; Wu, H. J.; Hao, S. Q.; Wu, C. I.; Zhou, X. Y.; Biswas, K.; He, J. Q.; Hogan, T. P.; Uher, C.; Wolverton, C.; Dravid, V. P.; Kanatzidis, M. G. *Energy Environ. Sci.* **2013,** *6*, 3346-3355.

(20) Biswas, K.; He, J.; Blum, I. D.; Wu, C.-I.; Hogan, T. P.; Seidman, D. N.; Dravid, V. P.; Kanatzidis, M. G. *Nature* **2012,** *489*, 414-418.

(21) Bhattacharya, S.; Bohra, A.; Basu, R.; Bhatt, R.; Ahmad, S.; Meshram, K. N.; Debnath, A. K.; Singh, A.; Sarkar, S. K.; Navneethan, M.; Hayakawa, Y.; Aswal, D. K.; Gupta, S. K. *J. Mater. Chem. A* **2014,** *2*, 17122-17129.

(22) Zhou, M.; Li, J.-F.; Kita, T. *J. Am. Chem. Soc.* **2008,** *130*, 4527-4532.

(23) Yang, L.; Chen, Z.-G.; Hong, M.; Wang, L.; Kong, D.; Huang, L.; Han, G.; Zou, Y.; Dargusch, M.; Zou, J. *Nano Energy* **2017,** *31*, 105-112.

(24) Han, C.; Sun, Q.; Li, Z.; Dou, S. X. *Adv. Energy Mater.* **2016,** *6*, 1600498.

(25) Heremans, J. P.; Jovovic, V.; Toberer, E. S.; Saramat, A.; Kurosaki, K.; Charoenphakdee, A.; Yamanaka, S.; Snyder, G. J. *Science* **2008,** *321*, 554-557.

(26) Heremans, J. P.; Wiendlocha, B.; Chamoire, A. M. *Energy Environ. Sci.* **2012,** *5*, 5510-5530.

(27) Wang, H.; Bahk, J.-H.; Kang, C.; Hwang, J.; Kim, K.; Kim, J.; Burke, P.; Bowers, J. E.; Gossard, A. C.; Shakouri, A.; Kim, W. *Proc. Natl. Acad. Sci.* **2014,** *111*, 10949-10954.

(28) Pei, Y.; LaLonde, A. D.; Heinz, N. A.; Snyder, G. J. *Adv. Energy Mater.* **2012,** *2*, 670-675.

(29) Banik, A.; Biswas, K. *J. Solid State Chem.* **2016,** *242, Part 2*, 43-49.

(30) Banik, A.; Vishal, B.; Perumal, S.; Datta, R.; Biswas, K. *Energy Environ. Sci.* **2016,** *9*, 2011-2019.

(31) Han, M.-K.; Androulakis, J.; Kim, S.-J.; Kanatzidis, M. G. *Adv. Energy Mater.* **2012,** *2*, 157-161.

(32) He, J.; Tan, X.; Xu, J.; Liu, G.-Q.; Shao, H.; Fu, Y.; Wang, X.; Liu, Z.; Xu, J.; Jiang, H.; Jiang, J. *J. Mater. Chem. A* **2015,** *3*, 19974-19979.

(33) Zhou, M.; Gibbs, Z. M.; Wang, H.; Han, Y.; Xin, C.; Li, L.; Snyder, G. J. *Phys. Chem. Chem. Phys.* **2014,** *16*, 20741-20748.

(34) He, J.; Xu, J.; Liu, G. Q.; Shao, H.; Tan, X.; Liu, Z.; Xu, J.; Jiang, H.; Jiang, J. *RSC Adv.* **2016,** *6*, 32189-32192.

(35) Al Rahal Al Orabi, R.; Mecholsky, N. A.; Hwang, J.; Kim, W.; Rhyee, J. S.; Wee, D.; Fornari, M. *Chem. Mater.* **2016,** *28*, 376-384.

(36) Wu, H.; Chang, C.; Feng, D.; Xiao, Y.; Zhang, X.; Pei, Y.; Zheng, L.; Wu, D.; Gong, S.; Chen, Y.; He, J.; Kanatzidis, M. G.; Zhao, L.-D. *Energy Environ. Sci.* **2015,** *8*, 3298-3312.

(37) Banik, A.; Shenoy, U. S.; Anand, S.; Waghmare, U. V.; Biswas, K. *Chem. Mater.* **2015,** *27*, 581-587.

(38) Tan, G.; Shi, F.; Doak, J. W.; Sun, H.; Zhao, L.-D.; Wang, P.; Uher, C.; Wolverton, C.; Dravid, V. P.; Kanatzidis, M. G. *Energy Environ. Sci.* **2015,** *8*, 267-277.

(39) Zhang, Q.; Liao, B.; Lan, Y.; Lukas, K.; Liu, W.; Esfarjani, K.; Opeil, C.; Broido, D.; Chen, G.; Ren, Z. *Proc. Natl. Acad. Sci. U.S.A.* **2013,** *110*, 13261-13266.

(40) Bhat, D. K.; Shenoy U, S. *J. Phys. Chem. C* **2017,** *121*, 7123-7130.

(41) Banik, A.; Shenoy, U. S.; Saha, S.; Waghmare, U. V.; Biswas, K. *J. Am. Chem. Soc.* **2016,** *138*, 13068-13075.

(42) Tan, X.; Tan, X.; Liu, G.; Xu, J.; Shao, H.; Hu, H.; Jin, M.; Jiang, H.; Jiang, J. *J. Mater. Chem. C* **2017,** *5*, 7504-7509.

(43) Roychowdhury, S.; Shenoy, U. S.; Waghmare, U. V.; Biswas, K. *J. Mater. Chem. C* **2017,** *5*, 5737-5748.

(44) Bhat, D. K.; Shenoy, U. S. *Mater. Today Phys.* **2018,** *4*, 12-18.

(45) Tan, X.; Liu, G.; Xu, J.; Tan, X.; Shao, H.; Hu, H.; Jiang, H.; Lu, Y.; Jiang, J. *J. Materiomics* **2018,** *4*, 62-67.

(46) Wang, L.; Tan, X.; Liu, G.; Xu, J.; Shao, H.; Yu, B.; Jiang, H.; Yue, S.; Jiang, J. *ACS Energy Lett.* **2017,** *2*, 1203-1207.

(47) Zhao, L.-D.; Zhang, X.; Wu, H.; Tan, G.; Pei, Y.; Xiao, Y.; Chang, C.; Wu, D.; Chi, H.; Zheng, L.; Gong, S.; Uher, C.; He, J.; Kanatzidis, M. G. *J. Am. Chem. Soc.* **2016,** *138*, 2366-2373.

(48) Tan, G.; Zhao, L. D.; Shi, F.; Doak, J. W.; Lo, S. H.; Sun, H.; Wolverton, C.; Dravid, V. P.; Uher, C.; Kanatzidis, M. G. *J. Am. Chem. Soc.* **2014,** *136*, 7006-7017.

(49) Tan, G.; Shi, F.; Hao, S.; Chi, H.; Zhao, L.-D.; Uher, C.; Wolverton, C.; Dravid, V. P.; Kanatzidis, M. G. *J. Am. Chem. Soc.* **2015,** *137*, 5100-5112.

(50) Tan, G.; Zeier, W. G.; Shi, F.; Wang, P.; Snyder, G. J.; Dravid, V. P.; Kanatzidis, M. G. *Chem. Mater.* **2015,** *27*, 7801-7811.

(51) Zhang, L.; Wang, J.; Cheng, Z.; Sun, Q.; Li, Z.; Dou, S. *J. Mater. Chem. A* **2016,** *4*, 7936-7942.

(52) Helgeson, H. C.; Kirkham, D. H. *Am. J. Sci.* **1974,** *274*, 1089-1198.

(53) Mason, B. *Geologiska Föreningen i Stockholm Förhandlingar* **1944,** *66*, 27-51.

(54) Zou, Y.; Chen, Z.; Lin, J.; Zhou, X.; Lu, W.; Drennan, J.; Zou, J. *Nano Res.* **2015,** *8*, 3011-3019.

(55) Zhou, D.; Jin, S.; Li, Y.; Qiu, F.; Deng, F.; Wang, J.; Jiang, Q. *CrystEngComm* **2013,** *15*, 643-649.

(56) Zhou, M.; Gibbs, Z. M.; Wang, H.; Han, Y.; Li, L.; Jeffrey Snyder, G. *Appl. Phys. Lett.* **2016,** *109*, 042102.

(57) Jaworski, C. M.; Wiendlocha, B.; Jovovic, V.; Heremans, J. P. *Energy Environ. Sci.* **2011,** *4*, 4155-4162.

(58) Kim, H.-S.; Gibbs, Z. M.; Tang, Y.; Wang, H.; Snyder, G. J. *APL Mater.* **2015,** *3*, 041506.

(59) Wells, A. F., *Structural Inorganic Chemistry / A.F. Wells*. 5th ed.; Oxford : Clarendon Press: Oxford, 1984.

(60) Kim, S. I.; Lee, K. H.; Mun, H. A.; Kim, H. S.; Hwang, S. W.; Roh, J. W.; Yang, D. J.; Shin, W. H.; Li, X. S.; Lee, Y. H.; Snyder, G. J.; Kim, S. W. *Science* **2015,** *348*, 109.

(61) Qiu, B.; Bao, H.; Zhang, G.; Wu, Y.; Ruan, X. *Comp. Mater. Sci.* **2012,** *53*, 278-285.

(62) Tian, Z.; Garg, J.; Esfarjani, K.; Shiga, T.; Shiomi, J.; Chen, G. *Phys. Rev. B* **2012,** *85*, 184303.

(63) Tan, G.; Zhao, L.-D.; Kanatzidis, M. G. *Chem. Rev.* **2016,** *116*, 12123-12149.

(64) Wu, L.; Zheng, J.-C.; Zhou, J.; Li, Q.; Yang, J.; Zhu, Y. *J. Appl. Phys.* **2009,** *105*, 094317.

(65) E. A. Skrabek and D. S. Trimer, *Crc Handbook of Thermoelectrics*. CRC, Boca Raton, FL: 1995.

(66) Ackerman, M. W.; Klemens, P. G. *J. Appl. Phys.* **1971,** *42*, 968-971.

(67) Zhao, L.-D.; Dravid, V. P.; Kanatzidis, M. G. *Energy Environ. Sci.* **2014,** *7*, 251-268.

(68) Brebrick, R. F.; Strauss, A. J. *Phys. Rev.* **1963,** *131*, 104-110.

(69) Li, W.; Chen, Z.; Lin, S.; Chang, Y.; Ge, B.; Chen, Y.; Pei, Y. *J. Materiomics* **2015,** *1*, 307-315.

(70) Lai, J.; Niu, W.; Luque, R.; Xu, G. *Nano Today* **2015,** *10*, 240-267.
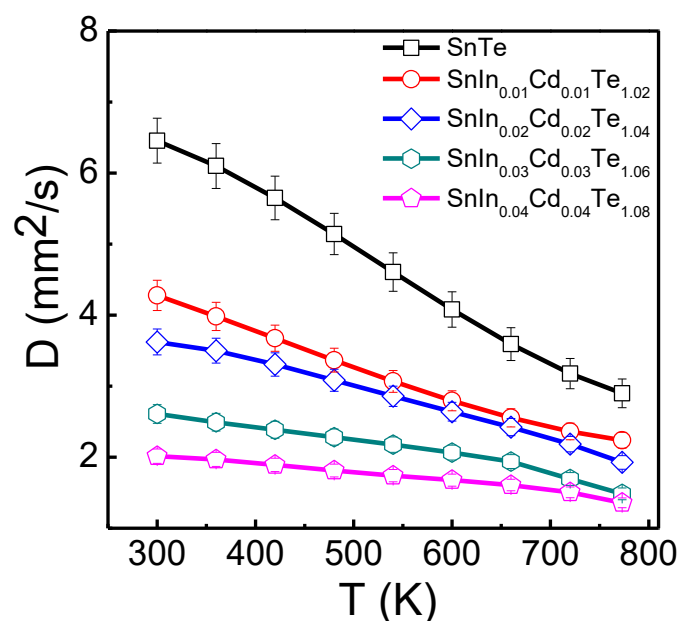
5.1.6 Supporting Information

Figure 5.S1 Thermal diffusivity, *D* as a function of temperature for different In, Cd co-doped SnTe samples.
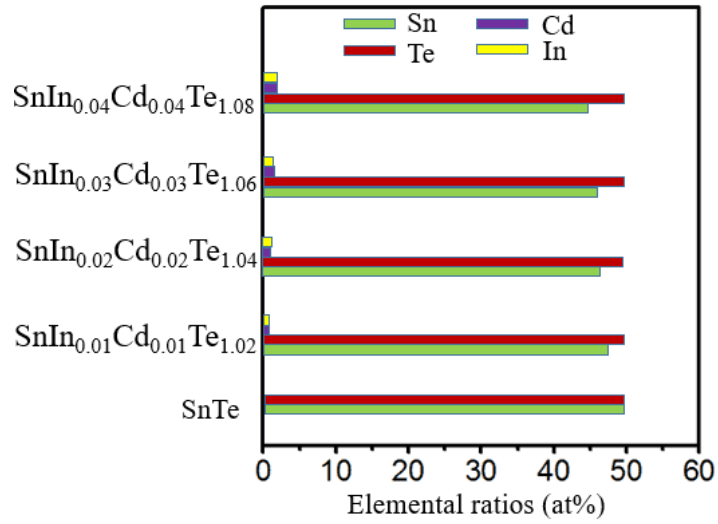
Figure 5.S2 EPMA results of SnIn$_x$Cd$_x$Te$_{1+2x}$ system.
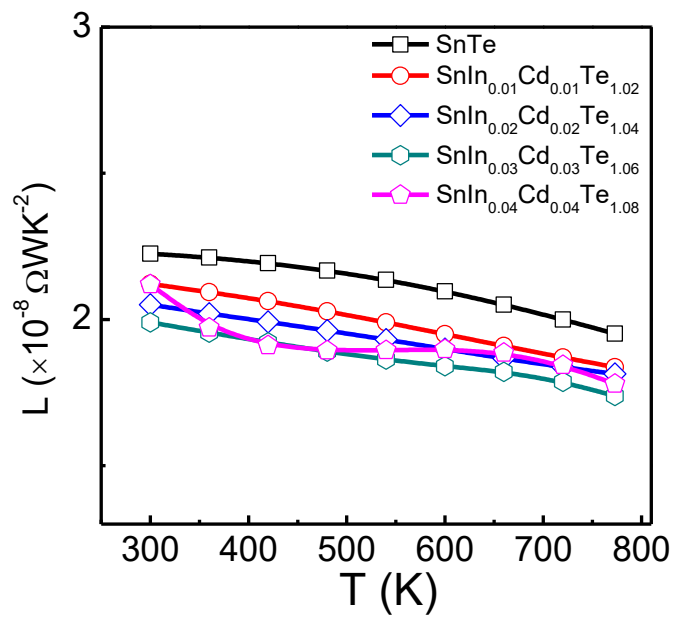
Figure 5.S3 Calculated Lorenz number, L as function of temperature for SnIn$_x$Cd$_x$Te$_{1+2x}$
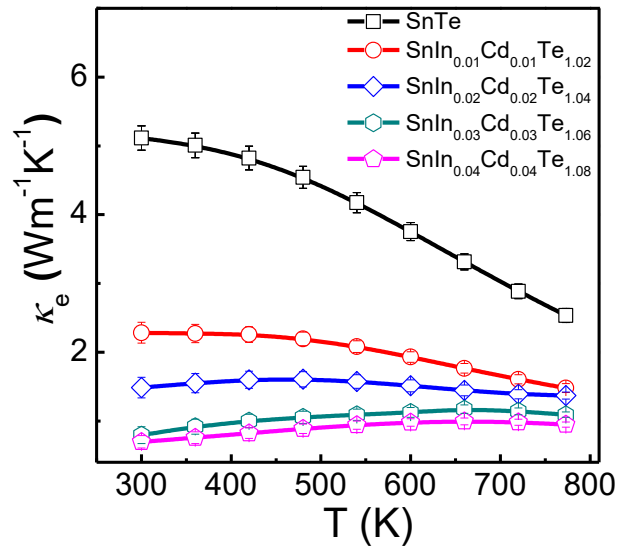
Figure 5.S4 Temperature dependent electronic thermal conductivities of $SnIn_xCd_xTe_{1+2x}$ system.
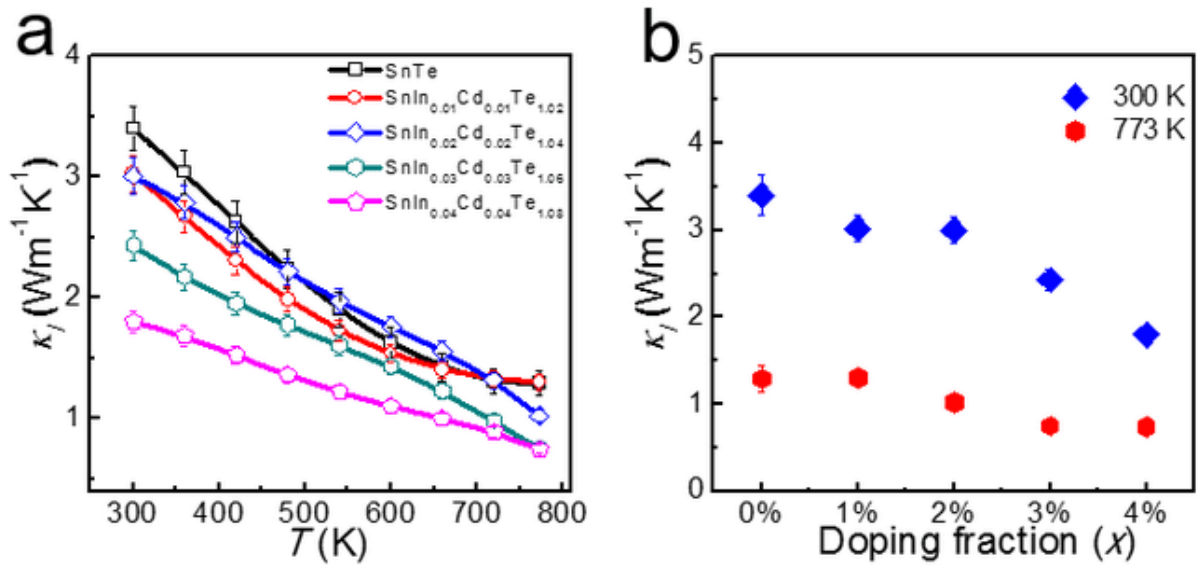
Figure 5.S5 (a) Temperature dependent lattice thermal conductivities and (b) comparative κ_l measured at room temperature and high temperature (773 K) as a function of x in $SnIn_xCd_xTe_{1+2x}$ with an error bar of 5 %.

Figure 5.S6 XRD Patterns of 200 peaks in **Figure 5.4a**.

Figure 5.S7 (a-d) Strain maps of **Figure** 5b showing strain distribution around nanoprecipitate.

Figure 5.S8 Temperature dependent Hall carrier concentration of In/Cd co-doped SnTe samples (error bar 15 %).

Chapter 6. Improved Thermoelectric Properties of SnTe *via* Synergistic Band Engineering and Structure Engineering

-Published as **Moshwan *et al.*,** Realizing High Thermoelectric Properties of SnTe *Via* Synergistic Band Engineering and Structure Engineering. *Nano Energy* **2019,** *65*, 104056.
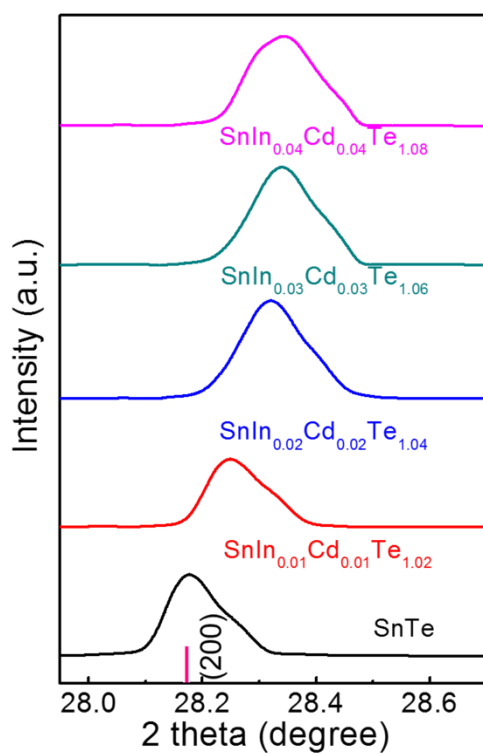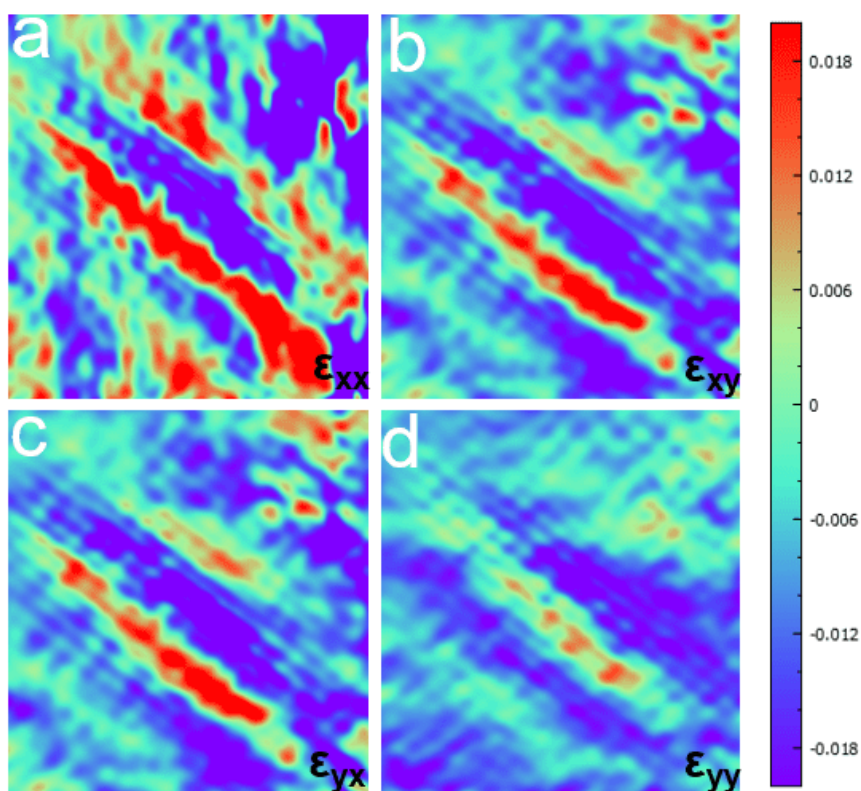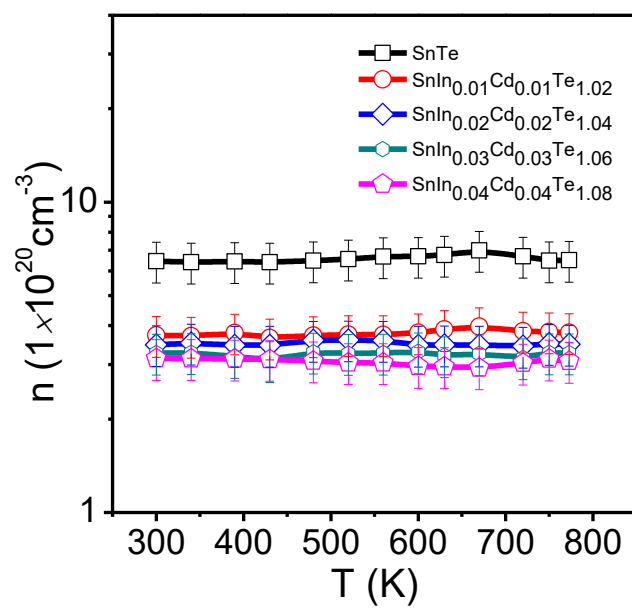
Full paper

Realizing high thermoelectric properties of SnTe *via* synergistic band engineering and structure engineering

Raza Moshwan[a], Wei-Di Liu[a], Xiao-Lei Shi[a,b], Yun-Peng Wang[d,e], Jin Zou[a,c,**], Zhi-Gang Chen[b,a,*]

[a] *Materials Engineering, The University of Queensland, St Lucia, QLD, 4072, Australia*
[b] *Centre for Future Materials, The University of Southern Queensland, Springfield Central, QLD, 4300, Australia*
[c] *Centre for Microscopy and Microanalysis, The University of Queensland, St Lucia, QLD, 4072, Australia*
[d] *School of Physics and Electronics, Hunan Key Laboratory for Super-micro Structure and Ultrafast Process, Central South University, 932 South Lushan Road, Changsha, PR China*
[e] *Department of Physics and Astronomy, Vanderbilt University, Nashville, TN, 37235, United States*

6.1 Publication

6.1.1 Abstract

Lead-free tin telluride (SnTe) has been drawn enormous attention recently due to their potential applications in the mid-temperature thermoelectric power generation. In this study, we systematic investigated the thermoelectric properties of In/Sr co-doped SnTe *via* first principles density functional theory calculation, coupled with extensive structural characterizations and property measurements. From which, we found that the co-doping of In and Sr in SnTe can significantly improve the electrical transport properties through unique interplay of band structure modifications, and the reduced lattice thermal conductivity can be achieved *via* strong phonon scattering by point defects, nanoprecipitates, and grain boundaries. Consequently, a record high power factor of ~ 33.88 $\mu Wcm^{-1}K^{-2}$ and a peak figure of merit of ~ 1.31 has been achieved at 823 K for the $Sn_{0.925}In_{0.025}Sr_{0.05}Te$ pellet. This study indicates that In/Sr co-doping can effectively make incorporation of resonant levels, band degeneracy, band gap tuning and nanostructuring, leading to the achieving high thermoelectric performance of SnTe material.

6.1.2 Introduction

Due to the continuing depletion of non-renewable energy sources, seeking new types of clean energy has become a major pursuit.[1] Thermoelectric materials, having the capability of directly converting large-scale untapped-waste heat into electricity, have been a promising solution for clean and sustainable energy technology.[2] The efficiency of thermoelectric energy conversion is generally expressed by the dimensionless figure of merit ZT, defined as

$$ZT = \frac{S^2\sigma}{\kappa}T = \frac{S^2\sigma}{\kappa_e + \kappa_l}T$$

(6-1)

where S, σ, T, κ_e, and κ_l are the Seebeck coefficient, electrical conductivity, absolute temperature, and electrical and lattice components of the total thermal conductivity (κ), respectively. A high ZT demands high S and σ, and low κ_e and κ_l.[3] Hence, the concurrent increase in power factor ($S^2\sigma$) and decrease in κ are key factors to achieve high ZT in a particular material system. A number of theoretical and experimental efforts have been made so far to enhance $S^2\sigma$ through band engineering,[4-9] and carrier concentration optimization.[10-13] κ can be reduced *via* broadband phonon scattering including nanostructuring,[14-19] all-scale

hierarchical nano/meso-architecturing,[20-23] bond anharmonicity,[24-25] defects engineering,[26-27] porous design,[28-30] and phonon-phonon interaction.[31]

Lead-free SnTe-based alloys have been widely investigated in recent years as analogues of PbTe thermoelectric material due to the fact that they have identical crystal structure and similar electronic band structure. The intrinsic high hole carrier concentration (n, ~10^{20} to 10^{21} cm^{-3}) that leads to high κ_e, and the large energy separation (~0.3-0.4 eV) between two valence bands (light hole and heavy hole) that results in low S, are the two major issues that hinder the potential of pure SnTe for thermoelectric applications.[1, 32-36] Many efforts have been carried out to improve the electrical and thermal transport properties of SnTe. For instance, Banik et al. suggested significant valence band convergence in SnTe by Ag,[34] Mg [33] doping. Tan *et al.* deployed Hg,[36] Mn[37] and Cd[38] to tune the valence band of SnTe and ended up with enhanced S. Dopants like In is very special for SnTe which introduces resonance energy near the Fermi level and increase the density of states, in turn leading to enhanced S. The effect of resonance energy level and valence band convergence have been demonstrated in In/Cd,[39-40] In/Mg,[41] In/Mn,[42] In/Ag,[34] In/Hg,[43] In/Ca[35] co-doped SnTe systems. Significant enhancement in thermal transport properties of SnTe have been achieved by Sb [44] doping by forming and Sb-rich layered intergrowth Sn$_m$Sb$_{2n}$Te$_{3n+m}$ nanostructure in SnTe matrix. A recent study of engineering ferroelectric instability shows excellent thermal properties in Ge-alloyed SnTe.[45] Although many co-doped and single element doped systems have been reported so far, co-doping of In/Sr in SnTe has not been investigated, although Zhao *et al.*[46] experimentally reported that Sr can improve the electrical transport properties of SnTe. In addition to this, Sr is more effective than Ca to tune the band structure of SnTe as reported by Dong *et al.*[47] Bhat *et al.*[35] carried out research on In/Ca co-doped SnTe system and they found significant enhancement in S of ~ 230 µVK^{-1}. Besides, the large mass fluctuation between Sr and Sn can induce severe atomic strain in the matrix that can yield low lattice thermal conductivity to a great extent. All of these phenomena motivate us to realize the synergistic effect of Sr and In on thermoelectric performance of SnTe system.

In this study, we performed a systematic theoretical and experimental study of In/Sr co-doped SnTe. First principles density functional theory (DFT) calculations were used to investigate the impact of co-doping In/Sr on the electronic structure of SnTe. We found a significant distortion of density of states (resonance energy level) in the valence band due to In, and to some extent of valence band convergence which leads to high S over a wide temperature range. In addition, a bandgap (gap between the conduction band and valence band) opening

also takes place which is an important attribute to reduce the bipolar conduction at the elevated temperature. A facile, highly energy efficient solvothermal method was used to fabricate $Sn_{1-3x}In_xSr_{2x}Te$ (x = 0 %, 0.5 %, 1 %, 1.5 %, 2 %, 2.5 % and 3 %) samples. 1:2 (In:Sr) ratio was chosen to avoid the rapid decrease in electrical conductivity.[25] Detailed structural characterization shows that the existence of In/Sr rich nanoprecipitates in the SnTe matrix together with point defects and grain boundaries lead to a ultra-low κ_l of ~ 0.57 $Wm^{-1}K^{-1}$. The synergistic impact of resonance energy level and reduction in total thermal conductivity due to In/Sr co-doping leads to a record high $S^2\sigma$ of ~33.88 $\mu Wcm^{-1}K^{-2}$ and ZT of ~1.31 at 823 K in $Sn_{0.925}In_{0.025}Sr_{0.05}Te$. These findings demonstrate great potential of SnTe-based materials for thermoelectric power generation, and open up a new avenue for the development of high performance thermoelectrics.

6.1.3 Experimental Section

6.1.3.1 Materials Synthesis

A series of $Sn_{1-3x}In_xSr_{2x}Te$ (x = 0 %, 0.5 %, 1 %, 1.5 %, 2 %, 2.5 % and 3 %) micro size crystals were synthesized by a facile solvothermal method. Na_2TeO_3 (99.99 %), $SnCl_2 \cdot 2H_2O$ (99.99 %), $SrCl_2 \cdot 6H_2O$, (99.99 %), and $InCl_3 \cdot 4H_2O$ (97 %) were purchased from Sigma-Alrich and used as a source of Te, Sn, Sr and In, respectively. The high purity precursors were put in a solution of ethylene glycol (99.8 %) and NaOH (99.99 %) at a teflon jar according to the stoichiometric molar ratio. The resultant solutions were stirred by magnetic stirrer for several minutes. After that, the teflon jars were put into a stainless steel autoclave, sealed and then put inside a CSK thermal oven. The oven temperature was raised to 230°C and maintained for 24 h. After cooling down to room temperature, the synthesized mixtures were poured into a centrifuging tube and subjected to centrifuging machine, washed several times with absolute ethanol and distilled water. The final as-synthesized product was dried at 60 °C for 12 h.

6.1.3.2 Thermoelectric Property Measurements

The dried final powders were densified by spark plasma sintering (SPS) under vacuum in order to measure their thermoelectric properties. The SPS parameters pressure, temperature and time were set 20 MPa, 773 K and 5 minutes, respectively. The sintered pellets were polished into a coin-shaped sample with ~12 mm diameter and ~1.5 mm thickness. Thermoelectric transport properties, such as S and σ, were simultaneously measured by ZEM-3 (ULVAC) in a helium atmosphere. The temperature difference steps for the S

measurements were 10, 20 and 30 °C. The measurement of thermal transport properties thermal diffusivity (D), was carried out in a LFA 457 (NETZSCH) machine (**Figure 6.S1**). To avoid any contamination on the samples, LFA analysis was performed in an argon atmosphere. Specific heat capacity (C_p) was derived based on the previous study.[48] The density (d) of the sintered samples was determined by the Archimedes' method,[49] which gave ~96 % of the theoretical density. κ was then calculated according to the relationship of: $\kappa=DC_pd$.[25] Measurements of the carrier concentration n and mobility μ were carried out using the four-probe Vanderpauw method under a reversible magnetic field of 1.5 T.

6.1.3.3 Phase and Microscopic Characterization

Structural analysis of sintered pellets was carried out by X-ray diffraction (XRD) with Cu Kα (λ = 1.5418 Å) radiation on a Bruker D8 diffractometer. The scan rate of XRD parameters were 1.2 sec/step and 1°/min, respectively. Scanning electron microscopy (SEM, JEOL 6610, operated at 20 kV) with energy-dispersive X-ray spectroscopy (EDS) and transmission electron microscopy (TEM, Philips Tecnai F20, operated at 200 kV) were used to investigate the morphology, structure and composition of the sintered pellets. Focused-ion beam (FEI-SCIOS FIB) was used to prepare thin lamella for TEM characterization.

6.1.3.4 Computational Details of Band Structure and Density of States Calculation

First-principles band structure and density of states (DOS) calculations are performed using the VASP code,[50-51] adopting the Perdew-Burke-Ernzerhof[52] generalized gradient approximation for the exchange –correlation potential. Sn atoms in a 3×3×3 rock-salt supercell containing 54 atoms are substituted by In and Sr impurity atoms to model the In/Sr doped SnTe. The cut-off energy for the plane wave basis is set to 300 eV. A Γ-centered Monkhorst-Pack[53] 4×4×4 k-mesh is adopted to sample the first Brillouin zone. All the systems are fully relaxed before the electronic structure calculations. Spin-orbit coupling is included.

6.1.4 Results and Discussion

6.1.4.1 Electronic Band Structure Calculation

Figure 6.1 shows the calculated electronic band structure of undoped (**Figure 6.1a**), In doped (**Figure 6.1b**), Sr doped (**Figure 6.1c**), and In/Sr co-doped (**Figure 6.1d**) SnTe systems. As can be seen from **Figure 6.1a**, the principal valence band (light hole) maximum and conduction band minimum locate at L point. The heavy hole valence band appear at Γ+δ point along Γ→K direction. The band gap and the energy separation values of different SnTe systems is listed in **Table 6.S1**. As can be seen from **Table 6.S1**, the energy separation

values between two valence bands for $Sn_{27}Te_{27}$, $Sn_{26}In_1Te_{27}$, $Sn_{26}Sr_1Te_{27}$, $Sn_{24}In_1Sr_2Te_{27}$ are 0.23 eV, 0.14 eV, 0.18 eV, 0.16 eV while the band gap values are 0.14 eV, 0.19 eV, 0.28 eV, 0.18 eV, respectively. After single In doping, **Figure 6.1b** shows a significant distortion of DOS in the valence band (highlighted by red dotted elliptical circles) while single Sr doping does not show such behavior as shown in **Figure 6.1c**. The distortion of DOS which represent the resonant energy level is crucial to increase the thermopower by strong electron energy filtering.[54] Single Sr doping shows the largest band gap of 0.28 eV between two principal bands which is higher than the band gap of single In doped SnTe. Such an increased bandgap is beneficial to suppress the bipolar conduction at the elevated temperature.[36, 55-56] As we mentioned earlier, previous calculation[47] shows that Sr is more effective than Ca to reduce energy separation between two valence bands and increasing the principal band gap, Orabi *et al.*[32] and Bhat *et al.*[35] independently carried out experimental work on Ca doped and In/Ca co-doped SnTe systems and they found significant enhancement in *S* of ~ 180 µVK^{-1} and ~ 230 µVK^{-1} owing to the band convergence, and both (resonance effect and band convergence), respectively. In addition to this, the energy separation of In/Ca co-doped SnTe system is lower than the individual In or Ca doped samples while in our present work dealing with In/Sr co-doping, it relies in between single In and Sr doping, although experimental results shows high *S* at elevated temperature. One might expect the energy separation value in In/Sr co-doped system should be lower than the individual In or Sr dopant, however, in this regard, we believe more future work is necessary to understand this issue especially when dealing with complex real materials, heavy element alloys like SnTe.
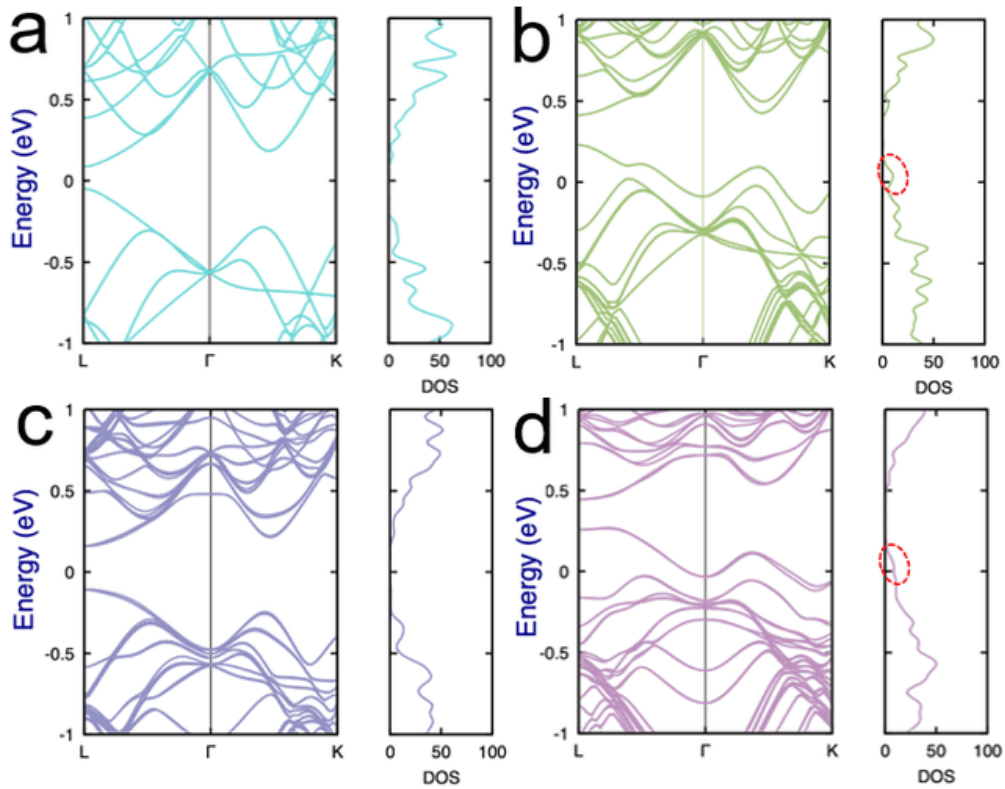
Figure 6.1 Electronic band structure and DOS of (a) $Sn_{27}Te_{27}$ (b) $Sn_{26}In_1Te_{27}$ (c) $Sn_{26}Sr_1Te_{27}$ (b) $Sn_{24}In_1Sr_2Te_{27}$ supercells as a function of wave vector in the Brillouin zone. The energies are altered with respect to the Fermi energy which is set to zero. The principal valence band (light hole) maximum and conduction band minimum occur at the L point. The heavy hole valence band appear at $\Gamma+\delta$ point along $\Gamma \rightarrow K$ direction.

6.1.4.2 Phase Compositions and Morphology

In order to investigate the phase purity of the sintered $Sn_{1-3x}In_xSr_{2x}Te$ (x = 0-0.03), we performed powder XRD analysis and the results are shown in **Figure 6.2a** and b. As can be seen from **Figure 6.2a**, the diffraction peaks can be exclusively indexed as the face-centered-cubic (FCC) structured SnTe (standard identification card, PDF #65−0239, the pink line in **Figure 6.2a**) with the lattice parameter of a = 6.32 Å and a space group of $Fm\bar{3}m$. No impurity peaks were observed, suggesting that the solvothermal synthesis can be effectively used to fabricate high-purity crystalline materials with lower energy consumption. The enlarged diffraction peaks of 222* shows a right shift with increasing the doping level up to x = 0.01 and then remain a constant, indicating a lattice shrinkage of the In/Sr co-doped SnTe samples. It should be noted that the ionic radius of Sr^{2+} (118 pm) is similar to the ionic radius of Sn^{2+} (118 pm). Hence, there is no obvious effect of Sr on the lattice parameter of SnTe and the lattice changing should be mainly attributed to the In doping because the ionic radius of

substitute In^{3+} (80 pm) is smaller than the substituted Sn^{2+} (118 pm) atoms. It should be noted that the solubility of In in SnTe is less than 1%,[37, 57] in agreement with our observation, i.e. there is no further lattice shift for In concentration above 1 at%. **Figure 6.2c** shows the typical SEM image of sintered and as-synthesized $Sn_{0.925}In_{0.025}Sr_{0.05}Te$ sample (inset). The as-synthesized samples have traditional octahedral-shape crystals with eight {111} planes. It should be noted that the low surface energy and the inherent Sn vacancies are responsible to form {111} instead of {100} planes.[25] **Figure 6.2(d-g)** shows respectively the EDS mapping analysis of Sn, Te, In and Sr elements, in which In and Sr are found in the matrix. **Figure 6.2h** is the typical EDS spectrum profile and shows the In and Sr peaks and its quantitative composition is presented in **Table 6.S2**, which is close to nominal values.
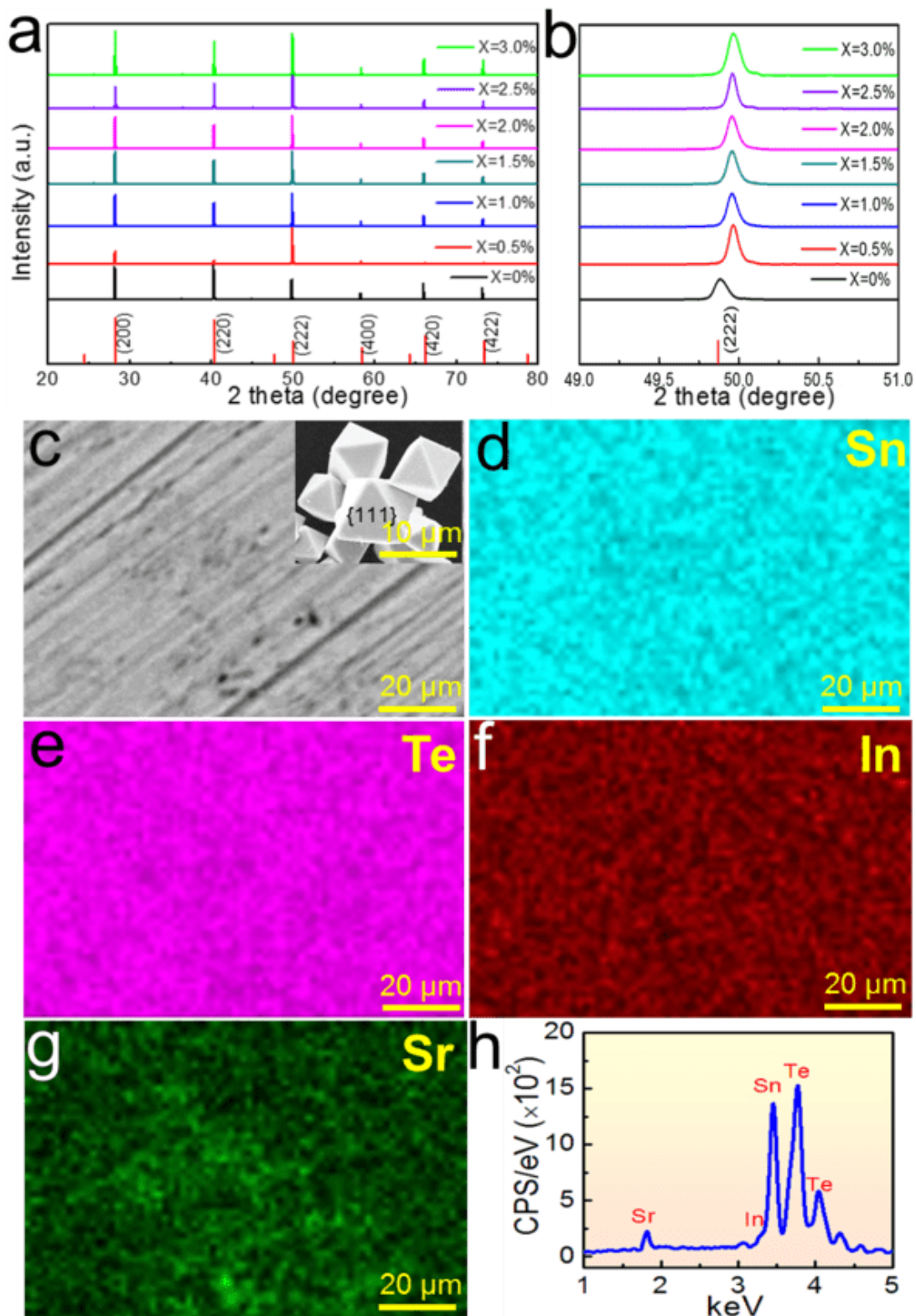
Figure 6.2 (a) XRD patterns of the sintered samples. (b) Extended (222) peaks of $Sn_{1-3x}In_xSr_{2x}Te$ (x = 0 %, 0.5 %, 1 %, 1.5 %, 2 %, 2.5 % and 3 %). (c) SEM micrograph of typical $Sn_{0.925}In_{0.025}Sr_{0.05}Te$ sample (inset is the solvothermally as-synthesized micro-crystals) and

corresponding (d-g) EDS mapping analysis of Sn, Te, In and Sr, respectively. (h) EDS spectrum shows the existence of Sr and In in the SnTe matrix.

6.1.4.3 Electronic Transport Properties

In order to evaluate the thermoelectric performance of In/Sr co-doped SnTe samples, the temperature-dependent electrical and thermal transport properties were measured in the range of 300 to 823 K. **Figure 6.3a** is the temperature-dependent σ of as-sintered $Sn_{1-3x}In_xSr_{2x}Te$ pellets, and shows that σ decreases gradually with increasing temperature, which is different from the reported sudden drop.[25] The gradual decrease in σ may be attributed to the In/Sr co-doping, resulting in the deterioration of Sn vacancies caused by the donor In (In $\rightarrow In^{3+}$+ 3e⁻) and the decreased μ (verified by the Hall measurement and will be discussed later). At room-temperature, σ decreases from 7240 S cm⁻¹ of undoped SnTe to 2459 S cm⁻¹ of $Sn_{0.091}In_{0.03}Sr_{0.06}Te$ with increasing the In/Sr concentration. The σ reduction with increasing the temperature shows a typical degenerated behavior of semiconductors.[25, 32-33, 57] **Figure 6.3b** represents the temperature-dependent S of $Sn_{1-3x}In_xSr_{2x}Te$ samples. Significant S enhancement both at room temperature and high temperature has been achieved by In/Sr co-doping. The positive value of S indicates the majority charge carrier is hole so as the p-type nature. The room-temperature S for the undoped SnTe is ~23 µVK⁻¹, which is then enormously enhanced to ~81 µVK⁻¹ for $Sn_{0.925}In_{0.025}Sr_{0.05}Te$. At high temperature (823 K), S is increased from ~95 µVK⁻¹ for undoped SnTe to ~175 µVK⁻¹ for $Sn_{0.925}In_{0.025}Sr_{0.05}Te$. Such a S enhancement in $Sn_{1-3x}In_xSr_{2x}Te$ may be attributed to the significant resonance effect of In and to some extent of band convergence of heavy hole and light hole valence bands induced by In and/or Sr co-doping. The resonance effect increases DOS near the Fermi level in the valence band that leads to the S increase based on the equation of,[25] $S = \frac{\pi^2}{3}\frac{\kappa_B}{q}k_BT[\frac{g(E)}{n(E)} + \frac{1}{\mu E}\frac{d\mu(E)}{dE}]$, where q is the electron charge, k_B is the Boltzmann constant, and *g(E)* is the DOS. The convergence of two valence bands facilitates the heavy hole valence band to participate in the electron-hole transport system and thereby increases S. Similar effects have been observed so far for the In/Cd,[40] In/Hg,[43] In/Mn,[42] In/Se [58] and In/Ag[34] doped SnTe systems. **Figure 6.3c** shows the calculated temperature-dependent $S^2\sigma$ of $Sn_{1-3x}In_xSr_{2x}Te$ samples. Comparing with the undoped SnTe, $S^2\sigma$ of In/Sr co-doped samples are significantly improved in the entire temperature range from 300 to 823 K. A peak $S^2\sigma$ value of ~33.88 µWcm⁻¹K⁻² at 823 K is observed in $Sn_{0.925}In_{0.025}Sr_{0.05}Te$. This value is 121 % higher than that of the undoped SnTe sample at 823 K. In order to understand

the valence band convergence and band gap enlargement, we schematically illustrate a diagram in **Figure 6.3d**. As stated earlier, when In/Sr co-doped with SnTe, the energy gap between two valence bands is reduced from 0.23 eV to 0.16 eV that allow heavy hole valence band to participate in the electron-hole transport system as shown by red wave-like arrow. In addition, the principal band gap is increased form 0.14 eV to 0.18 eV that help to suppress the bipolar conduction at the high temperature.
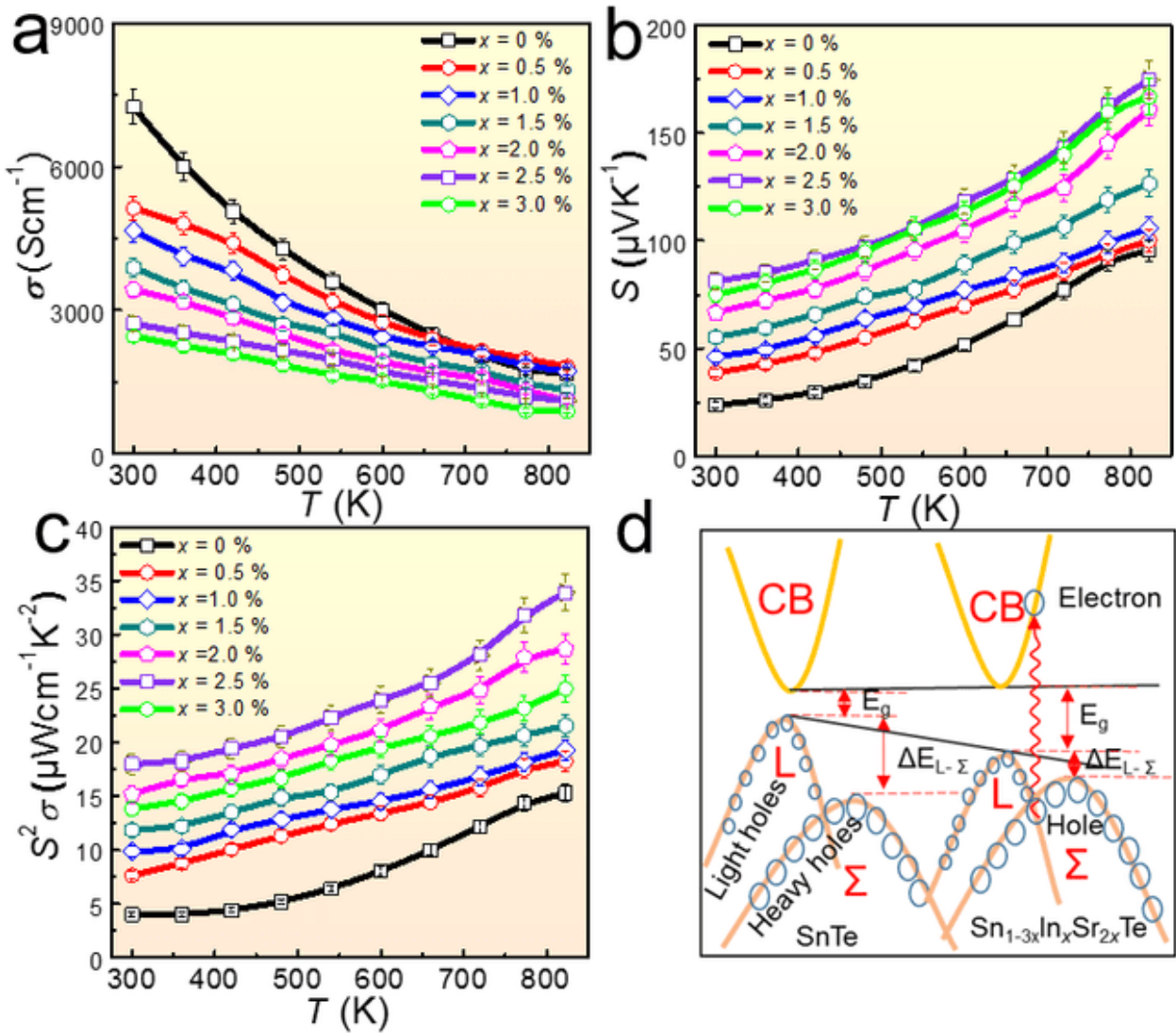
Figure 6.3 Temperature-dependent electrical transport properties of sintered $Sn_{1-3x}In_xSr_{2x}Te$ (x = 0 %, 0.5 %, 1 %, 1.5 %, 2 %, 2.5 % and 3 %) samples: (a) σ, (b) S, (c) $S^2\sigma$. (error bar: 5 %) (d) Schematic illustration of band convergence in SnTe due to In/Sr co-doping; CB = conduction band, Eg = band gap, $\Delta E_{L-\Sigma}$ = energy separation between light hole and heavy hole valence bands.

6.1.4.4 Thermal Transport Properties

Figure 6.4 shows the temperature-dependent thermal transport properties of In/Sr co-doped SnTe samples. **Figure 6.4a** shows κ of $Sn_{1-3x}In_xSr_{2x}Te$ as a function of the temperature, in which a significant κ reduction is seen with increasing the temperature, as well as with increasing the doping concentration. The room-temperature κ is ~8.5 W m^{-1} K^{-1} of undoped SnTe and then significantly reduces to ~3.15 W m^{-1} K^{-1} after In/Sr co-doping. The lowest κ of ~1.84 W m^{-1} K^{-1} at 823 K is obtained for $Sn_{0.91}In_{0.03}Sr_{0.06}Te$. This value is 49 % reduction over undoped SnTe at the same temperature. Since κ is the sum of κ_e and κ_l, we calculated κ_e using the Wiedemann-Franz law $\kappa_e = L\sigma T$,[59] where L is the Lorenz number and their values (**Figure S**2) for $Sn_{1-3x}In_xSr_{2x}Te$ samples can be estimated using the following equation,[59]

$$L = 1.5 + \exp\left(-\frac{|S|}{116}\right)$$

(6-2)

By deducting κ_e (**Figure 6.S3**) from κ, we obtained κ_l and the results are shown in **Figure 6.4b**. As can be seen, the κ_l values of all the In/Sr co-doped samples gradually reduce with increasing the temperature. The lowest κ_l of ~ 0.57 W m^{-1} K^{-1} at 823 K is obtained in $Sn_{0.925}In_{0.025}Sr_{0.05}Te$, which is far below that of undoped SnTe at this temperature. To elucidate such a low κ_l value in In/Sr co-doped SnTe samples, we use the Debye-Callaway model[60-61] by considering four dominant scattering mechanism, including Umklapp (U) phonon scattering, grain boundary (GB) phonon scattering, point defect (PD) phonon scattering and nanoprecipitates (NP) phonon scattering. According to the Debye-Callaway model, κ_l can be calculated by

$$\kappa_l = \frac{k_B}{2\pi^2 \upsilon}\left(\frac{k_B T}{\hbar}\right)^3 \int_0^{\frac{\theta_D}{T}} \tau_{tot} \frac{z^4 \exp(z)}{\left[\exp(z)-1\right]^2} dz$$

(6-3)

The integrand item in conjunction with the coefficient of the above equation is the spectral lattice thermal conductivity (κ_s) [62], namely

$$\kappa_s = \frac{k_B}{2\pi^2 \upsilon}\left(\frac{k_B T}{\hbar}\right)^3 \tau_{tot} \frac{z^4 \exp(z)}{\left[\exp(z)-1\right]^2}$$

(6-4)

where $z = \dfrac{\hbar \omega}{k_B T}$ (ω is the phonon frequency) is the reduced phonon frequency, $\hbar$ is the

reduced Plank constant, θ_D is the Debye temperature, $\upsilon = \left[\dfrac{1}{3}\left(\dfrac{1}{\upsilon_L^3} + \dfrac{2}{\upsilon_T^3} \right) \right]^{-1/3}$ (υ_L and υ_T are

the longitudinal and transverse sound velocities, respectively) is the sound velocity, and τ_{tot}

is the total relaxation time. The phonon scattering pathways generally comprised of phonon-

phonon Umklapp (U), grain boundaries (GB), point defects (PD), and nanoprecipitates (NP).

The relevant phonon relaxation times can be expressed as follows,

Umklapp phonon scattering,

$$\tau_U^{-1} = \frac{\hbar \gamma^2 \omega^2 T}{\overline{M} \upsilon^2 \theta_D} \exp\left(-\frac{\theta_D}{3T} \right),$$
(6-5)

Grain boundary phonon scattering,

$$\tau_{GB}^{-1} = \frac{\upsilon}{G_d},$$
(6-6)

Point defect phonon scattering,

$$\tau_{PD}^{-1} = \frac{\overline{V} \omega^4}{4\pi \upsilon^3} \Gamma, \text{ and}$$
(6-7)

Nano precipitates phonon scattering,

$$\tau_{NP}^{-1} = \upsilon \left[(2\pi R)^{-1} + \left(\pi R^2 \frac{4}{9} \left(\frac{\Delta d}{M_d} \right)^2 \left(\frac{\omega R}{\upsilon} \right)^4 \right)^{-1} \right]^{-1} N_P$$
(6-8)

In the above equations, γ is the Grüneisen parameter, $\overline{V}$ is the average atomic volume, $\overline{M}$ is

the average atomic mass, Γ is the point defect scattering parameter, G_d is the grain size, R

is the average radius for the precipitates, M_d is the matrix density, Δd is the density difference

between the precipitate and matrix, and N_p is the number density of precipitates, respectively.

The parameters for our phonon modeling studies is listed in **Table 6.S3**. The values of κ_s with

respect to the phonon frequency (ω) at 300 K is shown in **Figure 6.4c**. Typically there are

three regions; I, II and III. Since κ_s correspond to κ_l, thereby the area between U and U+GB

reflects the κ_l reduction due to grain boundaries. The region II is the area between U+GB and

U+GB+PD, representing the κ_l reduction due to high frequency phonons scattering by point

defects. The region III shows the κ_l reduction caused by the mid-frequency phonons

scattering due to the nanoprecipitates. Overall, the combination of point defects, grain boundaries and nanoprecipitates significantly reduced κ_l of In/Sr co-doped samples. **Figure 6.4d** shows a schematic illustration of different phonon scattering mechanisms where high frequency phonon scattered by point defects (phonon mean free path, MFP less than 1 nm), medium frequency phonon scattered by nanoprecipitates (MFP of 1-10 nm) and the low frequency phonons (MFP of 10-1000 nm) scattered by grain boundaries.[25, 63]

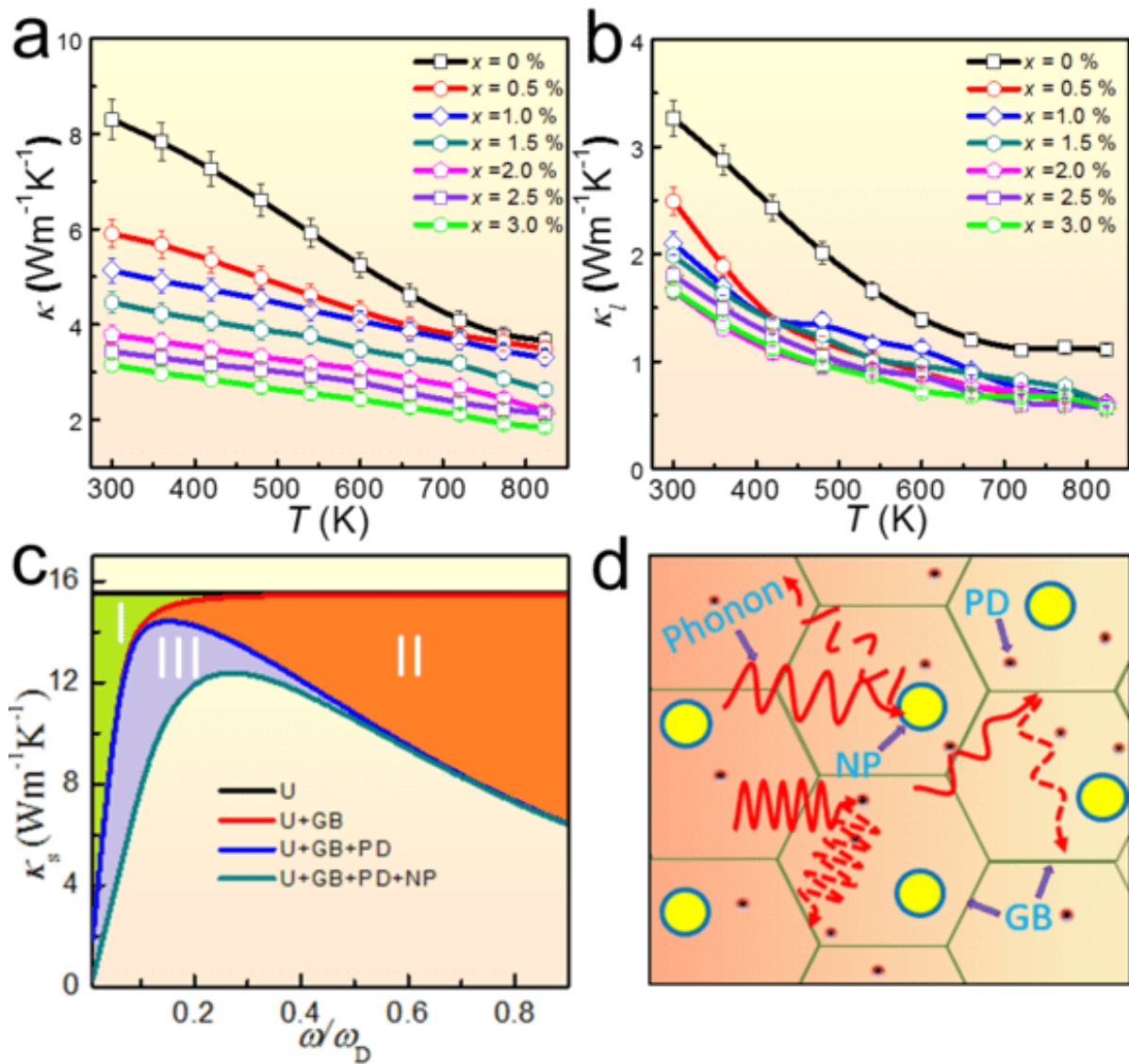

Figure 6.4 Temperature-dependent thermal transport properties of sintered $Sn_{1-3x}In_xSr_{2x}Te$ ($x = 0$ %, 0.5 %, 1 %, 1.5 %, 2 %, 2.5 % and 3 %) samples (a) κ, (b) κ_l. (error limit is 5 %) (c) Calculated spectral lattice thermal conductivity (κ_s) using Debye-Callaway model at 300 K. (d) Schematic illustration of various phonon scattering mechanisms in In/Sr co-doped SnTe system, PD (point defect), NP (nanoprecipitates), GB (grain boundaries).

6.1.4.5 Transmission Electron Microscopy Characterization

In order to understand the κ_l reduction in SnTe caused by the nanostructures, we further performed TEM analysis. **Figure 6.5a** is a typical TEM image of the $Sn_{0.925}In_{0.025}Sr_{0.05}Te$ sample (inset is its low magnification TEM image) and **Figure 6.5b** is its corresponding selected area electron diffraction (SAED) along the [001] zone-axis. As can be seen, there exist lattice defects in the sample which can play the same role as the grain boundaries to scatter low frequency heat carrying phonons.[27] **Figure 6.5c** is high resolution TEM image and shows that numerous nanoprecipitates with a size ranging from ~10 to 15 nm in $Sn_{0.925}In_{0.025}Sr_{0.05}Te$ matrix. In our SEM-EDS analysis, we have observed significant In and Sr peaks along with the matrix peaks which indicates nanoprecipitates are must be in In/Sr rich. It can be noted that the size of the nanoprecipitates are much smaller than the interaction volume of EDS detection which makes it difficult to eliminate signal from the matrix. **Figure 6.5d** shows that a typical nanoprecipitate generates a strain field in the matrix, and the inset showing the strain map (obtained by geometrical phase analysis). The color contrast clearly displays the high strain concentration around the nanoprecipitate area. Similar strain distributions have been observed in $PbTe-SrTe$[64] and $AgPb_{18}SbTe_{20}$[65] systems. These strains are responsible to impede the circulation of heat carrying phonons to a large extent and yield low κ_l in our material system. Carruthers[66-67] also reported that it is possible to reduce κ up to three orders of magnitude *via* proper tuning the strain field.
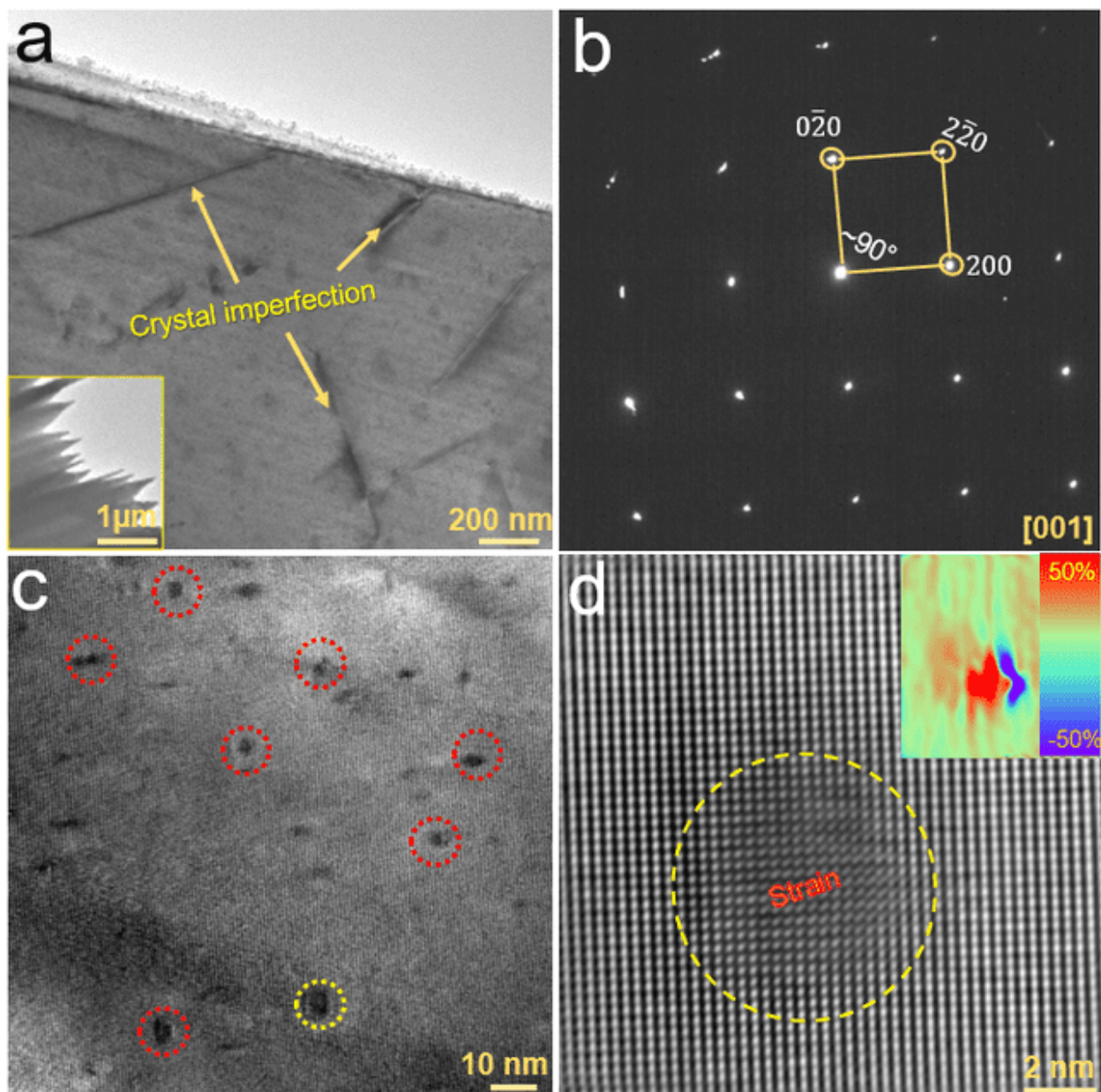
Figure 6.5 (a) Typical bright field TEM image of $Sn_{0.925}In_{0.025}Sr_{0.05}Te$ sintered sample shows multiple crystal imperfection (inset is the low magnification TEM image). (b) Selected area electron diffraction (SAED) pattern along [001] zone axis (c) High resolution transmission electron microscopy (HRTEM) image showing numerous nanoprecipitates in SnTe matrix (d) Enlarged view of a nanoprecipitate shows strain and inset is the calculated strain map associated with the nanoprecipitate.

6.1.4.6 Evaluation of Hall Carrier and Overall *ZT*

In order to understand the improved electrical transport properties, we further evaluated temperature-dependent *n* and *μ*, and the results are plotted in **Figure 6.6a** and **Figure 6.6b**. As can be seen, *n* decreases from ~6.45 × 10^{20} cm^{-3} of undoped SnTe to ~5.35 × 10^{20} cm^{-3}

of $Sn_{0.91}In_{0.03}Sr_{0.06}Te$ at room temperature. The electron donor-acceptor pair due to In and Sr co-doping prohibits the n reduction in a great extent. There is no remarkable changes in n with respect to temperature for the corresponded doping concentration (**Figure 6.6a**). However, μ is significantly reduced for all the doped samples with respect to undoped SnTe. As can be seen, the room-temperature μ is reduced from ~71.2 $cm^2v^{-1}s^{-1}$ of undoped SnTe to ~10.44 $cm^2v^{-1}s^{-1}$ of $Sn_{0.91}In_{0.03}Sr_{0.06}Te$. This may be attributed to the increase of the carrier effective mass, acoustic phonon scattering and grain boundary scattering.[33, 39]

The synergistic $S^2\sigma$ increase and κ decrease can effectively improve ZT values and the calculated value are shown in **Figure 6.6c** and **Figure 6.6d**. As can be seem, the maximum ZT value obtained in this study is ~1.31 at 823 K. This value is much higher than the previously reported co-doped systems; In/Cd (~0.97).[40] In/Hg (~0.78),[43] In/Mn (1.13),[42] In/Se (0.72)[68] and In/Ag (~0.92)[68] at the same temperature. It can be noted that thermoelectric conversion efficiency of a thermoelectric generator (TEG) can be determined from its material average ZT (ZT_{ave}) by the following relationship, $\eta = \frac{T_h - T_c}{T_h} \left[\frac{\sqrt{1+ZT_{ave}} - 1}{\sqrt{1+ZT_{ave}} + \frac{T_c}{T_h}} \right]$, where T_h and T_c are the hot side and cold side temperatures.[32, 46, 69] The ZT_{ave} of our In/Sr co-doped SnTe materials can be obtained from the expression, $ZT_{ave} = \frac{1}{T_h - T_c} \int_{T_c}^{T_h} ZT dT$.[46] **Figure 6.S4** plots a detailed comparison of our ZT_{ave} (~ 0.58) and a few reported values.[33, 36, 38, 40, 57, 68] Obvious our ZT_{ave} value is better than some of the reported work. A TEG efficiency can be achieved up to 9.9 % for our samples within a temperature difference between 300 K and 823 K. Our current study suggests the appropriate dopant ratio (1:2 for In:Sr in this study) can give rise to an appreciable ZT enhancement. Also, the synergistic band engineering and structure engineering can be a key strategy to develop high-performance thermoelectric materials.
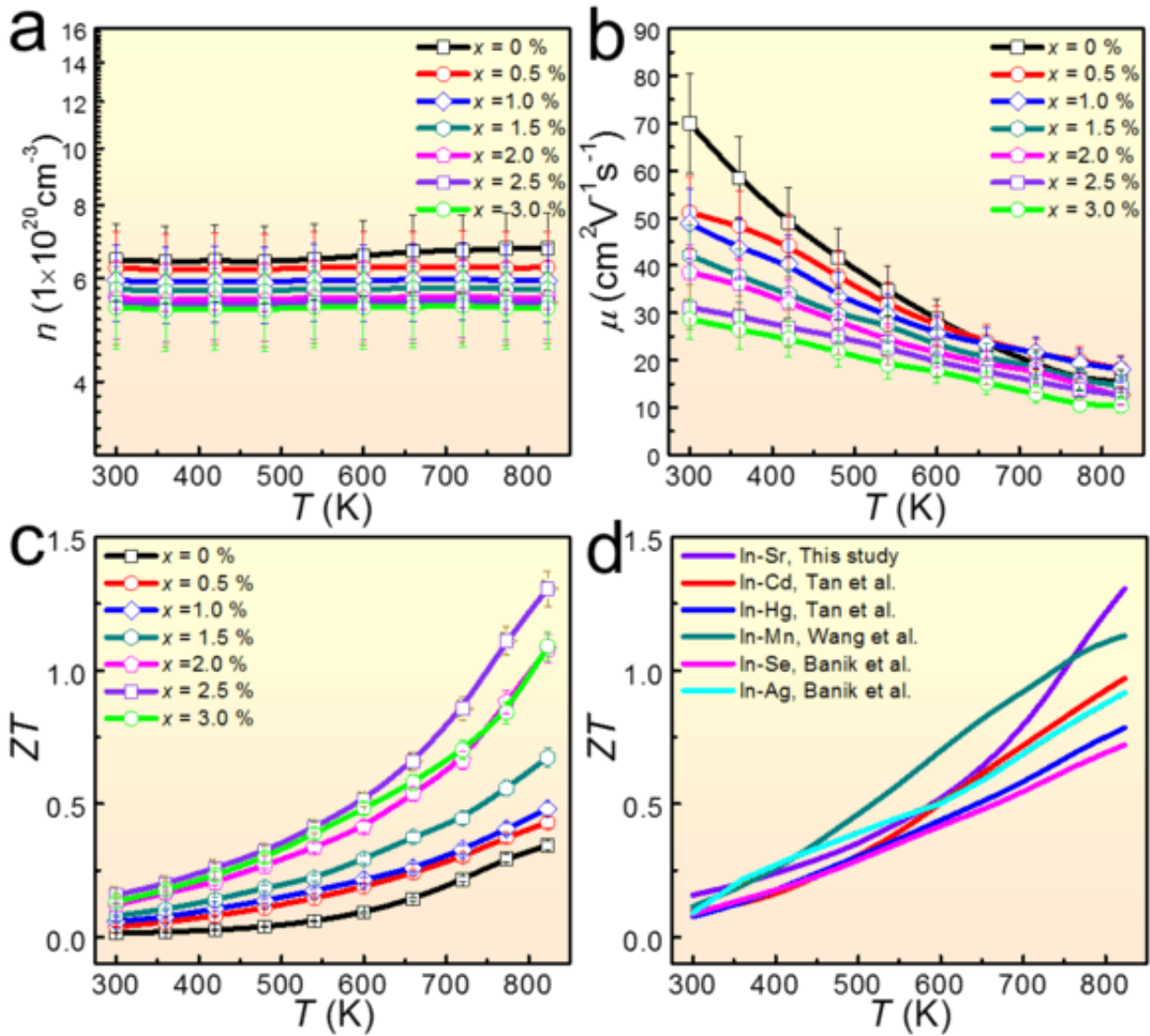
Figure 6.6 (a) Temperature dependent (a) n (error limit is 15 %) (c) μ, and (c) ZT values of Sn$_{1-3x}$In$_x$Sr$_{2x}$Te (x = 0 %, 0.5 %, 1 %, 1.5 %, 2 %, 2.5 % and 3 %) samples (error limit is 5 %) (b) A comparative thermoelectric performance of the current work and the previously reported results.[34, 40, 42-43, 68]

6.1.5 Conclusion

In this study, we obtained extraordinary thermoelectric properties in In/Sr co-doped SnTe materials, fabricated by facile, low-cost and highly energy efficient solvothermal method. Theoretical calculations demonstrate that the In/Sr co-doping can significantly introduces resonance energy level near the Fermi level in the valence band and reduce the energy separation between two valence bands to some extent from 0.23 eV to 0.16 eV and. The combination of electron donor/acceptor pairs by In/Sr co-doping significantly improve the

electrical transport properties in a wide temperature range. Such unique characteristic leads to a record $S^2\sigma$ of ~31.88 μWcm^{-1}K^{-2} at 823 K, which is 121 % higher than that of the undoped SnTe. Microstructure characterization shows that numerous nanoprecipitates and grain boundaries are dispersed in the SnTe matrix, leading to lower lattice thermal conductivity in all the In/Sr co-doped samples. The co-existence of band engineering and structure engineering due to In/Sr co-doping results in a peak ZT of ~1.31 at 823 K, which is 364 % higher than the peak ZT found in the undoped SnTe at the same temperature. These fascinating strategies show a promising pathway to develop high performance SnTe-based thermoelectric materials and can be extended to other materials as well.

Acknowledgement

References

(1) Moshwan, R.; Yang, L.; Zou, J.; Chen, Z.-G. *Adv. Funct. Mater.* **2017**, *27*, 1703278.

(2) Chen, Z.-G.; Han, G.; Yang, L.; Cheng, L.; Zou, J. *Prog. Nat. Sci.* **2012**, *22*, 535-549.

(3) Zhu, T.; Liu, Y.; Fu, C.; Heremans, J. P.; Snyder, J. G.; Zhao, X. *Adv. Mater.* **2017**, 1605884.

(4) Fu, C.; Zhu, T.; Liu, Y.; Xie, H.; Zhao, X. *Energy Environ. Sci.* **2015**, *8*, 216-220.

(5) He, J.; Tan, X.; Xu, J.; Liu, G.-Q.; Shao, H.; Fu, Y.; Wang, X.; Liu, Z.; Xu, J.; Jiang, H.; Jiang, J. *J. Mater. Chem. A* **2015**, *3*, 19974-19979.

(6) Pei, Y.; Shi, X.; LaLonde, A.; Wang, H.; Chen, L.; Snyder, G. J. *Nature* **2011**, *473*, 66-69.

(7) Pei, Y.; Wang, H.; Snyder, G. J. *Adv. Mater.* **2012**, *24*, 6125-6135.

(8) Xiaojian, T.; Hezhu, S.; Tianqi, H.; Guo-Qiang, L.; Shang-Fen, R. *J. Phys. Condens. Mat.* **2015**, *27*, 095501.

(9) Hong, M.; Chen, Z.-G.; Pei, Y.; Yang, L.; Zou, J. *Phys. Rev. B* **2016**, *94*, 161201.

(10) Krez, J.; Schmitt, J.; Jeffrey Snyder, G.; Felser, C.; Hermes, W.; Schwind, M. *J. Mater. Chem. A* **2014**, *2*, 13513-13518.

(11) Li, J.; Chen, Z.; Zhang, X.; Yu, H.; Wu, Z.; Xie, H.; Chen, Y.; Pei, Y. *Adv. Sci.* **2017**, *4*, 1700341.

(12) Pei, Y.; LaLonde, A. D.; Heinz, N. A.; Shi, X.; Iwanaga, S.; Wang, H.; Chen, L.; Snyder, G. J. *Adv. Mater.* **2011**, *23*, 5674-5678.

(13) Rausch, E.; Balke, B.; Deschauer, T.; Ouardi, S.; Felser, C. *APL Mater.* **2015**, *3*, 041516.

(14) Guin, S. N.; Negi, D. S.; Datta, R.; Biswas, K. *J. Mater. Chem. A* **2014**, *2*, 4324-4331.

(15) Cook, B. A.; Kramer, M. J.; Harringa, J. L.; Han, M.-K.; Chung, D.-Y.; Kanatzidis, M. G. *Adv. Funct. Mater.* **2009**, *19*, 1254-1259.

(16) Han, M.-K.; Hoang, K.; Kong, H.; Pcionek, R.; Uher, C.; Paraskevopoulos, K. M.; Mahanti, S. D.; Kanatzidis, M. G. *Chem. Mater.* **2008**, *20*, 3512-3520.

(17) Lan, J.-L.; Liu, Y.; Lin, Y.-H.; Nan, C.-W.; Cai, Q.; Yang, X. *Sci. Rep.* **2015**, *5*, 7783.

(18) Quarez, E.; Hsu, K.-F.; Pcionek, R.; Frangis, N.; Polychroniadis, E. K.; Kanatzidis, M. G. *J. Am. Chem. Soc.* **2005**, *127*, 9177-9190.

(19) Zhao, L.-D.; He, J.; Hao, S.; Wu, C.-I.; Hogan, T. P.; Wolverton, C.; Dravid, V. P.; Kanatzidis, M. G. *J. Am. Chem. Soc.* **2012**, *134*, 16327-16336.

(20) Bhattacharya, S.; Bohra, A.; Basu, R.; Bhatt, R.; Ahmad, S.; Meshram, K. N.; Debnath, A. K.; Singh, A.; Sarkar, S. K.; Navneethan, M.; Hayakawa, Y.; Aswal, D. K.; Gupta, S. K. *J. Mater. Chem. A* **2014**, *2*, 17122-17129.

(21) Biswas, K.; He, J.; Blum, I. D.; Wu, C.-I.; Hogan, T. P.; Seidman, D. N.; Dravid, V. P.; Kanatzidis, M. G. *Nature* **2012**, *489*, 414-418.

(22) Lee, Y.; Lo, S.-H.; Androulakis, J.; Wu, C.-I.; Zhao, L.-D.; Chung, D.-Y.; Hogan, T. P.; Dravid, V. P.; Kanatzidis, M. G. *J. Am. Chem. Soc.* **2013**, *135*, 5152-5160.

(23) Zhao, L. D.; Wu, H. J.; Hao, S. Q.; Wu, C. I.; Zhou, X. Y.; Biswas, K.; He, J. Q.; Hogan, T. P.; Uher, C.; Wolverton, C.; Dravid, V. P.; Kanatzidis, M. G. *Energy Environ. Sci.* **2013**, *6*, 3346-3355.

(24) Li, C. W.; Ma, J.; Cao, H. B.; May, A. F.; Abernathy, D. L.; Ehlers, G.; Hoffmann, C.; Wang, X.; Hong, T.; Huq, A.; Gourdon, O.; Delaire, O. *Phys. Rev. B* **2014**, *90*, 214303.

(25) Moshwan, R.; Shi, X.-L.; Liu, W.-D.; Wang, Y.; Xu, S.; Zou, J.; Chen, Z.-G. *ACS Appl. Energy Mater.* **2019**, *2*, 2965-2971.

(26) Lee, M. H.; Byeon, D.-G.; Rhyee, J.-S.; Ryu, B. *J. Mater. Chem. A* **2017**, *5*, 2235-2242.

(27) Shi, X.; Zheng, K.; Hong, M.; Liu, W.; Moshwan, R.; Wang, Y.; Qu, X.; Chen, Z.-G.; Zou, J. *Chem. Sci.* **2018**, *9*, 7376-7389.

(28) Liu, W.; Shi, X.; Moshwan, R.; Hong, M.; Yang, L.; Chen, Z.-G.; Zou, J. *Sustainable Mater.Technol.* **2018**, *17*, e00076.

(29) Shi, X.; Wu, A.; Liu, W.; Moshwan, R.; Wang, Y.; Chen, Z.-G.; Zou, J. *ACS Nano* **2018**, *12*, 11417-11425.

(30) Hong, M.; Wang, Y.; Xu, S.; Shi, X.; Chen, L.; Zou, J.; Chen, Z.-G. *Nano Energy* **2019**, *60*, 1-7.

(31) Hong, M.; Wang, Y.; Feng, T.; Sun, Q.; Xu, S.; Matsumura, S.; Pantelides, S. T.; Zou, J.; Chen, Z.-G. *J. Am. Chem. Soc.* **2019**, *141*, 1742-1748.

(32) Al Rahal Al Orabi, R.; Mecholsky, N. A.; Hwang, J.; Kim, W.; Rhyee, J. S.; Wee, D.; Fornari, M. *Chem. Mater.* **2016**, *28*, 376-384.

(33) Banik, A.; Shenoy, U. S.; Anand, S.; Waghmare, U. V.; Biswas, K. *Chem. Mater.* **2015**, *27*, 581-587.

(34) Banik, A.; Shenoy, U. S.; Saha, S.; Waghmare, U. V.; Biswas, K. *J. Am. Chem. Soc.* **2016**, *138*, 13068-13075.

(35) Bhat, D. K.; Shenoy, U. S. *Mater. Today Phys.* **2018**, *4*, 12-18.

(36) Tan, G.; Shi, F.; Doak, J. W.; Sun, H.; Zhao, L.-D.; Wang, P.; Uher, C.; Wolverton, C.; Dravid, V. P.; Kanatzidis, M. G. *Energy Environ. Sci.* **2015**, *8*, 267-277.

(37) Tan, G.; Shi, F.; Hao, S.; Chi, H.; Bailey, T. P.; Zhao, L.-D.; Uher, C.; Wolverton, C.; Dravid, V. P.; Kanatzidis, M. G. *J. Am. Chem. Soc.* **2015**, *137*, 11507-11516.

(38) Tan, G.; Zhao, L. D.; Shi, F.; Doak, J. W.; Lo, S. H.; Sun, H.; Wolverton, C.; Dravid, V. P.; Uher, C.; Kanatzidis, M. G. *J. Am. Chem. Soc.* **2014**, *136*, 7006-7017.

(39) Moshwan, R.; Shi, X.-L.; Liu, W.-D.; Yang, L.; Wang, Y.; Hong, M.; Auchterlonie, G.; Zou, J.; Chen, Z.-G. *ACS Appl. Mater. Interf.* **2018**, *10*, 38944-38952.

(40) Tan, G.; Shi, F.; Hao, S.; Chi, H.; Zhao, L.-D.; Uher, C.; Wolverton, C.; Dravid, V. P.; Kanatzidis, M. G. *J. Am. Chem. Soc.* **2015**, *137*, 5100-5112.

(41) Bhat, D. K.; Shenoy U, S. *J. Phys. Chem. C* **2017**, *121*, 7123-7130.

(42) Wang, L.; Tan, X.; Liu, G.; Xu, J.; Shao, H.; Yu, B.; Jiang, H.; Yue, S.; Jiang, J. *ACS Energy Lett.* **2017**, *2*, 1203-1207.

(43) Tan, X.; Liu, G.; Xu, J.; Tan, X.; Shao, H.; Hu, H.; Jiang, H.; Lu, Y.; Jiang, J. *J. Materiomics* **2018**, *4*, 62-67.

(44) Banik, A.; Vishal, B.; Perumal, S.; Datta, R.; Biswas, K. *Energy Environ. Sci.* **2016**, *9*, 2011-2019.

(45) Banik, A.; Ghosh, T.; Arora, R.; Dutta, M.; Pandey, J.; Acharya, S.; Soni, A.; Waghmare, U. V.; Biswas, K. *Energy Environ. Sci.* **2019**, *12*, 589-595.

(46) Zhao, L.-D.; Zhang, X.; Wu, H.; Tan, G.; Pei, Y.; Xiao, Y.; Chang, C.; Wu, D.; Chi, H.; Zheng, L.; Gong, S.; Uher, C.; He, J.; Kanatzidis, M. G. *J. Am. Chem. Soc.* **2016**, *138*, 2366-2373.

(47) Dong, X.; Yu, H.; Li, W.; Pei, Y.; Chen, Y. *J. Materiomics* **2016**, *2*, 158-164.

(48) Zhou, M.; Gibbs, Z. M.; Wang, H.; Han, Y.; Xin, C.; Li, L.; Snyder, G. *J. Phys. Chem. Chem. Phys.* **2014**, *16*, 20741-20748.

(49) Mason, B. *Geol. Foren. Stockh. Forh.* **1944**, *66*, 27-51.

(50) Kresse, G. *J. Non-cryst. Solids.* **1995**, *192-193*, 222-229.

(51) Kresse, G.; Furthmüller, J. *Phys. Rev. B* **1996**, *54*, 11169-11186.

(52) Perdew, J. P.; Burke, K.; Ernzerhof, M. *Phys. Rev. Lett.* **1996**, *77*, 3865-3868.

(53) Monkhorst, H. J.; Pack, J. D. *Phys. Rev. B* **1976**, *13*, 5188-5192.

(54) Heremans, J. P.; Wiendlocha, B.; Chamoire, A. M. *Energy Environ. Sci.* **2012**, *5*, 5510-5530.

(55) Wu, H.; Chang, C.; Feng, D.; Xiao, Y.; Zhang, X.; Pei, Y.; Zheng, L.; Wu, D.; Gong, S.; Chen, Y.; He, J.; Kanatzidis, M. G.; Zhao, L.-D. *Energy Environ. Sci.* **2015**, *8*, 3298-3312.

(56) Gong, J. J.; Hong, A. J.; Shuai, J.; Li, L.; Yan, Z. B.; Ren, Z. F.; Liu, J. M. *Phys. Chem. Chem. Phys.* **2016**, *18*, 16566-16574.

(57) Zhang, Q.; Liao, B.; Lan, Y.; Lukas, K.; Liu, W.; Esfarjani, K.; Opeil, C.; Broido, D.; Chen, G.; Ren, Z. *Proc. Natl. Acad. Sci.* **2013**, *110*, 13261-13266.

(58) Wang, H.; Wang, T.; Hwang, J.; Su, W.; Kim, H.; Zhai, J.; Wang, X.; Wang, C.; Kim, W. *Inorg. Chem. Front.* **2018**, *5*, 793-801.

(59) Kim, H.-S.; Gibbs, Z. M.; Tang, Y.; Wang, H.; Snyder, G. J. *APL Mater.* **2015**, *3*, 041506.

(60) Callaway, J.; von Baeyer, H. C. *Phys. Rev.* **1960**, *120*, 1149-1154.

(61) Bessas, D.; Sergueev, I.; Wille, H. C.; Perßon, J.; Ebling, D.; Hermann, R. P. *Phys. Rev. B* **2012**, *86*, 224301.

(62) Zhu, T. J.; Fu, C. G.; Xie, H. H.; Liu, Y. T.; Feng, B.; Xie, J.; Zhao, X. B. *Europhys. Lett.* **2013**, *104*, 46003.

(63) Tan, G.; Zhao, L.-D.; Kanatzidis, M. G. *Chem. Rev.* **2016**, *116*, 12123-12149.

(64) Biswas, K.; He, J.; Zhang, Q.; Wang, G.; Uher, C.; Dravid, V. P.; Kanatzidis, M. G. *Nat. Chem.* **2011**, *3*, 160-166.

(65) Wu, L.; Zheng, J.-C.; Zhou, J.; Li, Q.; Yang, J.; Zhu, Y. *J. Appl. Phys.* **2009**, *105*, 094317.

(66) Carruthers, P. *Phys. Rev.* **1959**, *114*, 995-1001.

(67) Carruthers, P. *Rev. Mod. Phys.* **1961**, *33*, 92-138.

(68) Banik, A.; Biswas, K. *J. Mater. Chem. A* **2014**, *2*, 9620-9625.

(69) Zhu, H.; He, R.; Mao, J.; Zhu, Q.; Li, C.; Sun, J.; Ren, W.; Wang, Y.; Liu, Z.; Tang, Z.; Sotnikov, A.; Wang, Z.; Broido, D.; Singh, D. J.; Chen, G.; Nielsch, K.; Ren, Z. *Nat. Commun.* **2018**, *9*, 2497

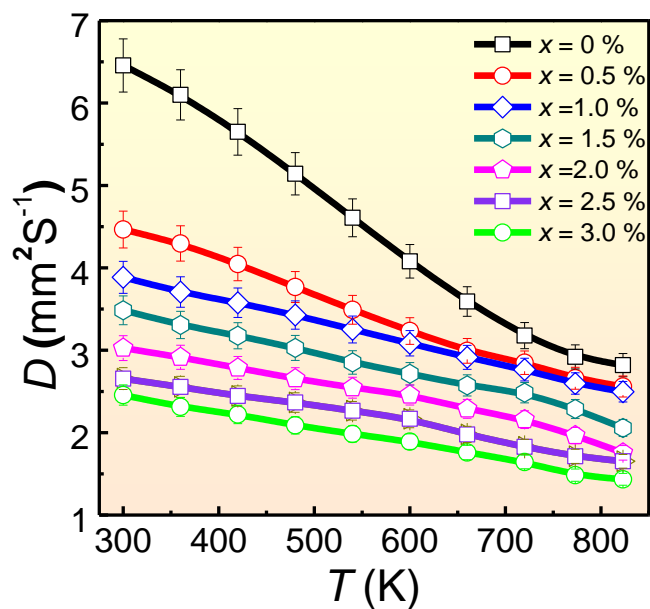**Figure 6.S1** Thermal diffusivity D as a function of temperature for different $Sn_{1-3x}In_xSr_{2x}Te$ samples.

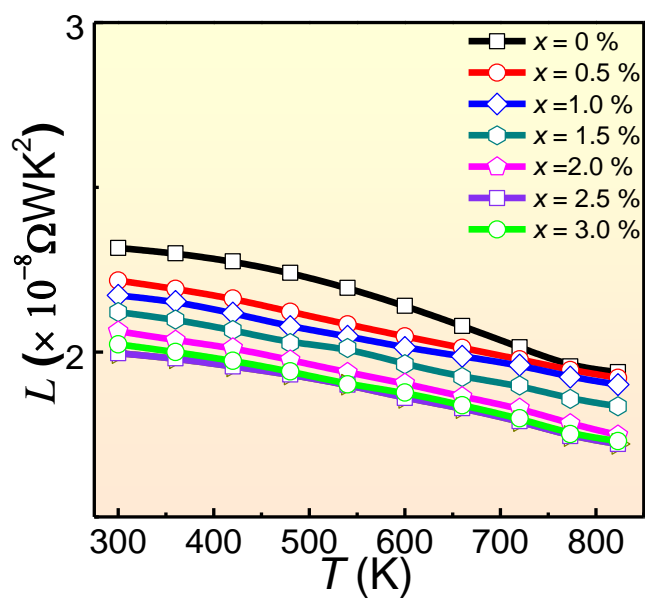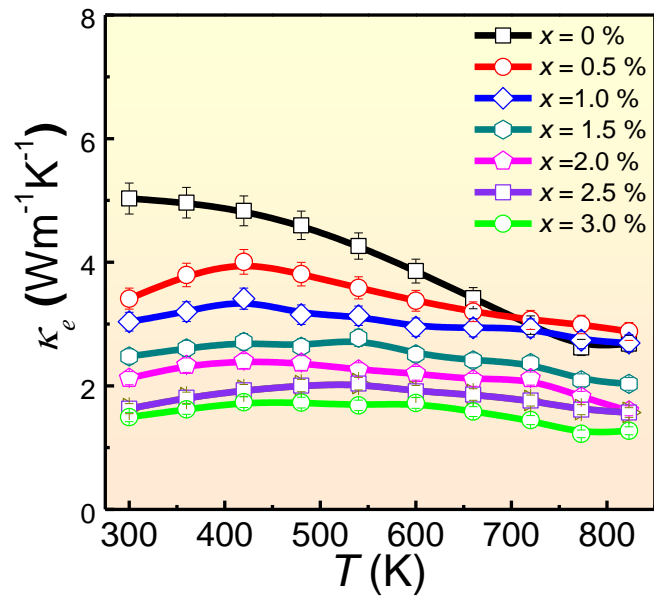**Figure 6.S2** Calculated Lorenz number L as function of temperature of $Sn_{1-3x}In_xSr_{2x}Te$.

Figure 6.S3 Temperature dependent electronic thermal conductivities of $Sn_{1-3x}In_xSr_{2x}Te$.
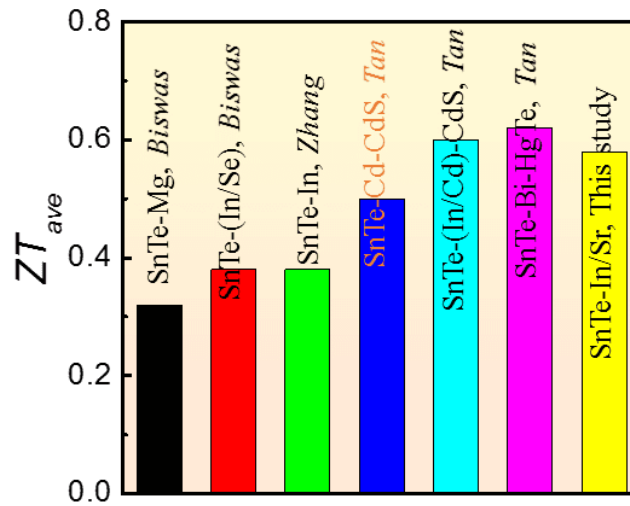

Figure 6.S4 Average *ZT* values of the current work and the previously reported work; SnTe system (300 K – 823 K).[1-6]

Table 6.S1 Band gap and energy separation values for different doped systems

System	Band gap (eV)	Energy separation (eV)
$Sn_{27}Te_{27}$	0.14	0.23
$Sn_{26}In_1Te_{27}$	0.19	0.14
$Sn_{26}Sr_1Te_{27}$	0.28	0.18
$Sn_{24}In_1Sr_2Te_{27}$	0.18	0.16

Table 6.S2 Quantitative data for EDS spectrum of **Figure 6.2h**

Element	At. %
Sn	41.86
Te	50.80
In	2.46
Sr	4.88

Table 6.S3 Parameters for phonon modelling studies

Parameters	Values
Longitudinal sound velocity υ_L (ms^{-1})	3171
Transverse sound velocity υ_T (ms^{-1})	1220
Sound velocity υ (ms^{-1})	1967
Atomic mass Sn (kg)	1.97×10^{-25}
Atomic mass Te (kg)	2.12×10^{-25}
Atomic mass In (kg)	1.91×10^{-25}
Atomic mass Sr (kg)	1.45×10^{-25}
Grain size G_d (µm)	10
Grüneisen parameter γ	1.5
Matrix density M_d (g cm^{-3})	6.44

Density difference between matrix and precipitates Δd (g cm^{-3})	0.95
Number density of precipitates N_p (m^{-3})	1.4×10^{19}

References

(1) Banik, A.; Biswas, K. *J. Mater. Chem. A* **2014**, *2*, 9620-9625.

(2) Banik, A.; Shenoy, U. S.; Anand, S.; Waghmare, U. V.; Biswas, K. *Chem. Mater.* **2015**, *27*, 581-587.

(3) Tan, G.; Shi, F.; Doak, J. W.; Sun, H.; Zhao, L.-D.; Wang, P.; Uher, C.; Wolverton, C.; Dravid, V. P.; Kanatzidis, M. G. *Energy Environ. Sci.* **2015**, *8*, 267-277.

(4) Tan, G.; Shi, F.; Hao, S.; Chi, H.; Zhao, L.-D.; Uher, C.; Wolverton, C.; Dravid, V. P.; Kanatzidis, M. G. *J. Am. Chem. Soc.* **2015**, *137*, 5100-5112.

(5) Tan, G.; Zhao, L. D.; Shi, F.; Doak, J. W.; Lo, S. H.; Sun, H.; Wolverton, C.; Dravid, V. P.; Uher, C.; Kanatzidis, M. G. *J. Am. Chem. Soc.* **2014**, *136*, 7006-7017.

(6) Zhang, Q.; Liao, B.; Lan, Y.; Lukas, K.; Liu, W.; Esfarjani, K.; Opeil, C.; Broido, D.; Chen, G.; Ren, Z. *Proc. Natl. Acad. Sci.* **2013**, *110*, 13261-13266.

Chapter 7. Outstanding Thermoelectric Properties of $Sn_{1-3x}In_xAg_{2x}Te$ Micro-crystals through Defect Engineering and Band Tuning

Journal of Materials Chemistry A

ROYAL SOCIETY OF CHEMISTRY

PAPER

Outstanding thermoelectric properties of solvothermal-synthesized $Sn_{1-3x}In_xAg_{2x}Te$ micro-crystals through defect engineering and band tuning†

Raza Moshwan,[ae] Wei-Di Liu,[a] Xiao-Lei Shi,[ab] Qiang Sun,[a] Han Gao,[a] Yun-Peng Wang,[c] Jin Zou [*ad] and Zhi-Gang Chen [*ab]

7.1 Publication

7.1.1 Abstract

Due to the eco-friendly nature, tin telluride (SnTe) based thermoelectric materials have attracted extensive attention. Pristine SnTe suffers from low thermoelectric performance because of its large energy separation between two valence bands (heavy hole and light hole) and high thermal conductivity. In this study, we use In and Ag co-dopants to ameliorate the electrical and thermal transport properties of SnTe-based materials using a facile solvothermal method. From the theoretical calculation and performance evaluation, it can be observed that high-level In and Ag co-dopants can significantly converge two valence bands and increase the density of states near the Fermi level, leading to the enhanced Seebeck coefficient from ~95 µV K^{-1} in the pristine SnTe to ~178 µV K^{-1} in the $Sn_{0.85}In_{0.05}Ag_{0.10}Te$. Comprehensive structural characterization shows that high-density strain fields and dislocations exist in the sintered pellets, together with the point defects, and grain boundaries secured the remarkably low lattice thermal conductivity of SnTe in the entire temperature range. As a result, a high peak figure of merit of ~1.38 at 823 K has been achieved in $Sn_{0.85}In_{0.05}Ag_{0.10}Te$, outperforming most of the SnTe-based materials. This study indicates that co-doping with high solubility can simultaneously tune the band structure and engineer defects for achieving enhanced thermoelectric performance of SnTe-based materials.

7.1.2 Introduction

Thermoelectric materials, enabling the conversion of heat directly into electricity, have been considered as an alternative solution to utilize large-scale waste heat emanated from industrial and automotive sectors.[1–6] As a sustainable and eco-friendly energy technology, thermoelectric generators offer zero pollution, no moving parts and high durability. The thermoelectric conversion efficiency of a material is determined by the dimensionless figure of merit, ZT, [7-14] defined as

$$ZT = \frac{S^2\sigma}{\kappa}T = \frac{S^2\sigma}{\kappa_e + \kappa_l}T \qquad (7\text{-}1)$$

where σ is the electrical conductivity, S is the Seebeck coefficient, κ is the thermal conductivity, T is the absolute temperature, and κ_e and κ_l are the electrical and lattice thermal conductivities. The strong interdependence among S, σ, and κ_e challenges the concurrent

rise in the power factor ($S^2\sigma$) and the reduction in κ. Several strategies have been executed to enhance the ZT of thermoelectric materials, including convergence of electronic bands,[15–20] carrier concentration optimization,[21–24] nanostructuring,[25–31] quantum confinement,[32,33] all-scale hierarchical architecturing,[34–37] phonon–phonon interaction,[39] defect engineering,[40,41] lattice anharmonicity[25,42–44] and porous design.[45–47]

Among different types of thermoelectric materials, eco-friendly SnTe has received extensive attention as an alternative for toxic PbTe.[9,42,48,49] SnTe possesses similar crystal and electronic structures to PbTe.[9] However, SnTe has much higher lattice thermal conductivity than PbTe at room temperature, which is attributed to the much lighter atomic mass of Sn (118 amu) than Pb (207 amu).[1] Besides, the energy separation between two valence bands in SnTe (~0.3–0.4 eV) is significantly higher than that in PbTe,[1] leading to a low S of the pristine SnTe. Due to the high concentration of intrinsic Sn vacancies, the high hole carrier concentration (n, ~10^{20} to 10^{21} cm^{-3}) is another inferior factor for the electronic and thermal transport of the pristine SnTe. Several strategies have been used to improve the electrical transport properties of SnTe. For instance, Banik et al.[50,51] introduced Mg and Ag dopants to reduce the energy separation between two valence bands. Tan et al.[4,8] studied the valence band convergence caused by Hg and Cd doping. Zhang et al.[2] first studied the resonance states introduced by In dopants in SnTe. Both band convergence and resonant states lead to the S enhancement. Moreover, the synergistic engineering of valence band convergence and resonance states has been realized in a few co-doped SnTe systems, such as In/Cd,[6,49] In/Mg,[52] In/Mn,[53] In/Hg,[54] In/Ca[55] and In/Sr.[48] A recent study on In/Ag co-doped SnTe fabricated by a conventional melting method showed an enhanced peak ZT of ~1 at $x =$ 2.5% in $SnIn_xAg_xTe_{1+2x}$.[5] The observed κ_l values for all $SnIn_xAg_xTe_{1+2x}$ samples are always higher than those of the pristine SnTe, which offsets the overall ZT enhancement.

In this study, we use a facile and low cost solvothermal method to synthesize $Sn_{1-3x}In_xAg_{2x}Te$ (x = 0, 1.0%, 3.0%, 5.0%, and 6.0%) micro-sized crystals. To realize the higher solubility of Ag and to avoid rapid decrease in electrical conductivity due to increase in In concentration, 1 : 2 (In : Ag) was chosen. Similar compositional ratios have been reported in the previous work by Bhat et al.[55] and Moshwan et al.[48] It should be noted that the solubility limit of the single In dopant in SnTe is <1% and when the amount of In is >1%, then the hole concentration of the system and the electrical conductivity significantly decreased which offset the overall power factor.[2,42] In order to retain the high power factor we introduced In : Ag at 1 : 2, which also maximizes the resonance effect and the band convergence. Through

systematic first-principles density functional theory (DFT) calculations, we found that In and Ag dopants lead to synergistically resonant states and valence band convergence, leading to remarkable enhancement in $S^2\sigma$ of $Sn_{1-3x}In_xAg_{2x}Te$ ($x > 0\%$). Moreover, high density strain field and dislocations can be observed in the sintered $Sn_{1-3x}In_xAg_{2x}Te$ pellets ($x > 5\%$), which together with the point defects and grain boundaries lead to intensive scattering of phonons and in turn yield ultra-low lattice thermal conductivity in a wide temperature range. Consequently, a peak ZT of ~1.38 has been achieved in $Sn_{1-3x}In_xAg_{2x}Te$ at 823 K, which outperforms most of the reported SnTe-based materials at a similar temperature.

7.1.3 Results and Discussion

Figure 7.1a and **b** show typical SEM images of the as-synthesized $Sn_{1-3x}In_xAg_{2x}Te$ ($x \leq 3\%$) powders and show that the products are octahedral-shaped micro-sized crystals. **Figure 7.1c** and d show SEM images of the as-synthesized $Sn_{1-3x}In_xAg_{2x}Te$ ($\geq 5\%$) severely deformed micro-sized crystals. **Figure 7.1e** shows a SEM image of a sintered $Sn_{0.85}In_{0.05}Ag_{0.10}Te$ pellet (as an example) in which small grains and grain boundaries can be seen in the sintered pellet, as indicated by orange arrows. In order to determine the compositions of the pellets, we performed EDS analyses and the typical results are shown in **Figure 7.1f**. After the statistically quantitative analysis, all these pellets have similar compositions with the nominal values of the solvothermal-synthesis products. The corresponding EDS profiles and quantitative analysis data are shown in **Figure 7.S3** of the ESI.[†] We provided an elemental map analysis of the $x = 5\%$ sample in **Figure 7.S4**. It is obvious that the composition of Sn, Te, In and Ag is uniform.
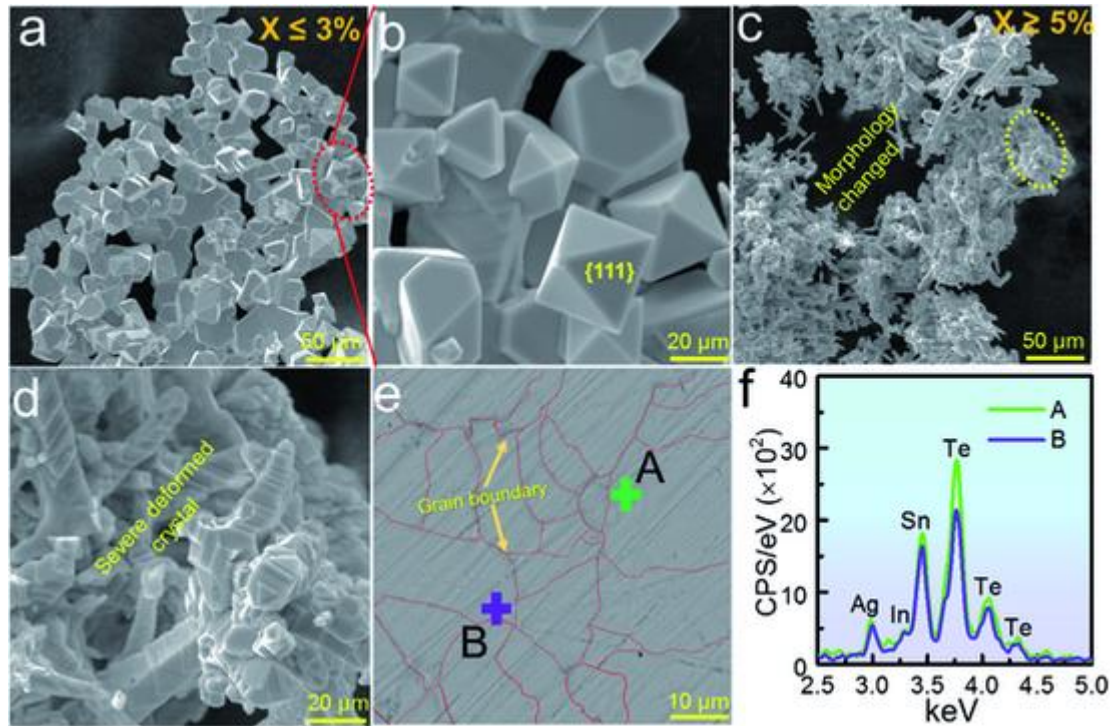
Figure 7.1 (a) Typical SEM micrograph of $Sn_{1-3x}In_xAg_{2x}Te$ ($x \le 3\%$) powders; (b) enlarged image of highlighted area of (a) shows the regular {111} planes of the as-synthesized crystal. (c) SEM micrograph of $Sn_{1-3x}In_xAg_{2x}Te$ ($x \ge 5\%$) powders; (d) enlarged image of highlighted area of (c) shows severe deformation of regular crystal shapes; (e) a typical SEM image of the sintered $Sn_{0.85}In_{0.05}Ag_{0.10}Te$ pellet; (f) corresponding EDS spectra of spot A and B of (e), showing significant peaks of Sn, Te, In and Ag.

Figure 7.2a shows the XRD patterns of the sintered $Sn_{1-3x}In_xAg_{2x}Te$ (x = 0%, 1.0%, 3.0%, 5.0%, and 6.0%) pellets, in which the diffraction peaks can be inclusively indexed as the FCC structured SnTe (standard identification card, PDF #65-0239, the pink line in **Figure 7.2a**) with a lattice parameter of a = 6.32 Å and a space group of *Fm-3m*. No secondary phases were identified within the detectability limits, indicating a high solubility of In and Ag co-doping in SnTe when compared with the reported results.[56] As shown in the calculated lattice parameter of the sintered $Sn_{1-3x}In_xAg_{2x}Te$ (x = 0%, 1.0%, 3.0%, 5.0%, and 6.0%) pellets (**Figure 7.2b**), the rate of the decreased lattice parameter is relatively high with increasing the In/Ag co-doping concentration from x = 0% up to x = 5% while the lattice parameter is almost stable at x = 6%, suggesting that the In/Ag co-doping is approaching the solubility limit. It should be noted that the decrease in the lattice parameter is attributed to the smaller ionic radius of In^{3+} (80 pm) and Ag^{1+} (115 pm) when compared with Sn^{2+} (118 pm).

Figure 7.S5 shows the extended XRD peak (200) planes and shows the peaks shift towards a higher angle confirming the lattice shrinkage after In/Ag co-doping.
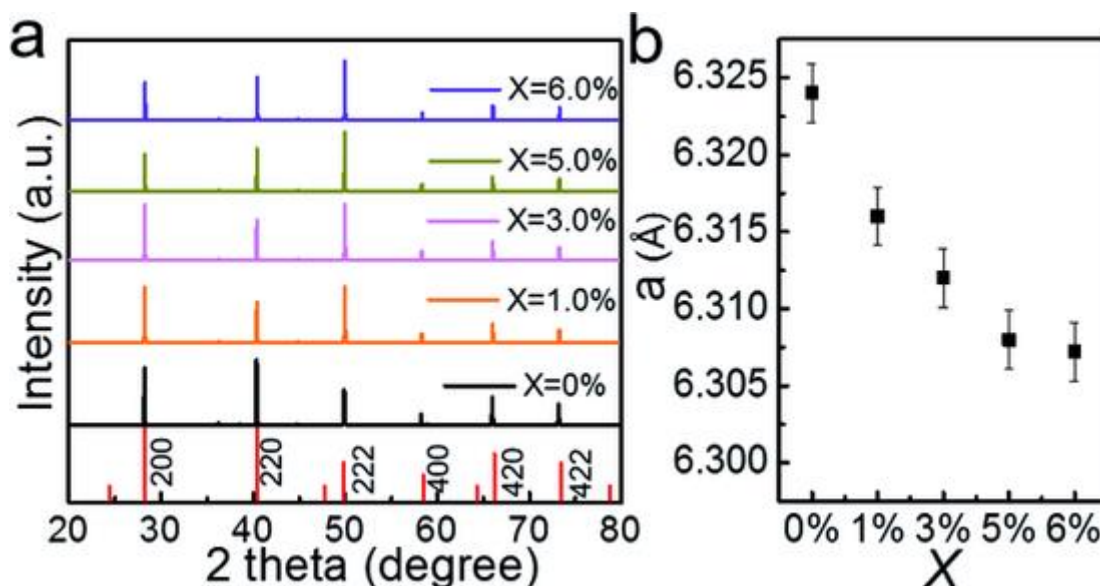

Figure 7.2 (a) XRD patterns of the sintered $Sn_{1-3x}In_xAg_{2x}Te$ (x = 0%, 1.0%, 3.0%, 5.0% and 6%) pellets. (b) Calculated lattice parameter with respect to In/Ag co-doping concentration.

Figure 7.3 shows the temperature-dependent electrical transport properties of sintered $Sn_{1-3x}In_xAg_{2x}Te$ (x = 0%, 1.0%, 3.0%, 5.0% and 6%) pellets. As shown in **Figure 7.3a**, the inherent high σ of pristine SnTe is gradually reduced with increasing the In/Ag co-doping content. At 300 K, σ of pristine SnTe is ~7240 S cm^{-1} and is decreased to ~2811 S cm^{-1} for x = 6%. **Figure 7.3b** shows the measured n and the calculated μ of the sintered $Sn_{1-3x}In_xAg_{2x}Te$ pellets, in which the room-temperature n does not fluctuate much with increasing the In/Ag doping concentration, due to the electron donor acceptor behaviour of In and Ag atoms. Room-temperature μ decreases gradually with increasing x from 0% to 6% (**Figure 7.3b**). For example, room-temperature μ reduces from ~70 cm^2 V^{-1} s^{-1} of pristine SnTe to ~30 cm^2 V^{-1} s^{-1} of $Sn_{1-3x}In_xAg_{2x}Te$ at x = 6%. The decrease in μ should be attributed to the higher effective mass (m^*) of the carriers from the heavy hole valence band, which is further verified by the calculation from a single parabolic band model. m^* can be determined using the following equations,[45]

$$S(\eta) = \frac{\kappa_B}{e} \left[\frac{\left(r + \frac{5}{2}\right) F_{r+\frac{3}{2}}(\eta)}{\left(r + \frac{3}{2}\right) F_{r+\frac{1}{2}}(\eta)} - \eta \right] \qquad (7\text{-}2)$$

$$n_H = \frac{1}{eR_H} = \frac{(2m^*\kappa_B T)^{\frac{3}{2}}}{3\pi^2 \hbar^3} \frac{\left(r + \frac{3}{2}\right)^2 F_{r+\frac{1}{2}}^{\,2}(\eta)}{\left(2r + \frac{3}{2}\right) F_{2r+\frac{1}{2}}(\eta)} \qquad (7\text{-}3)$$

where η, k_B, e, r, R_H, and $\hbar$ are the reduced Fermi level, Boltzmann constant, electron charge, carrier scattering factor ($r = -1/2$ for acoustic phonon scattering), Hall coefficient, effective mass, and reduced plank constant, respectively. $F_i(\eta)$ is the Fermi integral expressed as

$$F_i(\eta) = \int_0^\infty \frac{x^i}{1 + e^{(x-\eta)}} dx \qquad (7\text{-}4)$$
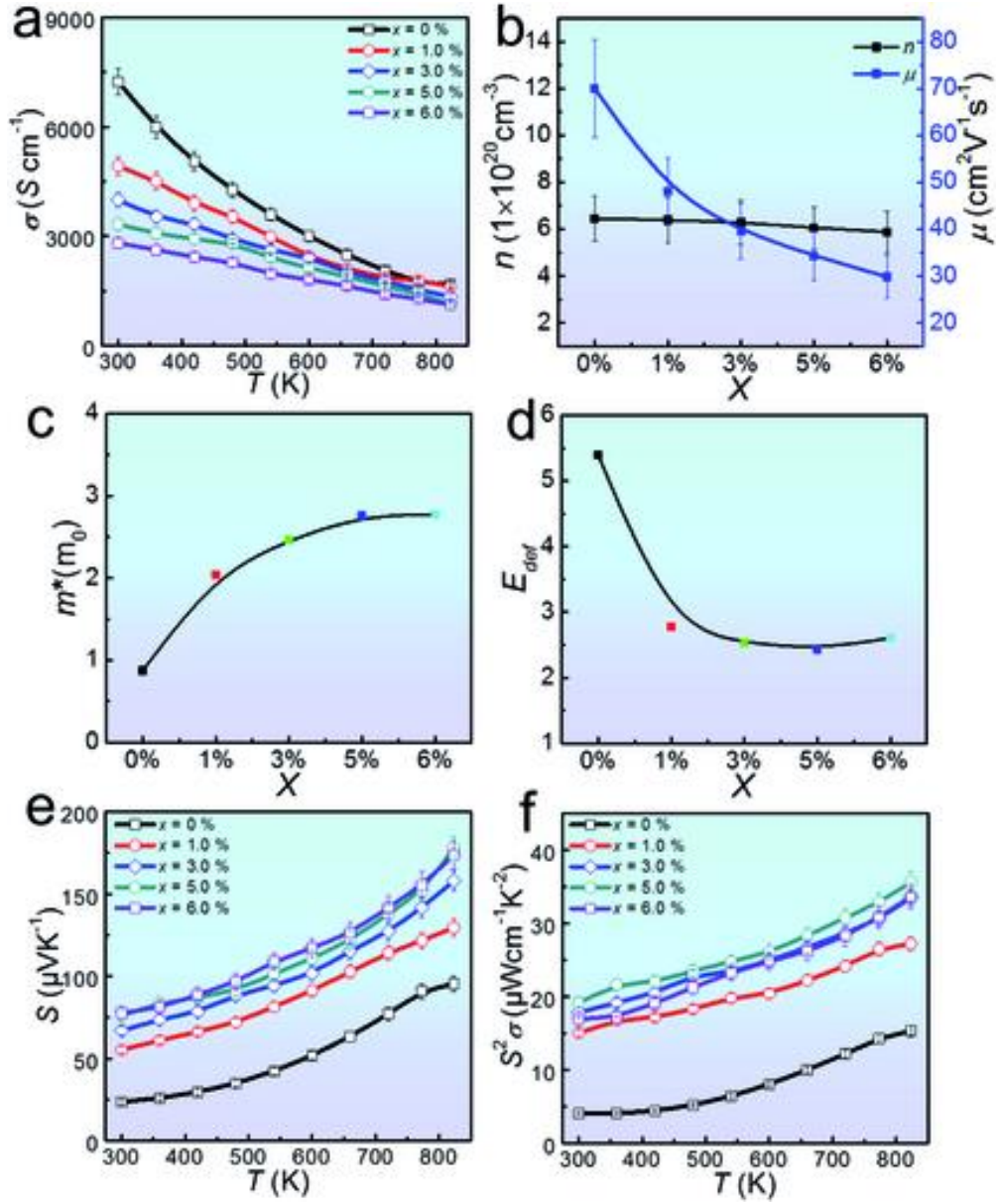
Figure 7.3 Electrical transport properties of sintered $Sn_{1-3x}In_xAg_{2x}Te$ (x = 0%, 1.0%, 3%, 5%, and 6%) samples: (a) σ, (b) n and μ, (c) m^* (d) E_{def} (e) S, and (f) $S^2\sigma$. (error bar 5%).

Figure 7.3c shows the determined m^* as a function of x, in which m^* increases from 0.87 m_0 of the pristine SnTe (x = 0%) to 2.78 m_0 of $Sn_{1-3x}In_xAg_{2x}Te$ for x = 6%, indicating that the heavy hole contribution to the electron hole transportation from the valence band to conduction band in $Sn_{1-3x}In_xAg_{2x}Te$. We also estimated the room-temperature deformation potential (E_{def}) of $Sn_{1-3x}In_xAg_{2x}Te$, and the results are shown in **Figure 7.3d**. The relationship between E_{def} and μ can be expressed as[45]

$$\mu_{\mathrm{H}} = \left[\frac{e\pi\hbar^4}{\sqrt{2}(\kappa_{\mathrm{B}}T)^{\frac{3}{2}}} \frac{C_{\mathrm{l}}}{E_{\mathrm{def}}^2 (m^*)^{\frac{5}{2}}} \right] \frac{\left(2r+\frac{3}{2}\right) F_{2r+\frac{1}{2}}^{(\eta)}}{\left(r+\frac{3}{2}\right)^2 F_{r+\frac{1}{2}}^{(\eta)}} \tag{7-5}$$

where C_{l} ($C_{\mathrm{l}} = v_{\mathrm{l}}^2 \cdot \rho$, v_{l} and ρ are the longitudinal sound velocity and density) is the elastic constant for longitudinal vibrations. The v_{l} was taken as 3371 ms^{-1}. As shown in **Figure 7.3d**, E_{def} of all Sn$_{1-3x}$In$_x$Ag$_{2x}$Te ($x > 0\%$) is lower than that of the pristine SnTe, theoretically suggesting the enhanced μ. However, the higher m^* offsets the influence of reduction in E_{def}.[45]

Figure 7.3e shows the temperature-dependent S of the sintered Sn$_{1-3x}$In$_x$Ag$_{2x}$Te ($x = 0\%$, 1.0%, 3.0%, 5.0% and 6%) pellets, in which S of the In/Ag co-doped SnTe is higher than that of the pristine SnTe in the entire temperature range. For instance, the room-temperature S of $x = 5\%$ is ~178 μV K^{-1} which is ~1.9 times higher than that of pristine SnTe, due to the significant valence band convergence and resonance energy level caused by the In/Ag co-doping. The resonance effect leads to increases in DOS near the Fermi level in the valence according to the following equation

$$S = \frac{\pi^2}{3} \frac{\kappa_{\mathrm{B}}}{q} k_{\mathrm{B}} T \left[\frac{g(E)}{n(E)} + \frac{1}{\mu E} \frac{\mathrm{d}\mu(E)}{\mathrm{d}E} \right]$$

, where q is the electron charge, k_{B} is the Boltzmann constant, and $g(E)$ is the DOS.[42] S steadily increases with increasing the temperature for all Sn$_{1-3x}$In$_x$Ag$_{2x}$Te ($x > 0\%$). The contribution of heavy mass carriers from the second sub-band manifests S.

Figure 7.3f shows the calculated temperature-dependent $S^2\sigma$ of the sintered Sn$_{1-3x}$In$_x$Ag$_{2x}$Te ($x = 0\%$, 1.0%, 3.0%, 5.0% and 6%) pellets. The $S^2\sigma$ values of In/Ag co-doped SnTe are well above those of the pristine SnTe due to the significant S enhancement. Specifically, room-temperature $S^2\sigma$ considerably increases from ~4.04 μW cm^{-1} K^{-2} of the pristine SnTe to ~19.18 μW cm^{-1} K^{-2} of Sn$_{0.85}$In$_{0.05}$Ag$_{0.10}$Te. A peak $S^2\sigma$ of ~35.67 μW cm^{-1} K^{-2} is obtained for Sn$_{1-3x}$In$_x$Ag$_{2x}$Te ($x = 5\%$) at 823 K.

In order to understand the underlying mechanism of the improved electrical transport properties of Sn$_{1-3x}$In$_x$Ag$_{2x}$Te pellets, we carried out theoretical calculation. **Figure 7.4a–d** show the spectral functions for four systems, namely, the pristine SnTe, Sn$_{0.95}$In$_{0.05}$Te, Sn$_{0.90}$Ag$_{0.10}$Te and Sn$_{0.85}$In$_{0.05}$Ag$_{0.10}$Te, respectively. The spectral function of the pristine

SnTe exhibits well-defined peaks. The positions of the peaks in the spectral function correspond to the ordinary band structure. For SnTe doped with foreign elements, the peaks in the spectral function are no longer well-defined, but are smeared due to the on-site disorders caused by the atomic substitutions. The spectral functions with energies −0.3 eV to 0.2 eV in $Sn_{0.95}In_{0.05}Te$ (**Figure 7.4b**) and 0 eV to 0.5 eV in the $Sn_{0.85}In_{0.05}Ag_{0.10}Te$ (**Figure 7.4d**) are too severely smeared to interpret as a band. The spectral function in other energy ranges can still be interpreted as bands. For example, the valence band edge of $Sn_{0.95}In_{0.05}Te$ is at −0.3 eV, and the conduction band edge of $Sn_{0.85}In_{0.05}Ag_{0.10}Te$ is at 0.5 eV.
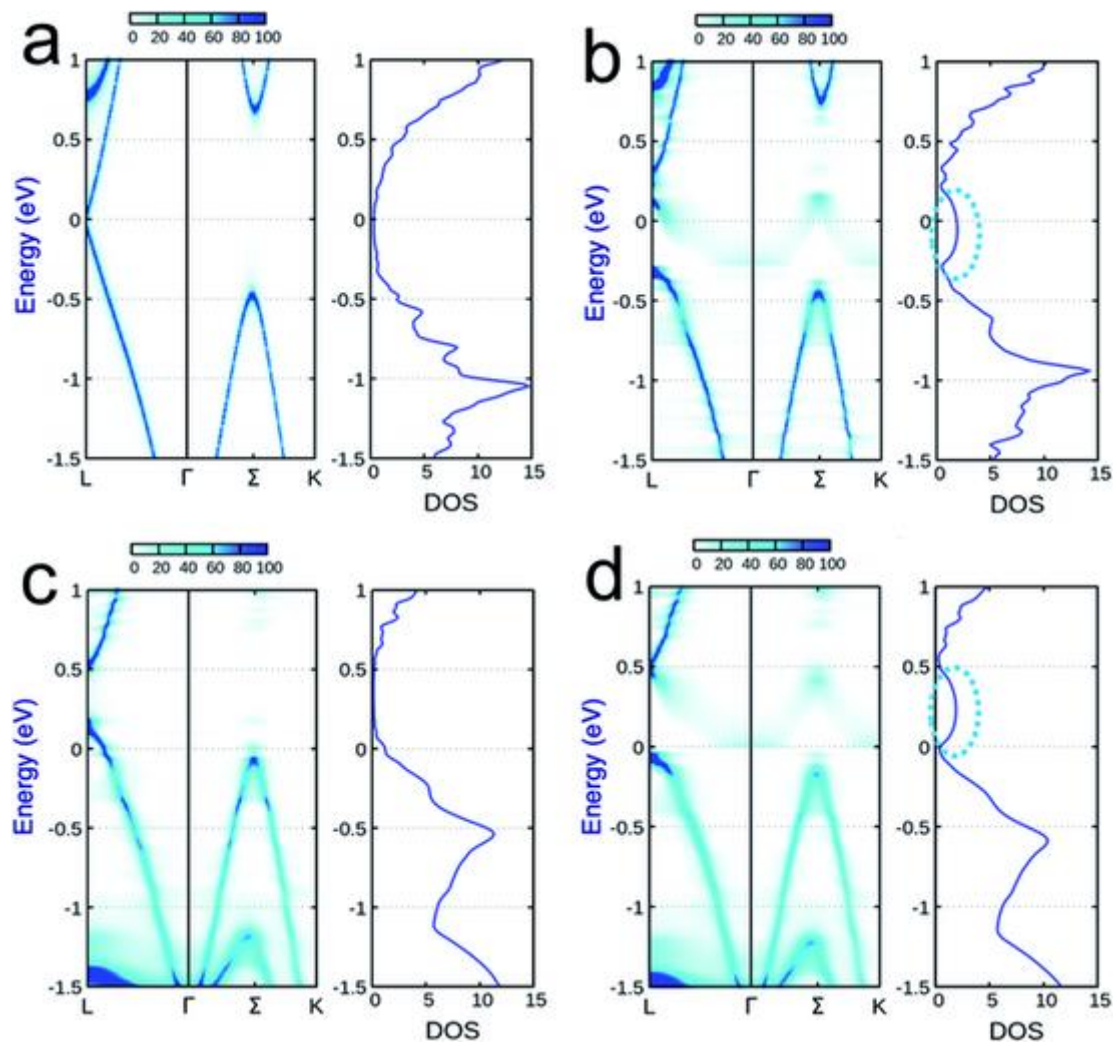

Figure 7.4 The spectral functions (left panels) and the density of states (right panels) of pristine and doped SnTe. (a) Pristine SnTe, (b) $Sn_{0.95}In_{0.05}Te$, (c) $Sn_{0.90}Ag_{0.10}Te$ and (d) $Sn_{0.85}In_{0.05}Ag_{0.10}Te$.

The substitution by Ag dopants induces p-type doping as indicated by the shifting towards higher energy of the entire band structure. **Figure 7.4c** shows enhanced energy band gaps. The band structure in In-doped SnTe is more complex. Although the band edge at the L point is shifted downwards in the energy scale, the energy of the band edge at the Σ point remains unchanged, as shown in **Figure 7.4b**. Therefore, little p-type doping is induced by In dopants. The most significant modification in the electronic structure brought by In dopants is the enhanced density of states within an energy range of 0.5 eV around the Fermi energy. The enhanced DOS corresponds to a severely smeared band-like feature in the spectral function, whose energy dispersion near the L and Σ points is parallel with the well-defined valence band below it (**Figure 7.4b**). In/Ag co-doped SnTe, as shown in **Figure 7.4d**, exhibits both the p-type doping due to Ag and the enhanced DOS above the valence band due to In dopants.

The enhancement in DOS induced by In dopants is referred to the resonant states.[2] The resonant states result from the strong hybridization between the impurity (In dopant) energy levels and the bands from the matrix material (SnTe). The severe smearing of spectral functions near the Fermi energy is shown in **Figure 7.4b**, providing the evidence for the impurity-matrix hybridizations. The band convergence effect is also visible in the calculated spectral functions. The band convergence refers to the reduction of the energy difference between the valence band edges at the L point and at the Σ point. Ag-dopants induce a sizable band convergence effect by reducing the energy difference from 0.42 eV in pristine SnTe to 0.2 eV in $Sn_{0.90}Ag_{0.10}Te$. The band convergence effect by In dopants is even more significant. The energy difference is reduced to 0.15 eV by 5% In dopants. Co-doping with In and Ag produces a larger band convergence than single doping. The energy difference is 0.1 eV in $Sn_{0.85}In_{0.05}Ag_{0.10}Te$ (**Figure 7.4d**). Therefore, we believe that the significant S enhancement observed in the In/Ag co-doped SnTe is attributed to the synergy of band convergence, band gap enlargement and the resonant states.

Figure 7.5a shows the temperature-dependent κ of the sintered $Sn_{1-3x}In_xAg_{2x}Te$ (x = 0%, 1.0%, 3.0%, 5.0% and 6%) pellets and shows that κ gradually decreased with increasing the x value (In/Ag content) in the whole temperature range from 300 to 823 K. Room-temperature κ is significantly reduced from ~8.5 W m^{-1} K^{-1} in the pristine SnTe to ~3.39 W m^{-1} K^{-1} in $Sn_{0.82}In_{0.06}Ag_{0.12}Te$. A minimum κ of ~2.07 W m^{-1} K^{-1} at 823 K is obtained in $Sn_{0.82}In_{0.06}Ag_{0.12}Te$, which is 44% lower than that in the pristine SnTe at 823 K. **Figure 7.5b** shows the calculated κ_e of $Sn_{1-3x}In_xAg_{2x}Te$ samples using Wiedemann–Franz

law $\kappa_e = L\sigma T$,[57] where L is the Lorenz number, and can be calculated by the following relationship:

$$L = 1.5 + \exp\left(-\frac{|S|}{116}\right) \qquad (7\text{-}6)$$
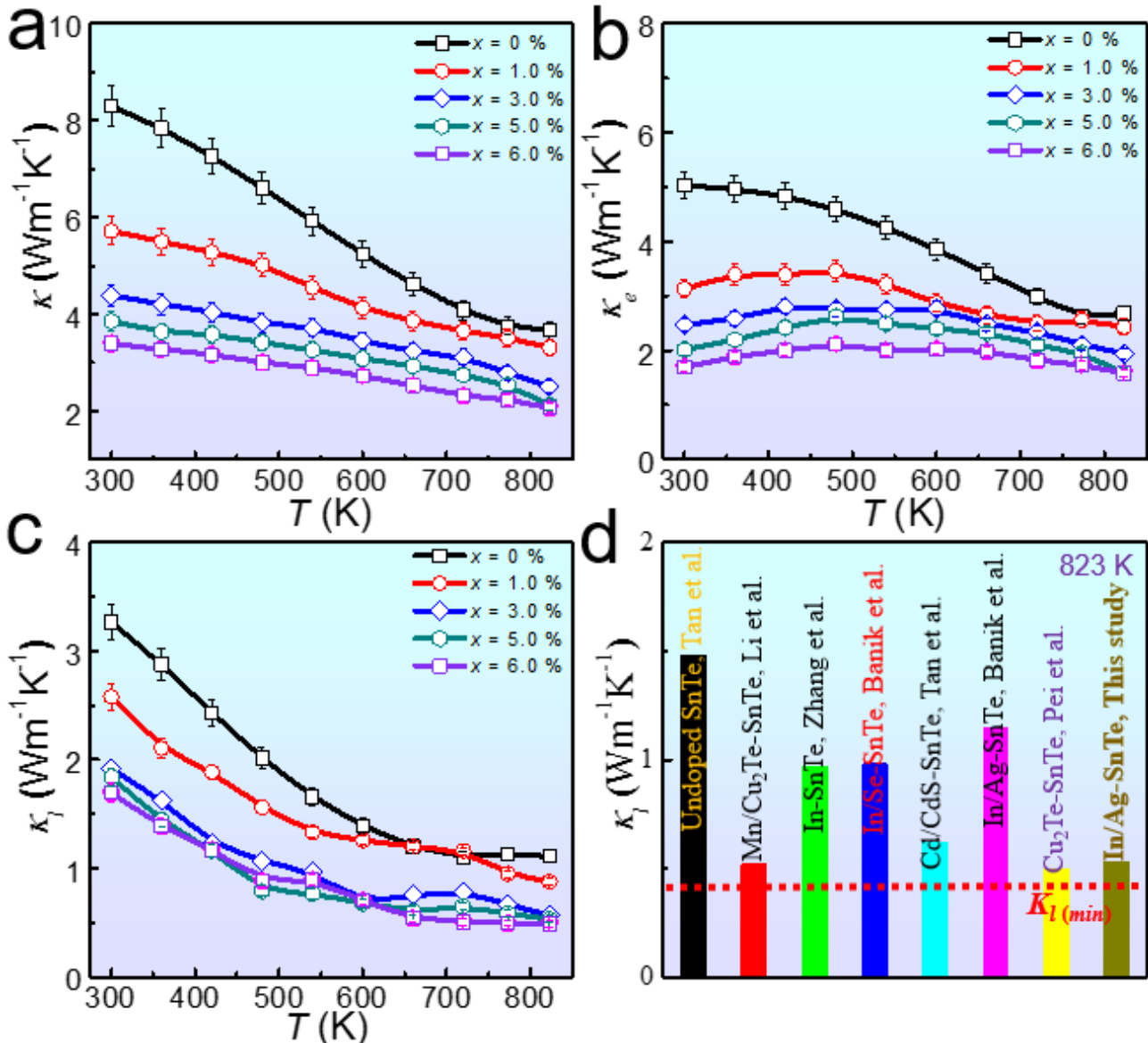

Figure 7.5 Temperature-dependent thermal transport properties of sintered Sn$_{1-3x}$In$_x$Ag$_{2x}$Te (x = 0%, 1.0%, 3.0%, 5.0%, 6.0%) samples (error limit is 5%) (a) κ, (b) κ_e and (c) κ_l (error limit is 5%). (d) Comparison of current κ_l with the reported results.[1–7]

The calculated L values lie in between the Sommerfeld value of the degenerated limit (L_{DEG} = 2.45 × 10^{-8} Ω W K^{-2}) and non-degenerate limit (L_{N-D} = 1.49 × 10^{-8} Ω W K^{-2})[58] (**Figure 7.S6**). We further calculated κ_l by subtracting κ_e from κ, and the results are shown in **Figure 7.5c**. Clearly, the κ_l values are remarkably reduced with increasing the In/Ag doping concentration. The room-temperature κ_l value is greatly reduced from ~3.4 W m^{-1} K^{-1} in the pristine SnTe to ~1.69 W m^{-1} K^{-1} in Sn$_{0.82}$In$_{0.06}$Ag$_{0.12}$Te. A lowest κ_l of ~0.48 W m^{-1} K^{-1} is observed in Sn$_{0.82}$In$_{0.06}$Ag$_{0.12}$Te at 823 K. This value is approaching the amorphous limit (~0.4 W m^{-1} K^{-1}).[7] **Figure 7.5d** shows the comparison between our determined κ_l and the reported values, in which our κ_l value is significantly lower than most of the reported κ_l values, including undoped SnTe (melting),[6] Mn/Cu$_2$Te doped (melting),[1] Cu$_2$Te doped,[7] In doped (ball milling),[2] In/Se doped (melting),[3] Cd/CdS doped (melting)[4] and In/Ag doped (melting)[5] SnTe systems, indicating the efficacy of our synthesis method to secure high-performance thermoelectric materials.

To understand the origin of the κ_l reduction in Sn$_{1-3x}$In$_x$Ag$_{2x}$Te, we performed transmission electron microscopy analyses. **Figure 7.6a** shows a typical bright-field TEM image of Sn$_{0.85}$In$_{0.05}$Ag$_{0.10}$Te, in which the high density of strain field exists in the matrix. **Figure 7.6b** shows the selected area electron diffraction (SAED) pattern along the [211] zone axis. A high-resolution transmission electron microscopy (HRTEM) image is shown in **Figure 7.6c**. The magnified image of the highlighted elliptical circle area of **Figure 7.6c** shows that dislocations exist in the matrix (**Figure 7.6d**). These strain field and dislocations in the matrix, together with the point defects and grain boundaries, significantly scatter heat carrying phonons in all scale and are responsible for the reduction of κ_l to a great extent.
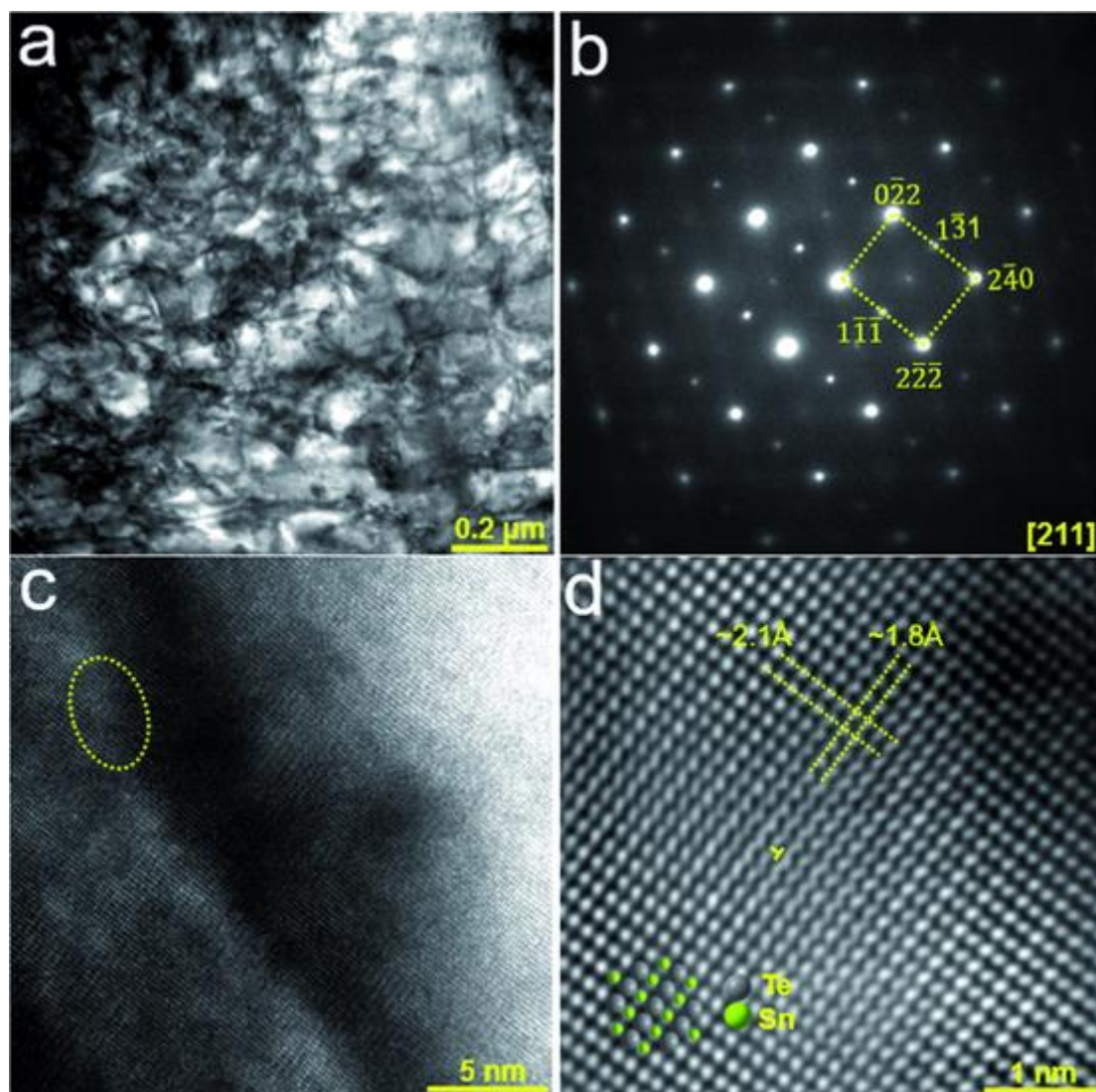
Figure 7.6 (a) Typical bright field TEM image of the $Sn_{0.85}In_{0.05}Ag_{0.10}Te$ sintered pellet shows high density strain field in the matrix. (b) Selected area electron diffraction (SAED) pattern along the [211] zone-axis. (c) High resolution transmission electron microscopy image of one strain field area, and (d) magnified image of highlighted area of (c) shows that dislocation exists in the matrix.

Figure 7.7a shows the calculated ZT of the $Sn_{1-3x}In_xAg_{2x}Te$ pellets, in which the peak ZT outstandingly enhanced from 0.34 in the pristine SnTe to 1.38 in $Sn_{0.85}In_{0.05}Ag_{0.10}Te$ at 823 K, which is attributed to the synergistic increase in $S^2\sigma$ and decrease in κ. This ZT enhancement is over ~3 times higher than that of the pristine SnTe. We also compare our results with some of the previously reported results, including Bi/Hg,[8] Bi/Sr,[38] Cd/CdS,[4] In,[2] In/Ag,[5] Mn/Cu$_2$Te[1] doped SnTe systems. As can be seen, our ZT value outperforms most of the reported ones (**Figure 7.7b**), indicating a great

potential of In/Ag co-doping with a ratio of $1:2$ to achieve significant enhancement in the electrical and thermal transport properties of SnTe systems. The synergistic defect engineering and band tuning can be a crucial strategy to obtain high-performance thermoelectric materials.
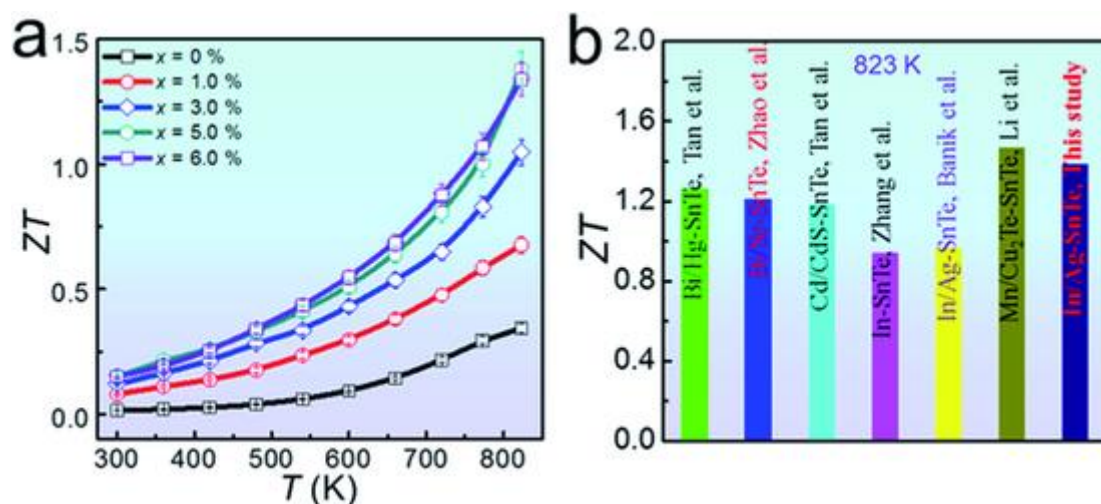

Figure 7.7 (a) Temperature-dependent (a) ZT values of $Sn_{1-3x}In_xAg_{2x}Te$ (x = 0%, 1.0%, 3.0%, 5.0%, 6.0%) samples (error limit is 5%); (b) comparing current ZT value with some of the previously reported results, including Bi/Hg,[8] Bi/Sr,[38] Cd/CdS,[4] In,[2] In/Ag[5] and Mn/Cu$_2$Te[1] doped SnTe systems at 823 K.

7.1.4 Conclusion

In this study, we demonstrated that high thermoelectric properties can be achieved in the In/Ag co-doped SnTe through comprehensive DFT electronic structure calculations, synthesis and structural and composition characterizations. The high-concentration In and Ag dopants induce resonant states, valence band convergence and band gap enlargement, leading to the enhanced S from ~95 µVK^{-1} in the pristine SnTe to ~178 µVK^{-1} in the $Sn_{0.85}In_{0.05}Ag_{0.10}Te$. The co-existence of point defects, strain field, dislocations and grain boundaries significantly reduced lattice thermal conductivity over a wide temperature range. Consequently, an outstanding peak ZT of ~1.38 was obtained in $Sn_{0.85}In_{0.05}Ag_{0.10}Te$ that is ~ 3.06 times higher than that in the pristine SnTe. This study reveals a promising pathway to achieve high-performance thermoelectric materials *via* synergistic band tuning and defect engineering by a facile solvothermal method.

7.1.5 Experimental Section

7.1.5.1 Materials Synthesis

A facile solvothermal method was used to synthesize $Sn_{1-3x}In_xAg_{2x}Te$ (x = 0%, 1.0%, 3.0%, 5.0%, and 6.0%) samples. Na_2TeO_3 (99.99%), $SnCl_2·2H_2O$ (99.99%), $AgNO_3$ (≥99.99%), and $InCl_3·4H_2O$ (97%), supplied by Sigma-Aldrich, were used as sources of Te, Sn, Ag and In. Ethylene glycol (99.8%) and NaOH (99.99%) were used as solvents to dissolve precursors. The solution was put into a Teflon jar and stirred with a magnetic stirrer for several minutes. These Teflon jars were then put into stainless-steel autoclaves and sealed to put into a CSK thermal oven, then heated to 230 °C and soaked for 24 h. After this, the synthesized products were collected in centrifuging tubes at room temperature. Absolute ethanol and deionized water were used for centrifuging until the appearance of the clear solution. Once the centrifuging was completed, the synthesized crystals were dried at 60 °C for 12 h.

7.1.5.2 Thermoelectric Property Measurements

The synthesized powders were sintered to form pellets using a spark plasma sintering (SPS) machine under high vacuum. The pressure, temperature and time for SPS were set as 50 MPa, 823 K and 5 minutes, respectively. In order to measure the thermoelectric properties of the sintered samples, different-grade grind papers were used to polish the sintered pellets. Thermoelectric transport properties, such as the Seebeck coefficient and electrical resistivity, were simultaneously measured with a ZEM-3 (ULVAC) under a helium atmosphere from room temperature to 823 K. Thermal transport properties, such as thermal diffusivity (D), were measured by a laser flash diffusivity method with an LFA 457 (NETZSCH) in the temperature range of 300 to 823 K (**Figure 7.S1**). Specific heat capacity, C_p, was measured with a DSC 404 F3 (NETZSCH) (**Figure 7.S2**). The density (d) of the sintered pellets was determined by the Archimedes method[59] which gave ~97% of the theoretical density. $κ$ of the pellets was then determined using the relationship $κ = DC_pd$. The room-temperature Hall carrier concentration and carrier mobility ($μ$) were determined using a homemade apparatus using a four-probe contact method with the van der Pauw technique under a reversible magnetic field of 1.5 T.

7.1.5.3 Structural and Compositional Characterizations

The phase and compositional analyses of the sintered pellets were carried out by X-ray diffraction (XRD) with Cu Kα ($λ$ = 1.5418 Å) radiation using a Bruker D8 diffractometer. Scanning electron microscopy (SEM, JEOL 6610, operated at 20 kV) with energy-dispersive

X-ray spectroscopy (EDS) and Hitachi's unique 200 kV aberration-corrected transmission electron microscopy (TEM, HF 5000, operated at 200 kV) were used to investigate the morphology, structure and composition of the sintered pellets. Focused ion beam (FEI-SCIOS FIB) was used to prepare thin lamella for nanoscale TEM characterization.

7.1.5.4 Computational Details of Band Structure and Density of States Calculation

We employed first-principles density functional theory (DFT) to investigate the effect of In/Ag atomic substitutions on the electronic structures of SnTe. The on-site disorders due to atomic substitutions were considered using the coherent potential approximation (CPA). We utilized the Korringa–Kohn–Rostocker (KKR) Green function formalism in the atomic sphere approximation (ASA) as implemented in the AkaiKKR code. The Perdew–Burke–Ernzerhof parameterization of the generalized gradient approximation was used for the exchange–correlation functional.[60] The supercell approach widely adopted in previous studies considered an ordered distribution of dopants, *i.e.*, an ordered alloy.[61] The calculated band structure depends sensitively on the precise distribution pattern of dopants in the matrix. The CPA method has several advantages over the supercell approach. First, the fractional atomistic occupation number allows one to simulate alloys with arbitrary doping concentrations by the same computational effort. Second, because the same primitive cell is used in simulating pristine and doped systems, the effects of dopants can be obtained by a direct comparison of the resulting band structures. Lastly, the CPA method is built upon the electronic Green's functions. The scatterings encountered by electrons due to the dopant-matrix hybridizations, such as the electrons in the resonant state, are manifested as the broadening and distortion in the calculated spectral functions. Benchmark calculations show that the band structure of pristine SnTe obtained by the KKR-ASA method matches well with the conventional plane-wave-pseudopotential method. SnTe possesses a rock-salt face centered cubic (FCC) structure with the room-temperature lattice parameter of $a = 6.32$ Å. Two empty spheres per unit cell were added. The self-consistent potential was calculated using a $6 \times 6 \times 6$ k-mesh with a tiny imaginary energy (10^{-6} Ry).

Acknowledgement

References

(1) W. Li, L. Zheng, B. Ge, S. Lin, X. Zhang, Z. Chen, Y. Chang and Y. Pei, *Adv.Mater.,* 2017, **29,** 1605887.

(2) Q. Zhang, B. Liao, Y. Lan, K. Lukas, W. Liu, K. Esfarjani, C. Opeil, D. Broido, G. Chen and Z. Ren, *Proc. Natl. Acad. Sci.,* 2013, **110,** 13261.

(3) A. Banik and K. Biswas, *J. Mater. Chem. A,* 2014, **2,** 9620.

(4) G. Tan, L.D. Zhao, F. Shi, J. W. Doak, S.H. Lo, H. Sun, C. Wolverton, V.P. Dravid, C. Uher and M. G. Kanatzidis, *J. Am. Chem. Soc.,* 2014, **136,** 7006.

(5) A. Banik, U. S. Shenoy, S. Saha, U. V. Waghmare and K. Biswas, *J. Am. Chem. Soc.,* 2016, **138,** 13068.

(6) G. Tan, F. Shi, S. Hao, H. Chi, L.-D. Zhao, C. Uher, C. Wolverton, V. P. Dravid and M. G. Kanatzidis, *J. Am. Chem. Soc.,* 2015, **137,** 5100.

(7) Y.Z. Pei, L. L. Zheng, W. Li, S.Q. Lin, Z. W. Chen, Y.Y. Wang, X.F. Xu, H. L. Yu, Y. Chen and B. H. Ge, *Adv. Electron. Mater.,* 2016, **2,** 1600019.

(8) G. Tan, F. Shi, J. W. Doak, H. Sun, L.-D. Zhao, P. Wang, C. Uher, C. Wolverton, V. P. Dravid and M. G. Kanatzidis, *Energy Environ. Sci.,* 2015, **8,** 267.

(9) R. Moshwan, L. Yang, J. Zou and Z.-G. Chen, *Adv. Funct. Mater.,* 2017, **27,** 1703278.

(10) T. Zhu, Y. Liu, C. Fu, J.P. Heremans, J.G. Snyder, X. Zhao, *Adv. Mater.* 2017, **29,** 1605884.

(11) G. J. Snyder and T. S. Ursell, *Phys. Rev. Lett.,* 2003, **91,** 148301.

(12) L. Yang, Z.-G. Chen, M.S. Dargusch and J. Zou, *Adv. Energy Mater.,* 2018, **8,** 1701797.

(13) L. Zhao, F.Y. Fei, J. Wang, F. Wang, C. Wang, J. Li, J. Wang, Z. Cheng, S. Dou and X. Wang, *Sci. Rep.,* 2017, **7,** 40436.

(14) L.-D. Zhao, S.-H. Lo, J. He, H. Li, K. Biswas, J. Androulakis, C.-I. Wu, T. P. Hogan, D.-Y. Chung, V. P. Dravid and M. G. Kanatzidis, *J. Am. Chem. Soc.,* 2011, **133,** 20476.

(15) C. Fu, T. Zhu, Y. Liu, H. Xie and X. Zhao, *Energy Environ. Sci.,* 2015, **8,** 216.

(16) J. He, X. Tan, J. Xu, G.Q. Liu, H. Shao, Y. Fu, X. Wang, Z. Liu, J. Xu, H. Jiang and J. Jiang, *J. Mater. Chem. A,* 2015, **3,** 19974.

(17) Y. Pei, X. Shi, A. LaLonde, H. Wang, L. Chen and G. J. Snyder, *Nature,* 2011, **473,** 66.

(18) Y. Pei, H. Wang and G. J. Snyder, *Adv. Mater.,* 2012, **24,** 6125.

(19) T. Xiaojian, S. Hezhu, H. Tianqi, L. Guo-Qiang and R. Shang-Fen, *J. Phys.: Condens. Matter,* 2015, **27,** 095501.

(20) M. Hong, Z.-G. Chen, Y. Pei, L. Yang and J. Zou, *Phys. Rev. B,* 2016, **94,** 161201.

(21) J. Krez, J. Schmitt, G. Jeffrey Snyder, C. Felser, W. Hermes and M. Schwind, *J. Mater. Chem. A,* 2014, **2,** 13513.

(22) J. Li, Z. Chen, X. Zhang, H. Yu, Z. Wu, H. Xie, Y. Chen and Y. Pei, *Adv.Sci.,* 2017, **4,** 1 700341.

(23) Y. Pei, A.   D. LaLonde, N.   A. Heinz, X. Shi, S. Iwanaga, H. Wang, L. Chen and G. J. Snyder, *Adv. Mater.,* 2011, **23,** 5674.

(24) E. Rausch, B. Balke, T. Deschauer, S. Ouardi and C. Felser, *APL Mater.*, 2015, **3,** 041516

(25) S. N. Guin, D. S. Negi, R. Datta and K. Biswas, *J. Mater. Chem. A,* 2014, **2,** 4324.
(26) B.A. Cook, M.J. Kramer, J. L. Harringa, M.K-. Han, D.Y. Chung and M.G. Kanatzidis, *Adv. Funct. Mater.,* 2009, **19,** 1254.

(27) M.-K. Han, K. Hoang, H. Kong, R. Pcionek, C. Uher, K. M. Paraskevopoulos, S. D. Mahanti and M. G. Kanatzidis, *Chem. Mater.,* 2008, **20,** 3512.

(28) J.-L. Lan, Y. Liu, Y.-H. Lin, C.-W. Nan, Q. Cai and X. Yang, *Sci. Rep.,* 2015, **5,** 7783.

(29) E. Quarez, K.-F. Hsu, R. Pcionek, N. Frangis, E.K. Polychroniadis and M. G. Kanatzidis, *J. Am. Chem. Soc.*, 2005, **127,** 9177.

(30) L.-D. Zhao, J. He, S. Hao, C.-I. Wu, T.P. Hogan, C. Wolverton, V.P. Dravid and M. G. Kanatzidis, *J. Am. Chem. Soc.,* 2012, **134,** 16327.

(31) Z.-G. Chen, G. Han, L. Yang, L. Cheng and J. Zou, *Prog. Nat. Sci.,* 2012, **22,** 535.

(32 Y. Tian, M.R. Sakr, J. M. Kinder, D. Liang, M.J. MacDonald, R. L.J. Qiu, H.-J. Gao and X. P. A. Gao, *Nano Lett.*, 2012, **12,** 6492.

(33) W.-X. Zhou, S. Tan, K.-Q. Chen and W. Hu, *J. Appl. Phys.,* 2014, **115,** 124308.

(34) S. Bhattacharya, A. Bohra, R. Basu, R. Bhatt, S. Ahmad, K. N. Meshram, A. K. Debnath, A. Singh, S.K. Sarkar, M. Navneethan, Y. Hayakawa, D.K. Aswal and S. K. Gupta, *J. Mater. Chem. A*, 2014, **2,** 17122.

(35) K. Biswas, J. He, I. D. Blum, C.-I. Wu, T. P. Hogan, D. N. Seidman, V. P. Dravid and M. G. Kanatzidis, *Nature,* 2012, **489,** 414.

(36) Y. Lee, S.-H. Lo, J. Androulakis, C.-I. Wu, L.-D. Zhao, D.-Y. Chung, T.P. Hogan, V.P. Dravid and M. G. Kanatzidis, *J. Am. Chem. Soc.,* 2013, **135,** 5152.

(37) L. D. Zhao, H. J. Wu, S. Q. Hao, C. I. Wu, X. Y. Zhou, K. Biswas, J. Q. He, T. P. Hogan, C. Uher, C. Wolverton, V. P. Dravid and M. G. Kanatzidis, *Energy Environ. Sci.,* 2013, **6,** 3346.

(38) L.D. Zhao, X. Zhang, H. Wu, G. Tan, Y. Pei, Y. Xiao, C. Chang, D. Wu, H. Chi, L. Zheng, S. Gong, C. Uher, J. He and M. G. Kanatzidis, *J. Am. Chem. Soc.,* 2016, **138,** 2366.

(39) M. Hong, Y. Wang, T. Feng, Q. Sun, S. Xu, S. Matsumura, S.T. Pantelides, J. Zou and Z.-G. Chen, *J. Am. Chem. Soc.,* 2019, **141,** 1742.

(40) M. H. Lee, D.-G. Byeon, J.-S. Rhyee and B. Ryu, *J. Mater. Chem. A,* 2017, **5,** 2235.

(41) X. Shi, K. Zheng, M. Hong, W. Liu, R. Moshwan, Y. Wang, X. Qu, Z.-G. Chen and J. Zou, *Chem. Sci.*, 2018, **9,** 7376.

(42) R. Moshwan, X.-L. Shi, W.-D. Liu, Y. Wang, S. Xu, J. Zou and Z.-G. Chen, *ACS Appl. Energy Mater.,* 2019, **2,** 2965.

(43) C. W. Li, J. Ma, H.B. Cao, A.F. May, D. L. Abernathy, G. Ehlers, C. Hoffmann, X. Wang, T. Hong, A. Huq, O. Gourdon and O. Delaire, *Phys. Rev. B: Condens. Matter Mater. Phys.,* 2014, **90,** 214303.

(44) G. A. S. Ribeiro, L. Paulatto, R. Bianco, I. Errea, F. Mauri and M. Calandra, *Phys. Rev. B: Condens. Matter Mater. Phys.,* 2018, **97,** 014306.

(45) W. Liu, X. Shi, R. Moshwan, M. Hong, L. Yang, Z.-G. Chen and J. Zou, *Sustainable Mater. Technol.,* 2018, **17,** e00076.

(46) X. Shi, A. Wu, W. Liu, R. Moshwan, Y. Wang, Z.-G. Chen and J. Zou, *ACS Nano*, 2018, **12,** 11417.

(47) M. Hong, Y. Wang, S. Xu, X. Shi, L. Chen, J. Zou and Z.-G. Chen, *Nano Energy*, 2019, **60,** 1.

(48) R. Moshwan, W.-D. Liu, X.-L. Shi, Y.-P. Wang, J. Zou and Z.-G. Chen, *Nano Energy*, 2019, **65,** 104056.

(49) R. Moshwan, X.-. Shi, W.D. Liu, L. Yang, Y. Wang, M. Hong, G. Auchterlonie, J. Zou and Z.-G. Chen, *ACS Appl. Mater. Interfaces,* 2018, **10,** 38944.

(50) A. Banik and K. Biswas, *J. Solid State Chem.,* 2016, **242,** 43.

(51) A. Banik, U.S. Shenoy, S. Anand, U. V. Waghmare and K. Biswas, *Chem. Mater.*, 2015, **27,** 581.

(52) D. K. Bhat and S. Shenoy U, *J. Phys. Chem. C,* 2017, **121,** 7123.

(53) L. Wang, X. Tan, G. Liu, J. Xu, H. Shao, B. Yu, H. Jiang, S. Yue and J. Jiang, *ACS Energy Lett.,* 2017, **2,** 1203.

(54) X. Tan, G. Liu, J. Xu, X. Tan, H. Shao, H. Hu, H. Jiang, Y. Lu and J. Jiang, *J. Materiomics*, 2018, **4,** 62

(55) D. K. Bhat and U. S. Shenoy, *Mater. Today Phys.,* 2018, **4,** 12.

(56) J. Q. Li, N. Yang, S. M. Li, Y. Li, F. S. Liu and W. Q. Ao, *J. Electron. Mater.*, 2018, **47,** 205.

(57) H.-S. Kim, Z. M. Gibbs, Y. Tang, H. Wang and G.J. Snyder, *APL Mater.*, 2015, **3,** 041506.

(58) M. Thesberg, H. Kosina and N. Neophytou, *Phys. Rev. B,* 2017, **95,** 125206.

(59) B. Mason, *Geol. Foren. Stockh. Forh.,* 1944, **66,** 27.

(60) J. P. Perdew, K. Burke and M. Ernzerhof, *Phys. Rev. Lett.,* 1996, **77,** 3865.

(61) J. Tang, B. Gao, S. Lin, J. Li, Z. Chen, F. Xiong, W. Li, Y. Chen and Y. Pei, *Adv. Funct. Mater.,* 2018, **28,** 1803586.
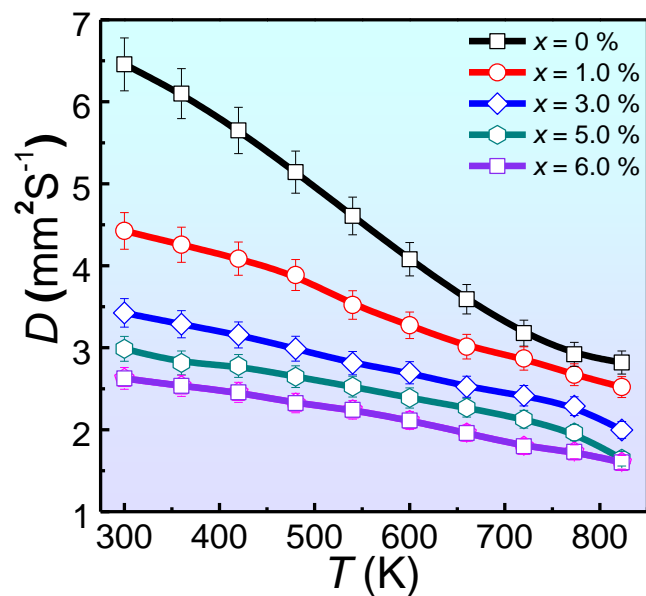
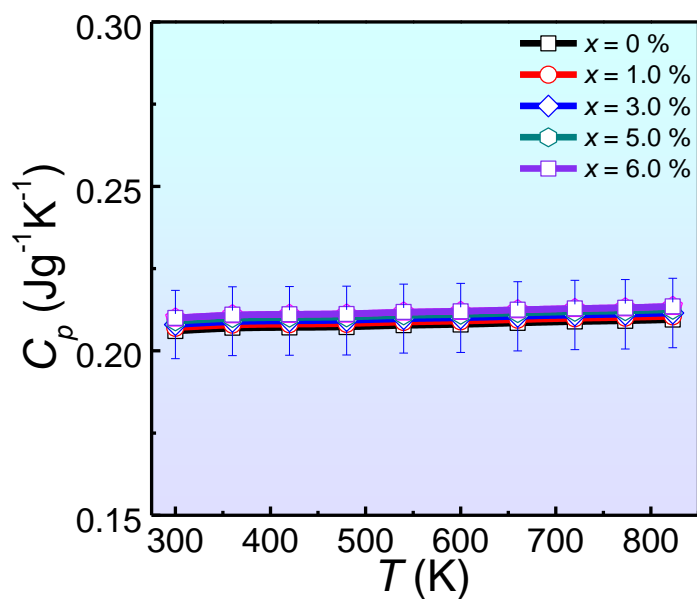**Figure 7.S1** Thermal diffusivity D as a function of temperature for different $Sn_{1-3x}In_xAg_{2x}Te$.

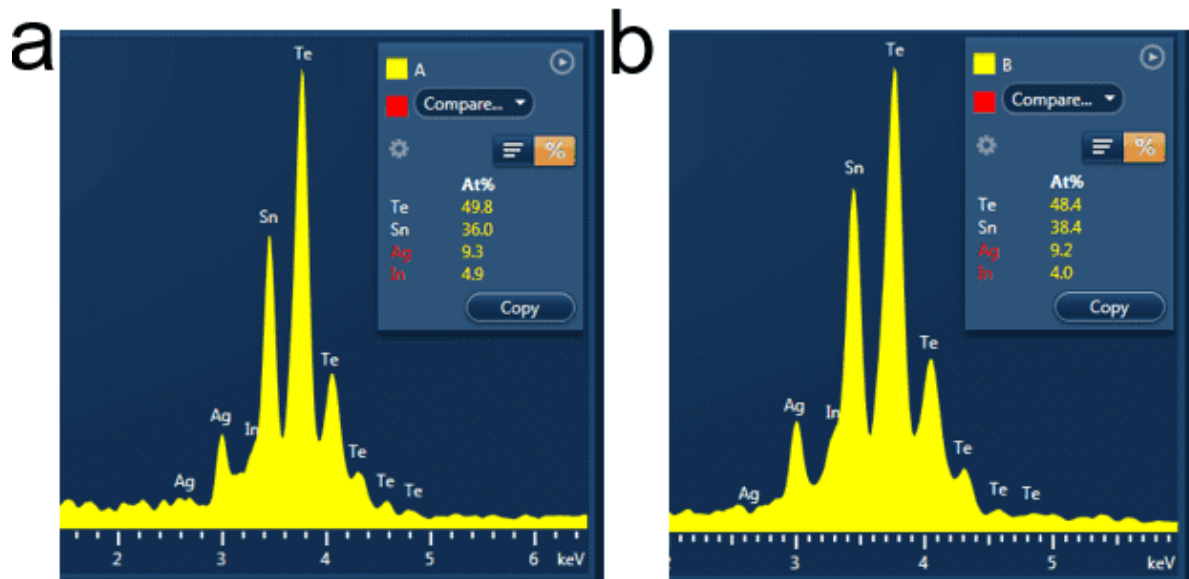**Figure 7.S2**. Specific heat (C_p) of $Sn_{1-3x}In_xAg_{2x}Te$ samples

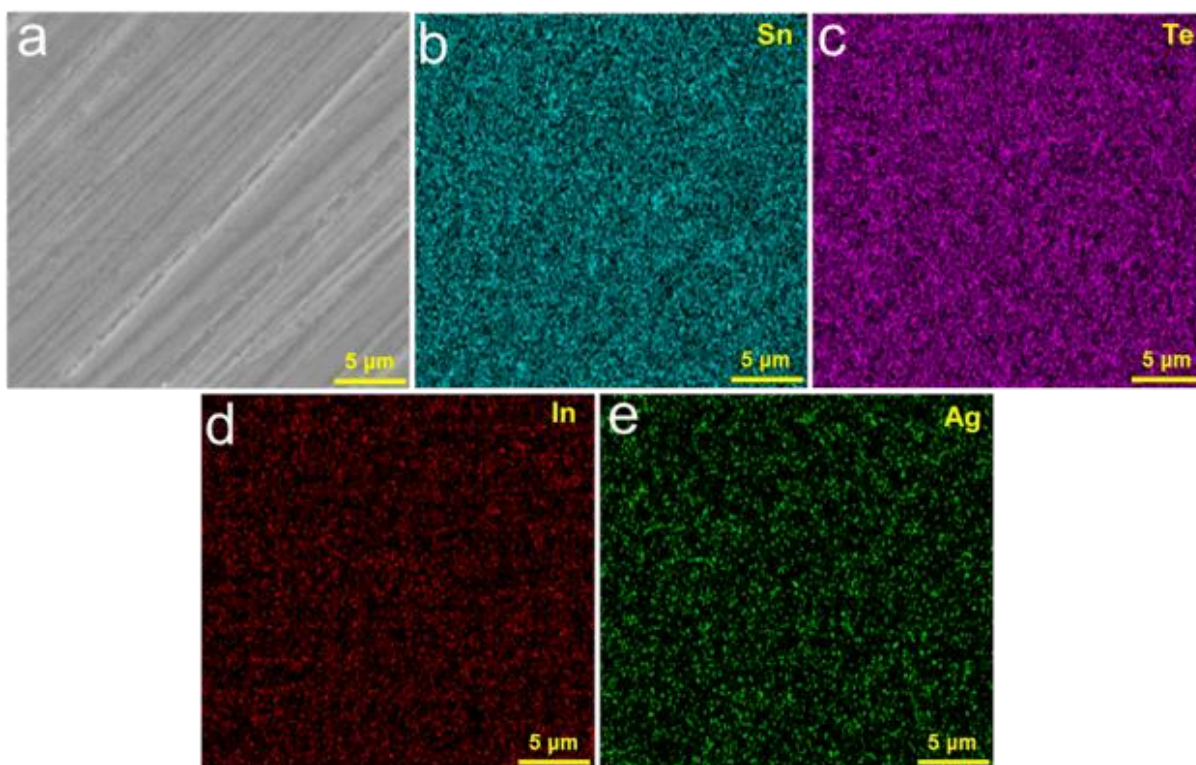**Figure 7.S3** EDS spectrum and compositional analyses of spot A and B from **Figure 7.1e**

Figure 7.S4 (a) A typical SEM image of the sintered $Sn_{0.85}In_{0.05}Ag_{0.10}Te$ pellet and (b-e) Corresponding EDS elemental map data of Sn, Te, In and Ag.
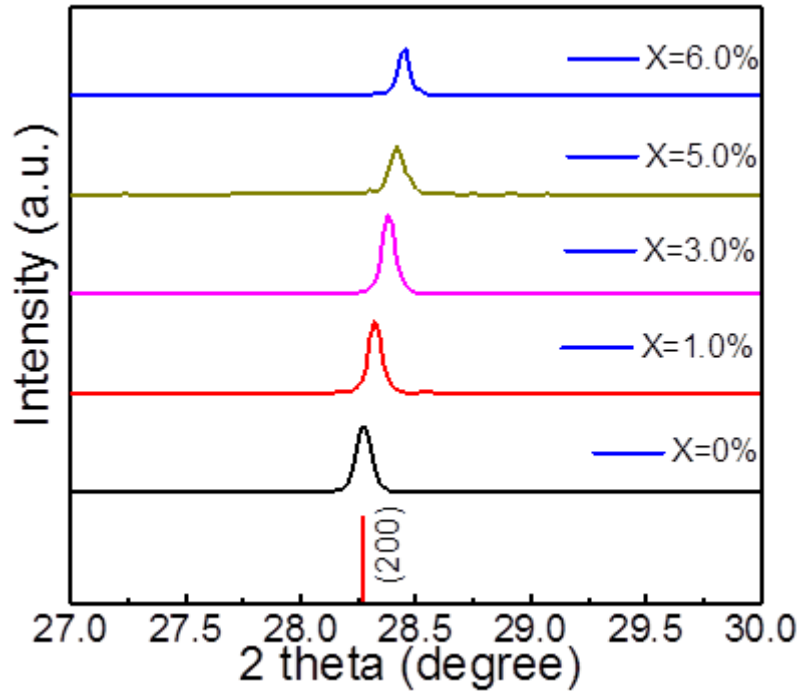
Figure 7.S5 Extended (200) peak of **Figure 2**a shows peaks are shifting towards higher angle demonstrating the lattice shrinkage of the lattice.
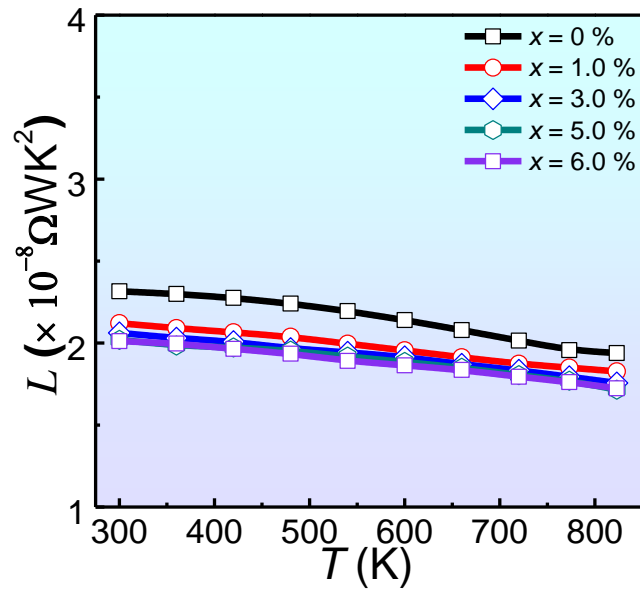

Figure 7.S6 Calculated Lorenz number L as function of temperature of $Sn_{1-3x}In_xAg_{2x}Te$.

Chapter 8. Conclusions and Recommendations

8.1 Conclusions

In this thesis, a comprehensive study on the key strategies responsible for thermoelectric performance enhancement of eco-friendly SnTe has been recapitulated. These include optimization of power factor by carrier optimization, resonance energy level, band convergence and band gap tuning and reducing lattice thermal conductivity by point defects, anharmonicity, grain boundaries and nanostructuring. The synergistic band engineering and structure engineering can improve the thermoelectric properties of SnTe to a great extent. We have carried out extensive experimental and theoretical studies consist of synthesizing micro-size particles, electronic microscopy characterization of synthesized and sintered samples, thermoelectric property measurements, density of states and band structure calculation. The existence of resonance energy level due to In doping in SnTe trigger the high power factor at room temperature. The co-doping of In/Cd with excess Te yielded superior figure of merit in SnTe. The appropriate ratio between In and Sr significantly enhance the thermoelectric properties of SnTe. The multi-scale phonon scattering source such as point defects, nanoprecipitates and grain boundaries is successfully realized through phonon modeling studies. In all, this PhD thesis provide a clear guidance to design high performance thermoelectric materials by doping, nanostructuring and band engineering. Specifically,

- In doped SnTe micro-size SnTe particles have been synthesized by solvothermal method. The distortion of density of states in the valence band of SnTe by In significantly enhance the pristine Seebeck from ~ 23 $\mu V K^{-1}$ to ~ 88 $\mu V K^{-1}$. In not only tune the density of states but also formed InTe nanoprecipitates. An extensive TEM analysis has been performed to investigate the structure of InTe nanoprecipitate and it is found that a face centred cubic structure. The slight variation of lattice parameters between InTe and SnTe evolves lattice dislocation in the matrix which is one of the key factor to reduce the lattice thermal conductivity of the system by scattering heat carrying phonons.

- Co-doping of In and Cd with excess Te has been well studied. Comparing with the Pisarenko plot based on a single parabolic band model the Seebeck coefficient of In/Cd co-doped SnTe system exhibited significantly high than the pristine SnTe. It is believed that the large valence band offset of SnTe considerably reduced by Cd which

allowed heavy hole valence band to participate in electron hole transport system. Additionally, numerous nanoprecipitates are formed in the matrix which is indexed as In_2Te_5 and CdTe. The existence of point defects, nanoprecipitates and grain boundaries significantly reduced total thermal conductivity of the system and thereby improved high thermoelectric performance.

- An appropriate dopant ratio of 1:2 between In and Sr synergistically improved electronic and thermal properties of In/Sr co-doped SnTe system through band engineering and structure engineering. The large atomic mass fluctuation between guest (Sr) and host (Sn) atoms strengthen the phonon scattering. Theoretical calculation suggest the modification of pristine SnTe band structure by In/Sr co-doping. The co-existence of resonance energy level and valence band convergence improved the electrical transport properties. High density of In and Sr rich nanoprecipitates cause strain defect which can strongly scatter phonons and reduce the lattice thermal conductivity leading to high *ZT*. We estimated the device efficiency based on average *ZT* and it is found that the device efficiency can be achieved up to 9.9 %.

- In/Ag co-doping in SnTe successfully realized by solvothermal synthesis method. Extensive theoretical calculations shows significant valence band convergence and principal band gap enlargement which enhanced *S* from ~95 μVK^{-1} in the pristine SnTe to ~178 μVK^{-1} in the $Sn_{0.85}In_{0.05}Ag_{0.10}Te$. The co-existence of point defects, strain field, dislocations and grain boundaries significantly reduced lattice thermal conductivity over a wide temperature range. Consequently, an outstanding peak *ZT* of ~1.38 was obtained in $Sn_{0.85}In_{0.05}Ag_{0.10}Te$ that is 4 times higher than that in the pristine SnTe

To conclude, this PhD thesis led to world leading journal publications including Advanced Functional Materials, Nano Energy, ACS Applied Materials & Interfaces and ACS Applied Energy Materials with one is submitted to Chemistry of Materials.

8.2 Recommendations

In terms of future work, following suggestions and recommendations can be marked

- The sizes of the synthesized crystals in this study are several micro-meters. It would be of interest to synthesize nano-meter size particles and their behavior on the thermoelectric properties of SnTe with suitable dopant. In this regard, the concentration and the amount of sodium hydroxide can be controlled during synthesis

process. Sintering parameters may need to be optimized to get a solid bulk sintered samples without any crack.

- Apart from the band structure calculation, phonon density of states calculation is also need to be studied to understand the phonon behavior in the system. Thus, one can get more clear idea about the phonon propagation, phonon scattering in the matrix.

- So far all the reported SnTe based thermoelectric materials are p-type. So, there is huge scope to do research to look for n-type SnTe materials.

It is also highly recommended to fabricate prototype device for the practical application. The *ZT* obtained from the bulk sample should be compared with the device efficiency.